ULB ECOLE POLYTECHNIQUE DE BRUXELLES

JG|U JOHANNES GUTENBERG UNIVERSITÄT MAINZ

Theoretical study of halos and neutron skins through nuclear reactions and electroweak probes

Thesis presented by Frederic COLOMER MARTINEZ

with a view to obtaining the PhD Degree in Engineering Science and Technology (ULB - "Docteur en Sciences de l'ingénieur et technologies") and in Physics (JGU)

Academic year 2019-2020

Supervisors :

Professor Pierre CAPEL (Université libre de Bruxelles)
Physique Nucléaire et Physique Quantique (CP 229)
Professor Marc VANDERHAEGHEN (Johannes Gutenberg Universität Mainz)
Institute for Nuclear Physics

Thesis jury :

Jean-Marc SPARENBERG (ULB, Chair)
Pierre CAPEL (co-supervisor ULB, Secretary)
Marc VANDERHAEGHEN (co-supervisor JGU)
Nathalie VAECK (ULB)
Concettina SFIENTI (JGU)
Peter SPICHTINGER (JGU)
Achim SCHWENK (Technische Universität Darmstadt)

PRISMA

Abstract

One-nucleon halo nuclei are exotic nuclei which can be seen as a core around which orbits a loosely-bound valence nucleon. They are usually studied through reactions such as elastic scattering and breakup. The ratio method has been developed as a tool to study one-neutron halo nuclei at high energies. It consists of the ratio of angular cross sections, breakup and elastic scattering, which removes most of the sensitivity to the reaction mechanism and to the reaction model. In the simple recoil excitation and breakup (REB) model, the ratio simplifies to a form factor dependent solely on the wave function of the projectile. By measuring this observable and comparing it to the REB form factor, i.e. in the ratio method, more detailed information on the structure of the halo could be obtained. For neutron-halo nuclei at high energy, the ratio observable obtained from accurate CDCC and DEA theoretical calculations follows its REB prediction. I study the extension of this method to lower energies of the reaction which could make the measurement appropriate to facilities such as SPIRAL2 (GANIL, Caen, France) and ReA12 at FRIB (Michigan State University) and to proton halos. This is done by comparing the REB form factor to dynamical calculations of the ratio. The reactions investigated are the reaction of ^{11}Be, the archetypical one-neutron halo nucleus, on ^{12}C, ^{40}Ca and ^{208}Pb targets at 20 MeV/nucleon and of ^{8}B, the archetypical one-proton halo nucleus, on ^{12}C, ^{58}Ni and ^{208}Pb targets at 44 MeV/nucleon.

For these reactions, the adiabatic assumption is no longer valid due to the effect of the Coulomb interaction. This effect is mainly visible at forward angle for ^{11}Be and is aggravated for ^{8}B by the fact that the halo is charged. The ratio works less well than for neutron-halos at intermediate and high energies. Nevertheless, the ratio is shown to be very sensitive to the orbital angular momentum l_0 in which the halo is bound and its binding energy E_0, i.e. the single-particle structure of the projectile. Variations of l_0 and E_0 induce visible changes in shape and in magnitude (up to several orders) of the ratio. Also, the agreement of the ratio with its REB prediction is best when the projectile is loosely-bound and for low l_0, i.e. for s and p waves. The validity of the method is not affected by the use of energy ranges—or bins— in the projectile continuum. These tend to increase the cross section without changing the agreement of the ratio with its REB prediction. The applicability of the method is finally explored at high energy for proton-rich nuclei ^{17}F, ^{25}Al and ^{27}P. I show that the ratio method works the latter since this nucleus is bound by a mere 0.870 MeV in the s-wave. For the other nuclei, although the agreement of the ratio with its REB prediction is less good than for neutron-halo nuclei at high energy, it still provides estimates of nuclear-structure features, such as l_0 and E_0 and could be applied in what can be called an approximate application of the ratio method.

Heavy nuclei exhibit a neutron skin, i.e. a thin layer around the nucleus where only neutrons are found. The thickness of the skin is highly correlated with the slope of the symmetry energy. The process of coherent neutral-pion photoproduction is used to extract the nuclear density and hence the neutron-skin thickness of heavy nuclei. In order to analyse recent data on the photoproduction on ^{12}C, ^{40,48}Ca, ^{116,120,124}Sn and ^{208}Pb, I build a reaction code. My model uses the formalism of Kerman, McManus and Thaler (KMT) which allows to build the photoproduction matrix on a nucleus from the ones describing the elementary process on a single nucleon. Within the impulse approximation,

the photoproduction is seen as the coherent sum of the photoproduction on each of the nucleons. In the plane wave impulse approximation (PWIA), no rescattering of the pion is considered after its production and the cross section is directly proportional to the Fourier transform of the density. Such process is taken into account at the distorted wave impulse approximation (DWIA) by considering a potential simulating the pion-nucleus interaction and built from the KMT formalism.

The agreement of my model with the data is good, especially for ^{208}Pb. The distortion has a significant impact on the photoproduction process. The sensitivity of the process to the density of the target is analysed by performing the calculations with several different densities calculated in different structure models. The distortion has the effect of deteriorating this sensitivity. In the particular case of a ^{208}Pb target, the impact of variations of the neutron-skin thickness Δr_{np} of around 0.1 fm on the photoproduction cross section is ten times smaller than the size of the error bars on the experimental data. These results, although less dramatic, hold for the tin targets, for which preliminary data exists. In the light of these results, the coherent neutral-pion photoproduction process does not seem to be suited in the study of the neutron-skin thickness. This conclusion goes in contrast to the results of recent measurements on ^{208}Pb, for which the method was shown to be sensitive to fine details of the density.

Keywords: Halo nuclei, ratio method, proton-rich nuclei, elastic scattering, breakup, CDCC, DEA, REB, neutron nkin, symmetry energy, coherent pion photoproduction, pion-nucleus potential, Kerman-McManus-Thaler formalism, impulse approximation, PWIA, DWIA.

Acknowledgements

On the one hand, this work is the accomplishment of several years of draining labour, where I have coped more than once with my incompetence. But on the other, it has also been an enlightening experience, where I have learned, learned from others and learned to know others. This formidable journey, in which I have oscillated between chaos, light, sadness, joy, despair, hope and all antonyms one could find, I could not have done it without the many people I have shared time with and who I would like to thank.

It would be difficult not to start by thanking Pierre Capel, my supervisor, who has supported me in all stages of this thesis. Thank you for giving me the taste of research, at the end of my bachelor degree already; for giving me the opportunity to experience research abroad at the start of my master's thesis, which was not only my first stay oversees but a confirmation that I wanted to become a doctor; for preparing me to this long journey and doing everything in your power to make sure I would be funded; and most of all, for your patience, kindness and unerring support during the early, middle and late stages of my work. Thank you for being the guide I have often needed.

Special thanks also go to Chloë, my colleague, my classmate but most of all my friend. She would probably not have started a PhD if I had not shown her the way... But I definitely would not have finished mine if she had not been there with me. What was once the distance separating a couple of doors in the hallway of the NO building has become the 350 km that separate Brussels and Mainz, but Chloë has always been there, pushing me forward in the bad moments and cheering for me in the good ones. At the time of writing these pages, she is preparing for her own defence. I wish her all the luck, even though I know she does not need any, and wish her all the best in her next adventure.

This thesis has been done in both the Université libre de Bruxelles and the Johannes Gutenberg-Universität Mainz, where I have met wonderful people that shaped the man I am today. This collaboration between both universities would not have been possible without the incredible help of Concettina Sfienti. Thank you for giving me this unique opportunity; for dealing with german burocracy nearly all by yourself to make it possible; for the help you have brought me throughout all this work. I would also like to thank Marc Vanderhaeghen, my co-supervisor, who accepted to foster me in his group.

I would like to thank all my colleagues, in Brussels and in Mainz, who have been there to exchange with me on physics but also on mundane subjects. A special thank to Jean-Marc Sparenberg, who has given me the wonderful opportunity to be one of his assistants and teach quantum mechanics to his bachelor students and another to Linda York, who has made everything possible to welcome me in Mainz in the best conditions and make me feel at home immediately.

Finally, I would like to thank my family, my friends and the friends I made along this journey for their support throughout these years. My warmest and deepest thank to my partner Sophie, who has never doubted me and has pushed me far more than she thinks she has (and trust me, this is a lot), for her love and her kindness and for enduring my long stays abroad; to Cédric and Dimitri, my room-mates, who accepted my strange sleep schedules and my laziness without (too much) complaining; to my brother Rafael and to Jean, my comrades from the Peña Barcelonista de la Plaine, with whom I have vibrated and cheered more than once; to Giom and Tim and *les meilleurs* and *les collègues* from Tops; to Alain and Breuls, who carried me through the deepness of tilt and bronze; to

Danny boy and Matthi boy, who met me with open arms when I arrived in Mainz for the first time and made sure I did not miss Belgian beer; to all that are not on this list but have made the man I am today. I don't thank half of you half as well as I should like, and I thank half of you only half as much as you deserve.

To my beloved grandfather, *papi Jorge*, who I deeply miss.

Seràs el vent que ens acarona.
El teu silenci serà la veu que ens abraça.

Contents

Introduction

Nuclear physics is the branch of physics that studies the nucleus, this object around which revolve the electrons to form the atom. About five orders of magnitude smaller than the atom, the nucleus is much denser. Thanks to Marsden and Geiger and their famous gold-foil experiment at the beginning of the 20^{th} century, we know the nucleus consists in a compact cluster of nucleons: the charged protons and the neutral neutrons. It is characterized by its mass number A, the number of nucleons of which it is made up, and its atomic number Z, the number of its protons. These Z protons and $N = A-Z$ neutrons are bound together through the nuclear strong interaction, an attractive force at short distances ($\sim$1 fm) but strongly repulsive at smaller scales. This short-range character and repulsive core causes the nuclear density to saturate around a density $\rho_0 \simeq 0.15$ fm^{-3}, the nuclear saturation density. As each nucleon then occupies an almost equal volume inside a nucleus, we can also define an average nucleon radius $r_0 \sim 1.2 - 1.4$ fm, which describes how much space it takes inside the nucleus. The nuclear radius R then goes as

$$R \simeq r_0 A^{1/3} \tag{1}$$

Because the strong interaction acts only at short distances, nucleons interact strongly only with their nearest neighbours. These properties are well described by liquid-droplet model of Bethe and Weiszäcker, which describes the nucleus as a quantum water droplet. As the forces on the nucleons of the surface are different from the forces in the interior where nucleons are completely surrounded by other attracting nucleons, a surface tension forms, just like it does for molecules in a drop of water. In this analogy, the binding energy of this drop can be defined as a volume contribution to which the surface tension is subtracted. As the volume goes as R^3, the volume term is hence proportional to the mass number A. The surface term is then proportional to R^2 and hence to $A^{2/3}$. In this *liquid-drop model* [1, 2] the Bethe-Weiszäcker semi-empirical formula describing the binding energy of a nucleus reads

$$B(Z,N) = a_V A - a_S A^{2/3} - a_C \frac{Z(Z-1)}{A^{1/3}} - a_A \frac{(N-Z)^2}{A} + \dots \tag{2}$$

where the first two terms are the volume and surface energies. Moreover, to account for the Coulomb repulsion between the protons, a Coulomb repulsive energy (proportional to the number of proton pairs $Z(Z-1)$) is added. Similarly, in order to model the Pauli exclusion and the strong interactions which both favour symmetric systems ($N = Z$), a symmetry energy (function of the asymmetry $\alpha = (N-Z)/A$) is added. Each of these four terms has a coefficient that is adjusted to reproduce the observed experimental value on the whole range of stable nuclei: a_V for the volume term, a_S for the surface term, a_C for the Coulomb repulsive term and a_A for the symmetry energy term. The binding energy per nucleon, which is the sum of the contributions of these different terms divided by the number of nucleons is shown in Fig. 1 as a function of the mass number. As should be noted, apart from some light nuclei, the Bethe-Weiszäcker semi-empirical formula works quite well.

As we have just seen, the proton and neutron distributions inside the nucleus are pretty much constant in the interior and then decay quickly at the surface, at a radius R. This type of behaviour can be modelled by a two-parameter Fermi-Dirac shape (2pF), which reads

$$\rho_{n,p}(r) \propto \frac{1}{1 + \exp\frac{(r-R_{n,p})}{d_{n,p}}} \tag{3}$$

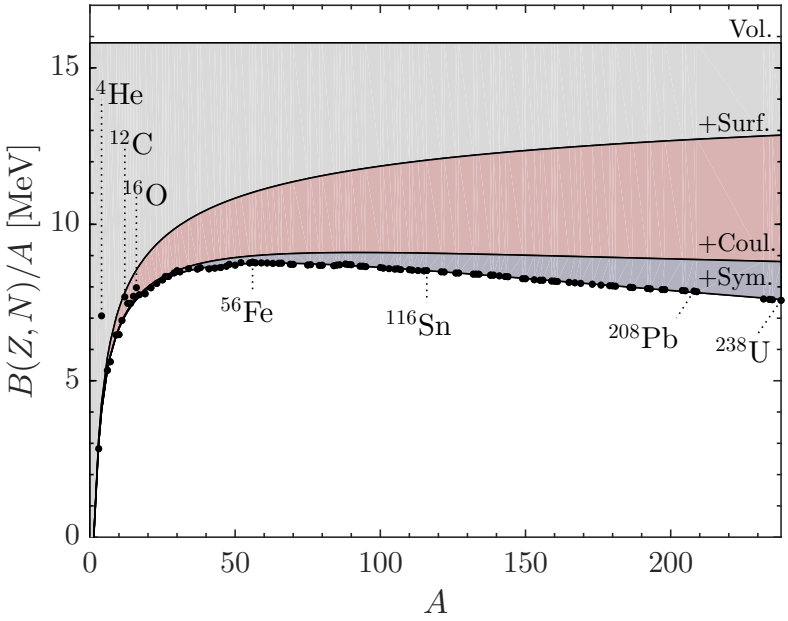

Figure 1: Experimental binding energy per nucleon and comparison to the different terms of the Bethe-Weizsäcker semi-empirical formula (2).

where $R_{n,(p)}$ is the neutron (proton) half-height radius and $d_{n,(p)}$ is the neutron (proton) diffuseness. Because of the charge independence of the strong interaction, stable nuclear symmetric systems exhibit very similar proton and neutron densities (their radii $R_n \simeq R_p$ and diffusenesses $d_n \simeq d_p$ are very similar). This situation is depicted on the left panel of Fig. 2.

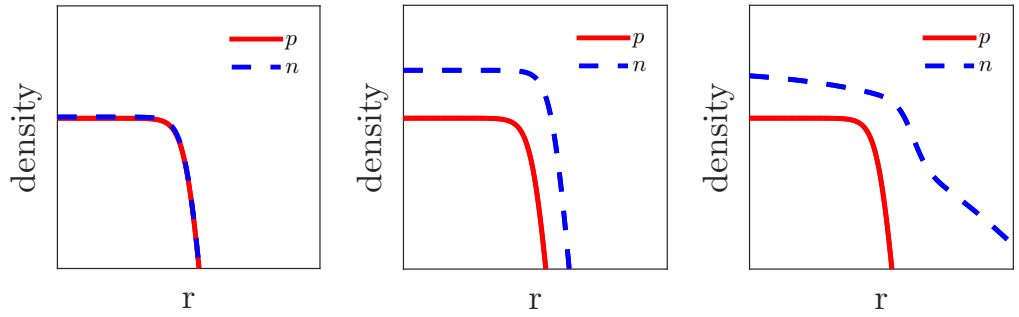

Figure 2: Typical shapes (in logarithmic scale) of proton (red) and neutron (blue) densities in the case of symmetric ($N = Z$) nuclear matter (left), asymmetric ($N \gg Z$) nuclear matter (middle) and halo-nuclei (right).

For heavy nuclei, for which $N \gg Z$, the excess neutrons are pushed towards the surface and the half-height radius of the neutron distribution is then larger than for protons $R_n > R_p$. However, their diffusenesses usually remain very similar $d_n \simeq d_p$. This is depicted on the middle panel of Fig. 2. As we can see from this cartoon, the nucleus seems to be surrounded by a thin layer, composed of only neutrons. This *neutron skin* can be characterized by its thickness Δr_{np}^A which is defined as the difference in the

root-mean-square (rms) radii of the neutron and proton distributions

$$\Delta r_{np}^{A} = \langle r_n^2 \rangle^{1/2} - \langle r_p^2 \rangle^{1/2}. \tag{4}$$

While charge-density measurements have confirmed this Fermi-Dirac shape to hold for stable isotopes with increasing precision throughout the years, this vision was challenged with the advent of Radioactive Ion Beams (RIB) facilities, which opened up the study of nuclear structure away from stability. This led to the discovery of *neutron halo nuclei* by Tannihata in 1985 [3], who showed that in the sector of light nuclei ($A < 20$) some radioactive nuclides have a matter radius much larger than their isobars, e.g. ^{11}Be, ^{11}Li or ^{6}He. This result was explained by their low one- or two-neutron separation energy. These loosely bound valence nucleons can tunnel way beyond the range of the strong interaction. Halo nuclei can thus be seen as a core, surrounded by a diffuse *halo*, as it was coined later in Ref. [4], formed by the loosely bound neutrons. Although less probable than neutron-halo nuclei, proton-halo nuclei also exist, such as ^{8}B, the archetypical one-proton halo nucleus.

To give an idea of the significance of this phenomenon, let us consider ^{11}Be, considered as the archetypical one-neutron halo nucleus. The size of its halo is comparable to the size of a gold nucleus, nearly 200 nucleons heavier [5]. The neutron density distributions of such nuclei, visible on the right panel of Fig. 2, is characterized by a long tail ($R_n \gg R_p$ and $d_n > d_p$) and challenges the naïve belief that the matter radius scales with $A^{1/3}$ [see Eq. (1)]. It thus questions the traditional vision of nuclei close to stability and the validity of nuclear structure models. By studying such exotic systems, nuclear physicists hope to better understand how the nuclear interaction works and hence improve their description of nuclear matter.

As we have just seen, the Bethe-Weizsäcker incompressible quantum liquid-drop model fails to reproduce exotic structures far from stability such as halos. While providing a fair description of the binding energy of stable nuclei with a handful parameters, the *incompressible* liquid-drop model obviously also fails to capture the response of the nucleus to variations of the density. Moreover, as the density of most of nuclei is usually found around but mostly below the saturation density ρ_0 and as only slightly asymmetric ($N \gtrsim Z$) nuclei can be found or created on earth, the properties of nuclear matter far from these conditions remains a mystery. All such knowledge is crucial for the study of one of the densest and asymmetric macroscopic system of our universe: the neutron stars.

Neutron stars are probably the most compact stars in the Universe. As their name states, they were first thought to be composed mainly of neutrons. However, it is not yet clear what their composition is. Their interior densities are larger than twice the nuclear saturation density ρ_0 [6]. Nuclear physicists often see them as the biggest neutron-rich nuclei in the Universe, with a number of nucleons around $A \sim 10^{56-57}$ [7]. Their masses range from 1 to 2 solar masses $M_\odot$ and their radii range from 10 to 14 km [7]. Our knowledge of the properties of such systems relies on theoretical models. One if not the main ingredient needed to calculate the structure of neutron stars is the equation of state of nuclear matter (EOSNM).

This equation that links the density to the energy of nuclear matter governs the properties of systems in an extremely wide range of sizes, from microscopic nuclei ($R \sim 10^{-15}$ m) to macroscopic objects such as neutron stars ($R \sim 10^{4}$ m). For this reason, it plays an essential role in our understanding of the links that exist between phenomena observed in laboratory experiments which probe the properties of exotic nuclei, nuclear structure, heavy ion collisions, *etc.* and phenomena of astrophysical interest such as

neutron stars cooling and their structure, supernovae, binary mergers, *etc.* [8, 9, 10]. Because the scope of this very elegant equation affects the nuclear structure, nuclear reactions as well as nuclear astrophysics, it is easy to understand why the knowledge of its details is so crucial to nuclear physics in general.

In order to better interpret the different terms of the EOSNM, it is insightful to start from the Bethe-Weizsäcker equation (2). When considering this equation for infinite nuclear matter in its thermodynamic limit (hence for A and the volume going to infinity while keeping the density of the system constant), the energy per nucleon reads (when neglecting the Coulomb force that would make the system unstable)

$$\frac{-B(Z,N)}{A} = \varepsilon_0 + J\alpha^2 + \dots \tag{5}$$

with the standrad notation $\varepsilon_0 = -a_V$ and $J = a_A$ and where we remind that $\alpha = (N-Z)/A$ is the neutron-proton asymmetry. When allowing for density fluctuations, this expression is usually written in the following compact form

$$\mathcal{E}(\rho,\alpha) = \mathcal{E}(\rho,\alpha=0) + \mathcal{S}(\rho)\alpha^2 + \mathcal{O}(\alpha^4) \tag{6}$$

where we have defined the sum of the neutron and proton densities $\rho = \rho_N + \rho_Z$ as the nuclear density and we have redefined the neutron-proton asymmetry as $\alpha = (\rho_N - \rho_Z)/\rho$. Here, $\mathcal{E}(\rho,\alpha=0)$ is the energy of symmetric nuclear matter (ε_0 at saturation $\rho=\rho_0$) and $\mathcal{S}(\rho)$ is what we usually define as the symmetry energy (J at saturation). It represents approximately the energy necessary to convert symmetric nuclear matter ($\alpha=0$) into pure neutron matter ($\alpha=1$). Decades of studies starting from the incompressible nuclear droplet model have rather well constrained the energy of symmetric matter. However, the knowledge of the symmetry energy and more particularly its density dependence, which makes the link between all the different nuclear physics fields, is still elusive. In the recent years, much effort has been devoted to the study of this fundamental quantity [8, 9, 10] and more particularly on its slope at saturation density which as the first order expansion of $\mathcal{S}(\rho)$, captures most of its density dependence around ρ_0. This slope (usually denoted by L) has important implications on the size of (asymmetric) heavy nuclei and more particularly on the thickness of their neutron skin (see Eq. (4)).

This can be qualitatively understood. In a nucleus, L quantifies the difference between the symmetry energy at the core (which is at saturation density) and at its surface (where the density is lower). While surface tension tends to push the excess neutrons inside the core to have a compact system, the symmetry energy term favours an equal number of protons and neutrons at saturation density and thus pushes these excess neutrons from the high-density core towards peripheral regions of the nucleus, where the density is lower. If L is large, the balance goes heavily in favour of the symmetry energy and the excess neutrons are strongly forced outwards, hence forming a thick neutron skin. The EOSNM is said to be *stiff*. If on the contrary L is small, this effect is smaller, and hence the neutron skin thinner. The EOSNM is then said to be *soft*. For this reason, the neutron skin should be highly correlated to L. This simple interpretation has been confirmed by mean-field calculations in Ref. [11] (see Fig. 3), where the predictions for the values of the neutron skin thickness and L of up to 50 relativistic and non-relativistic mean field models have shown to be nearly perfectly correlated.

As the heaviest nuclei in the universe, neutron stars are also influenced by the symmetry energy. Indeed, this term of the EOSNM impacts the pressure that reigns inside the star, and hence dictates the maximum mass they can reach [8]. This also has a direct

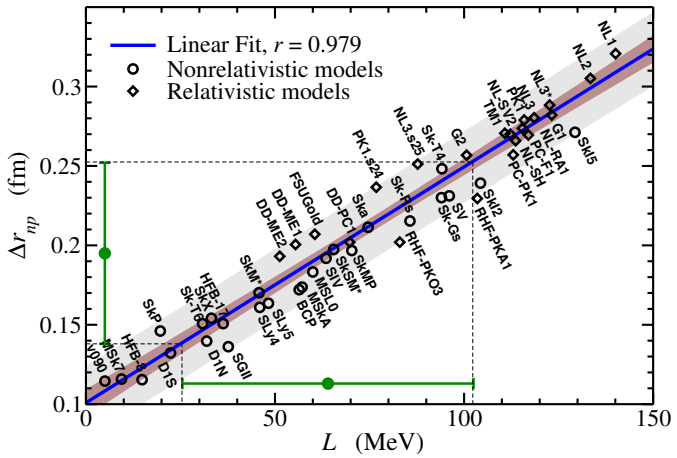

Figure 3: ^{208}Pb neutron skin thickness as a function of L for several mean field calculations. Figure taken from Ref. [11].

impact on the radius of such stars: if the symmetry energy is stiff, high densities are disfavoured as the energy increases rapidly with the density. The nuclear matter is then pushed outwards and the radius is large. If on the contrary the symmetry energy is soft, the energy grows much slower with density and high densities are not as much disfavoured. The radius is hence smaller. An example of soft and stiff symmetry energy dependencies are shown on left panel of Fig. 4. As we can see, the impact of L on the symmetry energy at densities above $2\rho_0$ is significant. The density dependence of the symmetry energy also influences how these stars cool [12].

The knowledge of the symmetry energy and its density dependence (especially L) is hence crucial in the study of nuclear systems in a whole range of scales and energies. Since the neutron-skin thickness Eq. (4) is strongly correlated to L [see Fig. 3], the measurement of Δr_{np} should be a nice way to constrain the symmetry energy.

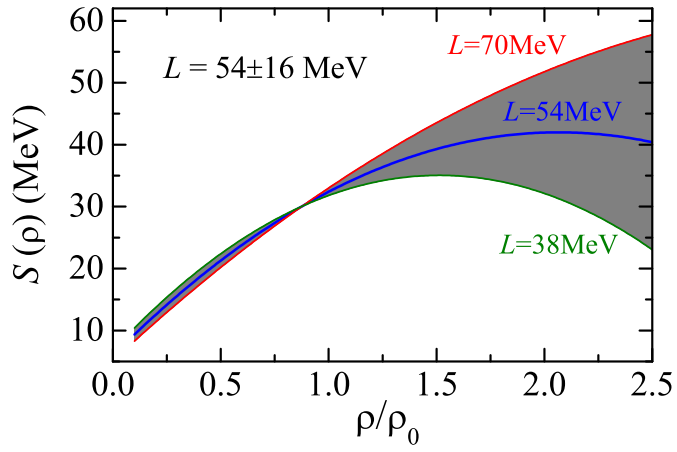

Figure 4: Density dependences of the symmetry energy. A "soft" symmetry energy is displayed in green while a "stiff" one is displayed in red. Figure taken from Ref. [13].

As we have seen, halos and skins have become two important talking point in today's nuclear physics. My thesis comes within the scope of these two hot topics and more particularly on the tools that are used in these two separate fields. On the one hand, my work on halos aims at the investigation of the reliability and the sensitivity of a new technique for the analysis of one-nucleon halo nuclei: the *ratio* method, which is the subject of Chapter I. On the other hand, my work on neutron-skins aims at the analysis the process of coherent neutral-pion photoproduction and its sensitivity to the neutron-skin thickness in heavy nuclei. This will be the subject of Chapter II.

Chapter I

The ratio method

1 Halo nuclei

Halo nuclei are very neutron-rich systems that can be found near or at the driplines. Since the discovery of ^{11}Li, ^{11}Be and ^{6}He as the first halo nuclei by Tanihata [3], several other nuclear systems with neutron halos have been reported such as ^{15}C and ^{19}C, which, like ^{11}Be, exhibit a *one*-neutron halo (see left panel of Fig. 1.1), and ^{14}Be, which, like ^{11}Li and ^{6}He, exhibits a *two*-neutron halo (see middle panel of Fig. 1.1). In addition to their unusual halo, two-neutron halos exhibit a very peculiar property: while the three-body system is bound, none of the two-body sub-systems are. They are also known as Borromean systems, in reference to the rings that symbolize the Borromeo family and which are depicted on the right panel of Fig. 1.1.

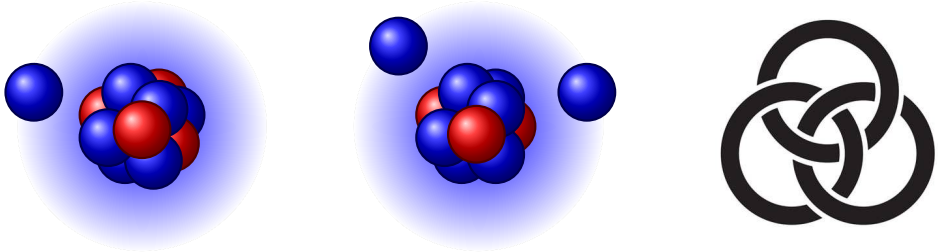

Figure 1.1: Schematic view of ^{11}Be, a one-neutron halo nuclei (left) and ^{11}Li, a two-neutron halo nuclei (middle) in addition to Borromean rings (right) that are present on the coat of arms of the Borromeo family and which are entangled in such a way that by breaking one ring, we release the others.

Note that, although less probable than for neutron halos, the formation of proton halos is also possible and nuclei such as ^{8}B and the first excited state of ^{17}F exhibit a one-proton-halo-candidate structure. A look at the light sector of the nuclei chart in Fig. 1.2 illustrates where halo nuclei can be found.

In this section, I briefly review the main characteristics of halos nuclei. We will also see how and why halos form and how we can probe their structure experimentally.

1.1 The halo structure

As we have already seen, halo nuclei have large matter radii. But is it sufficient to be spatially large to be considered as a halo? What differentiates a halo from a skin? What is meant by *large* anyway? In fact, there is no clear definition of what a halo nucleus is and whether a nucleus exhibits a halo or not is to some degree a matter of taste. In this work, we will define the halo as in Ref. [14]: *Quantum halos are defined as systems with dominating few-body structure and radii large compared to the sizes of the classically allowed regions.*

In other words, the total many-body wave function of a halo nucleus must thus first exhibit a clear cluster structure, in which the halo nucleon(s) is (are) decoupled from a core. The core therefore exhibits more or less the same properties as if it were considered without its halo. Second, the halo nucleon(s) must spend a significant part of their time in the non-classical region. Accordingly, their wave function must exhibit a large probability f_h of tunneling into the non-classical region outside of the field of the core. Some authors require $f_h > 0.5$ in order to consider the nucleus to exhibit a halo [14, 15]. This is rather

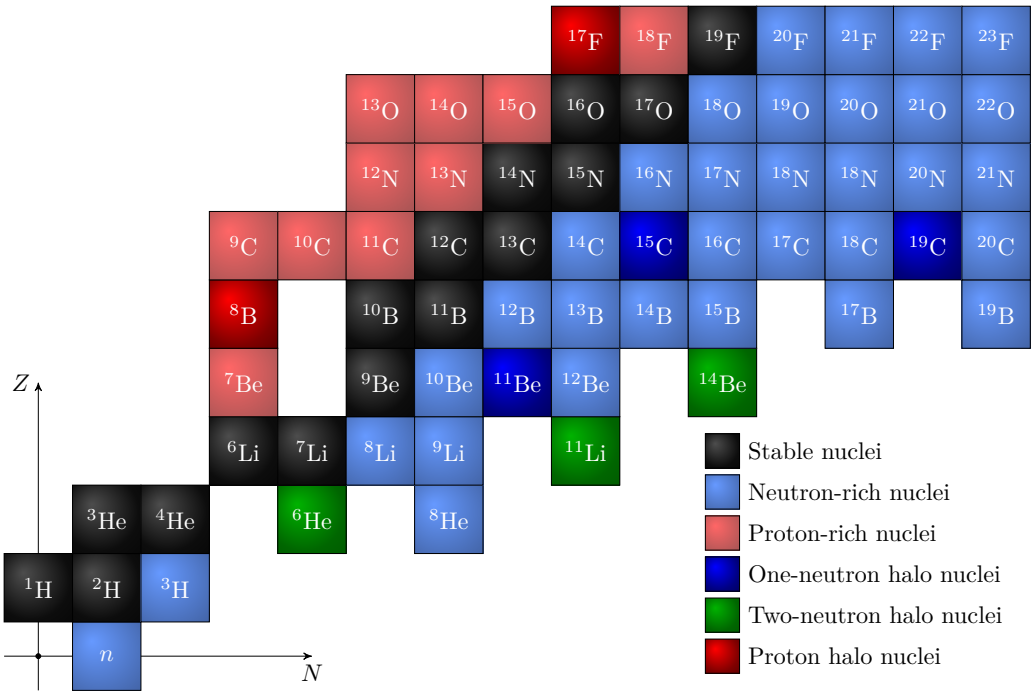

Figure 1.2: Nuclear chart for light nuclei.

restrictive and in fact, no actual halo nuclei exhibits this property. Here, we will not make such restrictive requirement. In order to get a significant tunneling, halo nucleon(s) must be (very) loosely bound to the core.

We see that from this definition, halos and skins are different in essence and arise from very distinct mechanisms. Whereas both the neutron skin (in heavy nuclei) and neutron halos (in light nuclei) originate from a very large neutron to proton asymmetry, the neutrons of the skin are part of the bulk of the neutron matter, which extends beyond the proton matter but exhibits a very similar surface diffuseness [15]. These skin neutrons do not decouple from the core like halo neutrons. This mainly originates from the fact that the halo phenomenon is a threshold effect that exists only close to (or even at) the driplines.

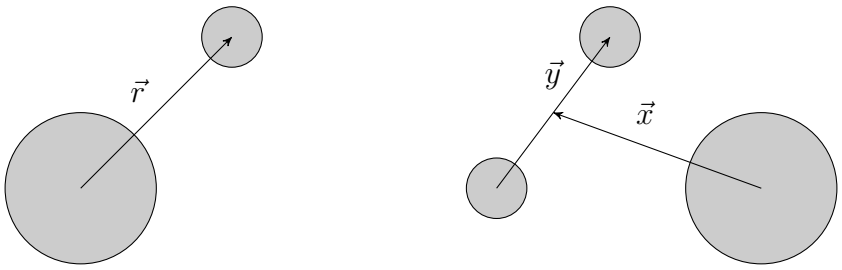

Figure 1.3: Jacobi coordinates of a two-body system (left) and three-body system (right).

To illustrate why halo form, let us describe a one neutron halo as a two-body system composed of a neutron of mass m_n bound by an energy S_n to an inert structureless core of mass m_c (see left panel of Fig. 1.3). The strong interaction between the valence neutron

and the core is modelled by a short-range potential V (whose range is typically 2 to 3 fm for light nuclei). For simplicity of the discussion, the spherical symmetry of the system is assumed and no spins are considered. The wave function $\psi_{lm}(\vec{r})$ that describes the halo-core relative motion in a given state of quantum numbers $\{lm\}$ can be separated into its radial and angular parts as

$$\psi_{lm}(\vec{r}) = R_l(r)Y_{lm}(\Omega) \tag{1.1}$$

where $Y_{lm}(\Omega)$ are the spherical harmonics. The radial wave-function $u_l(r) = rR_l(r)$ then obeys the Schrödinger equation

$$\left[-\frac{d^2}{dr^2} + \frac{l(l+1)}{r^2} + \frac{2\mu}{\hbar^2}V(r)\right] u_l(r) = -\kappa^2 u_l(r) \tag{1.2}$$

where l is the orbital angular momentum quantum number of the halo, $\kappa = \sqrt{2\mu S_n}/\hbar$ and $\mu = m_c m_n/(m_c + m_n)$ is the reduced mass of the neutron-core system. For $l \neq 0$, a centrifugal barrier appears and adds a repulsive component to the potential. This has the effect of pushing the neutron inside the well and hence leads to a smaller probability of presence of the neutron far from the core.

It is interesting to illustrate this on a specific example: the one neutron halo nucleus ^{11}Be. Let us pick a very simple real potential with a Woods-Saxon shape. On the left panel of Fig. 1.4, the effective potential that produces a bound state with 504 keV binding energy (note how much smaller this binding energy is than the ∼8 MeV per nucleon usually encountered in stable nuclei, see Fig. 1) is displayed in different orbitals. The classical turning point (the radius at which the effective potential equals the binding energy of the halo) is represented as a black dot. On the right panel, the radial wave function of these different bound states is represented with their rms radius (marked with a small circle on both panels). As we can see, because of the small binding energy, the exponential decay of the wave function is slow. But while it has the same (logarithmic) slope for all l (it only depends on the binding energy, see later Eq. (1.3)), we can see how the wave function at large distances is increasingly suppressed as l grows larger. For this reason, the rms radius of the halo decreases as l increases and as the centrifugal barrier becomes more significant. It should be noted how the rms radius of the halo extends well beyond the classical forbidden region in the $l = 0$ and 1 cases.

This can be explained very qualitatively. For a nucleus to exhibit a halo, its valence neutron must be have a high probability of presence outside of the potential well. Many of its properties will thus depend only on the asymptotic part of the halo-neutron wave function and the details of the internal part of the potential do not really matter in this discussion [4]. Outside the range of the potential, the tail of the valence radial wavefunction then reads

$$u_l(r) \xrightarrow{r\to\infty} e^{-\kappa r} \tag{1.3}$$

This exponential behaviour is visible on the right panel of Fig. 1.4. As the binding energy decreases, the exponential decrease of the tail is slower. To have a rough idea of the dependence of the size of such halo on the binding energy, we could also calculate an approximate rms radius, which in the case of an s-wave reads

$$\tilde{r}_{\text{rms}} = \sqrt{\langle r^2 \rangle} \propto \frac{1}{(\mu S_n)^{3/4}} \tag{1.4}$$

As we can see, as the binding energy goes to 0, the rms radius diverges and we could hence imagine halos of arbitrary size in the s wave. For $l = 1, 2, \ldots$ waves, the effective

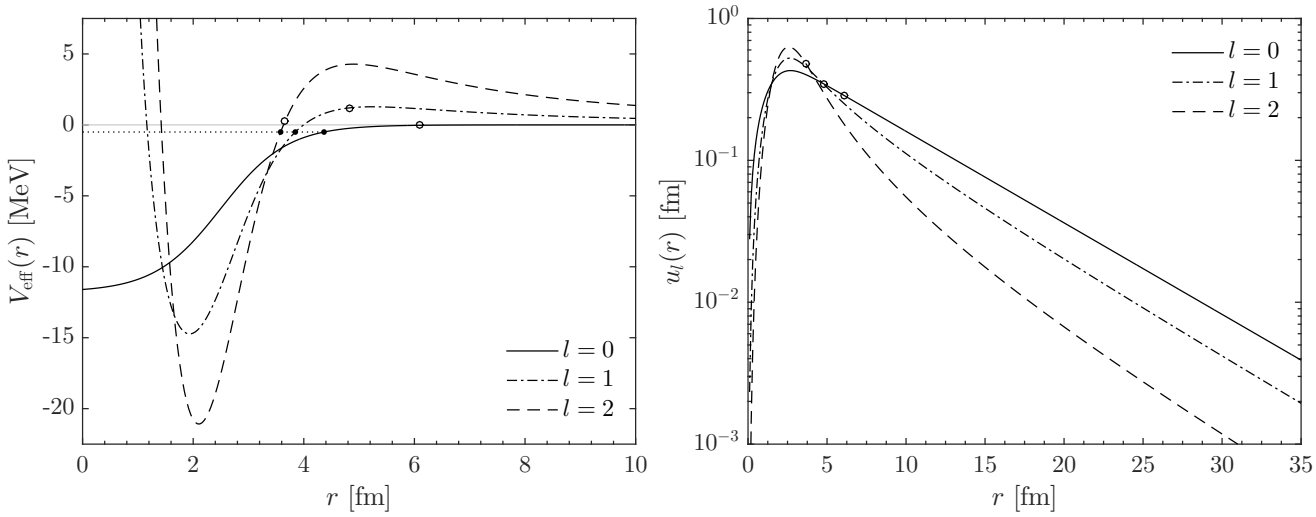

Figure 1.4: Left: effective potential of a one-neutron halo bound by 504 keV (the binding energy of the valence neutron in ^{11}Be). We use a very simple real potential shaped as a Woods-Saxon well. The classical turning point of each potential (black dot) and the rms radius of the bound state (circle) are also represented for each wave. Right: wave function in each partial wave. The rms radius is also represented (circle).

potential is modified by the centrifugal barrier which tends to push the neutron inside the well (see Fig. 1.4). The problem can be solved in the limit of low binding energy in order to generalise the result above for any l. It can be shown that [16]

$$\langle r^m \rangle \propto \begin{cases} (\mu S_n)^{(2l-1-m)/2} & \text{if } \; m > 2l-1 \\ \ln(\mu S_n) & \text{if } \; m = 2l-1 \\ \text{cst} & \text{if } \; m < 2l-1 \end{cases} \tag{1.5}$$

The rms radius ($m = 2$) can thus diverge only for $l = 0$ and 1. For $l \geq 2$, the radius remains bounded as the energy decreases. This very simple picture can be used to produce universal scaling plots that relate the scaled binding energies and radii of several nuclei. The scale of the system R is usually chosen as the range of the core-neutron interaction or as the classical turning point, the distance where binding energy and potential energy are equal. These scaling plots can be useful to evaluate halo candidates [14, 15]. They will not be discussed here.

A similar study can be extended to two-neutron halos. As there are now three bodies, the internal movement of the halo can be described by two vectors $\vec{x}$ and $\vec{y}$. These are shown on the right panel of Fig. 1.3 and are the Jacobi coordinates of the system. It should be noted that these are not simply spatial coordinates. Their definition contains mass ratios and is not unique and will not be explicitly displayed here. If we define $\rho_r = \sqrt{x^2 + y^2}$ as the hyper-radius, the wave function that describes the halo-core relative motion in a certain state ψ_{LM} can be separated into its (hyper-)radial and (hyper-)angular parts as [17]

$$\psi_{LM}(\vec{x}, \vec{y}) = \sum_{\gamma K} R_{\gamma K}(\rho_r) \mathcal{Y}^{LM}_{\gamma K}(\Omega_5) \tag{1.6}$$

where γ stands for the quantum numbers $\{l_x, l_y, L\}$ where l_x and l_y are the orbital angular momentum quantum numbers associated to the two coordinates, L is the total orbital

angular momentum of the state and M its projection, $\mathcal{Y}_{\gamma K}^{LM}(\Omega_5)$ are the hyper-spherical harmonics of the hyper-angle Ω_5 [18]. $K \geq l_x + l_y$ is the hyper-moment quantum number and can be seen as an extension of the concept of angular momentum to three-body systems. It should be noted however that unlike the orbital quantum number l encountered in the one-neutron halo, K is not a good quantum number. Indeed, in a given state $\{L, M\}$, an infinite number of values of K are possible and they hence need to be summed over.

The main interest of hyper-spherical coordinates is that we can reduce the three-body Schrödinger equation to a 'radial' equation in these hyper-spherical coordinates [18]. This leads to a Schrödinger equation on the only variable ρ_r which is very similar to Eq. (1.2). Outside of the range of the potential, the centrifugal barrier has the similar form $(K + 3/2)(K + 5/2)/\rho_r^2$ [19]. It can be shown that similarly to Eq. (1.3), the asymptotic part of the radial two-neutron halo reads [18]

$$R_{\gamma K}(\rho_r) \xrightarrow{\rho_r \to \infty} \frac{e^{-\kappa \rho_r}}{\rho_r^{5/2}} \tag{1.7}$$

where here $\kappa = \sqrt{2m_n S_{2n}}/\hbar$. The main difference between one and two-neutron halos in this approach is the fact that a centrifugal barrier exists in three-body systems even for $K = 0$, which corresponds to relative s-waves between the two neutrons and between their centre of mass and the core. This causes two-body halos to be much less divergent than their one-neutron counterparts ($K = 0$ has an "effective l" of $3/2$, which corresponds to logarithmic divergence, see Eq. (1.5)). However, the higher number of degrees of freedom in the halo and the correlations between the halo neutrons can increase the size of the system [15].

Proton halo nuclei are also possible. However, the long-range Coulomb repulsive potential acts just as the centrifugal barrier and pushes the proton inside of the well and reduces their probability of tunnelling into the non-classical region. For these reasons, proton halos are less probable. Notable one-proton halo nuclei are ^{8}B and the first excited state of ^{17}F. Finally, the ^{17}Ne is a strong candidate to be a two-proton halo [20].

Table I.1 summarizes the main configuration and binding energy of some established halo nuclei [21]. As it should be noted, their binding energy is often of the order of hundreds of keV. This illustrates the fact that the halo phenomenon is a threshold effect. Because of the strong decoupling between the halo and the core, the nucleon of the halo will usually exhibit a strong single-particle behaviour and will thus be found mainly in a single orbital, usually an s or p wave, as should be expected from our discussion above. However, two-body halos exhibit much larger contributions from several orbitals (even d waves in the case of ^{14}Be!).

1.2 Experimental probes of the halo structure

Because they are be found far from the valley of stability, halo nuclei are short-lived (usually less than a second) and cannot be studied easily through usual spectroscopic techniques. They are rather studied in *inverse kinematics*, that is, through reactions in which the halo nucleus is the projectile rather than the target. Such exotic beams can be produced either through in-flight separation of projectile fragments or through ISOL (isotope separation on line) techniques [22]. In the in-flight separation, heavy ions impinge on a thin and light target at high energy and are fragmented into lighter products that retain most of the momentum of the beam. These are then selected electromagnetically.

Halo nucleus	Main orbital(s)	$S_{n/2n}$ [MeV]	Half-life [s]
$^{11}\mathrm{Be} \equiv {}^{10}\mathrm{Be} + 1n$	$1s$	0.504	13.7
$^{15}\mathrm{C} \equiv {}^{14}\mathrm{C} + 1n$	$1s$	1.218	2.45
$^{19}\mathrm{C} \equiv {}^{18}\mathrm{C} + 1n$	$1s$	0.580	$46\ 10^{-3}$
$^{6}\mathrm{He} \equiv {}^{4}\mathrm{He} + 2n$	$0p$	0.972	0.806
$^{11}\mathrm{Li} \equiv {}^{9}\mathrm{Li} + 2n$	$0p$-$1s$	0.300	$8.74\ 10^{-3}$
$^{14}\mathrm{Be} \equiv {}^{12}\mathrm{Be} + 2n$	$0p$-$1s$-$0d$	1.260	$4.65\ 10^{-3}$
$^{8}\mathrm{B} \equiv {}^{7}\mathrm{Be} + 1p$	$0p$	0.138	0.770
$^{17}\mathrm{F}^{*} \equiv {}^{16}\mathrm{O} + 1p$	$1s$	0.105	64.4

Table I.1: Principal configuration, binding energy and half-lives of some established halo nuclei. Most values are from [Lect. Notes. Phys700, 1]. The half-lives come from http://www.tunl.duke.edu/nucldata/HalfLife.shtml and from the references therein. The halo state of $^{17}\mathrm{F}^{*}$ only exists in an excited state, which decays though electromagnetic decay into $^{17}\mathrm{F}$ ground state, which has the half-life given here.

In ISOL facilities, a beam of very light ions or neutrons bombard a thick and heavy target on which spallation and fusion occur. The reaction products diffuse then effuse from the target and are picked through chemical selection and electromagnetic separation and finally post accelerated. For more information on these techniques, we refer the reader to Refs. [23, 24, 25] and references therein.

Once these nuclei are produced, different experimental techniques can provide us with valuable information on the characteristics of the halo. Some of these techniques are briefly reviewed here.

Nuclear reactions have been studied in a wide range of energies, from low energies around and below the Coulomb barrier ($\lesssim$10 MeV/u) to high energies (>100 MeV/u) where the short reaction time allows for a simpler treatment of the interaction mechanism. The main types of nuclear reactions used to probe the structure of halo nuclei are elastic scattering (in which the halo nucleus is simply deflected by the target and remains in its groundstate), inelastic scattering (in which the projectile or the target are excited), transfer reactions (in which one or several nucleon(s) are transferred between the projectile and the target), knockout/breakup (in which the halo structure of the projectile breaks).

The first experiments on exotic beams measured the interaction cross section σ_I [3]. This observable is defined as the total cross section for the change of proton and/or neutron number in the incident nucleus. This measurement is quite simple as only charged nuclei need to be measured before and after the reaction. At high energies, the collision is so fast that the nucleons of the projectile and target nucleus appear frozen. The nucleons then can be assumed to interact individually. Both the projectile and the target can then be seen as spheres and in a simple geometrical model [3, 26], the interaction cross section reads

$$\sigma_I = \pi(R_{I,P} + R_{I,T})^2 \tag{1.8}$$

where $R_{I,P}$ ($R_{I,T}$) is the projectile (target) interaction radius (this radius can be seen as the matter radius defined in Eq. (1)). This simple expression was the one used in [3] in the analysis of the interaction cross section of several isotopes of He and Li. They observed for the first time a clear enhancement of the interaction radius in ^{11}Li and ^{6}He which was later attributed to the halo phenomenon [4]. The interaction radii of He, Be and Li nuclei

extracted from the analysis of Refs. [27, 28] are represented on Fig. 1.5. All halo nuclei have a significantly larger interaction radius compared to neighbouring isotopes and to Eq.(1). Note that ^{6}He, although seemingly following Eq.(1), is much larger than the very compact ^{4}He.

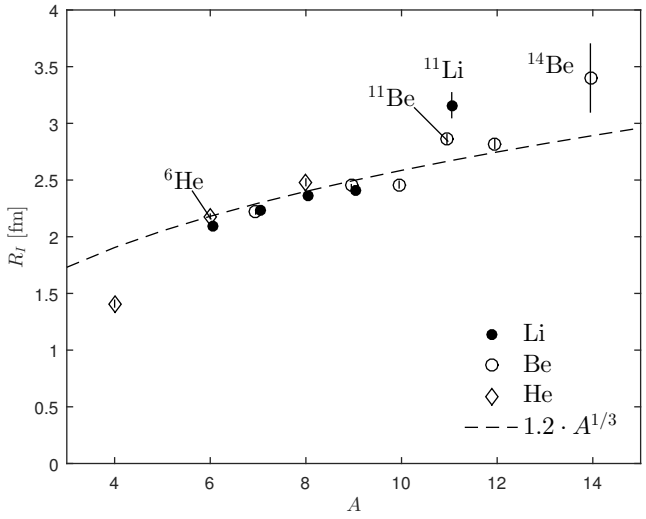

Figure 1.5: Interaction radii of Li, Be and He isotopes as a function of their mass number A and comparison to Eq.(1) for $r_0 = 1.2$ fm. Values taken from Refs. [27, 28].

Another observable that was analysed in the early days of exotic beams is the parallel and transverse momentum distributions of the fragments following the knockout of the nucleus. If we consider the reaction to be adiabatic, the core is seen as frozen during the reaction. As its nucleons have no time to rearrange, the core then keeps the same momentum distribution as before the reaction. If we then neglect the importance of the contribution of nucleons of the core to this cross section, the large spatial extent of the halo leads to narrow momentum distributions. This inevitably recalls the famous Heisenberg inequalities and the impossibility for canonically conjugate variables such as position and momentum to be known with arbitrary precision simultaneously. The less precisely the position of the halo is determined (i.e. the more extended the halo is), the more precisely its momentum can be known, and vice versa. This can be easily illustrated if we assume the wave function of an extreme halo nucleus as a simple Yukawa wave function of the type of (1.3). The Fourier transform of such wave function has a Lorentzian shape and hence in a simple geometrical model, the longitudinal momentum distribution cross section reads [19]

$$\frac{d\sigma}{dp_{||}} \propto \frac{1}{p_{||}^2 + \kappa^2} \tag{1.9}$$

As we can see, the smaller the binding energy, the larger the extent of the halo and hence the narrower the momentum distribution. By measuring the momentum distribution of the core or of the halo neutron(s), we then gain valuable information on the structure of the halo. This measurement is a bit more complex than the interaction cross section measurement above since we need to measure only one type of reaction product. Statistics are hence lower and a higher beam intensity is needed.

Parallel and transverse momentum distributions were first measured in Ref. [29], in which an extremely narrow transverse momentum distribution of ^{9}Li fragments was compared to the one of ^{12}C and confirmed for parallel momentum in Ref. [30]. A nice illustration of this phenomenon is shown in Fig. 1.6 where the comparison of such distribution is made on several light nuclei. The first feature that is apparent is the marked reduction of the core momentum distribution as the $N = 8$ shell (dashed red line) and $N = 14$ subshells (dashed blue line) are crossed. Secondly, we can see how the parallel momentum distribution for ^{15}C is significantly narrower than the neighbouring C isotopes, which is characteristic of halo nuclei.

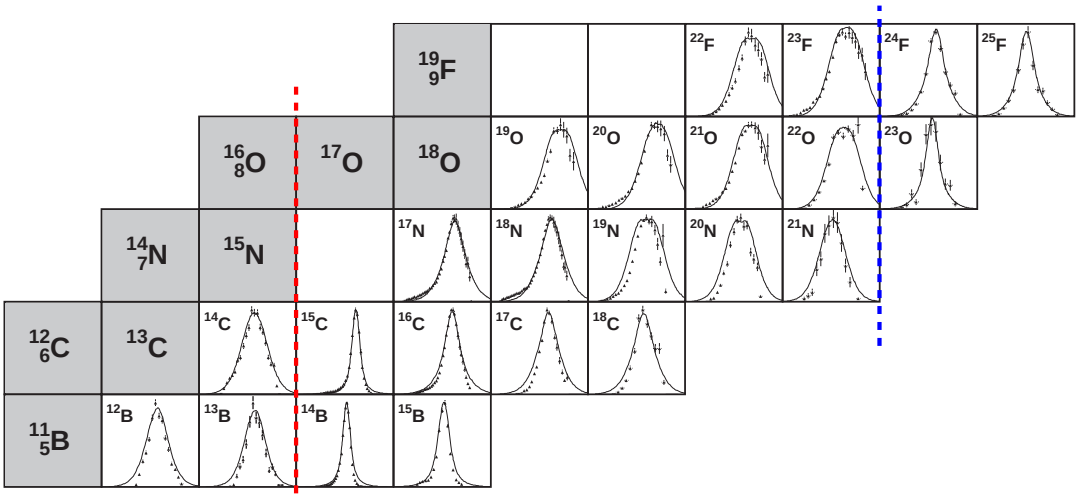

Figure 1.6: Core fragment parallel momentum distributions for one-neutron removal on a carbon target. The red and blue lines correspond to $N = 8$ shell and $N = 14$ sub-shell closures. It should be noted how the distribution for ^{15}C is significantly narrower than other isotopes of C. Figure taken from Ref. [31].

This method can also be used to gain information about the orbital in which the halo is bound. This is illustrated on Fig. 1.7 for the ^{11}Be halo nucleus. In this measurement, the parallel momentum distribution for the ^{10}Be fragment are compared to calculations where three different orbital configurations for the halo neutron are considered: an s, p and d waves. As can be seen, $l = 0$ calculations reproduce best the data, which means that the halo state of ^{11}Be can be seen as a $1s1/2$ neutron bound to a ^{10}Be core in its O^{+} ground state (see also Tab. I.1).

Another way to probe halos is through electromagnetic processes. Because of the r^{λ} term contained in the Eλ transitions operators, the strength of these processes are enhanced by the large extent of halos. Experimentally, the E1 strength can be probed through the measurement of the breakup of the halo after heavy-ion induced electromagnetic excitation (Coulomb breakup). The electromagnetic dissociation cross section of ^{11}Li on ^{208}Pb, indeed proved to be unusually large compared to the one with a ^{12}C beam in Ref. [33]. This was related to a soft E1 excitation at low excitation energy, as predicted in Ref. [4]. If the contribution to the E1 strength originating from the halo can be extracted then information on its spatial extent can be inferred. Note that because of the small binding energies of halo nuclei, the cross sections for these processes are large.

These "first generation experiments" were rather simplistic and did not have a full understanding of every detail of the reaction mechanism. As such, they only captured

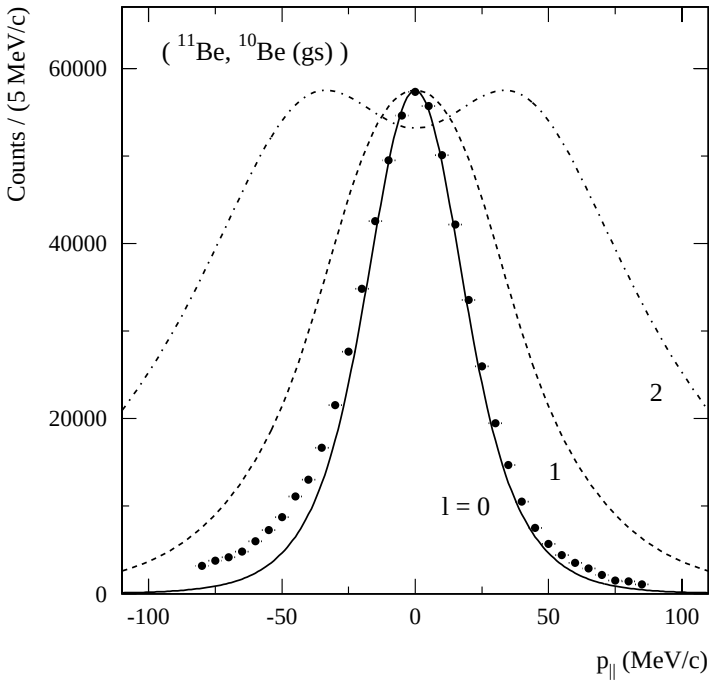

Figure 1.7: Parallel momentum distribution of the ^{10}Be fragments in the rest frame of the projectile and calculations assuming a knockout reaction from different orbitals. Figure taken from Ref. [32].

basic information on the structure of halos. Recent technical and theoretical advances allow for a much detailed characterization of halos.

Mass is now available through invariant mass measurements as recent progress in the particle detection allows for coincident detection of most of the outgoing fragments. Kinematically complete measurements (final-state exclusive measurement) are now feasible. By measuring accurately the four-momenta of all the fragments following a breakup reaction involving a halo nucleus, we can reconstruct its invariant mass. Such measurements usually involve the detection of one or several neutrons in coincidence and are extremely difficult. They are useful in electromagnetic studies, as the E1 strength distribution can now be mapped as a function of the relative energy between the fragments. As an example, an exclusive measurement of the Coulomb dissociation of ^{11}Li has been performed in Ref. [34] to study the low-energy (soft) E1 excitation. In this measurement, the three fragments $^{9}\mathrm{Li} + n + n$ have been detected in coincidence.

As we have seen, halo nuclei are usually studied using indirect methods. In these reactions, the halo nucleus is the projectile. Significant efforts have been made to improve the description of nuclear reactions. Some of these models are shortly described in the introduction. To account for the clustering of the projectile, they describe it as a two- or three-body object: a structureless core to which one or two nucleons are loosely bound. The internal structure of the target is usually neglected and its interaction with the projectile constituents is simulated by optical potentials chosen in the literature. Processes like elastic scattering [35], knockout [31] and breakup [36] are many examples of reactions that have been succesfully applied to the study of halo structure and that benefited from the technical and theoretical advances of these last 30 years.

Within these reaction models, the interactions between the different fragments of

the halo nucleus and the target are often simulated through phenomenological optical potentials. At the driplines however, information to build these potentials is lacking. Therefore, while the reaction models nowadays reproduce most of the features of the reaction observables such as elastic scattering or breakup cross sections, their dependence on these optical potentials hinders the clean extraction of halo properties. A solution to this problem might come from a new observable: the ratio.

The ratio consists in the ratio of breakup and summed cross sections

$$\mathcal{R}_{\rm sum}(E,\boldsymbol{Q}) = \frac{d\sigma_{\rm BU}/dEd\Omega}{d\sigma_{\rm sum}/d\Omega} \tag{1.10}$$

where $\boldsymbol{Q}$ is the transferred momentum and the summed cross section is defined as the sum of elastic, inelastic and integrated breakup cross sections.

$$\frac{d\sigma_{\rm sum}}{d\Omega} = \frac{d\sigma_{\rm el}}{d\Omega} + \frac{d\sigma_{\rm inel}}{d\Omega} + \int \frac{d\sigma_{\rm BU}}{d\Omega dE} dE \tag{1.11}$$

In the recoil excitation and breakup (REB) model of reactions induced by one-neutron halo nuclei [37] on which this observable is based (see also Sec. 2.4), it simplifies to a simple form factor of the wave function of the halo.

$$\mathcal{R}_{\rm sum}(E,\boldsymbol{Q}) \overset{\rm REB}{=} |F_{E,0}(\boldsymbol{Q})|^2 \tag{1.12}$$

which reads

$$|F_{E,0}(\boldsymbol{Q})|^2 = \frac{1}{2j_0+1}\sum_{m_0}\sum_{ljm}\left|\int \phi_0(\boldsymbol{r})\phi_{ljm}(E,\boldsymbol{r})e^{i\boldsymbol{Q}\cdot\boldsymbol{r}}\,d\boldsymbol{r}\right|^2, \tag{1.13}$$

Within the assumptions of the REB, the ratio is hence independent of the reaction mechanism, and, in particular, is insensitive to the optical potentials, whose influence on the different cross sections cancel out when taking their ratio. This new observable depends only on the projectile wave functions and should be much more sensitive to the halo internal structure than the individual reaction cross sections. These properties have been confirmed at intermediate/high energies of the projectile at which the REB works best [38]. The ratio has also been shown to be very sensitive to the projectile structure, in shape but also in magnitude. The ratio is hence a promising observable for the study of halo nuclei. It will be discussed in more details in the next section.

Aside from nuclear reactions, several other experimental techniques have proven valuable in the study of halos. I will discuss some of them very briefly.

The presence of a halo also has an influence on the electron binding energies [39]. Indeed, the halo affects the charge distribution of the nucleus which in turn affects the electron binding energies, particularly for s-wave electrons that have a non-zero probability of being inside the nucleus [40]. Electronic transitions are thus shifted between isotopes and are a signature of changes in the charge distribution. Isotopic shift measurements are performed and then compared to theoretical calculations that relate the shift to the difference in the rms radii of both isotopes. For example, in Ref. [41], the charge radius of ^{6}He is probed by laser spectroscopy on individual ^{6}He confined and cooled in a magneto-optical trap. Similar measurements have been performed on ^{11}Li [40] and on ^{11}Be [5].

It should be noted that these isotopic shifts occur also because of mass changes. They are actually much larger than volume shifts in light elements. However they can be

calculated through relativistic and high order QED/QCD corrected quantum mechanical calculations [39]. These computations rely heavily on the mass of the isotopes at study. Unfortunately, mass measurements are hard because of the very short lifetime and the marginal quantities at which halo nuclei can be created. Recent developments have showed that the use of Penning traps for mass measurements is possible. Despite the lifetime of ^{11}Li being of the order of a millisecond, a Penning trap has been connected to the ISOL facility ISAC and has been used successfully to pinpoint the mass of this two-neutron halo nucleus [42].

Finally, the halo structure can also be probed through β-decay [43]. The influence of the halo is twofold. First, because of the large spatial extension of the halo, the superposition of its wave function with the wave function of the daughter decay is reduced and thus the decay is suppressed. Second, because of the strong decoupling of the halo respective to the core, the decay can occur more or less independently and into different channels. An example of such process is the β-delayed deuteron emission in ^{11}Li, which is dominated by the β-decay of a neutron of the halo and was first reported in Ref. [42]. These measurements are complementary to those based on nuclear reactions but necessitate precise knowledge of the daughter structure [43].

1.3 Summary

In this section we have seen how the development of RIB facilities have challenged our vision of how matter is distributed inside of the nucleus. While it was thought that their density resembled the one of a water droplet, i.e. nearly constant in the interior and with a thin surface, the RIBs revealed the very peculiar behaviour of nuclei near the driplines. Indeed, as we depart from the valley of stability, some nuclei exhibit anomalously large matter radii. This feature is interpreted as the nucleus having one or several of its neutrons (protons) decoupled and at large distance from an inert core containing the rest of the nucleons. These very loosely-bound valence nucleons can be found outside of the range of the nuclear interaction with a high probability, leading to the appearance of a *halo*.

To be characterised as a halo, these nuclei must exhibit a dominating few-body structure in addition to large matter radii compared to the size of the classically allowed regions. Currently, three different types of halos have been established that satisfy these properties: one-neutron halos (such as ^{11}Be and ^{15}C), two-neutrons halos (such as ^{6}He and ^{11}Li) and one-proton halos (such as ^{8}B or one of the excited states of ^{17}F).

Because they are far from stability, these nuclei are very short-lived and are usually studied through indirect methods such as reactions measured in inverse kinematics, where they are the projectile. In the early days of the RIBs, halos were studied in simple reactions. The interpretation of observables such as the interaction cross section or the parallel momentum would then be made in very unsophisticated geometrical models. These first generation experiments were simple enough to highlight the main characteristics of halos but only captured basic information on the structure of halos. Recent progresses in reaction models and in experimental techniques such as coincidence measurements allow for the study of finer details of the halo structure. We have seen for example how they could be studied through spectroscopic techniques, i.e. isotopic shifts and Penning traps mass measurements, electromagnetic transitions or β-decay.

Most of the experiments probing the halo structure rely however on nuclear reactions such as elastic scattering, transfer, knock-out, breakup, etc. For the description of these reactions precise theoretical models that take the internal dynamics of the projectile are

needed [19]. State-of-the art reaction models are able to correctly take the clustering of the projectile into account and reproduce fairly well observables such as elastic-scattering or breakup cross sections. However, the information on the structure of the halo that can be extracted from these collisions is reaction and model dependent [44]. Indeed, these models still rely on optical potentials to simulate the interactions between the constituents of the reaction. Because halo nuclei are found far from stability, uncertainties on these potentials are large [45], which hinders the clean extraction of structure information. In this work, I will analyse how this could be circumvented by a new observable: the ratio.

In next sections, I will first start by describing some of the state-of-the art reaction models that are used in the study of halo nuclei as of today in Sec. 2. These are the *Continuum Discretised Coupled Channel* method [46] [see Sec. 2.2], the *Dynamical Eikonal Approximation* method [47, 48] [see Sec. 2.3], and the *Recoil and Excitation Breakup* model [37] already mentionned in last section and which I will describe into more details [see Sec. 2.4]. After the detailed descriptions of these models I will discuss the ratio observable in Sec. 3.1. The ratio observable will be defined in Sec. 3 and we will see how it can be approximated within the assumptions of the REB. Finally, the applicability of this observable to neutron-halos and to proton-halos will be studied in Secs. 3.2 and 3.3.

2 Model the reactions of one-nucleon halo nuclei

The reaction of halo nuclei is a complex many-body problem. These problems are challenging from the structural point of view. In this work, only one-neutron and one-proton halo nuclei are investigated. Because the one-nucleon halo is decoupled from the core, a rather good description of the reaction can already be achieved with a three-body model. In such a model, the projectile is seen as composed of an inert and structureless core around which orbits one valence nucleon. The target on which the projectile impinges is also assumed structureless.

In this section I will present and discuss several models that describe the reaction of a halo nucleus projectile on a target. Because the clustered character of halo nuclei, it tends to very likely dissociate from the core nucleus through the Coulomb and nuclear interactions with the target. When both the free nucleon and the core are detected in coincidence, the process is called *breakup*. While the elastic scattering (where the projectile nucleus remains in its ground state) is dominant at the energies considered in this work, it is still significantly influenced by the breakup process. Its proper treatment is thus necessary.

2.1 Elastic scattering and breakup of two-body projectiles

In the following, the two-body projectile will be referred to as P. It has a charge Z_P and mass m_P. It is composed of two fragments: the core c, of charge Z_c and mass m_c and the valence nucleon v, of charge Z_v and mass m_v. Note that the projectile mass and charge satisfy $m_P = m_c + m_v$ and $Z_P = Z_c + Z_v$. The projectile impinges on a a target T, of mass m_T and charge Z_T. The three bodies of the reaction are considered structureless. The spin of the valence nucleon is $s = 1/2$, while the spins of the core and the target are considered nil.

The core and the target are assumed to have no excited states. I hence consider only the elastic breakup, where the target nucleus stays in its initial state, i.e. its ground state. The projectile, initially in its ground state of (negative) energy E_0, impinges on the target in the $\hat{\boldsymbol{Z}}$ direction with a momentum $\hbar K_0$, in the P-T centre of mass frame. This initial P-T relative motion wave vector satisfies

$$\hbar K_0 = \sqrt{2\mu_{PT}(E_{\text{tot}} - E_0)} \tag{2.1}$$

where $\mu_{PT} = \frac{m_P m_T}{m_P + m_T}$ is the P-T reduced mass. The schematics of the collision are depicted on Fig. 2.1.

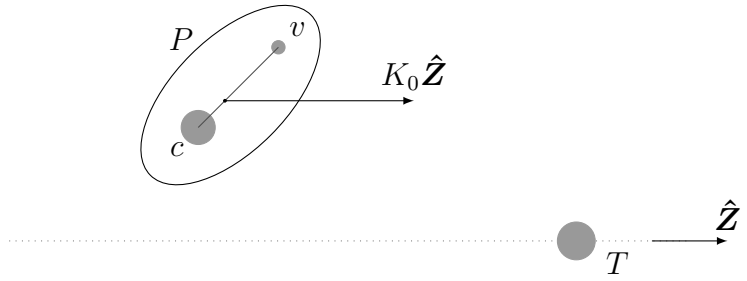

Figure 2.1: Schematics of the collision.

The Hamiltonian of the three-body system reads

$$H_{3b} = \hat{T} + V_{cv} + V_{vT} + V_{cT}. \tag{2.2}$$

where $\hat{T}$ is the kinetic energy operator of the whole system and V_{cv}, V_{vT} and V_{cT} are the potentials describing the interactions between v and c, v and T and between c and T, respectively. In the P-T centre of mass reference frame, the Schrödinger equation of this three-body system reads

$$\left[H_{3b} - E_{\text{tot}}\right]\ \Psi = 0. \tag{2.3}$$

where E_{tot} is the three-body system total energy and Ψ is the three-body wave function. Since the projectile is initially in its ground state, that I will define as ϕ_0, and impinges in the $\hat{\boldsymbol{Z}}$ direction, this equation has to be solved with the initial condition that

$$\Psi \xrightarrow[Z\to-\infty]{} \phi_0\, e^{iK_0 Z} \tag{2.4}$$

This three-body problem can be described within Jacobi set of coordinates, of which three different sets exist. These are illustrated on Fig. 2.2. The description of the three-body-system wave function Ψ within one single Jacobi set of coordinates is difficult. Indeed, one single Jacobi set of coordinates is not appropriate to describe all bound states between every partition in the system. To visualise this, let us consider the projectile in its ground state. The first set of Jacobi coordinates (see Fig. 2.2(a)) is obviously the most suitable set to describe this state. In this particular set of coordinates, the ground state wave function ϕ_0 is a function of the c-v relative coordinate $\boldsymbol{r}$ only. The initial wave function of the system Ψ is then described by the product of ϕ_0 with the plane wave $\exp(i\boldsymbol{K}\cdot\boldsymbol{R})$, that describes the asymptotic movement of the projectile towards the target. This form is no longer suitable if bound states of the v-T and c-T partitions exist. A factorisation of Ψ into a product of those bound states within the first set of Jacobi coordinates therefore rises convergence issues [49], while in contrast these partitions are easily described with the use of the set of coordinates ($\boldsymbol{r}'$,$\boldsymbol{R}'$) and ($\boldsymbol{r}''$,$\boldsymbol{R}''$), respectively (see Figs. 2.2(b) and 2.2(c)). Because of these possible bound states, the full system wave function can more easily be expressed as a sum of components expressed in the three different Jacobi sets of coordinates and reads

$$\Psi \to \Psi(\boldsymbol{r},\boldsymbol{R}) + \Psi'(\boldsymbol{r}',\boldsymbol{R}') + \Psi''(\boldsymbol{r}'',\boldsymbol{R}'') \tag{2.5}$$

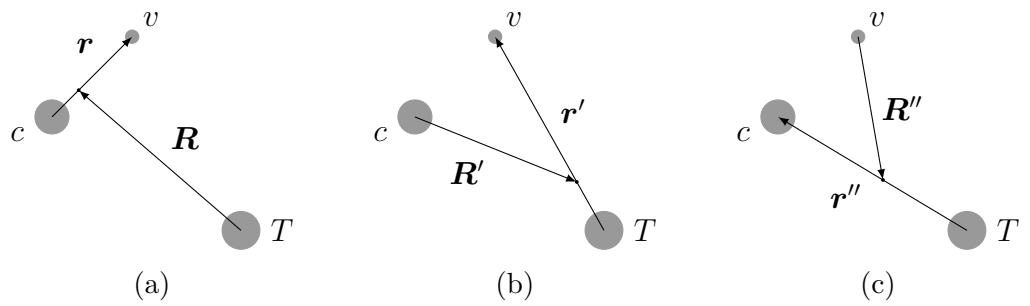

Figure 2.2: Illustration of the three different set of Jacobi coordinates. From left to right, (a) will be called the first set, (b) the second set and (c) the third set.

Because of this form, solving the Schrödinger equation (2.3) raises a problem. Indeed, each term of Ψ expressed in the i^{th} Jacobi set of coordinates still contains all bound states

and continuum states from the other partitions i' and i''. Asymptotically however, these are not decoupled and there is no way to completely describe these states by any unique partial-wave sum in the set of coordinates $(\boldsymbol{r}_i, \boldsymbol{R}_i)$.

In order to have a well-defined asymptotic behaviour, the Schrödinger equation should be rewritten in the form of a set of three coupled equations. This formulation is due to Faddeev (who introduced this formulation in [50]) and reads

$$\begin{cases} (E - \hat{T} \ - V_{cv})\Psi \ = V_{cv}\,(\Psi' + \Psi'') \\ (E - \hat{T}' \ - V_{vT})\Psi' \ = V_{vT}(\Psi \ + \Psi'') \\ (E - \hat{T}'' - V_{cT})\Psi'' = V_{cT}(\Psi \ + \Psi'), \end{cases} \tag{2.6}$$

where $\hat{T}$, $\hat{T}'$ and $\hat{T}''$ are simply the kinetic operator expressed in any choice of Jacobi set of coordinates. The interest of these equations is their behaviour at $R \to \infty$. Indeed, in this region, the right-hand side of these equations vanishes. This decouples the equations and the boundary conditions are then much better defined. This formalism allows an exact solution to the three-body problem. (For a less simplistic view of the Faddeev equations see [49, 50].)

In the case where bound states exist only for one pair of particles (or are negligible for other pairs), the multiple components are no longer useful. The Faddeev system can then be reduced to one single equation for only one component and written in one single Jacobi set of coordinates. This is the case when transfer channels are not significant. Since in this work I focus on elastic scattering and breakup at quite a high energy, transfers are negligible [49]. Note also that later when actually solving the equation, the interacting potentials V_{vT} and V_{cT} will be chosen as phenomenological optical potentials. These can simulate some of the channels described by the other sets of Jacobi coordinates

The breakup process connects a bound state of the projectile with its continuum states (or scattering states). Only low energy breakup will be considered in this work, the valence nucleon and the core hence stay relatively 'close' to each other after they dissociate ($r \ll R$). Moreover, as here, bound states only for the core and the valence nucleon are considered, I will obviously describe this problem within the first set.

The kinetic energy operator of Eq. (2.2) can be separated into the contribution from the c-v relative motion and the P-T one. The three-body Schrödinger equation then reads

$$\left[\frac{P^2}{2\mu_{PT}} + H_0 + V_{cT}\left(\boldsymbol{R} - \frac{m_v}{m_P}\boldsymbol{r}\right) + V_{vT}\left(\boldsymbol{R} + \frac{m_c}{m_P}\boldsymbol{r}\right) - E_{\text{tot}}\right]\Psi(\boldsymbol{r}, \boldsymbol{R}) = 0 \tag{2.7}$$

where $\boldsymbol{P}$ is the relative momentum between the centre of mass of the projectile and the target and where H_0 is the internal Hamiltonian, that describes the c-v projectile. The asymptotic boundary condition Eq. (2.4), with its coordinates made explicit, reads

$$\Psi(\boldsymbol{r}, \boldsymbol{R}) \xrightarrow[Z\to-\infty]{} \phi_0(\boldsymbol{r})\, e^{iK_0 Z} \tag{2.8}$$

In this set of coordinates, the internal Hamiltonian reads

$$H_0 = -\frac{\hbar^2}{2\mu_{cv}}\Delta_{\boldsymbol{r}} + V_{cv}(\boldsymbol{r}), \tag{2.9}$$

where $\mu_{cv} = \frac{m_c m_v}{m_c + m_v}$ is the reduced mass of the projectile. The ground state and all other states of the projectile are eigenstates of its Hamiltonian and are defined as

$$H_0\ \phi_{ljm}(E, \boldsymbol{r}) = E\ \phi_{ljm}(E, \boldsymbol{r}) \tag{2.10}$$

For bound states E (the c-v relative motion energy) is negative and these states are discrete. Note that because halo nuclei are loosely bound, they usually have very few bound states. In this work, I will consider that they have only one, i.e. the ground state ϕ_0 of energy $E_0 < 0$[1]. For continuum states on the contrary $E > 0$. These correspond to states where the projectile is unbound.

For central potentials, the wave functions ϕ_{ljm} can be expanded to separate radial from angular components in the form

$$\phi_{ljm}(E, \boldsymbol{r}) = \frac{u_{lj}(E, r)}{r} \left[Y_l(\hat{\boldsymbol{r}}) \otimes \chi_s\right]_{jm} \tag{2.11}$$

where Y_l are spherical harmonics ($\hat{\boldsymbol{r}}$ is a unit vector in the direction of $\boldsymbol{r}$). l is the orbital angular momentum of v relative to c and j is the total spin, resulting from the coupling between l and s, with m_b its projection. For bound states, an additional quantum number could be added: n, the number of nodes of the radial wave function u_{lj}. Note however that since I consider only the ground state here, this quantum number is not needed.

Like already done previously, the ground state of quantum numbers $\{l_0 j_0 m_0\}$ is referred to as $\phi_0 \equiv \phi_{l_0 j_0 m_0}$. Similarly, its radial part is referred to as $u_0 \equiv u_{l_0 j_0}$ and is normalised to 1. It behaves asymptotically as

$$u_0(r) \xrightarrow[r\to\infty]{} \mathcal{C}_{l_0 j_0} W_{-\eta_0, l_0+1/2}(2\kappa_0 r) \tag{2.12}$$

where $\hbar\kappa_0 = \sqrt{2\mu_{cv}|E_0|}$, W is the Whittaker function [51], η_0 is the Sommerfeld parameter of a c-v collision

$$\eta_0 = \frac{Z_c Z_v e^2}{\hbar} \left(\frac{\mu_{cv}}{2|E_0|}\right)^{1/2} \tag{2.13}$$

The strength of the exponential tail $\mathcal{C}_{l_0 j_0}$ is called the *asymptotic normalisation constant* or ANC. Note that in this development, the valence nucleon and the core are structureless and all excited states of the core are neglected. The ANC is then equivalent to the single-particle ANC (SPANC). In reality, in a less crude model, other configurations of the projectile may exist, in which case the SPANC and ANC differ [52].

For the continuum states, the radial parts are normalised according to

$$u_{lj}(E, r) \xrightarrow[r\to\infty]{} \cos\delta_{lj}(E) F_l(kr) + \sin\delta_{lj}(E) G_l(kr) \tag{2.14}$$

where k is the c-v wave number and describes the asymptotic c-v relative motion

$$\hbar k = \sqrt{2\mu_{cv} E} \tag{2.15}$$

F_l and G_l are the Coulomb functions [51] and δ_{lj} are the phase-shifts.

The solutions of Eq. (2.7) cannot be calculated exactly, unfortunately and some approximations need to be made. Two different methods will be presented in this work. The first one is the *Continuum Discretised Coupled Channel* (CDCC) method [46], which truncates and discretises the continuum. This method can be considered exact (even if obviously, the truncation and discretisation of the continuum makes it an approximate solution). The second one is the *Dynamical Eikonal Approximation* (DEA) method [47, 48],

[1] It should be noted that strictly speaking, there are much more states than that. Indeed, the potentials used to simulate the c-v interaction are usually deep (see Sec. 2.5). This causes deeply bound states to exist. These states are however "unphysical" for the valence nucleon. Indeed, they correspond to the states of the other nucleons of the core. They are hence forbidden for v due to the Pauli principle.

which is a variant of the eikonal approximation and which is not exact. Moreover, I will present the *Recoil and Excitation Breakup* model (REB) [37], a simplified model of breakup for one-neutron halo nuclei upon which the ratio observable is inspired and in which the system can be solved exactly.

2.2 Continuum Discretised Coupled Channel method (CDCC)

In the previous section, we have seen how the three-body problem could be reduced to Eq. (2.7). Let us expand the full wave function in the set of eigenstates of the internal Hamiltonian of the projectile H_0 (Eq. (2.9)). This set is composed by the sole bound state, i.e. the ground state, and the continuum states of Eq. (2.10). Hence, we have

$$\Psi(\boldsymbol{r},\boldsymbol{R}) = \phi_0(\boldsymbol{r})\psi^0_{K_0}(\boldsymbol{R}) + \sum_{ljm}\int \phi_{ljm}(E,\boldsymbol{r})\psi^{ljm}_K(E,\boldsymbol{R})\,dE, \tag{2.16}$$

where $\hbar K$ is the momentum between the projectile and the target and (similarly to Eq. (2.1) for K_0) satisfies the relation

$$\hbar K = \sqrt{2\mu_{PT}(E_{\rm tot} - E)} \tag{2.17}$$

The wave functions $\psi^{ljm}_K(E)$ correspond to the relative P-T motion when the projectile is in the $\phi_{ljm}(E)$ state.

Unfortunately, as visible in Eq. (2.16), the expansion of the wave function is made over a continuous variable E and a discretisation is thus needed to solve the three-body problem numerically. This was first proposed by Rawitscher in Ref. [53]. Three different types of discretisation exist in the CDCC method. In all three cases, the discretisation goal is to construct a finite set of functions $\tilde{u}_{l_ij_i}(r)$ to describe the continuum. If we replace the true scattering states in Eq. (2.11) by these, we have

$$\tilde{\phi}_{l_ij_im_i}(\boldsymbol{r}) = \frac{\tilde{u}_{l_ij_i}(r)}{r}\left[Y_{l_i}(\hat{\boldsymbol{r}})\otimes\chi_s\right]_{j_im_i}, \tag{2.18}$$

which is a discrete set of the projectile wave functions. The descriptions of these different discretisations come from [49].

The mid-point method

In this method, first proposed by Rawitscher, the finite set of functions is simply composed of the bound states and the scattering states calculated on a given finite discrete set $i = i_0, ..., i_n$ of energies E_i. These discrete functions in the continuum are thus the true scattering states $\tilde{u}_{l_ij_i}(r) \equiv u_{l_ij_i}(E_i, r)$. The energies in the continuum are chosen within an energy range from $E_{\rm min}$ (usually 0) to $E_{\rm max}$. Each set has a width $\Delta E_i = (E_{i+1} - E_{i-1})/2$. An extension of this method is the *average method*, or *continuum binning method*

The average method or continuum binning method

In the case of the average method, we construct the radial functions $\tilde{u}_{l_ij_i}$ by averaging the true scattering eigenstates $u_{l_ij_i}(E)$ over a small energy range (or bin) centred on E_i and of width ΔE_i. This is done with a weight function $w_i(E)$ which choice of the weight function is beyond the scope of this work (see Ref. [49]). The radial functions read

$$\tilde{u}_{l_ij_i}(r) \propto \int_{E_i-\Delta E_i/2}^{E_i+\Delta E_i/2} w_i(E)u_{l_ij_i}(E,r)\,dE, \tag{2.19}$$

where the normalisation will depend on the weight function. It should be noted that for non-overlapping intervals $[E_i - \Delta E_i/2, E_i + \Delta E_i/2]$ in the continuum, these radial functions form an orthonormal set. The functions $\tilde{u}_{l_i j_i}$ are then square integrable and are called *continuum bin states*. Averaged energies $\tilde{E}_i$ can be defined such that they satisfy

$$\tilde{E}_i = \left\langle \tilde{\phi}_{l_i j_i m_i} \right| H_0 \left| \tilde{\phi}_{l_i j_i m_i} \right\rangle . \tag{2.20}$$

They correspond to the averaged excitation of the i^{th} bin.

The use of pseudostates

This method consists in taking the eigenstates of the internal Hamiltonian on a given square-integrable basis (such as harmonic-oscillator wavefunctions) and express the scattering states of the continuum in that basis [54]. There is little control over the energies of the grid as these are fixed by the chosen basis. The correspondences between these eigenstates and the scattering solutions $u_{lj}(E)$ are not simple but the set has to be sufficiently complete in the reaction region.

Let us denote by N the number of bins included in the calculation and define p as the number of the considered bin or state as well as its quantum numbers and its energy (p thus now ranges from $p = 0$, i.e. the ground state, to $p = N$). The discretised expansion Eq. (2.16) reads now

$$\Psi_{\text{CDCC}}(\boldsymbol{R}, \boldsymbol{r}) = \sum_{p=0}^{N} \tilde{\phi}_p(\boldsymbol{r}) \psi_p(\boldsymbol{R}). \tag{2.21}$$

In this expression, ψ_p correspond to the coefficients of the development of the CDCC wave function. To obtain these, let us inject this expansion in Eq. (2.7) and project this equation on the projectile wave functions $\tilde{\phi}_q$. We finally have, in the Dirac notation

$$\sum_p \left\langle \tilde{\phi}_q \right| \frac{P^2}{2\mu_{PT}} + H_0 + V_{cT} + V_{vT} - E_{\text{tot}} \left| \tilde{\phi}_p \right\rangle \psi_p(\boldsymbol{R}) = 0. \tag{2.22}$$

If we inject the averaged energies Eq. (2.20) in this expression, we have

$$\left[\frac{P^2}{2\mu_{PT}} + V_{qq}(\boldsymbol{R}) - \tilde{E}_q \right] \psi_q(\boldsymbol{R}) + \sum_{p \neq q} V_{qp}(\boldsymbol{R}) \psi_p(\boldsymbol{R}) = 0, \tag{2.23}$$

where the definition of the coupling potentials V_{qp} reads

$$V_{qp}(\boldsymbol{R}) = \left\langle \tilde{\phi}_q \right| V_{vT} + V_{cT} \left| \tilde{\phi}_p \right\rangle . \tag{2.24}$$

As visible from Eq. (2.23), the coupling with states of the continuum have a retroactive effect on the elastic channel. We can expand ψ_p in multipoles, that is,

$$\psi_p(\boldsymbol{R}) = \sum_L i^L Y_L^0(\hat{\boldsymbol{R}}) \frac{\chi_{pL}(R)}{R}, \tag{2.25}$$

where capital L is the orbital angular momentum and describes the relative motion between the projectile and the target, the final CDCC equation reads [49]

$$\begin{aligned} \left[-\frac{\hbar^2}{2\mu_{PT}} \left(\frac{d^2}{dR^2} - \frac{L(L+1)}{R^2} \right) + V_{\alpha\alpha}^{J_{\text{tot}}}(R) + \tilde{E}_p - E_{\text{tot}} \right] \chi_\alpha^{J_{\text{tot}}}(R) \\ + \sum_{\alpha' \neq \alpha} i^{L'-L} V_{\alpha\alpha'}^{J_{\text{tot}}}(R) \chi_{\alpha'}^{J_{\text{tot}}}(R) = 0, \end{aligned} \tag{2.26}$$

where $J_{\rm tot} = L \otimes j$ is the total angular momentum of the three-body wave function. In the expression above, α represents all quantum numbers $\{p, L\}$ describing the partial-wave channel for a given $J_{\rm tot}$.

These equations couple the different projectile-target relative-motion states. The coupling potentials $V^{J_{\rm tot}}_{\alpha\alpha'}$ full expression reads

$$V^{J_{\rm tot}}_{\alpha\alpha'}(R) = \left\langle \left[\tilde{\phi}_p Y_L\right]_{J_{\rm tot}} \middle| V_{cT} + V_{vT} \middle| \left[\tilde{\phi}_{p'} Y_{L'}\right]_{J_{\rm tot}} \right\rangle . \tag{2.27}$$

The main advantage of the average method compared to the mid-point method can easily be understood from this form of the coupling potentials. As it should be noted, the interactions between the target and the core and between the target and the valence nucleon depend on the coordinates of the core and the valence nucleon, relative to the target. The use of true scattering states in the continuum would make the calculation of the coupling potentials Eq. (2.27) very tedious as the Coulomb range is infinite. On the contrary, averaged scattering functions do not raise this problem thanks to their square-integrability [49]. While the pseudostates also exhibit this property, the chosen basis has no simple relation to the c-v scattering solutions and there is little control over the energies of the grid.

Numerically, the procedure consists in calculating the bound and scattering states of the projectile with which the different continuum bin wave functions are built. The coupling potentials $V^{J_{\rm tot}}_{\alpha\alpha'}$ can then be calculated. The wave functions $\chi^{J_{\rm tot}}_{\alpha}$ are then obtained by solving Eq. (2.26). Asymptotically, they behave as

$$\chi^{J_{\rm tot}}_{\alpha}(R) \xrightarrow{R\to\infty} \frac{i}{2}\left[H^-_{L_0}(\eta_{\alpha_0}, K_{\alpha_0}R)\delta_{\alpha\alpha_0} - H^+_L(\eta_\alpha, K_\alpha R)\boldsymbol{S}^{J_{\rm tot}}_{\alpha\alpha_0}\right], \tag{2.28}$$

where the 0 index denotes the incident channel, $H^\pm$ are the Coulomb Hankel functions [49], η_α is the Sommerfeld parameter of the PT system in the channel α, defined as

$$\eta_\alpha = \frac{Z_P Z_T e^2}{\hbar}\left(\frac{\mu_{PT}}{2(E_{\rm tot} - \tilde{E}_\alpha)}\right)^{1/2} \tag{2.29}$$

and $\boldsymbol{S}^{J_{\rm tot}}_{\alpha\alpha_i}$ are the partial-wave S-matrices for the excitation to a state α with a centre-of-mass wave number K_α (which obeys a similar relation as Eq. (2.17) with E replaced by the energy of the channel $\tilde{E}_\alpha$). These matrices are then used to construct the desired cross sections [49]. The scattering amplitudes for a projectile that stays in its ground state and is deviated from momentum $\hbar\boldsymbol{K_0}$ to $\hbar\boldsymbol{K} = (\hbar K_0, \Omega_K)$, the elastic scattering amplitude reads

$$\begin{aligned} f_{{\rm el},mm_0}(\boldsymbol{K}, \boldsymbol{K}_0) = f_C(\theta,\phi) + \frac{4\pi}{K_0}\sum_{LL'J} &\langle L0, j_0 m_0|\, Jm_0\rangle\, \langle L'(m_0-m), jm|\, Jm_0\rangle \\ &\times \frac{e^{i[\sigma_L(\eta_{\alpha_0})+\sigma_{L'}(\eta_\alpha)]}}{2i}\left[\boldsymbol{S}^J_{\alpha_0\alpha_0} - \delta_{mm_0}\right]\, Y^0_L(\hat{\boldsymbol{K}}_0)\, Y^{m_0-m}_{L'}(\hat{\boldsymbol{K}}), \end{aligned} \tag{2.30}$$

where $\sigma_{L^{(\prime)}} = \arg\Gamma(1 + L^{(\prime)} + i\eta)$ are the initial (final) Coulomb phase shifts [49] and f_C is the pure Coulomb scattering amplitude [49]

$$f_C(\theta,\phi) = -\frac{\eta_{\alpha_0}}{2K_0\sin^2(\theta/2)}\exp\left[-i\eta_{\alpha_0}\ln(\sin^2(\theta/2)) + 2i\sigma_0(\eta_{\alpha_0})\right] \tag{2.31}$$

where θ and ϕ are the scattering and azimuthal angles of the direction Ω_K, all defined in the P-T centre of mass.

The elastic scattering cross section hence reads

$$\frac{d\sigma_{\rm el}}{d\Omega} = \frac{1}{2j_0+1}\sum_{mm_0}\left|f_{{\rm el},mm_0}(\boldsymbol{K},\boldsymbol{K}_0)\right|^2. \tag{2.32}$$

Note that because of the dominance of the Coulomb interaction at low scattering angles, and the divergence of the elastic cross section around $\theta = 0$, it is customary to present the elastic scattering as a ratio to the Rutherford cross section, which corresponds to the elastic cross section of two pointlike particles of charge Z_P and Z_T that interact through the Coulomb interaction only and which reads

$$\frac{\sigma_{\rm R}}{d\Omega} = |f_C(\theta,\phi)|^2 = \frac{\eta^2}{4K_0^2\sin^4(\theta/2)}. \tag{2.33}$$

Similarly for breakup, the scattering amplitudes $f_{mm_0}(\boldsymbol{K}_p,\boldsymbol{K}_0)$ for populating each bin state p of quantum numbers jm and final projectile momentum $\hbar\boldsymbol{K}_p = (\hbar K_p, \Omega_{K_P})$ from the initial state j_0m_0 of momentum $\hbar\boldsymbol{K}_0$. They contain a sum over all partial waves and read [49]

$$\begin{aligned} f_{mm_0}(\boldsymbol{K}_p,\boldsymbol{K}_0) = \frac{4\pi}{K_0}\sqrt{\frac{K_p}{K_0}}\sum_{LL'J}&\langle L0, j_0m_0|\ Jm_0\rangle\,\langle L'(m_0-m), jm|\ Jm_0\rangle \\ &\times\frac{e^{i[\sigma_L(\eta_{\alpha_0})+\sigma_{L'}(\eta_\alpha)]}}{2i}\boldsymbol{S}^J_{\alpha\alpha_0}\ Y^0_L(\hat{\boldsymbol{K}}_0)\ Y^{m_0-m}_{L'}(\hat{\boldsymbol{K}}_p). \end{aligned} \tag{2.34}$$

The differential cross sections of breakup to a bin state p of the projectile averaged over all spins is then given by [49]

$$\frac{d\sigma_{\rm BU}}{d\Omega} = \frac{1}{2j_0+1}\sum_{mm_0}\left|f_{mm_0}(\boldsymbol{K}_p,\boldsymbol{K}_0)\right|^2. \tag{2.35}$$

Note that in the case of breakup, the scattering angle θ is defined as the angle between the initial and final directions of the centre of mass of the projectile, just like for elastic scattering. In App. B, I present the code *Fresco*, which is an implementation of the CDCC method [55].

2.3 The Dynamical Eikonal Approximation (DEA)

In this section, an approximate method to solve the three-body problem is introduced. Only the basic principles of the method are presented. It has the advantage of being valid on both light and heavy targets and has been shown to successfully model reactions involving one-nucleon halo nuclei at intermediate energies [47, 56, 57]. The interested reader is referred to [48] on which most part of this section is based.

The eikonal approximation [26] is based on the assumption that the wavefunction of the movement of the projectile-target system does not differ much from the impinging wave function Eq. (2.8). This is usually the case when the projectile has a sufficient energy. Hence, the cylindrical coordinates is a convenient system of coordinates to work with. The coordinate $\boldsymbol{R}$ of the projectile relative to the target can be expressed as $(\boldsymbol{b}, Z)$, with $\boldsymbol{b}$ the transverse component of the coordinate (the impact parameter in a semiclassical interpretation) and $\hat{\boldsymbol{Z}}$ the beam direction (see Fig. 2.3).

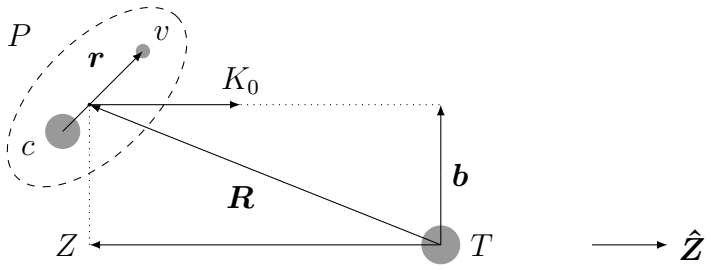

Figure 2.3: Cylindrical coordinates in the eikonal model.

The solutions of the three-body Schrödinger equation in the first set of Jacobi coordinates (2.7) should satisfy the asymptotic behaviour Eq. (2.8). Hence, we will factorise the three-body wave function $\Psi(\boldsymbol{R}, \boldsymbol{r})$ as

$$\Psi(\boldsymbol{R}, \boldsymbol{r}) = e^{iK_0 Z}\, \hat{\Psi}(\boldsymbol{R}, \boldsymbol{r}). \tag{2.36}$$

With this factorisation, the Schrödinger equation reads

$$\left[\frac{P^2}{2\mu_{PT}} + \frac{\hbar K_0}{\mu_{PT}} P_Z + H_0 + V_{cT} + V_{vT} - E_{\text{tot}}\right] \hat{\Psi} = 0, \tag{2.37}$$

where the term $\hbar K_0/\mu_{PT}$, the asymptotic projectile-target relative velocity, is usually noted v_0.

Up to now, no approximation has been made. But since we expect $\hat{\Psi}$ to be a slowly varying function of $\boldsymbol{R}$, the second-order derivatives of $\hat{\Psi}$ are small compared to the first order ones

$$\frac{P^2}{2\mu_{PT}} \ll v_0 P_Z \tag{2.38}$$

The *eikonal approximation* consists in neglecting the second-order term. It should be noted that by neglecting this second-order derivative, part of the interferences between neighbouring $\boldsymbol{b}$ are missing. The solution $\hat{\Psi}_{\text{DEA}}$ is then obtained by solving the equation

$$i\hbar v \frac{\partial}{\partial Z} \hat{\Psi}_{\text{DEA}}(\boldsymbol{b}, Z, \boldsymbol{r}) = (H_0 + V_{cT} + V_{vT} - E_{\text{tot}}) \hat{\Psi}_{\text{DEA}}(\boldsymbol{b}, Z, \boldsymbol{r}), \tag{2.39}$$

which we can see as a time-dependent Schrödinger equation by introducing the variable $t = Z/v_0$, with the initial condition that the projectile is in its ground state and thus

$$\hat{\Psi}^{(m_0)}_{\text{DEA}}(\boldsymbol{b}, v_0 t, \boldsymbol{r}) \xrightarrow{t \to -\infty} \phi_0(\boldsymbol{r}) \tag{2.40}$$

This equation must be solved for every value of $\boldsymbol{b}$ and m_0 [47]. The calculations are done with the algorithm presented in Ref. [58], in which the projectile wave-function is expanded over a spherical mesh. The coefficients of the partial wave expansion of $\hat{\Psi}_{\text{DEA}}$ and defined as

$$\hat{\Psi}^{(m_0)}_{\text{DEA}}(\boldsymbol{b}, Z, \boldsymbol{r}) = \frac{1}{r} \sum_{ljm} \hat{\Psi}^{(m_0)}_{\text{DEA},ljm}(b, r)\, [Y_l(\hat{\boldsymbol{r}}) \otimes \chi_s]_{jm} \tag{2.41}$$

can then be used to calculate the elastic scattering cross section. For a projectile going from its initial state of momentum $\hbar \boldsymbol{K_0}$ to the final $\hbar \boldsymbol{K} = (\hbar K_0, \Omega_K)$ it reads

$$\frac{d\sigma_{\text{el}}}{d\Omega} = K_0^2 \frac{1}{2j_0 + 1} \sum_{m_0 m} \left| \int_0^\infty db\; b J_{|m_0 - m|}(qb) \boldsymbol{S}^{(m_0)}_{\text{el},m}(b) \right|^2 \tag{2.42}$$

where J_M is a Bessel function [51]. The elastic scattering amplitudes then read [56]

$$\boldsymbol{S}^{(m_0)}_{\mathrm{el},m}(b) = \left\langle \phi_{l_0 j_0 m}(\boldsymbol{r}) \right| \hat{\Psi}^{(m_0)}_{\mathrm{DEA}}(\boldsymbol{R}, \boldsymbol{r}) \Big\rangle_{Z=+\infty} - \delta_{m m_0} \tag{2.43}$$

In these expressions, $\hbar\boldsymbol{q}$ is the transferred momentum

$$\boldsymbol{q} = \boldsymbol{K} - \boldsymbol{K_0} \tag{2.44}$$

and is assumed purely transverse. Its norm is thus linked to the scattering angle θ by

$$q = 2K_0 \sin\theta/2 \tag{2.45}$$

Similarly, the breakup amplitude matrix elements read [48]

$$\boldsymbol{S}^{(m_0)}_{ljm}(E, b) \underset{Z\to+\infty}{=} e^{i(\sigma_l + \delta_{lj} - l\pi/2)} \int_0^\infty u_{lj}(E, r) \hat{\Psi}^{(m_0)}_{\mathrm{DEA},ljm}(b, r) dr \tag{2.46}$$

and the differential breakup cross section from the initial state of momentum $\hbar\boldsymbol{K_0}$ to the final $\hbar\boldsymbol{K} = (\hbar K, \Omega_K)$ then reads

$$\frac{d\sigma_{\mathrm{BU}}}{dE d\Omega} = \frac{\mu_{cv} K_0 K}{\hbar^2 k} \frac{1}{2j_0 + 1} \sum_{m_0} \sum_{ljm} \left| \int_0^\infty db\, b J_{|m-m_0|}(qb) \boldsymbol{S}^{(m_0)}_{kljm}(b) \right|^2 \tag{2.47}$$

In these expressions, the $\boldsymbol{q}$ is also assumed purely transverse.

It should be noted that at low energies, a correction is needed to take into account the deflection of the projectile due to its interaction with the target. As proposed in Ref. [59] we can replace the impact parameter by the distance of closest approach b_{eff} of the corresponding classical Coulomb trajectory (see Fig. 2.4). This semiclassical correction showed to give good results for Coulomb-dominated collisions [59]. In a pure Coulomb collision, this distance reads [60, 61]

$$b_{\mathrm{eff}} = \frac{\eta}{K_0} + \sqrt{\frac{\eta^2}{K_0^2} + b^2} \tag{2.48}$$

This Coulomb-corrected DEA will usually be referred simply as the DEA, or as the CC-DEA in cases where the distinction is needed.

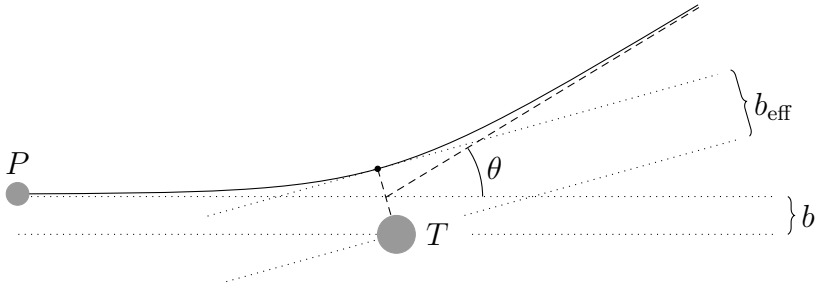

Figure 2.4: Distance of closest approach in the Coulomb corrected DEA.

Relation to the usual eikonal approximation

In addition to the Eq. (2.38), the *standard* eikonal approximation (what people usually consider as the eikonal approximation) an additional assumption is made: the *adiabatic*—or *sudden*—*approximation*. It consists in considering the internal

coordinates of the projectile to be frozen during the collision in Eq. (2.39). This holds if the impinging energy in the P-T centre of mass is large, so that the collision occurs in a very brief time. The internal Hamiltonian H_0 is then replaced by the energy of the ground state E_0 and they cancel out in Eq. (2.39). The solution to such equation is then [56]

$$\hat{\Psi}_{\text{eik}}(\boldsymbol{b}, Z, \boldsymbol{r}) = \exp\left[i\chi(\boldsymbol{b}, Z, \boldsymbol{r})\right] \phi_0(\boldsymbol{r}) \tag{2.49}$$

where the phase of the exponential is the eikonal phase

$$\chi(\boldsymbol{b}, Z, \boldsymbol{r}) = -\frac{1}{\hbar v} \int_{-\infty}^{Z} (V_{cT}(\boldsymbol{b}, Z', \boldsymbol{r}) + V_{vT}(\boldsymbol{b}, Z', \boldsymbol{r}))dZ' \tag{2.50}$$

In a semiclassical view, this phase describes the projectile following a straight-line trajectory at a constant impact parameter. Along its path, the projectile wave function accumulates a (complex) phase that results from the interaction of its fragments with the target.

Note that since this expression is obtained from an adiabatic expression, it fails to properly take the Coulomb potential into account and diverges. Indeed, because of the infinite range of the Coulomb potential, the assumption of a sudden reaction lapses. Several solutions exist to compensate for this issue. One way is to correct the eikonal phase as suggested in Ref. [62] in what is known as the Coulomb corrected eikonal model (CCE) [63]. The first order term of the Coulomb eikonal phase leading to the divergence is then replaced by the first-order term obtained in a perturbative treatment of the interaction [63].

2.4 The Recoil Excitation and Breakup model (REB)

The recoil excitation and breakup model (referenced as REB later on), relies on two simplifying assumptions [37]:

1. the projectile dynamics are treated adiabatically
2. the valence particle's interaction with the target is neglected ($V_{vT} = 0$) in comparison to the c-T interaction.

As we have seen in previous Sec. 2.3, the first approximation means that the projectile Hamiltonian can be considered as a constant, which for a projectile impinging in its ground state is the energy E_0 of the ground state. It should be noted that the second approximation was originally introduced in the context of reactions involving one-neutron halo nuclei. In these collisions, the v-T interaction can be neglected in comparison to the c-T interaction, which is constituted of a larger nuclear contribution as well as a Coulomb one. The term V_{vT} of the three-body Hamiltonian is thus nil. Hence, the Schrödinger equation (2.7) simplifies to

$$\left[\frac{P^2}{2\mu_{PT}} + E_0 + V_{cT}\left(\boldsymbol{R} - \frac{m_v}{m_P}\boldsymbol{r}\right) - E_{\text{tot}}\right] \Psi_{\text{REB}}(\boldsymbol{r}, \boldsymbol{R}) = 0. \tag{2.51}$$

Moreover, as E_0 is the internal energy of the projectile, the term $E_{\text{tot}} - E_0$ is simply the center-of-mass kinetic energy of the system, which can also be written as $\hbar^2 \boldsymbol{K}_0^2 / 2\mu_{PT}$.

A second consequence of the adiabatic approximation is the fact that $\boldsymbol{r}$ can be considered as a parameter [37]. By posing $\boldsymbol{R'} = \boldsymbol{R} - m_v\boldsymbol{r}/m_P$, we simplify the Schrödinger equation even further, the term between brackets then being an expression that only depends on the variable $\boldsymbol{R'}$. This allows us to factorise the wavefunction into the product

$$\Psi^{\mathrm{REB}}(\boldsymbol{r},\boldsymbol{R}) = \phi_0(\boldsymbol{r})\, e^{i\frac{m_v}{m_P}\boldsymbol{K_0}\cdot\boldsymbol{r}}\, \psi^{\mathrm{REB}}_{\boldsymbol{K}_0}(\boldsymbol{R'}). \tag{2.52}$$

which satisfies the boundary condition (2.8) and hence

$$\psi^{\mathrm{REB}}_{K_0}(\boldsymbol{R'}) \xrightarrow[Z\to-\infty]{} e^{i\boldsymbol{K}_0\cdot\boldsymbol{R'}} \tag{2.53}$$

The wave function $\psi^{\mathrm{REB}}_{K_0}(\boldsymbol{R'})$ is solution to the Schrödinger equation

$$\left[\hat{T}_{\boldsymbol{R'}} + V_{cT}(\boldsymbol{R'}) - \frac{\hbar^2\boldsymbol{K}_0^2}{2\mu_{PT}}\right]\psi^{\mathrm{REB}}_{K_0}(\boldsymbol{R'}) = 0, \tag{2.54}$$

where $\hat{T}_{\boldsymbol{R'}}$ is the kinetic energy operator on the variable $\boldsymbol{R'}$. It should be noted that $\psi^{\mathrm{REB}}_{\boldsymbol{K}_0}(\boldsymbol{R'})$ is the wavefunction of a particle of mass μ_{PT} and momentum $\hbar\boldsymbol{K}_0$ scattered by the potential V_{cT}. In other words, it corresponds to the wavefunction of a pointlike projectile scattered by a structureless target through V_{cT}. The fact that the projectile is seen as pointlike does not mean that breakup is not accounted for. Indeed, the wavefunction still keeps a dependence in $\boldsymbol{r}$ through the exponential but also through the argument $\boldsymbol{R'}$ of $\psi^{\mathrm{REB}}_{\boldsymbol{K}_0}$ [37].

Let us now look at the elastic scattering transition amplitude from the initial momentum $\hbar\boldsymbol{K}_0$ to the final one $\hbar\boldsymbol{K}$, noted $T_{\mathrm{el}}(\boldsymbol{K},\boldsymbol{K}_0)$. The elastic scattering final state is given by $\phi_0(\boldsymbol{r})\, e^{i\boldsymbol{K}\cdot\boldsymbol{R}}$. $T_{\mathrm{el}}(\boldsymbol{K},\boldsymbol{K}_0)$ is thus given by [37]

$$T_{\mathrm{el}}(\boldsymbol{K},\boldsymbol{K}_0) = \iint \phi_0^*(\boldsymbol{r})\, e^{i\boldsymbol{K}\cdot\boldsymbol{R}}\, V_{cT}\left(\boldsymbol{R} - \frac{m_v}{m_P}\boldsymbol{r}\right)\, \Psi_{\mathrm{REB}}(\boldsymbol{r},\boldsymbol{R})\, d\boldsymbol{r}\, d\boldsymbol{R}. \tag{2.55}$$

If we now make the change of variable from $\boldsymbol{R}$ to $\boldsymbol{R'}$, it reads

$$T_{\mathrm{el}}(\boldsymbol{K},\boldsymbol{K}_0) = \iint \phi_0^*(\boldsymbol{r})\, e^{-i\boldsymbol{K}\cdot\left(\boldsymbol{R'}+\frac{m_v}{m_P}\boldsymbol{r}\right)}\, V_{cT}(\boldsymbol{R'})\, \phi_0(\boldsymbol{r}) e^{i\frac{m_v}{m_P}\boldsymbol{K}_0\cdot\boldsymbol{r}} \psi^{\mathrm{REB}}_{\boldsymbol{K}_0}(\boldsymbol{R'})\, d\boldsymbol{r}\, d\boldsymbol{R'} \tag{2.56}$$

$$= \left[\int |\phi_0(\boldsymbol{r})|^2\; e^{i\boldsymbol{Q}\cdot\boldsymbol{r}}\, d\boldsymbol{r}\right] \times \left[\int e^{-i\boldsymbol{K}\cdot\boldsymbol{R'}}\, V_{cT}(\boldsymbol{R'})\, \psi^{\mathrm{REB}}_{\boldsymbol{K}_0}(\boldsymbol{R'})\, d\boldsymbol{R'}\right]. \tag{2.57}$$

where $\boldsymbol{Q} = m_v/m_P(\boldsymbol{K}_0 - \boldsymbol{K})$ is proportional to the difference between the outgoing momentum $\hbar\boldsymbol{K}$ and the incoming momentum $\hbar\boldsymbol{K}_0$ and has the norm

$$Q = 2\frac{m_v}{m_P}K_0 \sin(\theta/2). \tag{2.58}$$

We note that the scattering amplitude is factorised into two factors. The first one is a form factor and the second can be identified as the scattering transition amplitude from initial state $\psi^{\mathrm{REB}}_{\boldsymbol{K}_0}(\boldsymbol{R'})$ to final state $e^{-i\boldsymbol{K}\cdot\boldsymbol{R'}}$ by the potential V_{cT}. In other words, as we have seen previously, it represents the elastic scattering transition amplitude for a pointlike projectile when scattered by the core-target potential V_{cT}.

The two assumptions of the REB model thus allow us to factorise the elastic scattering cross section into the form [37]

$$\left(\frac{d\sigma}{d\Omega}\right)_{\mathrm{el}} = |F_{0,0}(\boldsymbol{Q})|^2 \left(\frac{d\sigma}{d\Omega}\right)_{\mathrm{pt,el}}, \tag{2.59}$$

where $|F_{0,0}(\boldsymbol{Q})|^2$ is a form factor of the projectile and $(d\sigma/d\Omega)_{\text{pt,el}}$ is the cross section of a pointlike projectile of mass μ_{PT} scattered by the core-target interaction. The form factor reads

$$|F_{0,0}(\boldsymbol{Q})|^2 = \frac{1}{2j_0+1}\sum_{m_0}\left|\int |\phi_0(\boldsymbol{r})|^2 e^{i\boldsymbol{Q}\cdot\boldsymbol{r}}\, d\boldsymbol{r}\right|^2, \tag{2.60}$$

We see from this expression that $F_{0,0}(\boldsymbol{Q})$ acts as a modulation of the diffraction pattern of the pointlike cross section and hence accounts for the extension of the halo. It characterises the relevant scattering angles and energies at which a halo, of a given size and structure, will cause the cross section to deviate from the scattering of a pointlike projectile. Moreover, we see from the form of Eq. (2.60) that the form factor is actually the Fourier transform of the halo-ground state density. Its calculation is nearly immediate once the projectile wave function ϕ_0 is known. The computation of the cross section Eq. (2.59) is thus less involved than CDCC or DEA.

As done in Refs. [38, 64], the factorisation can be extended to breakup. Hence, we can write

$$\left(\frac{d\sigma}{dEd\Omega}\right)_{\text{bu}} = |F_{E,0}(\boldsymbol{Q})|^2 \left(\frac{d\sigma}{d\Omega}\right)_{\text{pt,el}} \tag{2.61}$$

with $F_{E,0}$ being the form factor in the case of a breakup to the energy E in the c-v continuum and which reads

$$|F_{E,0}(\boldsymbol{Q})|^2 = \frac{1}{2j_0+1}\sum_{m_0}\sum_{ljm}\left|\int \phi_0(\boldsymbol{r})\phi_{ljm}(E,\boldsymbol{r}) e^{i\boldsymbol{Q}\cdot\boldsymbol{r}}\, d\boldsymbol{r}\right|^2, \tag{2.62}$$

The expressions (2.59) and (2.61) are the REB predictions for the elastic cross section and the breakup to an energy E in the $c-v$ continuum. They are obtained by simply multiplying the form factors for the different processes by the pointlike term $(d\sigma/d\Omega)_{\text{pt,el}}$. It should be noted that this pointlike cross section is the same for both processes!

2.5 Interaction potentials

The form of the potentials that simulate the interactions of the different bodies of the reaction still needs to be defined. Both the potentials V_{cT} and V_{vT} that simulate the projectile-target interaction in the three-body Schrödinger equation (2.7) as well as the potential V_{cv} that simulates the core-valence nucleon interaction in Eq. (2.9) should reproduce the nuclear and Coulomb interaction of the nucleons of the different fragments. In this work, these will be chosen as phenomenological potentials. These potentials are composed of a Coulomb real part and a nuclear part, usually complex. The mathematical expressions of these potentials is presented hereafter.

The Coulomb potential

The V_{cT} potential will always contain a Coulomb part, as it simulates the interaction of two charged nuclei. Additionally, when the halo is charged, both the V_{cv} and V_{vT} will contain a Coulomb part since they simulate the interaction of a proton with a nucleus.

Due to the finite size of the core and the target, neither of these Coulomb potential has the form of a pure $1/r$ Coulomb potential. We can approximate the charge of the core and the target to be uniformly distributed over a radius R_C. For such a charge

distribution, the Coulomb interaction of a proton with some nucleus of mass number A is often reproduced by a potential of the form

$$V_C(r) = Z_P Z_T e^2 \times \begin{cases} \left(\frac{3}{2} - \frac{r^2}{2R_C^2}\right)\frac{1}{R_C} & \text{for } r \leq R_C \\ \frac{1}{r} & \text{for } r \geq R_C. \end{cases} \tag{2.63}$$

where the radius R_C is usually chosen to be equal to $r_C A^{1/3}$. This form of the potential is can be used as is for the v-T and v-c interactions if the valence nucleon is a proton, A thus being replaced by the mass number of the target or the core. In the case of the Coulomb interaction between the core and the target, the same expression is used but uses a rescaled radius

$$R_C = r_C(A_c^{1/3} + A_T^{1/3}) \tag{2.64}$$

Note that usually, r_C is chosen between 1.2 and 1.4 fm.

The nuclear potential

As said before, the phenomenological potential that simulate the nuclear interaction are complex. They can be cast in the form

$$V_{\text{nucl}}(r) = V(r) - iW(r). \tag{2.65}$$

This form is handy when some of the reaction channels that are open in reality cannot be accounted by the model that is used to calculate the reaction (e.g. transfer reactions, excitations of the target, ... which cannot be accounted for in the models). Note that this absorption causes the phase shifts to become complex and the S-matrix to lose its unitarity.

The use of a negative complex component to simulate removal of flux is reminiscent of the use of complex refractive indices in optics when studying the propagation of light beams through a cloudy refractive medium [49]. Because of this similarity, these complex potentials are usually called *optical* potentials.

Different potential shapes have been developed to reproduce the different features of nuclear reactions. Usually however, the shape of the real and complex parts of the optical potentials is chosen as a Woods-Saxon well. This shape has been first brought by Roger D. Woods and Davis S. Saxon in 1954 [65] to describe the interaction between a nucleon and a nucleus or between a nucleus and another nucleus. Its form reads

$$f(r, R, a) = \frac{1}{1 + e^{(r-R)/a}}. \tag{2.66}$$

where a is the diffuseness (typically about 0.6 fm) and R is the nuclear radius, which is proportional to the size of the nucleus. For a nucleon-nucleus collision and in a similar fashion as what was done for the Coulomb interaction, the radius R is chosen equal to $r_0 A^{1/3}$, where A is the nucleus mass number and where the reduced radius r_0 is usually chosen in the range $\simeq 1.2 - 1.4$ fm. For nucleus-nucleus interactions (i.e. the c-T nuclear interaction) the radius can be scaled in the same way as in Eq. (2.64).

The nuclear interaction can be modeled by a potential that contains several of these wells. As an example, the nucleon-nucleus potentials of the Koning and Delaroche parametrisation have the form [66]

$$V_{\text{nucl}}(r) = -V_r\, f(r, R_r, a_r) - i\left[W_i\, f(r, R_i, a_i) + 4a_D W_D \frac{d}{dr}\left(f(r, R_D, a_D)\right)\right] \tag{2.67}$$

$$= \quad V_V(r) \quad + iW_V(r) \quad + iW_S(r). \tag{2.68}$$

where in addition to the first real term of central depth $V_V < 0$ and known as the volume term, they include an imaginary volume term of depth $W_V < 0$ and a surface-peaked imaginary term of depth W_S which has the shape of a derivative of a Woods-Saxon well.

In some cases, the potentials can also be spin dependent. The spin-orbit interaction is a $\lambda = 1$ multipole component and corresponds to the coupling of the spin of one particle and its motion. The vector-potential for a single nucleon interacting with its motion and reads

$$V_{\rm so}(r) = 2\,\mathcal{F}_{\rm so}(r)\,\boldsymbol{l}\cdot\boldsymbol{s} \tag{2.69}$$

where $\boldsymbol{l}$ is the angular momentum of the nucleon and $\boldsymbol{s}$ its spin angular momentum and where $\mathcal{F}_{\rm so}(r)$ is the spin-orbit form factor and has the form [67]

$$\mathcal{F}_{\rm so}(r) = V_{\rm so}\left(\frac{\hbar}{m_\pi c}\right)^2 \frac{1}{r}\frac{d}{dr}\left(\frac{1}{1+e^{(r-R_{\rm so})/a_{\rm so}}}\right) \tag{2.70}$$

where the factor $(\hbar/m_\pi c)^2 \simeq 2$ fm^2 is an arbitrary scaling factor.

Because little information is known about the actual interaction that exists between the different bodies of the reaction, all these potentials are usually fitted to reproduce some features of the studied systems, e.g. elastic scattering cross sections.

3 The ratio method

3.1 The ratio observable

In order to introduce the ratio observable, it is useful to have a look at the elastic scattering and the angular breakup cross sections of a reaction involving a neutron halo nucleus. These are shown on Fig. 3.1 for the reaction of ^{11}Be, the best known one-neutron halo nucleus, on a ^{12}C target at 20 MeV/nucleon as functions of the scattering angle θ between the initial and final directions of the projectile centre of mass, whether it breaks up or not. Because it diverges at forward angle, the elastic scattering cross section is divided by Rutherfords. The breakup cross section is calculated for a breakup of the projectile to a final c-n scattering state of energy E=125 keV. As it can be observed, both cross sections seem to oscillate in phase. Also, they exhibit similar decay patterns.

This similar diffraction pattern is also present if we change the target. On Fig. 3.2, the elastic scattering cross sections (left, in black) and differential breakup cross sections calculated at the same energy as above (right, in red) are displayed for a ^{12}C (solid), ^{40}Ca (dashed) and ^{208}Pb (dash-dotted) targets. These cross sections are given as a function of the momentum transfer Q [Eq. (2.58)] to remove the target-mass dependence. The differences between these cross sections can be seen both in shape and in magnitude, with discrepancies up to three orders of magnitude. They are due to the very different reaction mechanisms at play in these collisions. Because of these discrepancies, the clean extraction of valuable information on the halo structure itself can be hindered. It should be noted however that the differential breakup cross sections seem to oscillate in phase and have a similar decay pattern to their corresponding elastic scattering cross sections.

This behaviour is reminiscent of the expressions of these cross sections in the REB model [Eqs. (2.59) and (2.61)] where they are both proportional to the same pointlike elastic cross section $(d\sigma/d\Omega)_{\rm pt,el}$. In the assumptions of the REB, we should thus observe a similar oscillation pattern for all these cross sections (if the form factors do not vary too quickly with Q). This is exactly what we see in Fig. 3.1 for fully-dynamical calculations. It should be noted that since $(d\sigma/d\Omega)_{\rm pt,el}$ contains all the c-T interaction dependences of the differential cross sections in which we are not interested, it is tempting to take their ratio in order to cancel out this pointlike cross sections and hence remove all the angular dependence that does not originate from the projectile structure. This gives rise to an observable in the form of a ratio of form factors. This ratio should be sensitive only to the structure of the projectile and should hence remove all dependences on the core-target interaction. As these can be ambiguous to describe since the core of halo nuclei is most often radioactive, this is an additional valuable property for this observable. Note that any linear combination of elastic or breakup cross sections should also exhibit this property [see Eqs. (2.59) and (2.61)].

In this work, I will consider the summed ratio

$$\mathcal{R}_{\rm sum}(E,\boldsymbol{Q}) = \frac{(d\sigma/dEd\Omega)_{\rm bu}}{(d\sigma/d\Omega)_{\rm sum}}, \tag{3.1}$$

where $(d\sigma/dEd\Omega)_{\rm bu}$ is simply the angular distribution cross section for breakup at the energy E in the c-n continuum and where the summed cross section reads

$$\left(\frac{d\sigma}{d\Omega}\right)_{\rm sum} = \left(\frac{d\sigma}{d\Omega}\right)_{\rm el} + \int \left(\frac{d\sigma}{dEd\Omega}\right)_{\rm bu} dE, \tag{3.2}$$

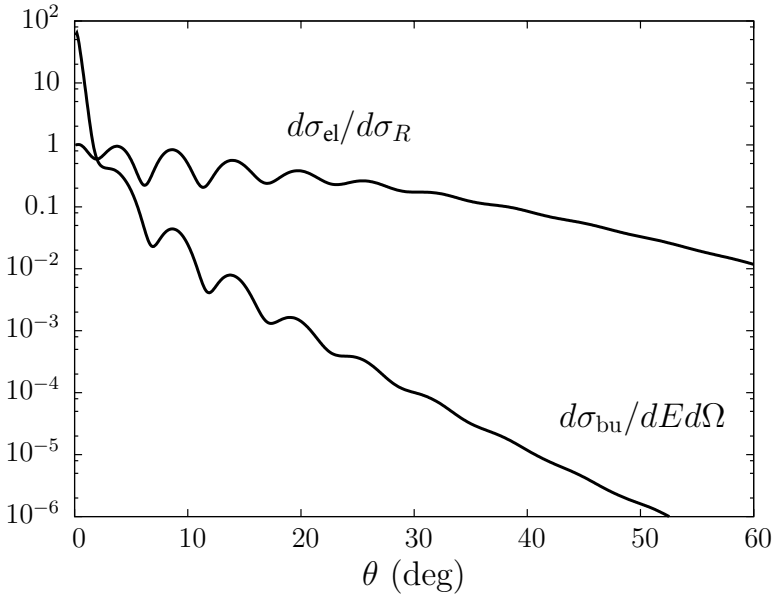

Figure 3.1: Elastic scattering and breakup angular distributions for the reaction of ^{11}Be on ^{12}C at 20 MeV/nucleon as a function of the scattering angle θ. Note that the elastic scattering cross section is given as a ratio to Rutherford's and the breakup angular distributions are given in units of b/MeV sr.

i.e. the sum of the elastic-scattering cross section with the integrated breakup cross section[2]. In the REB approximation [see Eqs. (2.59) and (2.61)], this ratio of cross sections reads

$$\frac{(d\sigma/dEd\Omega)_{\rm bu}}{(d\sigma/d\Omega)_{\rm sum}} \overset{\rm (REB)}{=} \frac{|F_{E,0}(\boldsymbol{Q})|^2}{|F_{0,0}(\boldsymbol{Q})|^2 + \int |F_{E',0}(\boldsymbol{Q})|^2 \, dE'}. \tag{3.3}$$

where the form factors are defined in Eqs. (2.62) and (2.60). As the sum of the form factors for every possible process is 1 because of closure relations (this result is demonstrated in Appendix A), the ratio simplifies and reads finally

$$\mathcal{R}_{\rm sum}(E,\boldsymbol{Q}) \overset{\rm (REB)}{=} |F_{E,0}(\boldsymbol{Q})|^2. \tag{3.4}$$

The ratio $\mathcal{R}_{\rm sum}(E,\boldsymbol{Q})$ leads to the observable with the simplest expression. It has also been shown to be more optimal to consider and is probably the easiest to measure experimentally [68]. As seen from expression (3.4), the ratio $\mathcal{R}_{\rm sum}(E,\boldsymbol{Q})$ represents the ratio of the differential angular distribution cross section for breakup, $(d\sigma/dEd\Omega)_{\rm bu}$, at a given energy E, on the summed angular distribution cross section, $(d\sigma/d\Omega)_{\rm sum}$. It should be noted that because it is the ratio of two cross sections, this observable is not sensitive to normalization. This is a valuable experimental quality.

In the work of Capel *et al.* [68], the REB prediction and the ratio observable have been studied and compared to DEA calculations at an energy of roughly 70 MeV per nucleon for the reaction of ^{11}Be on carbon and lead targets. DEA and REB predictions proved to be in quite a good agreement. This original study has been carried out at 70 MeV per nucleon because breakup experiments have been performed at this intermediate

[2]Note that in my work, no other bound state than the ground state are considered for my calculations. In the expression of the summed cross section, no inelastic process is hence considered. If those were included in the model, a more general expression of the summed cross section would be Eq. (1.11) which includes inelastic contributions.

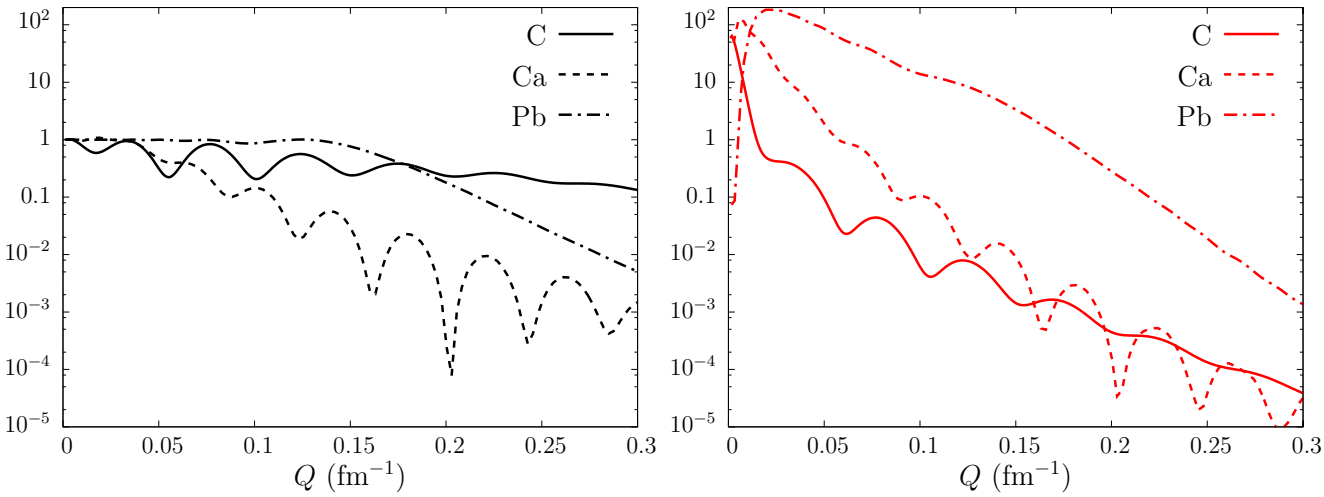

Figure 3.2: Elastic scattering (black, left) and breakup (red, right) angular distributions for the reaction of ^{11}Be on ^{12}C, ^{40}Ca and ^{208}Pb at 20 MeV/nucleon as a function of Q. Note that the elastic scattering cross section is given as a ratio to Rutherford's and the breakup angular distributions are given in units of b/MeV sr.

energy. However, at such energies, all differential cross sections are very forward focused and it is rather challenging to measure them accurately.

To explore the limits of the ratio method, it is interesting to study this observable for lower energy reactions. By going to lower energies, the angular range would extend to larger angles. This becomes clear by noticing how the projectile energy dependence of $|F_{E,0}(\boldsymbol{Q})|^2$ appears only through the momentum transfer Q [see Eq. (2.58)]. For a given target, the smaller the beam energy, the smaller the impinging momentum K_0, and therefore reducing the beam energy widens the distribution to larger angles. Identically, for a given beam energy, a decrease in the target mass decreases K_0, producing a similar effect. The aim of this work is hence to test the ratio at lower energies of the projectile that would make the measurement easier as well as appropriate to facilities such as SPIRAL2 (GANIL, Caen, France) and ReA12 at FRIB (Michigan State University). Note that the energies at which these facilities will operate are outside of the hypotheses of the REB and it is not trivial that the idea of the ratio will remain valid.

While the REB model, on which the ratio idea is based, was originally thought for neutron halos at intermediate and high energies, I will also explore the validity of the ratio for proton halo nuclei. These tests will be carried out for a ^{8}B projectile, which exhibits a very clear one-proton halo structure and at intermediate energy, at which the ratio should work best. The study will then be extended to other proton-rich nuclei. All these tests will allow me to explore the limits of the ratio and hopefully lay the ground for future experiments.

In order to study the ratio observable, I will perform fully dynamical calculations for the reactions I have just briefly discussed. The dynamical ratio observable $\mathcal{R}_{\text{sum}}(E, \boldsymbol{Q})$ will then be compared to its REB approximation $|F_{E,0}(\boldsymbol{Q})|^2$ [see Eq. (3.4)] to evaluate if it remains valid. As seen in Ref. [57], while there is a good agreement between CDCC and DEA breakup-problems calculations for energies of the projectile of about 70 MeV per nucleon, the DEA is no longer valid at energies of 20 MeV per nucleon. In the case of the ^{11}Be halo nucleus, I will thus study the reliability of the REB prediction and of the ratio

at such low energies with the CDCC method. In the case of ^{8}B, for which data exist at an intermediate energy of 44 MeV per nucleon[3] [69], calculations will be performed with the DEA. The use of the DEA has been shown to work well for this reaction [70] and allows for shorter computation times than CDCC.

3.2 Neutron halos at low energy

In this section, the reaction of a ^{11}Be projectile impinging at 20 MeV/nucleon on several targets is analysed. Before analysing the validity of the REB hypothesis (3.4) and its agreement with the dynamical ratio observable $\mathcal{R}_{\rm sum}(E, \boldsymbol{Q})$, the sensitivity of the form factor, and hence the ratio, to the projectile structure is studied. After that, calculations on a light (^{12}C), a medium-mass (^{40}Ca) and a heavy (^{208}Pb) target are considered to further test the ratio observable. In this way, the whole spectrum of reactions are probed, from nuclear-dominated processes to Coulomb-dominated ones. The results reported in this section have led to the publication of Ref. [71].

3.2.1 Numerical details for reactions involving ^{11}Be

Before going through the results of the calculations, let me summarise the parameters of the optical potentials that I have chosen to simulate the interaction between the valence fragment—a neutron—and the core V_{cn} (Tab. I.2) and between the constituents of the projectile and the target V_{nT} and V_{cT} (Tab. I.3).

In the low-energy spectrum of ^{10}Be, we find a $1/2^+$ ground state with a binding energy of 503 keV (with respect to the neutron emission threshold). This state is reproduced as a neutron in the $1s$ orbital by the optical potential given in Tab. I.2. Note that another bound state $1/2^-$ which sits 320 keV above the ground state [72] exists but will not be considered in this work. In this case, the valence neutron is considered spinless. These parameters are taken from [45]. The shapes are chosen as in Eqs. (2.68) and (2.69).

Table I.2: Parameters of the single-particle potentials simulating the c-n interactions for ^{11}Be. The binding energy (in keV) of the ground state and partial wave of the ground state is also given. The depth of the real potential is given in MeV while radii and diffusenesses are given in fm. See Ref. [45]

c-n	E_0 [keV]	$n_0 l_{0j_0}$	V_r	R_r	a_r
^{11}Be	-503	$1s_{1/2}$	62.52	2.585	0.6

The n-T interaction parameters are taken from the Koning and Delaroche parametrisation [66], which describes the global interaction of a nucleon with a nucleus[4] in a wide range of energies. The parameters of the ^{10}Be-target interaction have been taken from Ref. [73], where ^{12}C is impinging on ^{12}C and ^{208}Pb at 25 MeV/nucleon, and have been rescaled to our problem according to (2.64). Note that to study the influence of the c-T interaction, a different potential developed by Robson [74] to reproduce the elastic scattering of ^{10}B on a carbon target at 18 MeV (total energy) and listed in the Perey and

[3] Note however that unfortunately, while data indeed exists for this reaction, no breakup angular distributions nor elastic scattering angular cross sections are provided.

[4] I am aware that the parameters taken from this paper are not really fit to interactions of a neutron with nuclei with $A < 24$ but the large energy range covered by the paper makes this choice convenient.

Perey compilation [75] is also used. The corresponding parameters of the potential, which shape potential is given as in Eqs. (2.63) and (2.68), are summarized in Tab. I.3.

Table I.3: Parameters of the optical potentials simulating the interaction between the fragments of the ^{11}Be projectile and the different target nuclei. Potential depths are given in MeV while radii and diffusenesses are given in fm. See Eqs. (2.63) and (2.68) for the shape of these potentials. See Refs. [66, 73, 74, 75, 76]

P	T	V_r	R_r	a_r	W_i	R_i	a_i	W_D	R_D	a_D	R_C
n	^{12}C	46.9395	2.5798	0.676	1.8256	2.5798	0.676	28.6339	2.9903	0.5426	–
	^{40}Ca	46.709	4.054	0.672	1.728	4.054	0.672	28.926	4.406	0.538	–
	^{208}Pb	41.4872	7.3202	0.6469	1.1858	7.3202	0.6469	26.4580	7.3973	0.5102	–
^{10}Be	^{12}C	250	3.053	0.788	247.9	2.982	0.709	0	–	–	5.777
	^{12}C	100	5.40	0.5	18	5.40	0.5	0	–	–	5.40
	^{40}Ca	200	4.465	0.837	276.9	5.000	0.653	0	–	–	4.465
	^{208}Pb	95	7.0129	1.168	250	7.9582	0.662	0	–	–	10.503

3.2.2 Sensitivity to the projectile structure

In order to illustrate the properties of the form factor for a ^{11}Be projectile and see how sensitive it is to the structure of the projectile, we can modify the c-n potential V_{cn}. By varying the depth of the s-wave of V_{cn}, we can modify the halo binding energy. On Fig. 3.3, the form factor $|F_{E,0}|^2$ (2.62) for halos bound in the $1s$ wave by 50 keV (dashed), the realistic ^{11}Be binding energy 0.5 MeV (solid) and 5 MeV (dotted) are represented. Are also represented the form factors for a halo bound in a $0p$ (long-dashed line) and $0d$ (dash-dotted line) orbitals. These are obtained by fitting the 0.5 MeV binding energy in these orbitals. As expected from the results of Ref. [38], the form factor exhibits a strong dependence on the projectile structure, both in shape and in magnitude. This shows that the ratio could be a very useful method to measure precisely and simultaneously these two quantities.

To further test the dependence to the halo structure, the sensitivity to the radial wave function is also explored. These can be varied by modifying the shape of the c-n potential in the s-wave and then readjusting the depth of the interaction to reproduce the physical bound state. On Fig. 3.4 the radial wave functions for the original ^{11}Be wave function (solid), small (dotted) and large (dashed) radii of the potential (R_r in Tab. I.2) and for a $0s$ state (dash-dotted), that shows the effect of the removal of a node in the wave function, are represented.

On the left panel of Fig. 3.5, the corresponding form factors $|F_{E,0}|^2$ are shown. While the differences are less pronounced than for changes in the binding energy or the orbital, the form factors still exhibit some dependence on the internal and external parts of the wave function. Interestingly, this dependence can be pinpointed to a different angular range depending on the part of the wave function that is probed. For example, most of the sensitivity to the external part of the wave function is found at forward angles. Indeed, as visible on the right panel of Fig. 3.5, where the form factors have been scaled to the square of the ANC of the wave function $|\mathcal{C}_{00}|^2$ [see Eq. (2.12)], they are superimposed at

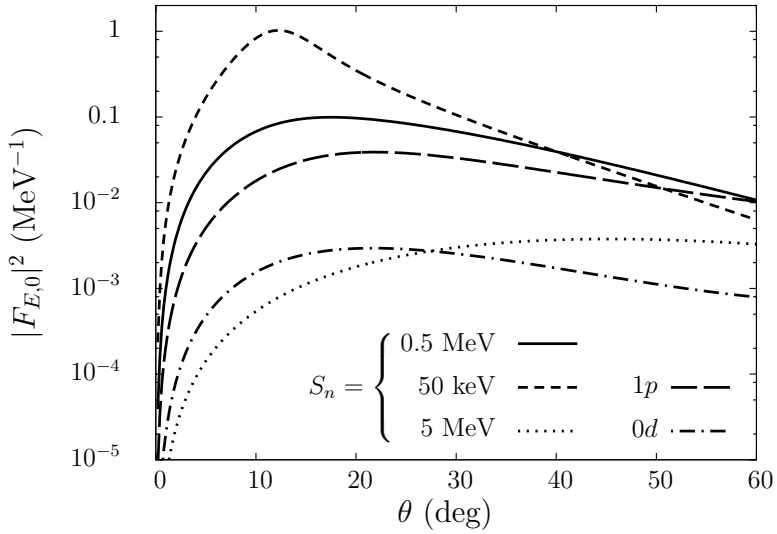

Figure 3.3: Sensitivity of the form factor $|F_{E,0}|^2$ (Eq. (2.62)) to the binding energy and the partial wave of the halo neutron to the core: included are the realistic ^{11}Be, i.e. a $1s$ state bound by 0.5 MeV (solid line), a loosely bound $1s$ state $S_n = 0.05$ MeV (short-dashed line), and a well bound $1s$ state $S_n = 5$ MeV (dotted line). Also shown are the ratios for a $1p$ (long-dashed line) and a $0d$ state (dash-dotted line) both bound by 0.5 MeV.

forward angles. At larger angles, on the contrary, they still exhibit a different behaviour. This shows that the form factor $|F_{E,0}|^2$ is sensitive to the radial wave function of the bound state, although the breakup and elastic scattering observables are not [77]. This result confirms the observations made in Ref. [68].

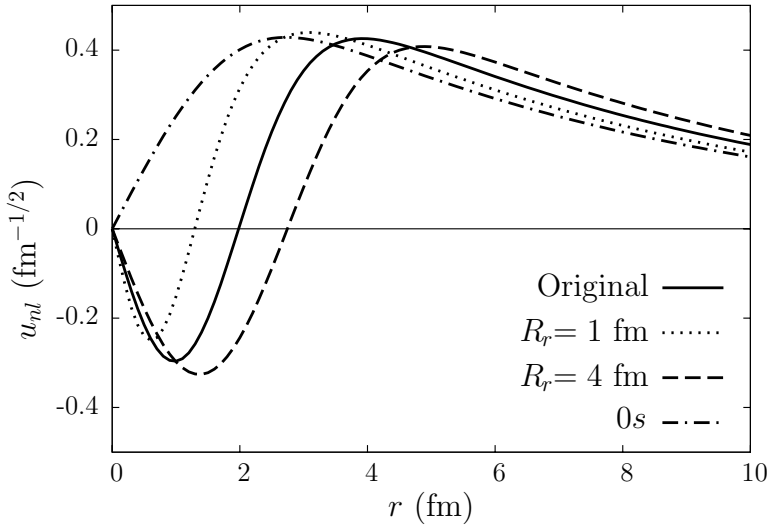

Figure 3.4: Reduced radial wave function for the original ^{11}Be wave function (solid line), for small (dotted line) and large (dashed line) radii (R_r in Tab. I.2) as well as for a 0s state (dash-dotted line).

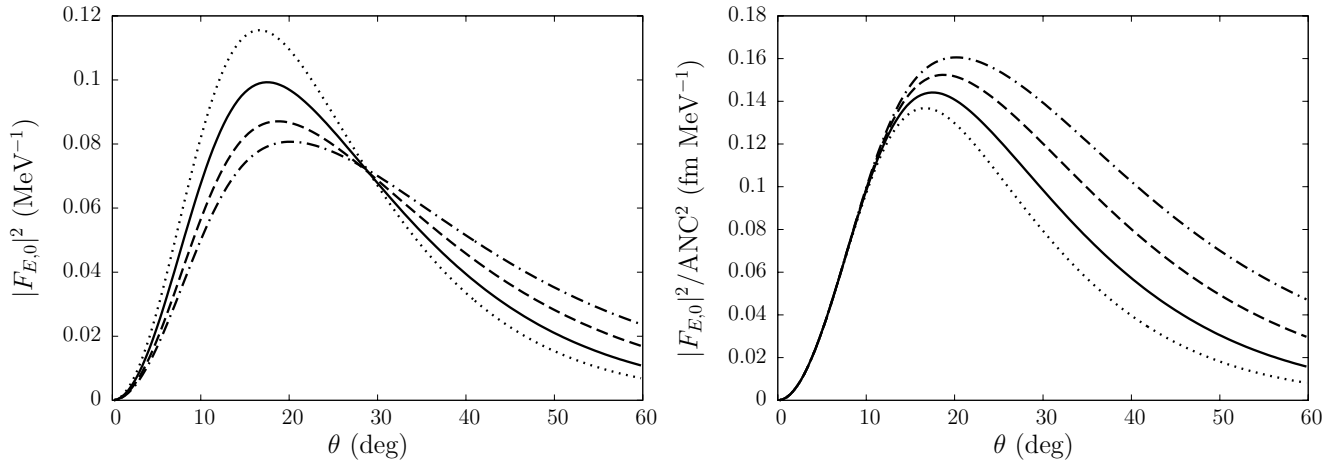

Figure 3.5: Sensitivity of the form factor to the radial wave function (see Fig. 3.4). The form factor $|F_{E,0}|^2$ (left) and $|F_{E,0}|^2$ divided by the square of the ANC $|\mathcal{C}_{00}|^2$ of the ground state wave function u_{00} [see Eq. (2.12)] (right).

3.2.3 Analysis of the ratio method at low energy

^{12}C target

I will start the analysis of the ratio observable at low energy on a light target, namely ^{12}C. As the target is light, the reaction is nuclear dominated. Since the range of the (nuclear) potential is small, this reaction should therefore better fit in the adiabatic assumption of the REB than a Coulomb dominated reaction.

CDCC computations for this reaction are shown on Fig. 3.6 as solid lines. While DEA calculations (corrected for the Coulomb interaction Eq. 2.48) should not be valid at these energies, they are still displayed as dashed lines. I will comment on them later. The figure displays the summed cross section defined in Eq. (3.2) divided by Rutherford's, the differential breakup cross section for a n-^{10}Be continuum energy $E = 125$ keV (in b/MeV sr) as well as the ratio $\mathcal{R}_{\rm sum}$ (in MeV^{-1}) (3.1) calculated from these cross sections and the form factor $|F_{E,0}|^2$ obtained in the REB model (thick grey line), all as a function of the scattering angle θ.

As already observed at higher energies [78, 38, 68] and in Sec. 3.1, the breakup and summed cross sections exhibit a very similar oscillatory pattern. This is also reminiscent of the cross sections discussed in the REB model. By taking the ratio of these cross sections, these oscillations are hence strongly reduced. They give rise to a pretty smooth ratio $\mathcal{R}_{\rm sum}$ that follows quite well its REB prediction. Since the oscillations are not exactly in phase, the ratio still exhibits remnant oscillations. As observed in Ref. [37], they originate from the slight shift caused by the n-T interaction. Indeed, in the REB model where the valence nucleon is seen as a spectator, the breakup occurs solely because of the recoil of the core due to its interaction with the target. The additional n-T interaction contained in these calculations (compared to the REB model) is hence responsible for an extra kick on the valence neutron and hence induces a shift.

As we have seen in the previous sections, the purpose of the ratio is to provide with an observable that is independent of the reaction mechanism and hence of the potentials used to simulate the interaction between the projectile components and the target. In order to test this property, let us analyse the sensitivity of the ratio to the P-T interaction. On Fig. 3.7, the summed and differential breakup cross sections are plotted as a function of the scattering angle. The calculations involving both $c-T$ and $n-T$ interactions (and referred to as the *full* calculations in the following) (solid) are compared to calculations where the c-T interaction is modelled with a different potential V'_{cT} (dash-dotted, see grey line in Tab. I.3). Additionally, these are compared to calculations involving a non-interacting valence neutron $V_{nT} = 0$ (dotted) which is one of the assumptions of the REB model. The ratio of these cross sections (scaled for readability purposes) is compared to the REB prediction (thick grey). It should be observed how the differential breakup cross section drops rapidly under the mb/MeV sr past 15-20°, probably making the measurements difficult beyond this angle. A zoom at forward angles is hence given on the right panel of the figure.

The remnant oscillations of the ratio are very clearly visible on the right panel. As observed in Ref. [37] and discussed previously, they originate from the slight shift caused by the n-T interaction. This is confirmed if the calculations are performed by switching off the interaction of the valence neutron with the target ($V_{nT} = 0$). In this case, the oscillations are on phase and the ratio is hence perfectly smooth. It should be noted how the ratio is then in perfect agreement with its REB prediction despite the low energy of the reaction.

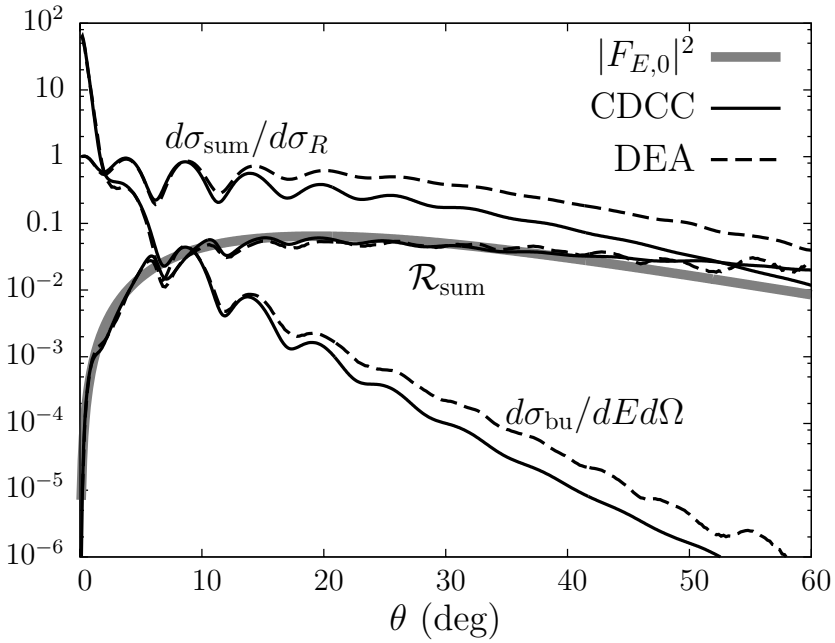

Figure 3.6: Comparison between the dynamical ratio $\mathcal{R}_{\rm sum}$ (see Eq. (3.1)) with its REB prediction $|F_{E,0}|^2$ (2.62) (thick grey line) for a ^{11}Be projectile impinging on a C target at 20 MeV/nucleon. I consider the breakup to a final c-n scattering state of energy $E = 125$ keV. CDCC (solid black lines) and DEA (dashed lines) calculations are displayed. See text for details.

The most interesting observation is probably the influence of the c-T potential on the individual cross sections and on the ratio. The full and V'_{cT} calculations are different not only in their oscillatory pattern but also in their large discrepancies at large angles. This shows how heavily dependent both the breakup and summed cross sections are on the choice of potential. But despite these large differences, their ratio remains nearly unchanged. Up to the remnant oscillations, their shape and magnitude is indeed very similar and closely follow the REB prediction. This result is a nice illustration of the (in)sensitivity of the ratio to the c-T interaction.

The logarithmic scale of these figures makes it easier to capture the trend and shape of the curves at all angles. However, it hinders some of their fine details. It is hence interesting to have a look at these results in linear scale. These are displayed on Fig. 3.8 (the labels are the same as for Fig. 3.7, note however that the ratio and its REB prediction are not scaled here). These theoretical cross sections are convoluted with a Gaussian of standard deviation 2° to simulate the experimental resolution that we could expect from such measurement. This smoothing is displayed in red.

As already observed on the logarithmic scale, the ratio $\mathcal{R}_{\rm sum}$ obtained by considering a spectator valence neutron $V_{nT} = 0$ is in perfect agreement with its REB prediction. When considering the n-T interaction however, the ratio exhibits remnant oscillations that are clearly visible here. By choosing a different c-T interaction, the oscillatory patterns is shifted differently but is very similar in magnitude. The ratio is hence not totally insensitive to the V_{cT} potential, but its dependence on the c-T is small. This is particularly true if we fold the ratios with a realistic angular resolution of 2° (red), simulating a finite experimental resolution. In both cases however, the ratios do not seem to follow the REB as closely as the logarithmic scale hinted or as it did for a

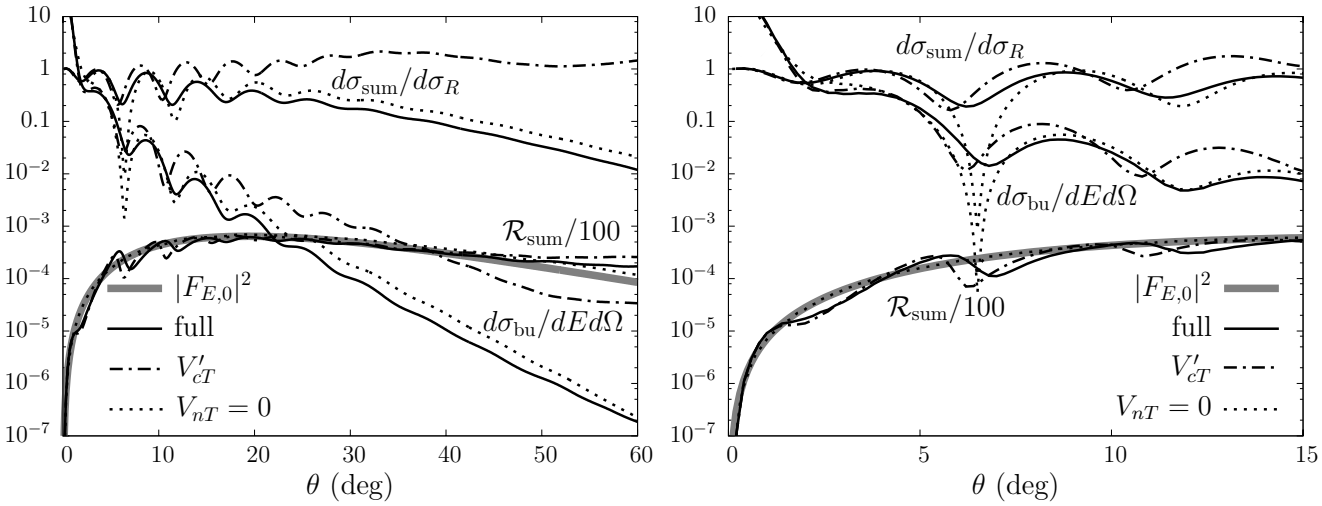

Figure 3.7: Sensitivity of the ratio to the P-T interaction for a C target at 20 MeV/nucleon. The breakup is considered to a final c-n scattering state of energy $E = 125$ keV. The full calculation (solid lines) is compared to the results obtained when $V_{cT} =$ RPP (dash-dotted lines) [see grey line of Tab. I.3] and with $V_{nT} = 0$ (dotted lines). The REB form factor $|F_{E,0}|^2$ is plotted as well (thick grey line). (Left) Full angular range (using CDCC). (Right) Forward-angle region.

collision at higher energy (see Fig.4 of Ref. [68]). While the ratio for a spectator valence neutron superimposes to its REB prediction, the other two exhibit the same trend but are overestimated by $|F_{E,0}|^2$.

These results on a light target at low energy show that the ratio does not exhibit the same agreement with its REB prediction as it did at intermediate energies. Nevertheless, it shows that while the conditions of the reaction are beyond the hypotheses of the REB, the ratio still exhibits some interesting properties, i.e. the attenuation of the oscillatory pattern of the individual cross sections, its near independence to the c-T interaction compared to the variations induced by this interaction on the individual cross sections.

As already stated above, at an energy of 20 MeV/nucleon, the CDCC method is the most reliable model. The calculations shown in Figs. 3.7 and (3.8) have thus been carried out with this model. Since eikonal models are built on high-energy assumptions which are not met here, one should not rely on such calculations at this energy. It is nevertheless interesting to compare these two methods. If we go back to Fig. 3.6, where both these calculations are displayed, we can see how CDCC and DEA calculations are in good agreement at forward angles but disagree at larger ones. This behaviour is expected given that by going to large angles we depart from the eikonal assumptions of the DEA (see Sec. 2.3). Also, the reaction is there completely dominated by the nuclear part of the interaction [79]. The Coulomb correction Eq. (2.48) is hence not sufficient to reliably calculate these individual cross sections [80]. However, very interestingly, even though the CDCC and DEA individual cross sections do not agree past 15°, their ratio (3.1) are in good agreement much beyond that angle. This result indicates that using DEA calculations seems reasonable to test the validity of the REB prediction, especially since the DEA is much less computationally expensive than CDCC. For the heavier targets (Ca and Pb), for which the (repulsive) Coulomb force between the projectile and the target plays a more dominant role and for which the correction Eq. (2.48) gives better results, I will only use the DEA to study the ratio method.

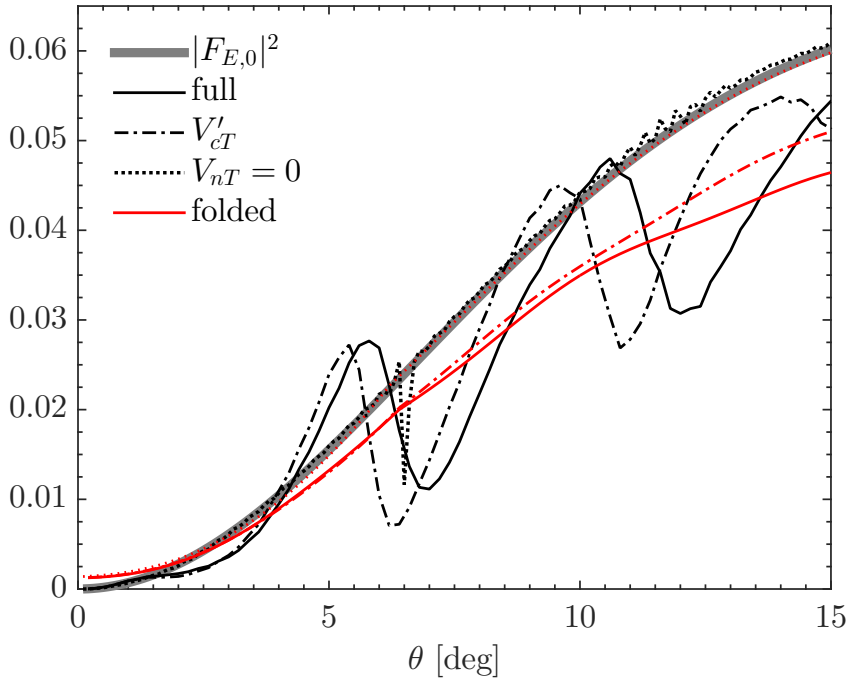

Figure 3.8: The ratios $\mathcal{R}_{\rm sum}$ (black) and REB form factor $|F_{E,0}|^2$ (thick grey) visible on Fig. 3.7 plotted in a linear scale. Smoothing of the ratios by the folding with an arbitrary experimental angular resolution of 2° is also displayed (red).

^{40}Ca target

As the target mass increases, the reaction becomes less nuclear dominated. On Fig. 3.9, the results of a series of calculations for a ^{40}Ca target, still at 20 MeV/nucleon. Note how for this target, the differential breakup cross section decays more rapidly than for a carbon target [see Fig. 3.7]. This pushes the angular range of interest towards forward angles. Attaining convergence for the CDCC method turned difficult. But since the angular region of interest is limited to forward angles where the reaction is dominated by Coulomb and the DEA is hence reliable, only results obtained with the DEA are shown here.

As observed for a light target, both summed and differential breakup cross sections exhibit very similar oscillatory patterns. By taking their ratio, these oscillations are significantly damped. These are however larger than for a light target. Up to these remnant oscillations, the ratio nonetheless follows a similar trend as its REB prediction (thick grey). Like for light targets, $\mathcal{R}_{\rm sum}$ seems to be slightly below $|F_{E,0}|^2$. As previously, by neglecting the n-T interaction ($V_{nT} = 0$), the REB assumptions are better satisfied and the ratio then becomes smooth and in perfect agreement with $|F_{E,0}|^2$. It should be noted that contrary to the light target case, a slight discrepancy exists at very forward angles. At these angles ($\theta \leq 2°$), the REB prediction over-estimates the ratio. This behaviour is due to the adiabatic approximation inherent to the REB model. At forward angles the reaction is completely dominated by Coulomb. This can be seen from the much flatter summed cross section (which is dominated by the elastic scattering). As the Coulomb interaction has an infinite range, the collision can hardly be considered adiabatic as it does not occur in a brief time, causing the REB assumptions to lapse. This also explains why this effect is barely visible for light targets (see very-forward angles on the right panel

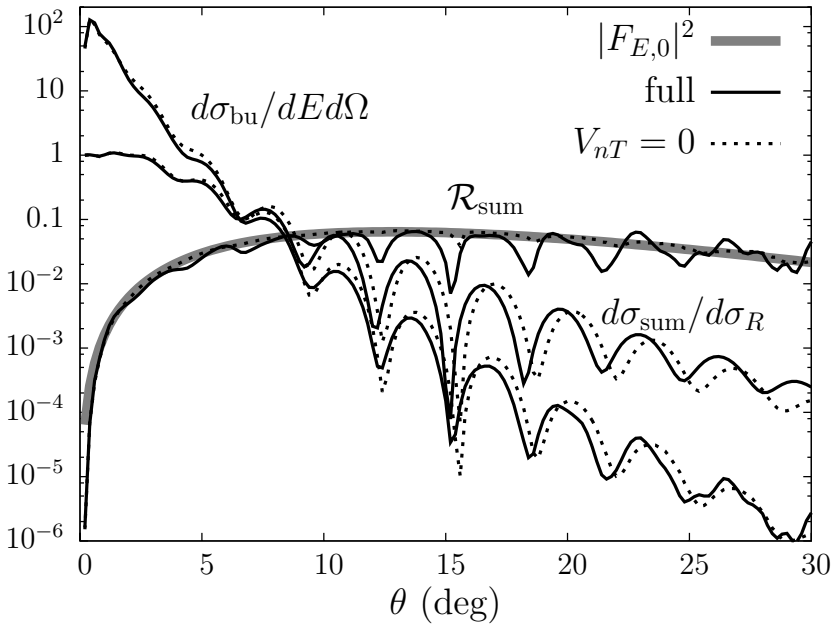

Figure 3.9: Sensitivity of the ratio to the P-T interaction for a ^{40}Ca target at 20 MeV/nucleon. The breakup is considered to a final c-n scattering state of energy $E = 125$ keV. The full calculation (solid lines) is compared to the results obtained with $V_{nT} = 0$ (dotted lines). The REB form factor $|F_{E,0}|^2$ is plotted as well (thick grey line).

of Fig. 3.7), for which the interaction is nuclear dominated. Note however that since cross sections are hardly measured in this angular range, this might not be noticeable in actual data taking.

^{208}Pb target

Finally, the same calculations have been performed on a ^{208}Pb target. These are shown on Fig. 3.10. As in the case of a ^{40}Ca target, convergence of the CDCC calculations has not been attained. Note however that very interestingly, the convergence rate of the ratio was better than the one from the individual cross sections. Only CC-DEA calculations, which have been shown to be reliable for this target at this energy [59] are shown here. Due to numerical instabilities beyond that angle, results are shown only up to 20°.

Results are less good than for lighter targets. Indeed, while the ratio $\mathcal{R}_{\rm sum}$ is rather smooth (mainly because the individual cross sections are also smooth) and has a similar trend to its REB prediction, it remains away from it. As for the lighter targets, by removing the n-T interaction, the ratio is in much better agreement with its REB prediction. However, as it should be expected, the much flatter summed cross section (divided by Rutherford's) at forward angles shows that the reaction on this target is totally dominated by Coulomb in this angular range. At these angles, the adiabatic approximation is hence even more poorly satisfied than for the calcium target (see Fig. 3.9). This thus leads to an overestimation of the breakup by the REB model and hence to a overestimation of the ratio, even for $V_{nT} = 0$. This observation, already discussed in Ref. [68], is significantly worsened by the low projectile energy.

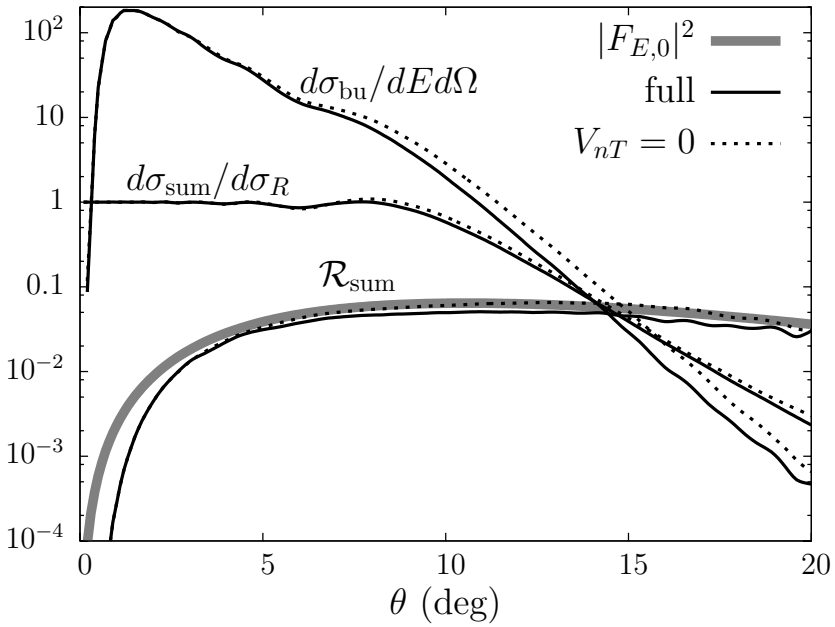

Figure 3.10: Same as Fig. 3.9 for a ^{208}Pb target.

Summary on all targets

It is interesting to have a look at the differential breakup and summed cross sections as well as their ratio for all targets in the same axes. These are displayed on Fig. 3.11 as a function of Q (2.58). For clarity, the ratio and its REB prediction are divided by 10 and the differential breakup cross section by 10^4. The main interest of the ratio is clearly illustrated here. Although all individual cross sections are significantly different in shape and magnitude, which shows how different the reaction mechanisms can be for all these targets, all ratios $\mathcal{R}_{\rm sum}$ lie near from their REB prediction $|F_{E,0}|^2$. As we have seen, some remnant oscillations still exist, especially for light targets, for which the reaction is nuclear dominated. But these are much smaller than the oscillations of the individual cross sections. The effect of the adiabatic approximation inherent to the REB model and more specifically the impact of the low energy of the reaction is also clearly seen here. At very forward angles, which correspond to small values of Q, the REB prediction overestimates the actual ratio. As the target mass increases and the infinite ranged Coulomb interaction becomes dominant, the sudden approximation lapses. Note however that while the ratio for the different targets exhibit clear differences, these are orders of magnitude smaller than the differences that can be observed in their respective individual cross sections.

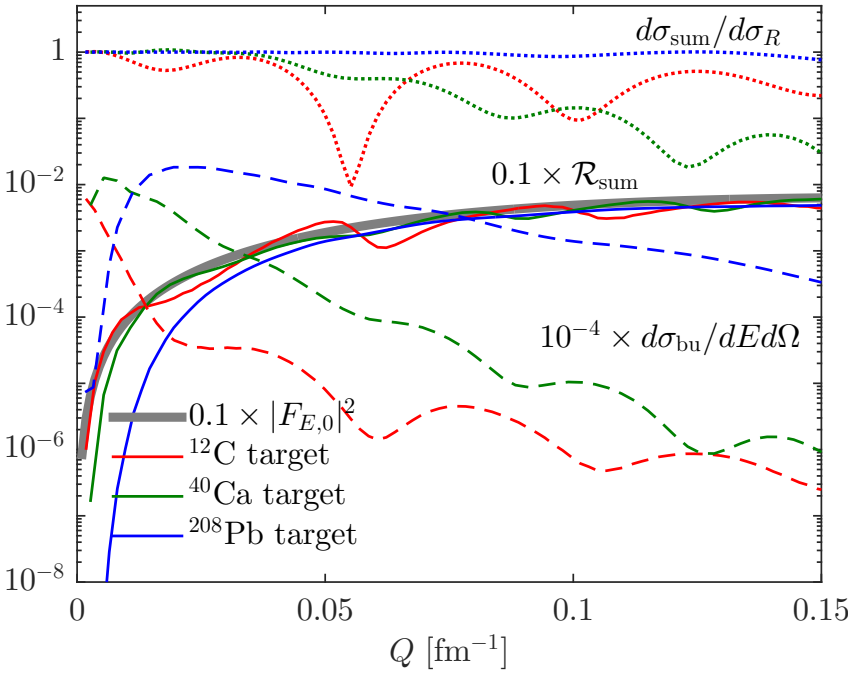

Figure 3.11: Sensitivity of the ratio to the target choice: DEA calculations on ^{12}C, ^{40}Ca, and ^{208}Pb at 20 MeV/nucleon are displayed as a function of Q [see Eq. (2.58)]. The differential breakup angular distributions, the ratio $\mathcal{R}_{\rm sum}$ and the REB form factor $|F_{E,0}|^2$ (thick grey line) are calculated at an energy $E = 125$ keV in the ^{10}Be-n continuum. Note the very small differences in the ratio observable for the different targets compared to the differences in the breakup and summed cross sections.

3.3 Proton halos

Originally thought for high-energy reactions involving neutron-halo nuclei, we have just seen how some of its valuable properties were still valid outside of the assumptions of the REB. It is then also interesting to see if the ratio method can be applied to proton-halos. Because the halo is charged, its interaction with the target includes the Coulomb force. Because of its infinite range, the Coulomb interaction can be hardly neglected and collisions with proton-rich nuclei are thus beyond the REB assumptions, which assumes the process to be adiabatic and neglects the v-T interaction. To study the applicability of the method at the other extreme of the nuclear chart, tests similar to those shown in previous section will be performed on the reaction of a ^{8}B projectile, the archetypical one-proton halo nucleus, at 44 MeV/nucleon. These conditions are the ones of the MSU breakup experiments of Davids *et al.* [69]. Calculations of this section will be performed using the DEA.

To illustrate the idea, some preliminary calculations are displayed on Fig. 3.12, where the angular distribution for the breakup of ^{8}B into ^{7}Be and p at the continuum energy $E = 125$ keV (in b/MeV sr), the summed cross section Eq. (3.2) divided by Rutherford's, their ratio $\mathcal{R}_{\rm sum}$ expressed in MeV^{-1}, and the corresponding REB form factor $|F_{E,0}|^2$ (thick grey line) are shown. As observed for a neutron-halo projectile, the breakup and summed cross sections oscillate in a very similar pattern. By taking their ratio, these oscillations are once more strongly reduced. However, due to the slight shift that exists between the elastic and breakup angular distributions, some remnant oscillations are still

visible. Nonetheless, even though collisions with proton-rich nuclei are beyond the REB assumptions, the ratio method seems to be applicable to ^{8}B and $\mathcal{R}_{\rm sum}$ is in a fair agreement with its REB prediction. The application of the ratio to this nucleus thus makes sense and will be studied thoroughly in this section.

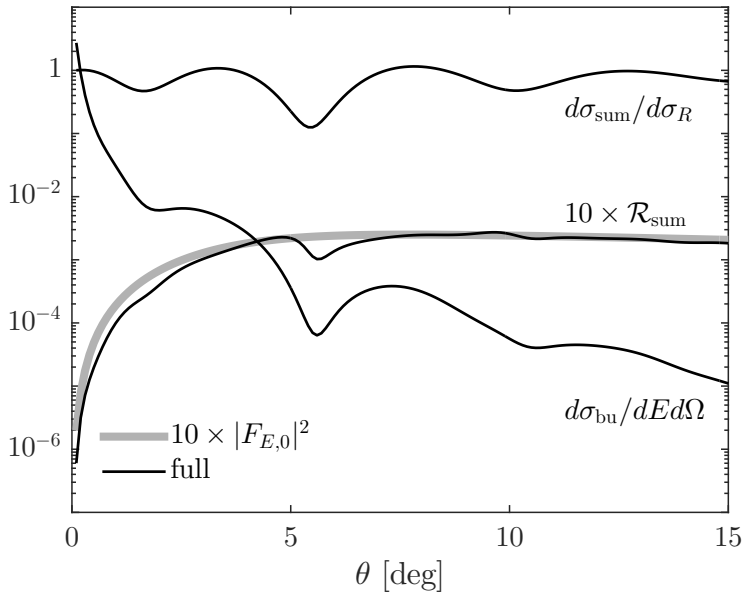

Figure 3.12: Comparison of the ratio $\mathcal{R}_{\rm sum}$ and REB form factor $|F_{E,0}|^2$ (thick grey line) for the reaction of ^{8}B impinging on ^{12}C at 44 MeV/nucleon. $\mathcal{R}_{\rm sum}$ and REB form factor $|F_{E,0}|^2$ are considered for an energy $E = 125$ keV in the ^{7}Be-p continuum and given in units of MeV^{-1}. Breakup angular distributions are given in units of b/MeV sr. Note that the ratio is multiplied here by 10 to improve the readability.

First, I will study the agreement of the ratio with its REB prediction through calculations on a light (^{12}C), a medium-mass (this time ^{58}Ni) and a heavy (^{208}Pb) target. Second, I will analyse the sensitivity of the form factor to the projectile structure. Finally, other proton-rich nuclei than this archetypical proton halo nucleus, i.e. ^{17}F, ^{25}Al and ^{27}P, will be explored to try and extend the ratio method to heavier proton-rich systems. The results of this section have led to the publication Ref. [81].

3.3.1 Numerical details for reactions involving ^{8}B

Before going through all the calculations made on ^{8}B, I will here summarise the parameters of the optical potentials that I have chosen to simulate the interaction between the valence nucleon—a proton this time—and the core V_{cp} (Tab. I.4) and between the constituents of the projectile and the target V_{pT} and V_{cT} (Tab. I.5).

The spectrum of ^{8}B includes only one bound state with a binding energy of merely 137 keV below the one-proton separation threshold. It has a 2^+ spin and parity and is obtained predominantly from the coupling of a $0p_{3/2}$ proton with the $3/2^-$ spin of the ground state of ^{7}Be [82]. Following Refs. [70, 83], I use the simplified version of the description of ^{8}B developed by Esbensen and Bertsch in [84], which neglects the spin of the core, i.e. ^{7}Be. The ground state is then seen as a $0p_{3/2}$ state. This potential reproduces a non-physical resonance around 2 MeV in the c-p continuum. The effect of

this resonance will be discussed later. Note that here, because the calculations are done in the DEA and are hence significantly shorter than for CDCC, I will consider the spin of the valence proton.

Table I.4: Parameters of the single-particle potentials simulating the c-p interactions for ^{8}B. The binding energy (in keV) of the ground state and partial wave of the state are also given. The depth of the real potential is given in MeV while radii and diffusenesses are given in fm. The depth of the spin orbit part is given in units of MeV fm^2. See Eqs. (2.63) and (2.68) for the shape of these potentials. See Ref. [45]

p-c	E_0	$n_0l_{0j_0}$	V_r	R_r	a_r	V_{so}	R_{so}	a_{so}	R_C
^{8}B	-137	$0p_{3/2}$	44.65	2.391	0.52	19.59	2.391	0.52	2.391

In order to simulate the p-T interaction for a ^{8}B projectile, I use the Koning-Delaroche nucleon-nucleus global parametrization [66] for the ^{12}C and ^{58}Ni targets. For the ^{208}Pb target, I consider the global optical potential of Becchetti and Greenlees [76]. The ^{7}Be core being the mirror nucleus of ^{7}Li, I choose to follow Refs. [70, 83] and simulate the c-T interaction with optical potentials that were fitted to ^{7}Li elastic-scattering data. For the ^{208}Pb target, the global potential of Cook of Ref. [85], which reproduces the elastic scattering of ^{7}Li on a ^{24}Mg target in an energy range 28–88 MeV, is rescaled to ^{208}Pb according to (2.64). For the ^{12}C target, I consider the potential developed in Ref. [86] to fit elastic-scattering data of ^{7}Li off ^{12}C at 350 MeV. Finally for the ^{58}Ni target instead, the potential developed in Ref. [87] to fit elastic-scattering data of ^{4}He off ^{58}Ni at 240 MeV is rescaled according to (2.64). A second set of potentials (in grey) is used to test the independence of the ratio to the c-T interaction. These come from Refs. [88, 89], which are listed in the Perey and Perey compilation [75]. The first reproduces the elastic scattering of ^{6}Li on ^{208}Pb at 30 MeV and is rescaled according to (2.64) whereas the second simulates the scattering of ^{7}Li off ^{12}C at 36 MeV. It should be noted how these potentials have been developed for energies well below the ones considered here. Since these are only used to test the independence of the ratio to the c-T interaction, the energy dependence of these interactions is neglected.

Table I.5: Parameters of the optical potentials simulating the interaction between the fragments of the ^{8}B projectile and the different target nuclei. Potential depths are given in MeV while radii and diffusenesses are given in fm. See Eqs. (2.63) and (2.68) for the shape of these potentials. See Refs. [66, 70, 76, 83, 85, 87, 88, 89]

P	T	V_r	R_r	a_r	W_i	R_i	a_i	W_D	R_D	a_D	R_C
p	^{12}C	40.748	2.58	0.676	4.873	2.58	0.676	19.542	2.99	0.512	3.52
	^{58}Ni	37.231	4.642	0.669	6.516	4.642	0.669	14.736	4.959	0.489	4.875
	^{208}Pb	50.5	6.93	0.75	6.98	7.82	0.66	13.35	7.82	0.66	7.41
^{7}Be	^{12}C	107.6	3.148	0.854	37.9	3.826	0.758	0	–	–	2.747
	^{12}C	245	2.77	0.759	14.7	4.58	0.909	0	–	–	2.98
	^{58}Ni	76.6	5.03	0.8	24.2	5.817	0.8	0	–	–	5.032
	^{208}Pb	114.2	7.62	0.853	9.44	10.3	0.809	0	–	–	7.70
	^{208}Pb	250	7.19	0.5	13.5	10.23	0.91	0	–	–	8.4

3.3.2 Analysis of the ratio for proton halos

^{12}C target

As I did for neutron halos, I will start the analysis of the ratio observable on proton halos on a ^{12}C target. As the target is light, the reaction is nuclear dominated and should therefore better fit with the adiabatic assumption of the REB. The energy of the reaction is 44 MeV/nucleon which corresponds to the conditions of the MSU breakup experiments of Davids *et al.* [69]. At this energy, calculations are best done with the DEA.

On Fig. 3.13 are represented the angular distributions for the breakup of ^{8}B into ^{7}Be and p at the continuum energy $E = 125$ keV (in b/MeV sr), the summed cross section divided by Rutherford, their ratio $\mathcal{R}_{\rm sum}$ expressed in MeV^{-1}, and the corresponding REB form factor $|F_{E,0}|^2$ (thick grey line). The solid curves correspond to the *full* calculation, including both p-^{12}C and ^{7}Be-^{12}C interactions and already shown on Fig. 3.12. In addition, calculations using the alternative ^{7}Be-^{12}C potential V'_{cT} (see grey line in Tab. I.5) are displayed with the dash-dotted lines and calculations which do not include the p-^{12}C interaction (neither the nuclear nor the Coulomb one) and hence consider a spectator valence proton are displayed by the dotted lines ($V_{pT} = 0$).

As already briefly discussed in Fig. 3.12 and already observed for a neutron-halo projectile, the breakup and summed cross sections oscillate in a very similar pattern. By taking their ratio, these oscillations are strongly reduced. Due to the slight shift that exists between the elastic and breakup angular distributions, some remnant oscillations are still visible. Very similarly to what has been observed for neutron-halo nuclei above and in Ref. [68], they arise from the kick given by the target to the valence proton through V_{pT} [37, 64]. This is confirmed by considering a spectator proton ($V_{pT} = 0$, dotted), for which the DEA ratio is in perfect agreement with the REB prediction.

At forward angle (viz. $\theta \lesssim 3°$), the REB form factor overestimates the full DEA calculation. This is reminiscent of the problem observed for the reaction of a neutron halo projectile impinging on a Pb target at low energy (see Fig. 3.10). In both cases, this overestimation is caused by the adiabatic assumption of the REB. Note however that

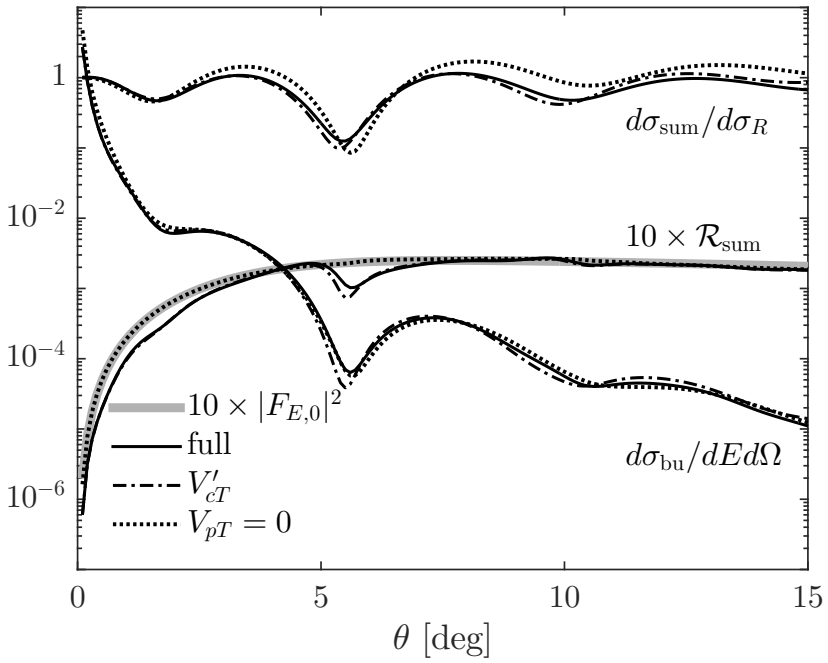

Figure 3.13: Analysis of the ratio method for ^{8}B impinging on ^{12}C at 44 MeV/nucleon. The ratio $\mathcal{R}_{\rm sum}$ and REB form factor $|F_{E,0}|^2$ (thick grey line) are considered at an energy $E = 125$ keV in the ^{7}Be-p continuum and are given in units of MeV^{-1}. Differential breakup angular distributions $d\sigma_{\rm BU}/dEd\Omega$ are given in units of b/MeV sr. DEA calculations using different sets of potentials are displayed (see text for details). Note that the ratio is multiplied here by 10 to improve the readability.

different aspects of this assumption enter into account here. In the case of the low-energy reaction of a neutron halo on a heavy target, the overestimation originates mainly from the low energy of the reaction (compare Fig. 3.10 to Fig. 2(b) from Ref. [68]). Contrary, here, the effect is clearly caused by the p-T interaction. Indeed, as the latter is neglected, the ratio and its REB prediction are in perfect agreement even at very-forward angles. Additional tests—not plotted here for the sake of clarity—have shown that this difference is solely due to the Coulomb part of the p-T interaction. We can explain this result by noting that, in the REB model, the breakup is caused by the sole recoil of the core due to its interaction with the target, the valence nucleon being seen as a spectator. Unlike in one-neutron halo nuclei, the halo nucleon is charged here, which implies that the repulsive Coulomb interaction between this valence proton and the target reduces the tidal force, which is responsible for the dissociation. Due to its coulomb interaction with the target, the proton recoils with the core and the actual breakup and hence the ratio are then smaller than those predicted by the REB at forward angles. The reactions on ^{12}C being nuclear dominated, this reduction happens only at forward angles and is small.

To study the independence of the ratio to the choice of the c-T interaction, an alternative ^{7}Be-^{12}C potential (V'_{cT}, dash-dotted lines, see Tab. I.5). Unfortunately, both potentials provide nearly identical angular distributions. Nevertheless, at large angles (i.e., for $\theta \gtrsim 8°$) they produce noticeable differences in the cross sections that are completely washed out within the ratio, confirming that this observable removes most of the sensitivity to the c-T optical potential.

^{58}Ni target

As the target mass increases, the reaction becomes less nuclear dominated, and hence less adiabatic. But the cross sections are enhanced, which on an experimental point of view, could be interesting as it would lead to a ratio easier to measure. The same calculations are hence done for a ^{58}Ni target. The results are displayed on Fig. 3.14. They are similar to those computed with a ^{12}C target. Here also, the breakup and summed angular distributions decay and oscillate in a very similar fashion. By taking their ratio, this oscillatory pattern roughly cancels out and their ratio is smoother. However, it is in less good agreement with the REB form factor than on ^{12}C: at forward angle ($\theta \lesssim 5°$), the DEA ratio lies below its REB prediction, while at larger angles, it exhibits more significant remnant oscillations. Both problems fully disappear when the calculation is performed without the p-T interaction. As discussed previously, the former issue is due to the dominance in the forward angle region of the Coulomb part of the p-T interaction, which hinders the breakup. The second issue is related to the whole V_{pT}, which produces a shift in the angular distributions, as already discussed in the case of neutron-halo projectiles. Despite its larger cross sections, the Ni target does not seem the optimal choice for a measurement of the ratio for ^{8}B because the ratio it produces cannot be directly related to the REB prediction.

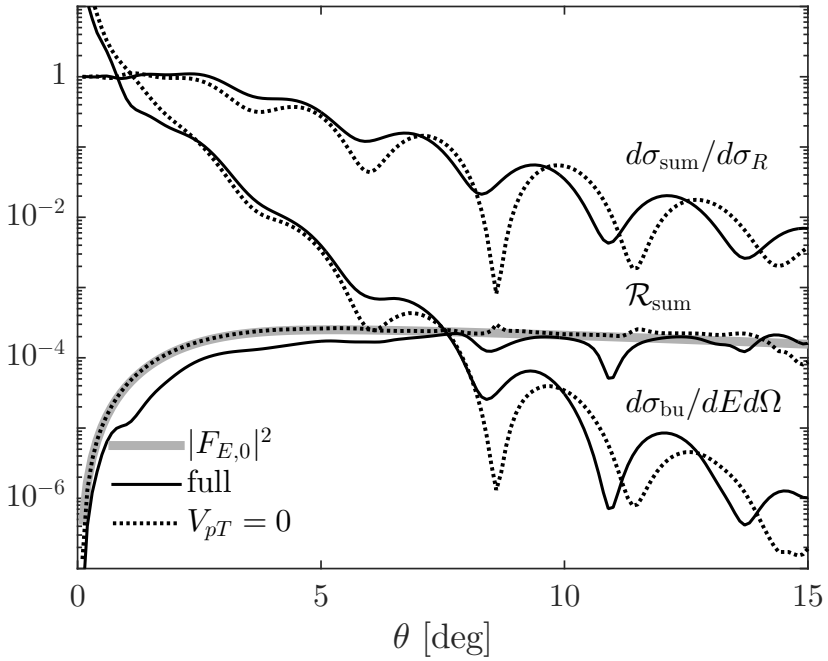

Figure 3.14: Same as Fig. 3.13 but for a ^{58}Ni target.

^{208}Pb target

Finally, the same calculations are performed on a ^{208}Pb target. These are displayed on Fig. 3.15. The results obtained on this heavy target are similar to those computed for the two previous targets. The breakup and summed angular distributions exhibit very similar decays and oscillatory patterns. Accordingly, their ratio removes most of these features, leading to a smooth curve that shows a similar trend as the REB prediction $|F_{E,0}|^2$. Note however that similarly to the case of a neutron halo nucleus in Sec. 3.2.3,

the smoothness of the ratio is mainly due to the absence of oscillations of the breakup and summed cross sections at the angles considered here. This result exhibits little dependence on the choice of the c-T interaction: the ratio obtained with the alternative potential V'_{cT} (dash-dotted) is nearly superimposed on the first one. At forward angles, this simply reflects the fact that both potentials lead to indistinguishable cross sections, which is to be expected for a Coulomb-dominated reaction. However, at angles $\theta \gtrsim 8°$, where the reaction is more sensitive to the choice of nuclear potential and the individual cross sections exhibit noticeable differences, both ratios remain superimposed. This result shows that the independence of the ratio to the optical-potential choice is confirmed in a reaction that has a totally different mechanism.

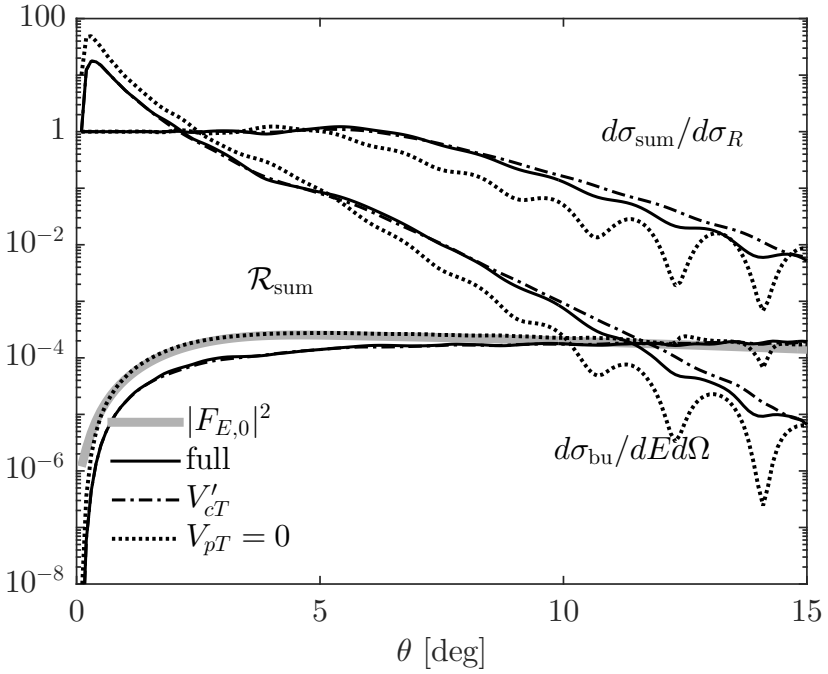

Figure 3.15: Same as Fig. 3.13 but for a ^{208}Pb target.

As for the light and medium-mass targets, the REB prediction $|F_{E,0}|^2$ overestimates the DEA calculations of the ratio $\mathcal{R}_{\rm sum}$ at forward angle. Accordingly it has the same root, viz. the Coulomb p-T interaction, which hinders the breakup and leads to a larger REB prediction compared to the actual ratio. However, the reactions on ^{208}Pb being Coulomb dominated, this reduction is significantly larger than in a nuclear-dominated reaction. Note however that the adiabatic approximation made in the REB is responsible for an additional overestimation of the actual ratio by the REB prediction. That adiabatic effect takes place only at very forward angles. This is confirmed when the p-T interaction is set to zero (V_{pT}=0, dotted). The ratio then superimposes nearly perfectly with the REB form factor except at very-forward angles ($\theta \lesssim 0.5°$), where it is smaller. This behaviour was already observed for neutron halos in Fig. 3.10 at low energy. However, as expected from the very small binding energy of ^{8}B and the higher impinging energy of the projectile, the adiabaticity of the reaction assumed within the REB is better fulfilled here. This overestimation is thus much more forward-focused.

These results show that the overestimation of the ratio observed for ^{8}B with a lead target is mainly due to the Coulomb repulsion that exists between the proton halo and the target.

Summary on all targets

As I have done for a neutron halo projectile, it is interesting to have a look at these results on all targets in the same axes. These are displayed on Fig. 3.16 as a function of Q [see Eq. (2.58)]. For clarity, the ratio and its REB prediction are multiplied by 10 and the differential breakup is divided by 10. The results are very similar to what can be observed on Fig. 3.11 for neutron halos. While for different targets, the differential breakup and elastic cross sections exhibit very different behaviours, both in shape and magnitude, their ratios $\mathcal{R}_{\rm sum}$ are pretty similar to one another, as predicted by the REB. This confirms that the ratio removes most of the dependence on the reaction mechanism. As observed for neutron halos, there still remains a target dependence. The ratio is however fairly close to the REB form factor $|F_{E,0}|^2$. This is especially true for light targets, for which the reaction is dominated by the nuclear interaction. Note however that this leads to a ratio which exhibits some remnant oscillations. For heavier targets, for which the Coulomb interaction is dominant, the individual cross sections and hence their ratio are smoother. As the mass of the target increases however, the overestimation of $\mathcal{R}_{\rm sum}$ by $|F_{E,0}|^2$ increases. As we have seen, this is due to adiabatic approximation inherent to the REB model and has two origins. First, the Coulomb interaction between the core and the target, which dominates the very forward angle region and second, at larger angles, the presence of the p-T Coulomb interaction, which reduces the tidal force responsible for the dissociation. Note however that because of the higher energy of the proton-halo projectile compared to the case of ^{11}Be considered in Sec. 3.2 and its lower binding energy, the adiabatic assumption of the REB is better satisfied than for the reaction of neutron halos at low energy.

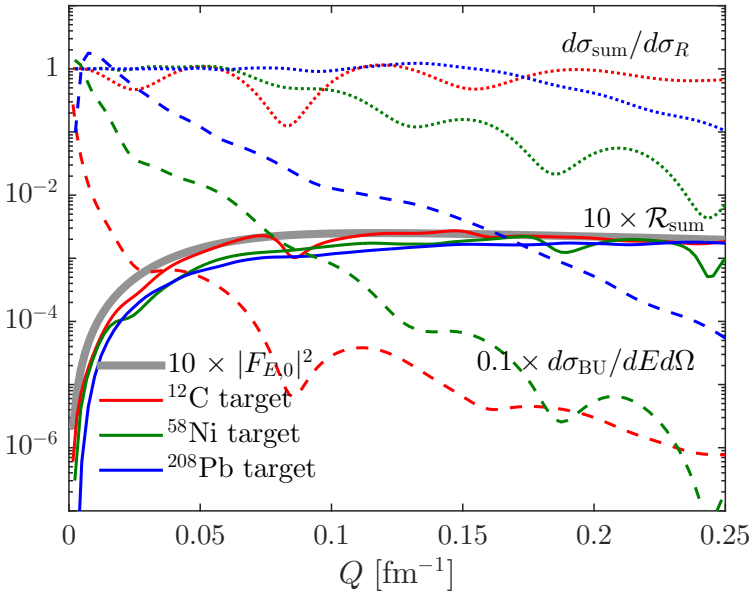

Figure 3.16: Sensitivity of the ratio to the target choice: DEA calculations on ^{12}C, ^{58}Ni, and ^{208}Pb at 44 MeV/nucleon are displayed as a function of Q [see Eq. (2.58)]. The differential breakup angular distributions, the ratio $\mathcal{R}_{\rm sum}$ and the REB form factor $|F_{E,0}|^2$ (thick grey line) are calculated at an energy $E = 125$ keV in the ^{7}Be-p continuum.

3.3.3 Sensitivity to the projectile structure

It is also interesting to analyse the sensitivity of $\mathcal{R}_{\rm sum}$ on the description of the projectile. In this section, I will first study the sensitivity of the ratio to the ^{7}Be-p potential for a $0p_{3/2}$ proton bound to a ^{7}Be core by 137 keV. I will then proceed with the study of the sensitivity to the binding energy and partial wave of the valence proton. As we have seen in previous section, the most favourable case for the application of the ratio is on light targets. I will thus perform this analysis for a ^{12}C target.

Calculations for ^{8}B projectiles described by different ^{7}Be-p potentials all fitted to reproduce a physical ^{8}B nucleus are shown on Fig. 3.17 in a linear scale. The ratio calculated using the simplified version of the ^{7}Be-p potential of Esbensen and Bertsch [84] detailed in Tab. I.4 and already shown in Fig. 3.12 is displayed in solid black. Alongside this calculation, the results for two modified potentials are also displayed. First, two potentials adjusted in the s-wave to reproduce the scattering length either in the spin 1 (dash-dotted blue) or spin 2 (dashed green) channels [90] and second, a potential with its diffuseness modified in all partial waves from $a_r = a_{\rm so} = 0.52$ fm to $a_r = a_{\rm so} = 0.65$ fm (dotted red). These calculations will allow me to study the sensitivity of the ratio to the low-energy ^{7}Be-p continuum and to the potential geometry, respectively. The corresponding DEA ratios (thin lines) are plotted alongside the REB form factors (thick lines).

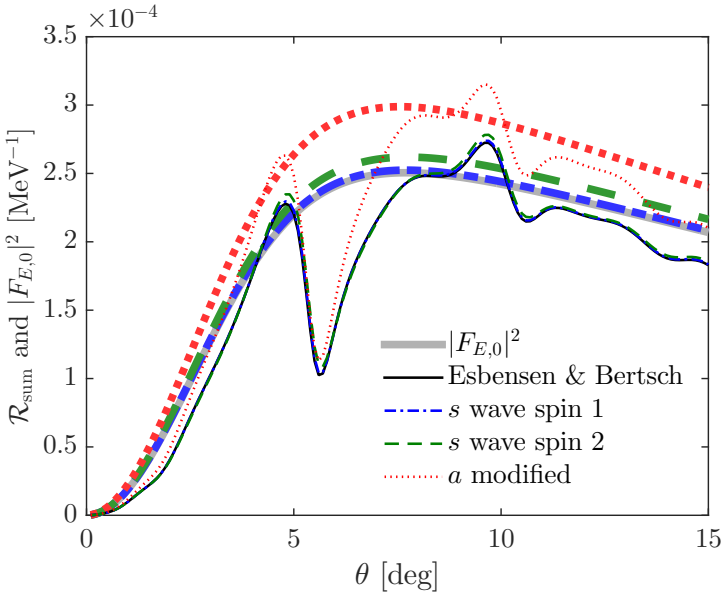

Figure 3.17: Sensitivity of $\mathcal{R}_{\rm sum}$ to the projectile description for a ^{8}B impinging on ^{12}C at 44 MeV/nucleon. The breakup is considered at an energy of $E = 125$ keV in the ^{7}Be-p continuum. Besides the Esbensen and Bertsch ^{8}B potential (black) [84], potentials modified in the s wave continuum that reproduce the scattering length of the spin-1 (blue) and spin-2 (green) channels, as well as a potential with a modified diffuseness (red) are also considered. Their corresponding form factor $|F_{E,0}|^2$ is given as thick lines of the same type and color.

Before analysing the sensitivity of the form factor to the ^{7}Be-p potential, let me first remind some of the observations made in previous Sec. 3.3.2, i.e. first, remnant oscillations

are clearly visible and second, $|F_{E,0}|^2$ overestimates the DEA ratio at very-forward angles. The reasons for this behaviour have been discussed extensively in Sec. 3.3.2. It should be noted that all form factors are very similar in magnitude, except for the one that has a larger diffuseness (red). They are also akin in shape, as if they are a scaled version of the same curve. The influence of the continuum is thus smaller than the one caused by the change in geometry. Further tests (not displayed here for clarity) have confirmed this conclusion. Indeed, by setting the c-p potential to zero in all partial waves but the $0p_{3/2}$ ones, no strong changes have occurred neither in $\mathcal{R}_{\rm sum}$ nor $|F_{E,0}|^2$.

In the light of the results discussed from Fig. 3.5 and the similar shape these curves exhibit, it is interesting to scale them by the square of the ground-state ANC. It can then be shown in a very similar way as in the right panel of Fig. 3.5, that all curves fall quite close to one another. At a given energy, the ratio and REB form factor are thus sensitive mostly to differences in the ANC. This confirms the observations of Ref. [68] and of previous sections, which showed $\mathcal{R}_{\rm sum}$ to be a peripheral observable at forward angles, meaning that it probes the tail of the wave function, viz. its ANC. In order to probe internal parts of the halo ground-state wave function, one would need to measure the ratio at sufficiently large angles.

In order to study the sensitivity of the ratio to the binding energy and to the partial wave of the halo, let me proceed as for neutron halos. In Fig. 3.18, similar to Fig. 3.3, the ratio is plotted for ^{8}B-like projectiles in which the valence proton is bound to the ^{7}Be core within different orbitals (left, in linear scale) and with different binding energies (right, in logarithmic scale). The REB form factors (thick lines) are also displayed alongside their corresponding DEA ratios (thin lines). In addition to the physical ^{8}B (a $0p_{3/2}$ proton bound by 137 keV to the ^{7}Be core; solid black and grey lines), I consider $1s_{1/2}$ (dashed lines) and $0d_{5/2}$ (dash-dotted lines) valence protons bound by 137 keV on the left panel of Fig. 3.18. Additionally, the ratio for a physical ^{8}B is compared to a ^{8}B bound in the $0p_{3/2}$ states with binding energies of 1 MeV (green lines) and 4 MeV (red lines) on the right panel of Fig. 3.18. Since for a given binding energy the ANC dominates the magnitude of the ratio (see Fig. 3.17), I divide the ratios and form factors by the squared ANC of their respective ground-state wave function, viz. by 5.81 fm^{-1}, 0.504 fm^{-1}, and 0.010 fm^{-1}, for the $1s_{1/2}$, $0p_{3/2}$, and $0d_{5/2}$ states, respectively.

As seen before for neutron-halo nuclei and in Ref. [68], the ratio and its REB prediction are strongly dependent on the binding energy of the halo and the orbital angular momentum in which it is bound. This dependence is visible both in magnitude and in shape. It should be noted that the square of the ANC for these different partial waves decreases by one order of magnitude each time l_0 is increased by one unit. Therefore, although the ratios are seemingly of similar magnitude on the left panel of Fig. 3.18, they in fact exhibit large changes in their magnitude for variations of the orbital momentum. Because of these large sensitivity to the ANC, it could thus be inferred by merely confronting the order of magnitude of the data to the REB form factor. Except for the remnant oscillations and the dip around 5 and 6°, the REB prediction for a projectile bound in the s or p wave follows fairly well the trend of the DEA ratio. For a projectile bound in the d wave however, the agreement is not good. This confirms the results already observed for neutron halos above and in Ref. [68]: the agreement between the REB form factor and the actual ratio is better for low orbital angular momentum l_0. While the binding energy does not influence the shape of the ratio as significantly as the orbital momentum, it has a similar influence on its magnitude, as seen on the right panel of Fig. 3.18. The agreement of the ratio and its REB prediction deteriorates as the binding energy increases,

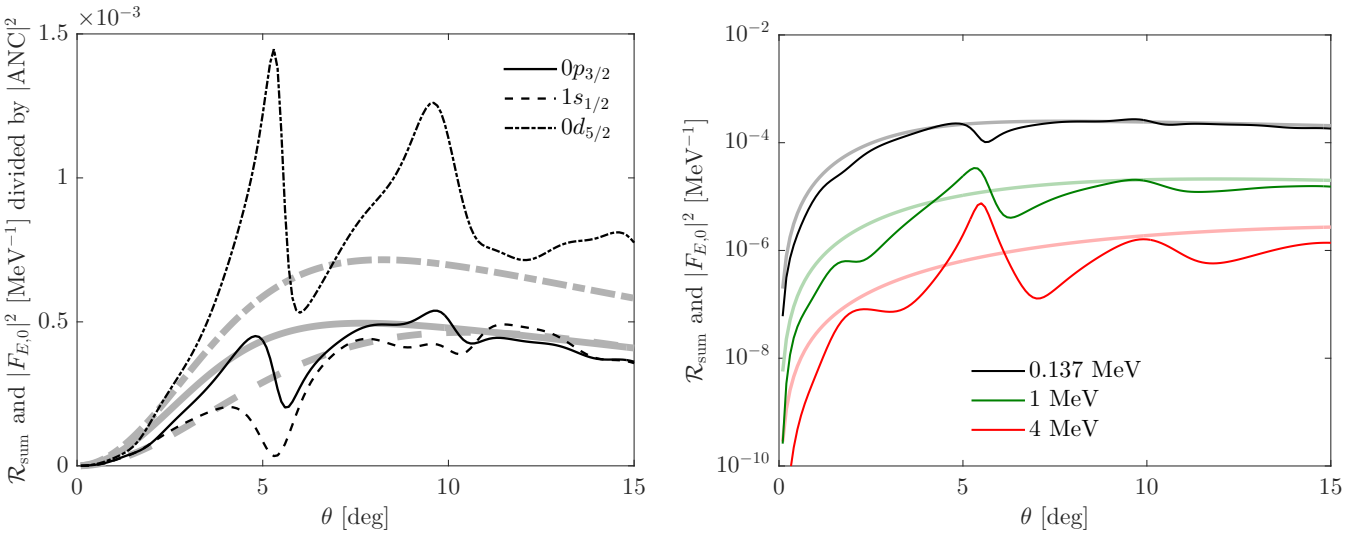

Figure 3.18: Sensitivity of $\mathcal{R}_{\rm sum}$ to the projectile structure of a one-proton halo nucleus for the reaction of a ^{8}B on a ^{12}C target at an energy of 44 MeV/nucleon. Besides the realistic ^{8}B (valence p bound by 137 keV in the $0p_{3/2}$ orbit), projectiles with (left) different orbitals ($1s_{1/2}$ and $0d_{5/2}$), and (right) different ground-state energies ($|E_{0p3/2}| = 1$ and 4 MeV) are also considered. Their corresponding form factor $|F_{E,0}|^2$ is given as thick lines of the same type and color. Note that on the left panel, the curves are divided by the square of the ANC of the ground state wave function u_{nlj} [see Eq. (2.12)].

indicating that the ratio method works at best for loosely bound systems. This can be easily understood as an increase of the binding energy causes the adiabatic assumption to lapse. This confirms again the results observed in Ref. [68].

3.3.4 Sensitivity to the choice of continuum energy

Up to now, all calculations of the ratio have been performed considering a single continuum energy $E = 125$ keV between the core and the halo fragment in the breakup channel. But no measurement of the ratio can be performed at a single continuum energy. Instead, such data taking requires a continuum-energy range or *bin* (such bins are also used in the CDCC expansion, see Sec. 2.2). As this bin is chosen broader, the statistics is improved. Let us study how influent is the choice of this energy and the width of the bin on the ratio method. Also, the influence of the presence of a resonance in the continuum will be considered.

I consider the following bin ratio

$$\mathcal{R}_{\rm sum}(\text{bin}, \boldsymbol{Q}) = \int_{E_{\rm min}}^{E_{\rm max}} \mathcal{R}_{\rm sum}(E, \boldsymbol{Q})\, dE \tag{3.5}$$

$$= \frac{\int_{E_{\rm min}}^{E_{\rm max}} (d\sigma/dEd\Omega)_{\rm bu}\, dE}{(d\sigma/d\Omega)_{\rm sum}}, \tag{3.6}$$

where $E_{\rm min}$ and $E_{\rm max}$ are respectively the lower and higher bounds of the bin. This ratio is associated to the bin-integrated REB form factor

$$|F_{\text{bin},0}(\boldsymbol{Q})|^2 = \int_{E_{\rm min}}^{E_{\rm max}} |F_{E,0}(\boldsymbol{Q})|^2\, dE. \tag{3.7}$$

The energy distribution for the breakup of ^{8}B described by the potential of Tab. I.4 on a ^{12}C target at 44 MeV/nucleon is presented on left panel of Fig. 3.19. The different contributions from the s, p, d, and f partial waves in the continuum are shown separately. The shape of this cross section is typical of the nuclear-dominated breakup reaction of halo nuclei [45, 36]. A peak is clearly visible around 2 MeV. It arises from a $p_{1/2}$ resonance at 2.3 MeV above the one-proton threshold with a width of 1.6 MeV (see [PRC 70, 05460-6] where it was observed for the first time). This unphysical state originates from the simplified version of the ^{7}Be-p potential of Esbensen and Bertsch [84] presented in Tab. I.4 and will allow me to study how the presence of a resonance influences the ratio.

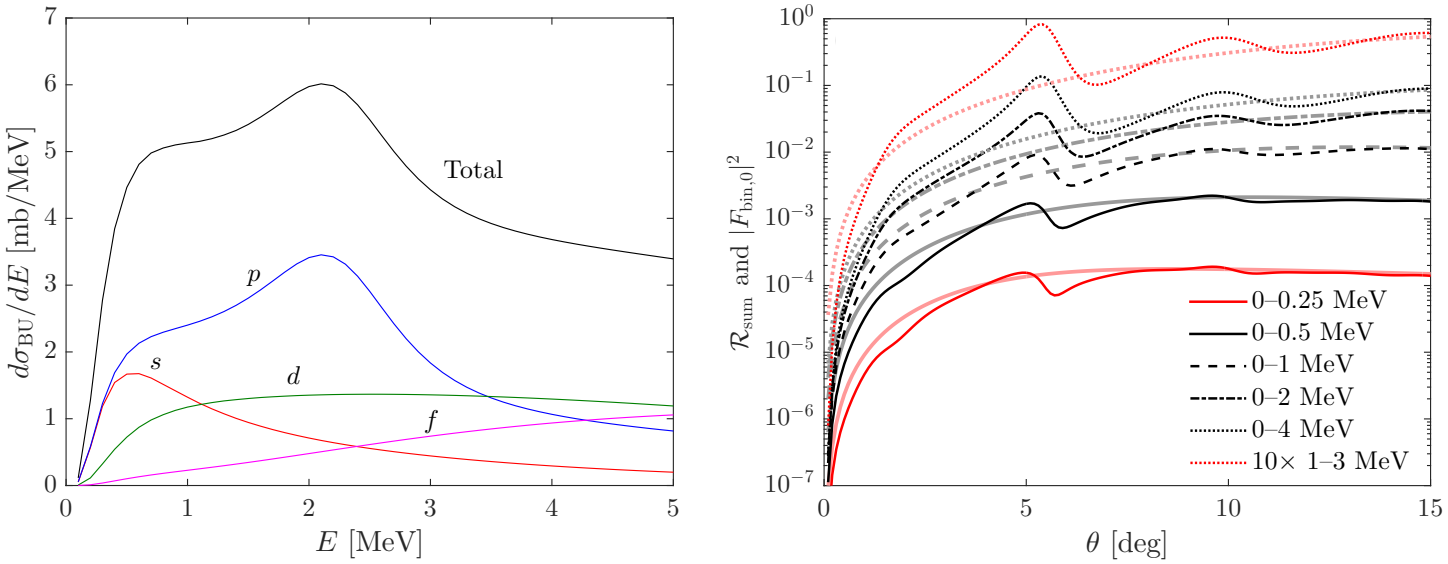

Figure 3.19: Choice of the continuum energy bin for the experimental exploitation of the ratio method. (Left) The breakup cross section plotted as a function of the continuum energy E. (Right) $\mathcal{R}_{\rm sum}$ computed within the DEA (thin lines) and its REB estimate (thick lines) for different energy bins in the ^{7}Be-p continuum.

The ^{7}Be-p continuum will be divided into six different bins of increased width, whose characteristics are summarised in Tab. I.6. The first is chosen such that it is centred on the energy $E = 125$ keV used in the previous sections. The next two are chosen in the low-energy part of the non-resonant continuum. They have an increasing width of 0.5 MeV and 1 MeV, respectively. The fourth and fifth bins are chosen even broader such as to encompass partly or fully the resonance. Finally, in order to clearly see the influence of the resonance, we consider a sixth bin centred on it. The corresponding results are displayed on the right panel of Fig. 3.19.

Table I.6: Interval of energies of the continuum bins considered for the calculation of the ratio. Energies are given in MeV.

	Bin 1	Bin 2	Bin 3	Bin 4	Bin 5	Bin 6
$[E_{\rm min}, E_{\rm max}]$	[0, 0.250]	[0, 0.500]	[0, 1]	[0, 2]	[0, 4]	[1, 3]

The ratios calculated with the first two bins (0–0.25 MeV and 0–0.5 MeV) provide ratios very similar to that of the sole $E = 125$ keV. However, the larger the bin, the

larger the breakup cross section. The magnitude of the ratio for the second bind is indeed up to ten times as large as the one calculated with a single continuum energy with no noticeable worsening of the disagreement between the actual ratio and its REB prediction. This would be useful in an experimental application of the method. By increasing the width of the bin however, disagreements between the DEA ratio and their REB prediction also increase as it can be seen for the third and fourth bins (0–1 MeV and 0–2 MeV). The much broader bin (0–4 MeV) confirms that trend. For the broader bins, the form factor is in less good agreement with the DEA ratio. This is expected because higher excitation energies are less compatible with the adiabatic approximation of the REB. However, they provide a larger ratio, which could significantly improve the statistics uncertainty in actual data taking. For practical purposes, a balance will thus have to be sought between the accuracy of the method and the practicality of its experimental implementation.

The calculation performed with the sixth bin centred on the resonance (1–3 MeV) does not exhibit any peculiar behaviour when compared to the fourth and fifth bins. This suggests that the resonance and hence the description of the continuum as a whole (see the results on the non-resonant continuum of Sec. 3.3.3) does not really affect the ratio method.

3.3.5 Extension to other proton-rich nuclei: ^{17}F, ^{25}Al and ^{27}P

After the detailed examination of the ^{8}B nucleus, I explore how the ratio behaves when applied on other proton-rich nuclei with a clear single-particle structure. The cases studied are ^{17}F, ^{25}Al and ^{27}P. These proton-rich *s-d* nuclei are all seen as composed of a core of spin nil (^{16}O, ^{24}Mg, and ^{26}Si, respectively) and a loosely bound valence proton. The results obtained so far show that the ratio works best at high energy and for light targets. The reaction of these nuclei is thus first studied on a ^{12}C target at an energy of 60 MeV/nucleon, which can be produced at various RIB facilities. The effect of choosing a Ni target on the method is then analysed. As we have seen in Sec. 3.3.2, this target has the effect of enhancing the cross section significantly. The tests on this target will thus serve as a check whether choosing an easier experimental feasibility over a better agreement (on light targets) is a worth trade-off. All the following calculations on these three nuclei have been performed with the DEA and analysed in collaboration with X. Y. Yun and D. Y. Pang.

3.3.5.1 Numerical details

Before going through the results of these calculations, I will summarise the parameters of the optical potentials that have been chosen to simulate the interaction between the valence proton and the core V_{cp} and between the constituents of the projectile and the target V_{pT} and V_{cT}.

The loosely bound nucleus ^{17}F exhibits a $\frac{5}{2}^+$ ground state of binding energy 601 keV below the one-proton threshold. In addition it also has a $\frac{1}{2}^+$ bound excited state at 106 keV below the one-proton separation threshold, which is usually depicted as exhibiting a one-proton halo structure. In an extreme shell-model viewpoint, they can be seen as a $0d_{5/2}$ and $1s_{1/2}$ proton bound to an ^{16}O core, respectively. This vision has recently been confirmed by a coupled-cluster calculation by Hagen *et al.* in [91]. In addition to these two bound states, ^{17}F exhibits a $\frac{3}{2}^+$ resonance at 4.4 MeV above the one-proton threshold. It is seen as the $d_{3/2}$ spin-orbit partner of the ground state. Sparenberg, Baye and Imanishi have developed an ^{16}O-nucleon potential that describes the low-energy spectra of the

mirror nuclei ^{17}F and ^{17}O [92]. It includes a central plus a spin-orbit terms of Woods-Saxon form [see Sec. 2.5], and reproduces the three aforementioned states. Its parameters are given in the first line corresponding to ^{17}F in Tab. I.7.

Being closer to the proton dripline, the other nuclei have a less-known structure. The one-proton separation energy of ^{25}Al is 2.272 MeV and its ground state has spin and parity $\frac{5}{2}^+$. It is therefore seen as a proton bound to a ^{24}Mg core in the $0d_{5/2}$ orbit. Interestingly, ^{27}P exhibits a $\frac{1}{2}^+$ ground state seen as a $1s_{1/2}$ proton bound by 870 keV[5] to a ^{26}Si core. To describe these two nuclei, I consider simple Woods-Saxon potentials without spin-orbit term. The potential V_{cp} is chosen with the usual diffuseness $a = 0.65$ fm and reduced radius $r_0 = 1.25$ fm. For each nucleus, its depth is adjusted to reproduce the experimental one-proton separation energy in the physical partial wave. The same potential is considered in all partial waves. Their parameters are given in the first line corresponding to ^{25}Al and ^{27}P, respectively, in Tab. I.7. It should be noted that following the results of Sec. 3.3.3, thanks to its loose binding energy of a mere 870 keV and the orbital angular momentum $l_0 = 0$ of its valence proton, ^{27}P could be an interesting test case for the ratio method close to the proton dripline (see also Sec. 1.1).

In order to study the influence of that choice of description upon the ratio method applied to these three nuclei, I consider a second set of c-p potential, V'_{cp}. I use the Woods-Saxon geometry of the ^{7}Be-p potential of Esbensen and Bertsch [84], viz. with $a = 0.52$ fm and $r_0 = 1.25$ fm. In the case of ^{17}F, the central depth is then adjusted to bind the valence proton at the right energy in the $0d_{5/2}$ orbit. For simplicity, I ignore the spin-orbit splitting. The parameters of this second potential are listed in the second line corresponding to ^{17}F in Tab. I.7, in grey colour. In that potential, the $1s_{1/2}$ is bound by 760 keV, hence below the ground state, and the $0d_{3/2}$ state is degenerated with the $0d_{5/2}$ state. For ^{25}Al and ^{27}P, the depth of the potential is adjusted to reproduce the correct binding energy of the nucleus. The parameters are given in the second lines corresponding to ^{25}Al and ^{27}P, respectively, in Tab. I.7, and given in grey colour.

Table I.7: Parameters of the single-particle potentials simulating the c-p interactions for the ^{17}F, ^{25}Al, and ^{27}P proton halo nuclei or proton halo nuclei candidates. The binding energy (in MeV) of the ground state and partial wave of the state [94, 95] are also given. Depths of the real potential are given in MeV while reduced radii and diffusenesses are given in fm. The depth of the spin orbit part is given in units of MeV fm^2. Two sets of potentials V_{cp} and V'_{cp} are given, the latter being in grey colour.

p-c	E_0 [MeV]	$n_0 l_{0j_0}$	V_r	r_r	a_r	V_{so}	r_{so}	a_{so}	R_C
^{17}F	-0.600	$0d_{5/2}$	56.700	1.20	0.642	25.14	1.20	0.642	1.2
			57.090	1.25	0.52	0	–	–	1.25
^{25}Al	-2.272	$0d_{5/2}$	50.342	1.25	0.65	0	–	–	1.25
			49.346	1.25	0.52	0	–	–	1.25
^{27}P	-0.870	$1s_{1/2}$	47.377	1.25	0.65	0	–	–	1.25
			48.136	1.25	0.52	0	–	–	1.25

For the optical potentials that simulate the P-T interactions, I use the systematic

[5] Note that recent results give an even lower value of 807 keV [93].

nucleus-nucleus potential of Xu and Pang [96] for V_{cT} and the Chappel-Hill global nucleon potential for V_{pT} [97]. The former is obtained by folding the effective JLMB nucleon-nucleon interaction [98] with the nucleon density distributions of the projectile and target obtained with Hartree-Fock calculations using the SkX interaction [99]. For all three projectiles, the real and imaginary parts of the nucleus-nucleus potential are renormalized with the factors $N_r = 0.68$ and $N_i = 1.22$, respectively. To study the effect of different c-T interactions on the ratio method, calculations are also made with another V'_{cT}, which is arbitrarily chosen to have $N_r = 0.58$ and $N_i = 1.02$. These potentials have been provided numerically by D. Y. Pang.

^{12}C target

The breakup and the summed cross sections (divided by Rutherford) as well as their ratio $\mathcal{R}_{\rm sum}$ and the REB form factor $|F_{E,0}|^2$ (thick grey line) are displayed in Fig. 3.20. Note that following the results of Sec. 3.3.4, it is interesting to consider the breakup to an energy contained in an energy bin. This enhances the cross section but keeps the agreement qualitatively the same as long as the bin is not too wide. Because the 0–1 MeV bin gave the best results for ^{8}B, I will also choose this bin in the present cases. The breakup is thus expressed in b/sr since it is integrated on a bin of energy. The first potential V_{cp} is used in this study, the influence of that choice on these calculations is analysed later. The full calculations including both the c-T and p-T interactions (solid lines) are displayed along with those that do not include the latter ($V_{pT} = 0$, dashed red lines), and those using the second c-T potential (V'_{cT}, dash-dotted lines).

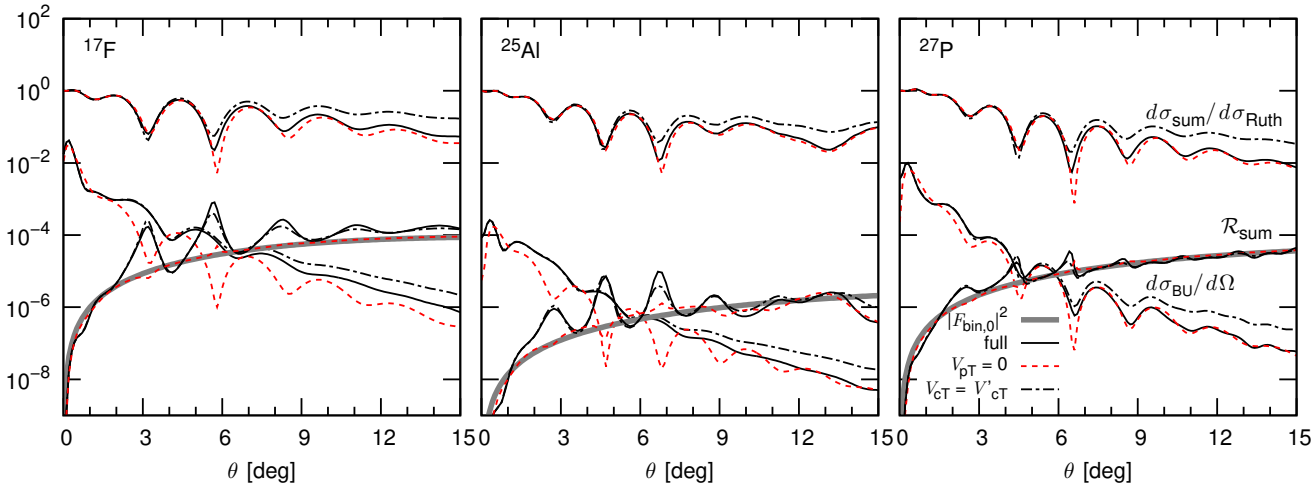

Figure 3.20: Analysis of the ratio method for ^{17}F (left), ^{25}Al (middle) and ^{27}P (right) impinging on a ^{12}C target at 60 MeV/nucleon. The ratio $\mathcal{R}_{\rm sum}$ and REB form factor $|F_{\rm bin,0}|^2$ (thick grey line) are considered in the bin energy E = 0–1 MeV in the c-p continuum and have no units. Breakup angular distributions $d\sigma_{\rm BU}/d\Omega$ over that bin are given in units of b/sr. The summed cross section is given as a ratio to Rutherford's. Calculations using different sets of potentials are displayed (see text for details).

Contrary to the ^{11}Be and ^{8}B cases studied above, it should be noted that the breakup and summed cross sections are out of phase for the ^{17}F and ^{25}Al projectiles. Consequently, their ratios exhibit large remnant oscillations. These strong oscillations indicate that for

these two nuclei, the ratio method does not work and does not fully remove the dependence on the reaction process. This means that the REB does not work for these nuclei. For the ^{27}P projectile on the contrary, both cross sections are in phase and exhibit a very similar oscillatory behaviour. Consequently, like in the case of ^{11}Be and ^{8}B, their ratio removes most of their features. Additionally, in this case $\mathcal{R}_{\rm sum}$ follows quite fairly its REB prediction. These results are easily explained in the light of the conclusions drawn from Fig. 3.18, i.e. that the ratio works better for projectiles loosely bound in a low orbital angular momentum l_0. Because of its large binding energy and its proton being bound in a d wave, ^{25}Al is the less favourable case for the application of the ratio method. This conclusion is further confirmed when the p-T interaction is neglected (red dashed in Fig. 3.20). Indeed, while the ratio is then in a near perfect agreement with its REB prediction for ^{17}F and ^{27}P projectiles, the ratio for ^{25}Al still exhibits significant oscillations, which further shows that the REB does not work for ^{25}Al.

Interestingly however, the ratios of these three nuclei exhibit very little dependence on the choice of the c-T interaction. When the reaction calculations are performed with the alternate potential V'_{cT}, significant differences are seen in the individual cross sections. However the corresponding changes in the ratios are much smaller. This is especially true for the ^{27}P. For this projectile, although the changes in the individual cross sections are the largest, the differences between both ratios are barely visible.

These results confirm both the interest and limitation of the ratio method applied to proton-rich nuclei. A direct comparison of the actual ratio to the REB form factor will be accurate only for loosely bound systems with the last proton in a low-l orbital, i.e. the ideal cases in which a proton halo may develop. However, in all cases $\mathcal{R}_{\rm sum}$ still follows at least coarsely $|F_{\rm bin,0}|^2$ and is independent of V_{cT}. Since the ratio exhibits such a large sensitivity to the binding energy E_0 and l_0 (see Fig. 3.18), the method could still be used to get reliable information about the single-particle structure of nuclei close to the proton dripline even if the valence proton is significantly bound in a d wave. However this information will not reach the fine details that can be extracted for s and p wave loosely-bound halo nuclei such as ^{11}Be. For ^{27}P, the ratio could probably be compared directly to the REB form factor. For the d-wave projectiles ^{17}F and ^{25}Al, this direct comparison is not possible, due to the significant effects of the reaction dynamics. Note however that some information might be gathered by focussing on the order of magnitude and general shape of the ratio in those cases.

It is interesting to have a look at the ratios in a linear scale, in order to better focus on the details of these calculations. These are displayed on Fig. 3.21. In addition to the calculations performed with the first V_{cp} potentials (solid black and grey lines), the ratios obtained with V'_{cp} (green dashed lines) are also presented to study the influence on the ratio method of the c-p potential used to describe ^{17}F, ^{25}Al and ^{27}P.

As already seen in Fig. 3.20, the ratio method applied to ^{17}F and ^{25}Al merely reproduces the order of magnitude of the form factor. Hence, for these d-bound nuclei, at best an estimate of l_0 and/or E_0 could be inferred from the comparison of an experimental ratio to its REB prediction. On the contrary, for ^{27}P there is a fair agreement between $\mathcal{R}_{\rm sum}$ and the form factor $|F_{\rm bin,0}|^2$. Although it does not exhibit the perfectly smooth angular dependence of the latter, the ratio merely oscillates around the REB. This suggests that in this case the direct comparison of the ratio to its REB prediction is possible. In a practical application of the ratio, it is not clear that the remnant oscillations observed in Fig. 3.21 (right) will be visible. Depending on the experimental angular resolution of the detector setup, these rapid variations of $\mathcal{R}_{\rm sum}$ might be smoothed/washed away.

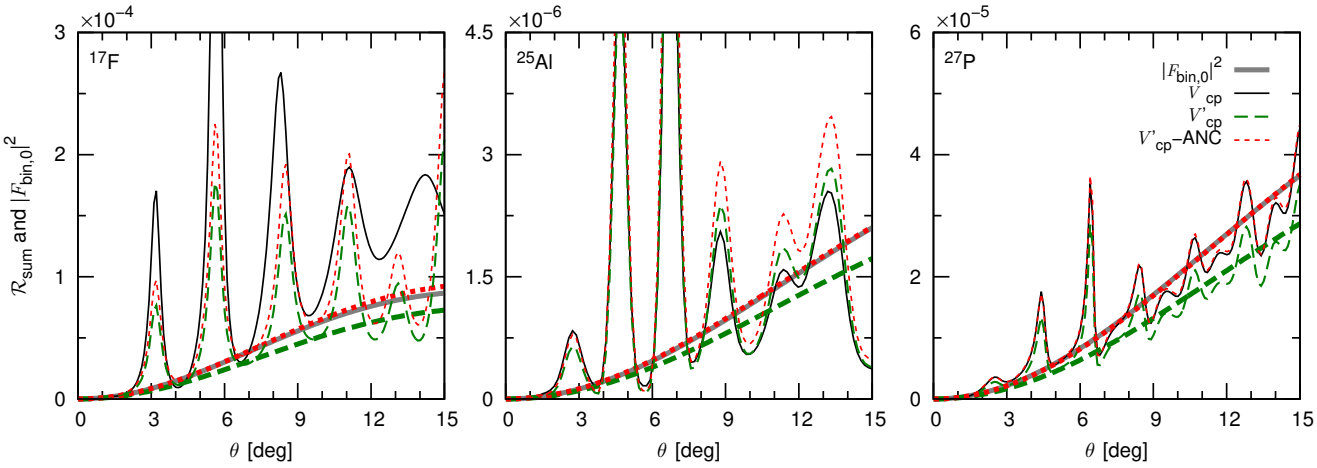

Figure 3.21: Ratios for a ^{17}F (left), a ^{25}Al (middle) and a ^{27}P (right) projectile impinging on a ^{12}C target at 60 MeV/nucleon in linear scale. The ratio $\mathcal{R}_{\rm sum}$ and REB form factor $|F_{\rm bin,0}|^2$ (thick grey line) are considered in the bin energy E = 0–1 MeV in the c-p continuum and have no units. Calculations using different sets of potentials are displayed (see text for details).

In order to test the aforementioned idea of measuring the ratio with a coarse angular resolution, let me divert briefly from the analysis of Fig. 3.21 and display in Fig. 3.22 the calculations on ^{27}P shown in the right panel of Fig. 3.21 folded with an arbitrary angular resolution of 2° (red), simulating an experimental resolution. The REB prediction $|F_{E,0}|^2$ is now in very good agreement with the ratio $\mathcal{R}_{\rm sum}$. This confirms that in these conditions—light target, high-energy beam, broad energy bin in the continuum and coarse angular resolution—the ratio could be directly compared to its REB prediction in order to extract fine details of its structure experimentally.

Let me now go back to Fig. 3.21. The c-p potential used to describe the projectile has a visible influence on the ratio and its REB prediction. As we have seen in Fig. 3.17, most of the differences in magnitude between both sets of calculations might be due to the corresponding change in ANC of the bound state. To test this idea, the red dotted lines of Fig. 3.21 show the results obtained with the alternate V'_{cp} normalised to the ANC generated by the original V_{cp} (i.e. they are multiplied by $|{\rm ANC}_{V_{cp}}|^2/|{\rm ANC}_{V'_{cp}}|^2$). For ^{27}P, the scaled results are superimposed on the original V_{cp} calculations, confirming that the reaction process is peripheral and probes only the tail of the ground-state wave function. For this nucleus, very similarly to what has been observed from Fig. 3.18 for ^{8}B, the ANC could probably be inferred by confronting the data to the REB form factor. On the contrary, for ^{17}F and ^{25}Al, this test confirms that the ratio method does not work. Indeed, for these two nuclei, although the scaled REB form factors are nearly on top of the V_{cp} ones, this is not the case for the DEA ratios. The reaction process for these projectiles is consequently less peripheral and hence more sensitive to the internal part of the wave function. This is not unexpected for systems bound in a d wave. These dynamical effects breach the adiabatic approximation of the REB and hence spoil the original idea of the ratio method [38]. As already concluded from Fig. 3.20, the ratio method works only at the qualitative level for these nuclei. Fine details on their structure, like the ANC of their ground state cannot be inferred with this method.

As we have seen, the ^{27}P nucleus seems to be the best choice to apply the ratio method. In order to complete this study on this particular nucleus, I analyse in Fig. 3.23

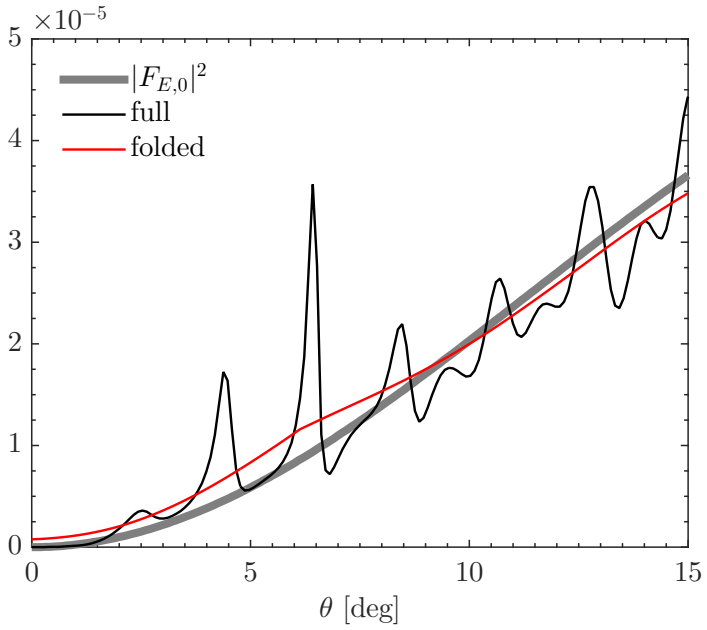

Figure 3.22: The ratio $\mathcal{R}_{\rm sum}$ (black) and REB form factor $|F_{E,0}|^2$ (thick grey) visible on the right panel of Fig. 3.21. Smoothing of the ratio by the folding with an arbitrary experimental angular resolution of 2° is also displayed (red).

the best choice of continuum bin upon which to measure the ratio. The bins $E = 0 - 0.5$ MeV (dashed), $E = 0 - 1$ MeV (solid), $E = 0 - 2$ MeV (dash-dotted) and $E = 0 - 4$ MeV (long dashed) are displayed. As previously observed for ^{8}B (see right panel of Fig. 3.19) and as expected from the adiabatic assumption inherent to the REB model, the agreement between the ratio and its REB prediction deteriorates when the continuum energy increases. Since the breakup cross section increases significantly with the size of the energy bin, it is interesting on an experimental point of view to consider it as broad as possible. As for ^{8}B, the range $E = 0$–1 MeV seems optimal: the ratio is quite close to the form factor and provides a breakup cross section roughly two orders of magnitude larger than the $E = 0$–0.5 MeV bin.

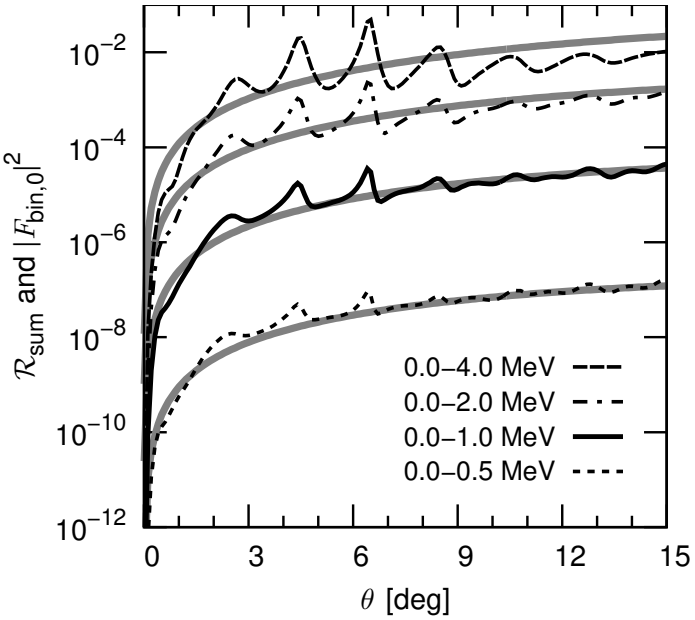

Figure 3.23: Ratios for a ^{27}P projectile impinging on a ^{12}C target at 60 MeV/nucleon. The ratio $\mathcal{R}_{\rm sum}$ and REB form factor $|F_{\rm bin,0}|^2$ (thick grey line) are considered in different bin energies in the *c-p* continuum and have no units. The bins $E = 0 - 0.5$ MeV (dashed), $E = 0 - 1$ MeV (solid), $E = 0 - 2$ MeV (dash-dotted) and $E = 0 - 4$ MeV (long dashed) are displayed.

^{58}Ni target

To see if another target choice could increase the magnitude of the breakup cross sections and hence ease the experimental use of the ratio method, the same calculations are performed on a ^{58}Ni target at the same 60 MeV/nucleon beam energy. The corresponding summed and breakup cross sections are displayed in Fig. 3.24 as a function of the scattering angle θ as well as the ratio and its REB prediction (thick grey line); the calculations correspond to the first V_{cp} listed in Tab. I.7. Note that due to instabilities beyond 8°, the results are shown only up to this angle.

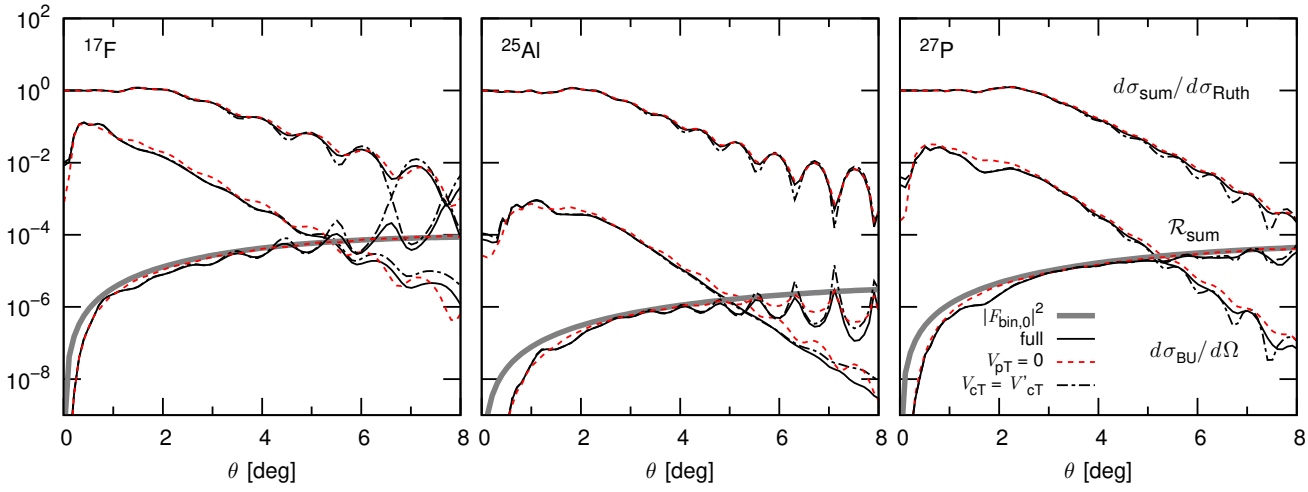

Figure 3.24: Same as Fig. 3.20 but on a ^{58}Ni target at 60 MeV/nucleon.

As expected, the larger Coulomb *P-T* interaction leads to a larger breakup cross

section. It also significantly affects the general shape of the angular distributions, both the summed and breakup ones. We see the clear appearance of a Coulomb rainbow and the shift of the oscillatory pattern to larger angles. However, as already observed on the ^{12}C target, for ^{17}F and ^{25}Al the summed and breakup cross sections do not exhibit the same behaviour. This shows that for these nuclei, the ratio method can be qualitative at best. For ^{27}P however, both cross section behave similarly, leading to a rather smooth ratio. Unfortunately, as explained in Sec. 3.3.2, the larger Coulomb interaction leads the REB form factor to overestimate the ratio. It is therefore not clear that the gain in the breakup channel will improve the accuracy of the ratio method.

When the p-T interaction is removed (V_{pT}=0, dashed red lines), the conclusions are very similar to those made for the ^{12}C target. For ^{27}P and ^{17}F the remnant oscillations in the ratio disappear and the ratio and its REB prediction are superimposed for $\theta > 2°$. For ^{25}Al, on the contrary, the ratio still exhibits clear remnant oscillations, showing again that the ratio method works best for loosely bound systems with the last proton in an s or p orbital.

Results in Fig. 3.24 also show that the potential V_{cT} used to simulate the c-T interaction has little to no influence on the cross sections, especially at small angles. This is to be expected from this more Coulomb-dominated process. However, at larger angles, at which some differences can be observed in the individual cross sections, the ratios are nearly unaffected by the choice of that interaction. Again, this is particularly true for ^{27}P.

To study the influence of the choice of c-p potential on the ratio, we perform the same series of calculations as in Fig. 3.21 for this ^{58}Ni target; the results are displayed in Fig. 3.25. Before analysing the difference between the first V_{cp} (black and grey solid lines) and the second V'_{cp} (red dotted lines), let us first note that the agreement between the ratio and its REB prediction is not as good as on a light target. Although it leads to a larger—and hence easier to measure—breakup cross section, this choice of target is not fit for a direct comparison of the ratio to the REB form factor, even for ^{27}P. On a nickel target, the ratio could be qualitative at best.

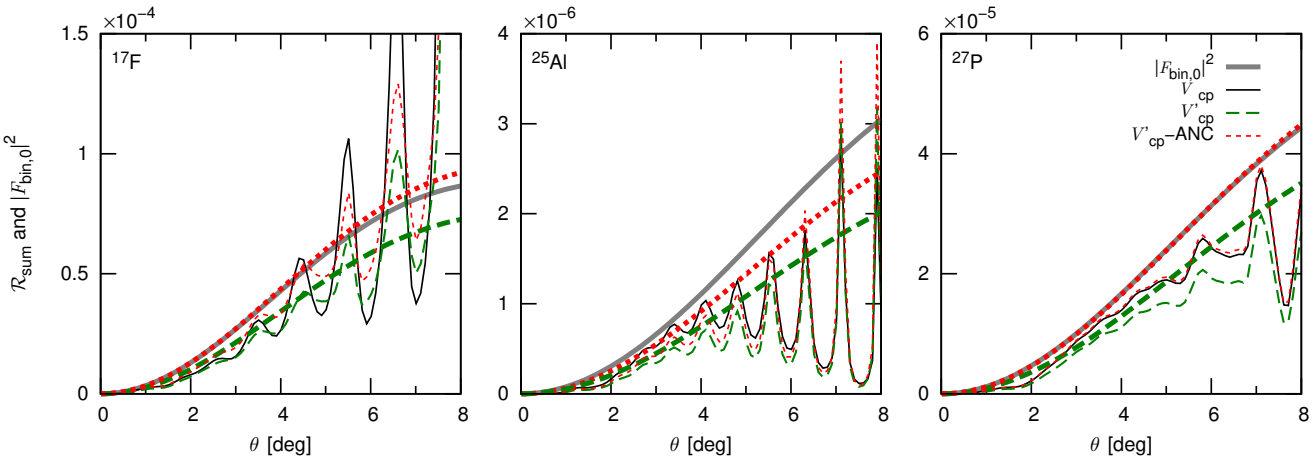

Figure 3.25: Same as Fig. 3.21 but on a ^{58}Ni target at 60 MeV/nucleon.

The sensitivity of the method to the projectile description is very similar to what has been observed in Fig. 3.21 on a ^{12}C target. In the case of ^{27}P, the choice of the c-p potential does not affect the quality of the method: the agreement of the REB prediction with the ratio does not vary much when V'_{cp} is used instead of the original V_{cp}. That change is solely due to the difference in the ground-state ANC, as proven by the red

dashed lines, which display the V'_{cp} results scaled to the ANC obtained with V_{cp}. In the case of ^{17}F, we observe again that the dynamical calculation of the reaction is less peripheral than predicted by the REB, the ratio obtained with V'_{cp} not being superimposed on the V_{cp} calculation after its scaling by the ANC. For ^{25}Al, both the DEA and REB models indicate that the reaction is not peripheral. Since the DEA calculation deviates so much from its REB estimate, only estimates of l_0 and/or E_0 could be extracted. Finally, it should be mentioned that the ratios $\mathcal{R}_{\rm sum}$ for several continuum bins are similar to the carbon-target case: broadening the bin leads to larger breakup cross sections with a quality of the agreement between the DEA calculation and the REB prediction that worsens at high energy for ^{27}P.

3.4 Summary and prospects of the analysis

As we have seen in previous sections, the breakup and elastic scattering cross sections obtained for the collision of halo nuclei exhibit very similar oscillatory and decay patterns. These characteristics have been observed both for neutron halos and proton halos and on light, medium-mass and heavy targets but do not carry much information on the halo projectile. As such, by taking the ratio of some combination of the breakup and elastic scattering cross sections, these features are mostly removed and give rise to an observable $\mathcal{R}_{\rm sum}$ which is sensitive mostly to the structure of the studied projectile. In the REB model, which assumes the reaction to be adiabatic and considers that the halo does not interact with the target, the breakup and elastic scattering cross sections can be written as a product of a some form factor and a pointlike cross section. While the former depends on the structure of the projectile and on the process (breakup or elastic scattering), the latter is the same for both processes and represents the elastic scattering cross section of the core of the halo nucleus with the target. By taking the same ratio of cross sections as for $\mathcal{R}_{\rm sum}$ in the assumptions of the REB, this pointlike cross section is hence removed. This gives rise to the REB form factor $|F_{E,0}(\boldsymbol{Q})|^2$, the REB prediction, which approximates the dynamical observable $\mathcal{R}_{\rm sum}$.

In the work of Capel *et al.* [68], the dynamical ratio and its REB predictions proved to be in quite a good agreement for the reaction of ^{11}Be, a halo nucleus, on carbon and lead targets at an energy of roughly 70 MeV per nucleon. To explore the limits of the ratio method, I have performed the same kind of analysis at a lower energy of 20 MeV/nucleon. Additionally, I have studied the validity of the ratio for ^{8}B, a proton halo nucleus as well as for several other proton-halo candidates.

The results obtained in this work show that when the energy of the projectile is low or when the halo is charged, that is, when the assumptions of the REB are breached, the ratio method is not as convincing as for neutron halos at high energies. Contrary to the results for a neutron halo projectile at higher energy [Capel, ratio...], here the agreement between the ratio $\mathcal{R}_{\rm sum}$ and its REB prediction $|F_{E,0}|^2$ is less good. For neutron halos on light targets, for which the reaction is dominated by the nuclear interaction, the ratio calculated dynamically (through CDCC or DEA) is closer to the REB form factor. However, it exhibits remnant oscillations that are not observed in the REB prediction. On heavy targets, for which the reaction is dominated by Coulomb, the ratios for neutron halos are smooth but are slightly overestimated by $|F_{E,0}|^2$. As it was already observed at high energy, the ratio is overestimated at very forward angle, where the reaction is completely dominated by the Coulomb interaction between the core and target. In the case of low energies of the projectile however, this effect is significantly enhanced and extends to larger

angles, especially for heavy targets. For proton halos, similar observations to the ones for neutron halos can be made. On light targets, i.e. nuclear dominated reactions, the dynamical ratio is closer to its REB prediction. However, it exhibits remnant oscillations not present in $|F_{E,0}|^2$. On heavy targets, i.e. for reactions dominated by Coulomb, the dynamical ratios are smooth but slightly overestimated by $|F_{E,0}|^2$. This effect is however exacerbated for proton halos, for which the overestimation occurs on the whole angular range and originates from the additional Coulomb interaction of the fragment.

Therefore, because the Coulomb interaction of the projectile with the target has such a significant impact on the ratio, there remains a substantial sensitivity to the target choice. This is displayed in Figs. 3.11 and 3.16. But while this sensitivity is limited to the very forward angle region for neutron halos, it is stronger and extends further in angle for charged halos, as it is expected from the charge of the valence proton.

Because it is the ratio of two cross sections, this observable is not sensitive to normalisation. This is a valuable experimental quality. Moreover, as visible in Figs. 3.7, 3.13 and 3.15, the ratio keeps its independence of the optical potentials used to simulate the interaction between the core and the target. Because the individual reaction observables can be strongly sensitive to this choice (see also Ref. [45]), this is another appreciable quality that can help in the extraction of spectroscopic information from cross sections. Furthermore, the ratio exhibits significant variations in both shape and magnitude with modifications in the halo structure. In particular, changes in the core-halo orbital angular momentum l_0 and binding energy in the ground state E_0 can impact the ratio by several orders of magnitude, as illustrated in Figs. 3.3 and 3.18.

It seems therefore that albeit less accurate than for neutron halos at high energy, the ratio could still enable experimentalists to infer pertinent structure information from the analysis of actual data. As seen in the previous sections, this is particularly true when the valence nucleon is loosely bound to a core in a low orbital angular momentum l_0, viz. for halo nuclei. Three variants of the method can be applied in practice to benefit from this new observable.

In its *strict application*, i.e. the one suggested in Refs. [38, 68, 71] for the study of one-neutron halo nuclei, an experimental measurement of the ratio $\mathcal{R}_{\text{sum}}$ is to be compared directly to the REB form factor $|F_{E,0}|^2$ (2.62). As observed in Secs. 3.2 and 3.3, even on a light target, there can be too large a difference between the DEA ratio and its REB prediction to allow for this comparison to provide us with fine details about the structure of the projectile. This is visible on Fig. 3.17 for a proton halo at intermediate energy and Fig. 3.8, for a neutron halo at low energy. In the particular case of ^{27}P, a possible proton halo nucleus, with $S_p \simeq 0.8$ MeV and most likely a valence proton in an s orbit, such strict application would still make sense for a reaction on a light target at high energy. However, this would have to be done with a coarse angular resolution, to smooth out the remnant oscillations of the ratio (see Fig. 3.22).

Nevertheless, thanks to the strong sensitivity in shape and magnitude of the ratio to the projectile structure, pertinent information pertaining to that structure could be obtained by confronting the order of magnitude and general shape of the experimental ratio to the REB prediction. In this *approximate application* of the ratio, the small differences in the ANC or in the continuum of the projectile such as the ones displayed in Fig. 3.17 cannot be distinguished. However, it could still provide with a good estimate of l_0 and E_0, which are difficult to measure directly far from stability. This approximate application could be done at high energy on nuclei such as ^{17}F and ^{25}Al (see Fig. 3.21) or at lower energies on ^{8}B (see Fig. 3.17) and ^{11}Be at low energy (see Fig. 3.8).

In a third application of the ratio, which I coin *dynamical*, measurements are compared not to the REB prediction, but to the results of state-of-the-art dynamical reaction calculations like CDCC or DEA. The gain in this case over the more usual analysis of cross sections for individual reactions lies in the complete independence of the ratio to the choice of V_{cT}. This is of course the least practical use of the ratio since it requires an accurate calculation of the reaction, instead of the calculation of the mere form factor $|F_{E,0}|^2$. On an experimental point of view, this third application would be best used on heavy targets, for which the breakup cross section is the largest, and hence for which the statistical experimental uncertainty would be the lowest. This more computationally involved application of the ratio would provide the most precise information about the single-particle structure of unstable nuclei near the driplines. It would be applicable to any nucleus that exhibits a clear single-particle structure but would be cumbersome to perform.

It should be noted that the major part of the disagreement between the REB form factor and the dynamical ratio comes from the interaction between the halo fragment and the target. For neutron halos, these discrepancies are mostly found in the form of remnant oscillations of the ratio. In the case of proton halos, the Coulomb interaction of the fragment with the target causes an overestimation of the ratio which adds to these remnant oscillations. Accounting for interaction between the valence nucleon and the target, e.g., at the first order of the perturbations, might hence improve the REB prediction and enable the direct comparison suggested in Refs. [38, 68, 71].

Chapter II

The neutral-pion photoproduction as a tool to measure the neutron skin

4 State of the art in neutron skin measurements

As we have seen in the introduction, the EOSNM which governs the properties of nuclear matter from microscopic nuclei ($R \sim 10^{-15}$ m) to macroscopic neutron stars ($R \sim 10^{4}$ m), can be written in its compact form as [see Eq. (6)]

$$\mathcal{E}(\rho, \alpha) = \mathcal{E}(\rho, \alpha = 0) + \mathcal{S}(\rho)\alpha^2 + \mathcal{O}(\alpha^4) \tag{4.1}$$

an expansion in the asymmetry of the system $\alpha = (\rho_N - \rho_Z)/\rho$, where ρ is the nuclear density and where we recognise the energy of symmetric nuclear matter $\mathcal{E}(\rho, \alpha = 0)$ and the symmetry energy $\mathcal{S}(\rho)$ on the right-hand side. We can also expand these quantities in $x = (\rho - \rho_0)/3\rho_0$, which characterizes the deviation from nuclear saturation density $\rho_0 \simeq 0.15$ fm^{-1}. With the help of a few bulk parameters, we can write the energy of symmetric nuclear matter as

$$\mathcal{E}(\rho, \alpha = 0) = \varepsilon_0 + \frac{1}{2}K_0 x^2 + \dots \tag{4.2}$$

where, like in Eq. (5), the parameter ϵ_0 can be interpreted as the energy per nucleon and K_0 represents the incompressibility coefficient of symmetric nuclear matter. Similarly, for the symmetry energy

$$\mathcal{S}(\rho) = J + Lx + \frac{1}{2}K_{\rm sym}x^2 + \dots \tag{4.3}$$

where J and $K_{\rm sym}$ are the symmetry energy counterparts of ε_0 and K_0. It should be noticed that an additional linear term exists in the symmetry energy: L, the *slope* of the symmetry energy. This term arises from the fact that contrary to its symmetric nuclear matter energy counterpart, the pure neutron matter pressure does not vanish at saturation density.

While $\varepsilon_0 \simeq -16$ MeV, $K_0 \simeq 230 \pm 20$ MeV and $J \simeq 31.7 \pm 3.2$ MeV are rather well constrained, for example by measurement of density, masses and collective excitations of nuclei at saturation density [100, 101, 102, 103], L and $K_{\rm sym}$ are not. This results from the very small asymmetry that exists in stable nuclei (e.g. $\alpha^2 \simeq 0.04$ in ^{208}Pb, the most asymmetric stable nucleus) and from the fact that these quantities are extracted indirectly, increasing the uncertainties on their value. Of particular interest is the slope of the symmetry energy $L \simeq 58.7 \pm 28.1$ MeV, which captures most of the density dependence of $\mathcal{S}(\rho)$ around nuclear saturation density [100].

As we have seen in Fig. 3, L is nicely correlated to the neutron skin of (asymmetric) heavy nuclei and several experimental techniques have thus been developed to measure this quantity. But while the precision on the charge distribution has been growing with the years, the measure of the neutron distribution remains challenging. Indeed, on the one hand, charge distribution measurements often rely on elastic scattering of electrons, whose interaction with the nucleus is known for decades. On the other hand, measurements of the neutron distribution often rely on processes with large theoretical and/or experimental uncertainties which hinder its clean extraction. Hereafter are discussed some of the most relevant experimental techniques that have contributed to the study of the neutron skin. Because ^{208}Pb has the largest asymmetry for a stable (and doubly magic) nucleus and hence most probably the thickest skin, a significant amount of experiments have studied this nucleus in the last decades. To illustrate the pros and cons of these experimental techniques, I will thus discuss and compare some selected results mostly on this particular nucleus.

4.1 Hadronic probes

Hadronic probes and especially the scattering of hadrons from atomic nuclei have been the main method to probe the neutron distribution and the difference between the neutron and proton distributions. They offer the main advantage of exhibiting large cross sections, due to the strong interaction. This ensures low experimental errors, which are dominated by systematic uncertainties. However, while the elementary electromagnetic interaction is known with accuracy for decades and does not change much in the medium, there is still no clear understanding of the details of the strong interaction even for elementary processes. This induces large uncontrolled uncertainties on the theory side: poor understanding of the reaction mechanism, multiple scattering effects, in-medium modification such as absorption, density dependences, *etc.* [104, 105]. Moreover, the strong interaction lacks isospin selectivity and probes the isoscalar part of the density (the sum of the proton and neutron densities). Among the experimental techniques that involve hadron probes, we could list α-, π- and p-nucleus scattering and antiprotonic atoms.

Among all hadronic experiments, p-nucleus scattering has probably been the most widely used one. Measurements have been made in a large range of energies (mostly from 200 MeV to 1 GeV, where uncertainties are smaller). However, all these results still show inconsistencies that are energy and model dependent [104, 106]. More recently, in order to evaluate the sensitivity of the p-nucleus scattering to the neutron density, a measurement on ^{204,206,208}Pb has been carried out with low energy protons $\sim$ 300 MeV. At these energies, the impulse approximation is valid and the optical potential dynamical content is simple. The authors extract a neutron skin of $\Delta r_{np}^{208} = 0.211^{+0.054}_{-0.063}$ fm [107]. Most of these uncertainties come from the theory: they first introduce a phenomenological medium modification in a nucleon-nucleon (NN) interaction in terms of density-dependent parameters, they then calibrate this medium-modified NN interaction on a ^{58}Ni target in the framework of the relativistic impulse approximation and they finally apply it to ^{208}Pb.

This result provides a measurement of the skin that agrees with several different theoretical calculations but also illustrates how the recent progress in relativistic parametrizations of the NN interaction have strongly reduced the discrepancies between relativistic and non-relativistic models. But while these progresses are encouraging, recent works have also shown the p-nucleus cross section to be sensitive only to the isoscalar part of the density and hence to be very weakly dependent on the details of the neutron distribution. In Ref. [108], several ground state densities from 4 different mean field models are used to fold a free NN interaction to simulate the p-scattering on ^{40}Ca and ^{208}Pb. The results are shown on Fig. 4.1. While they all provide a very good description of the experimental cross sections, there is no way to discern between these models even though the range of their prediction for the neutron skin thickness (see legend in Fig. 4.1) is wider than the result cited above. This puts the method at stake.

As early as in the 70's, α-nucleus scattering was thought as a promising method for the measurement of the neutron radius of ^{208}Pb. In Ref. [109], a neutron skin of $\Delta r_{np}^{208} = 0.30 \pm 0.07$ fm is extracted. However, because of the plethora of assumptions on the neutron distributions but also on the optical potential used to simulate the α-nucleon interaction, we have the right to doubt that such a precision is possible on these measurements. Moreover, a re-analysis of these results found a significantly different thickness of $\Delta r_{np}^{208} = 0.00 \pm 0.10$ fm [110], which would be compatible with a negative skin thickness. The scattering of pions on nuclei suffers from the same issues and sometimes also results in contradictory measurements of the neutron skin thickness in the same

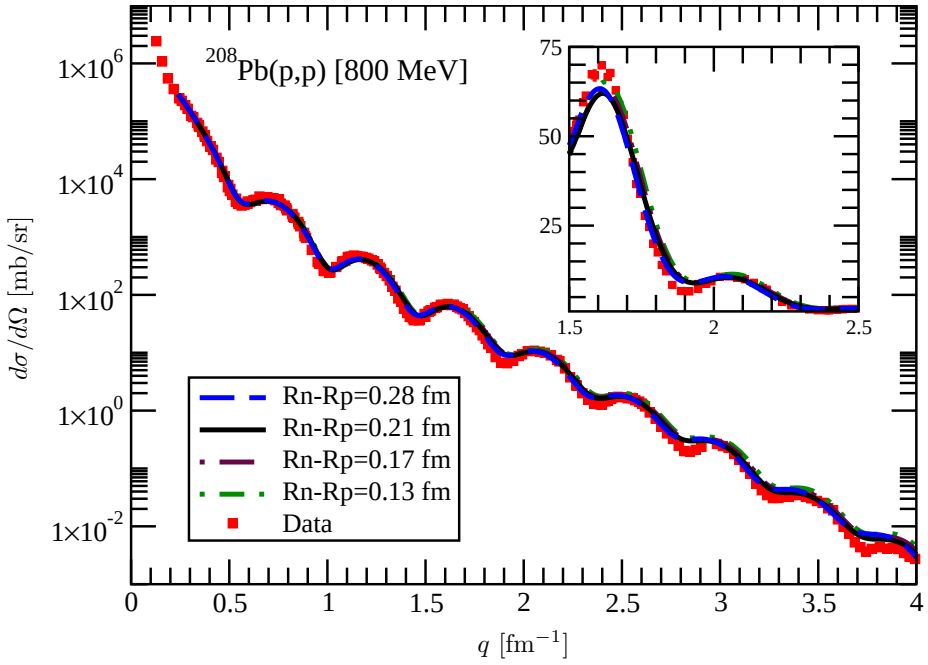

Figure 4.1: Influence of the density on the p-^{208}Pb elastic scattering cross section as a function of the momentum transfer to the nucleus. The differential cross section over a limited range of momentum transfers is shown in the inset. Figure adapted from Ref. [108].

experiment if π^+ and π^- are considered [111].

In antiprotonic-atom experiments, antiprotons are sent towards a target at low energy. If they are slow enough, they can form a molecular system with the nucleus of the target. The periphery of the nucleus can then be probed in two ways. On the one hand, the nuclear levels and their widths are altered by the antiproton-nucleus strong interaction. Because these modifications are density dependent, x-ray measurements of the atomic levels provide information on the neutron to proton density ratio at the periphery of the nucleus [112]. After extrapolating these densities towards the interior, they provide the nucleon densities and hence the neutron skin thickness. However, as we have seen before, the strong interaction is poorly known, which induces significant theoretical uncertainties. Moreover, this extraction assumes a 2-parameter Fermi Dirac (2pF) nuclear densities. While this type of densities reproduces rather well the nuclear distribution inside the nucleus, their applicability at large radii is dubious.

On the other hand, the neutron skin can also be extracted through radiochemical methods [113]. After some time spent in the vicinity of the nucleus, the antiproton annihilates with a nucleon and creates a shower of particles (pions mainly). To reduce the complexity of the mechanism, we are only interested in cold annihilation processes, which occur far enough from the interior of the nucleus so that most of the pions miss the nucleus and excite it below the nucleon emission threshold. In this case, only $(Z,N-1)$ and $(Z-1,N)$ reaction residues are detected. Their relative yield then provides us with a neutron to proton density ratio at the annihilation site, which is then extrapolated in the same way as before, by 2pF densities. Both these methods can be used simultaneously to provide us with the neutron skin on a wide range of stable nuclei (see Fig. 4.2) [114]. Their result on ^{208}Pb, $\Delta r_{np}^{208} = 0.15 \pm 0.02$ fm, has a remarkable precision of 0.02 fm. However, one can

ask if this tiny number faithfully represents the error on this measurement considering the model assumptions to extract these values.

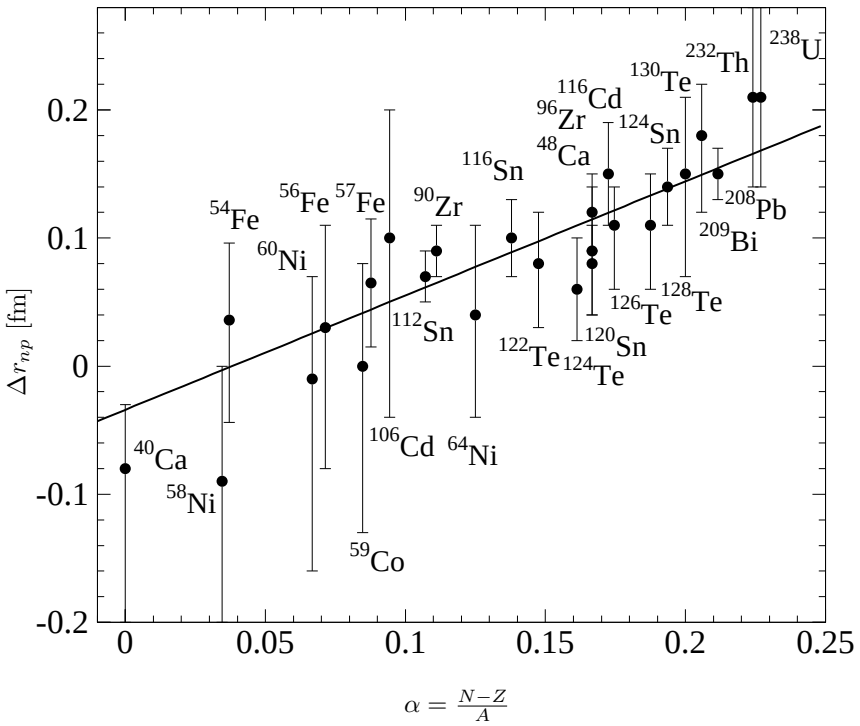

Figure 4.2: Neutron skin extracted from antiprotonic data. Figure adapted from Ref. [114].

As we have seen, the neutron skin measurements with hadronic probes are complex to analyse, mainly because of the large uncontrolled uncertainties induced by the strong interaction therefore *a truly model-independent determination of the density distribution is impossible* [106]. But because hadronic probes exhibit such large cross sections, they certainly remain one of the fundamental tools to probe nucleon densities in future radioactive beam facilities.

4.2 Parity-violating electron scattering

In order to circumvent the hadronic uncertainties due to the complexity of the strong interaction and its nearly identical treatment of protons and neutrons due to charge symmetry, a measurement based on parity violating electron scattering (PVES) was suggested 30 years ago [115]. This purely electroweak process relies on the vector coupling of the neutron with the weak-neutral Z^0 boson. Because the weak charge of the neutron ($Q_W^N = -1$) is much larger than that of the proton ($Q_W^Z \simeq 0.075$), electroweak processes are highly sensitive to the neutron distribution. This offers a clean and model-independent way to extract this isospin-dependent quantity.

In PVES, longitudinally polarized electrons scatter off a polarized target. Because of the interference between the virtual γ and Z^0 boson exchanges, an asymmetry exists between the cross section of right and left-handed electrons. In the Born approximation,

the fractional difference between these cross sections

$$A_{\mathrm{PV}} = \left(\frac{d\sigma_R}{d\Omega} - \frac{d\sigma_L}{d\Omega}\right) \Big/ \left(\frac{d\sigma_R}{d\Omega} + \frac{d\sigma_L}{d\Omega}\right) \tag{4.4}$$

is directly proportional to the weak form factor F_W, which is mostly sensitive to the neutron distribution. Coulomb distortions caused by the electrons interacting with the charged nucleus must be included in the calculations but while important, these are well known and can be computed with accuracy. However, because A_{PV} can be as small as 10^{-7}, PVES measurements are challenging and require a very high precision in order to maintain statistical and systematic errors low.

Recently, the first PVES measurement has been carried out by the Lead (^{208}Pb) Radius EXperiment (PREX) collaboration. They have measured A_{PV} at Jefferson Lab (JLab) with a precision of 10% at a given 4-momentum transfer $\bar{Q}^2 \simeq 0.0088$ GeV^2 [116]. This measurement allows for the determination of the weak form factor $F_W(\hat{Q}^2)$ at this 4-momentum and hence, after minor assumptions on the surface thickness of the density, provides a skin thickness of $\Delta r_{np}^{208} = 0.33^{+0.16}_{-0.18}$ fm [116, 117]. While the error bars on this result are much larger than what hadronic measurements claim, they come in this case almost exclusively from experimental resolution. This method is hence much less sensitive to the theoretical systematic errors.

PREX has showed that the control of systematic and satistical uncertainties is possible in PVES measurements. A second run (PREX II [118]) that aims at reducing the error bars to ± 0.06 fm and the Calcium Radius EXperiment (CREX [119]) that will measure the neutron skin of ^{48}Ca have been scheduled to run during this year. Moreover, at the soon-to-be-commissioned Mainz Energy-Recovering Superconducting Accelerator (MESA), the Mainz Radius EXperiment (MREX) will repeat this experiment. While the maximum incident energy at MESA will be lower than at JLab, the higher beam intensities and full azimuthal coverage will allow to measure the neutron skin of ^{208}Pb with an even higher precision [120]. Aside from providing with a model-independent way of extracting the neutron skin, PVES will also help in the interpretation of future measurements with exotic nuclei at future radioactive beam facilities by serving as a calibration of experiments involving hadronic probes.

4.3 Electric dipole resonances

Electric dipole resonances originate from collective vibration modes of the nucleons inside the nucleus. When an external electric field is applied to a nucleus, protons of the nucleus are displaced relative to neutrons. Spatial regions of high asymmetry then arise, which are energetically disfavored by the increase of symmetry energy. When the external field is turned off, the symmetry energy acts as a restoring force. Protons and neutrons move in opposite directions to regain the (near-)symmetric configuration of the nucleus. This out-of-phase oscillation is known as the isovector Giant Dipole Resonance (GDR) [121]. Moreover, for heavy nuclei which exhibit a large number of excess neutrons, the development of the neutron skin also offers the possibility of a vibration of the symmetric core against the excess neutrons of the skin. This soft mode of vibration is known as the Pygmy Dipole Resonance (PDR) and while its purely isovector character is still debatable [122], it contributes significantly to the electric dipole response of the nucleus.

The quantity that characterizes the electric dipole response of a nucleus to an external electric field is the electric dipole polarisability α_D. It is proportional to the inverse

squared energy weighted sum of the photoabsorption cross section $\sigma_{\rm abs}(\omega)$ which is itself proportional to the nuclear electric dipole response $R(\omega; E1)$ times the photon energy ω

$$\alpha_D \propto \int_0^\infty \frac{\sigma_{\rm abs}(\omega)}{\omega^2}\, d\omega \propto \int_0^\infty \frac{R(\omega; E1)}{\omega}\, d\omega \tag{4.5}$$

By measuring the E1 strength on a wide range of energies that includes both the GDR and the PDR, we avoid any model dependency in the attempt to separate these two contributions. This quantity is usually probed through Coulomb excitation, a process in which a nucleus is excited by the Coulomb interaction in an inelastic collision. Recently, a new experimental tool has been used to measure α_D through the inelastic scattering of polarized protons at extreme forward angles (including 0°) [123, 124]. Such forward angles ensure that the reaction is purely electromagnetic. At proton energies of 200–400 MeV at which the experiment is run, isovector Coulomb excitation of the non-spin-flip E1 transitions is dominant in the cross section. Spin-flip M1 transitions also contribute and these must be removed. This can be done for example by a multipole decomposition analysis technique of the angular distribution of the cross sections and polarization transfer information analysis [123, 124]. These measurements are shown on Fig. 4.3.

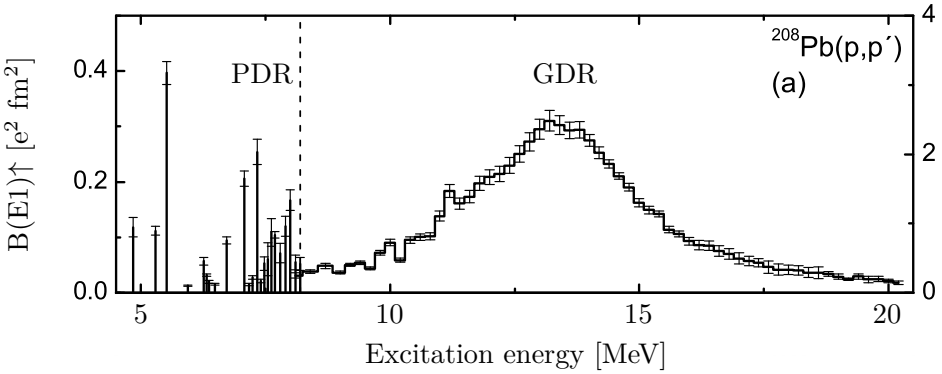

Figure 4.3: Experimental E1 strength distribution in ^{208}Pb (top). (Note the different scales below or above 8.2 MeV.) The GDR is clearly visible around 14 MeV. The PDR is located around 7-8 MeV. Figure modified from Fig. 4 in Ref. [123].

A covariant analysis performed within a model with a single Skyrme energy density functional [125] has shown α_D to be strongly correlated to the neutron skin thickness of ^{208}Pb. This covariant analysis has been used to constrain the neutron skin thickness of ^{208}Pb to be $\Delta r_{np}^{208} = 0.156^{+0.025}_{-0.021}$ fm. But while this correlation has been shown to hold for a large set of nuclear energy density functionals, it has also been shown not to be universal [126]. Indeed, systematically varied models display such a correlation but a significantly better correlation can be found when scaling α_D by J, the symmetry energy at saturation density (see Eq. (4.3)). This is illustrated on Fig. 4.4, where α_D (left) and the product $\alpha_D J$ (right) are represented as a function of Δr_{np}^{208} for several mean-field models. The dipole polarizability shows a linear dependence within each different model. However, the results are scattered significantly. The scatter disappears when considering the product $\alpha_D J$ and all models are then aligned. The extraction of the neutron-skin thickness from α_D must then be handled with care, as it involves several model-dependent assumptions.

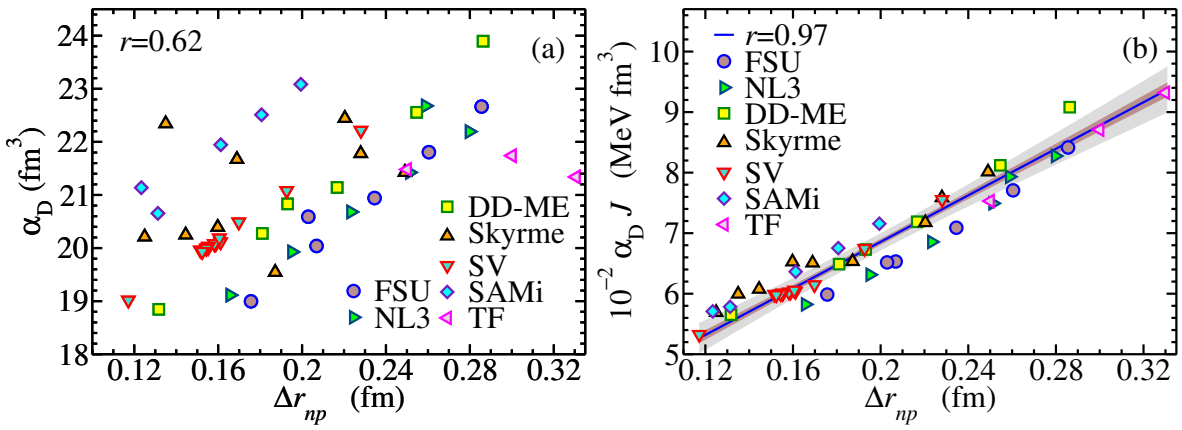

Figure 4.4: α_D (left) and $\alpha_D J$ (right) are represented as a function of Δr_{np}^{208} for several mean-field models. Note how the scatter present in the left panel disappears as we take its product with J. Figure taken from Ref. [127].

4.4 Coherent neutral-pion photoproduction (a primer)

The last way of studying the neutron skin that I will present is the coherent photoproduction of a neutral pion. In this process, a photon impinges on a target and produces a π^0 while the target remains in its ground state (coherent). In the incident photon energy range from threshold to 250 MeV, this reaction is dominated by Δ-resonance excitation and because of the dominance of QED in this process, it is known with great accuracy. Protons and neutrons contribute with the same amplitude and the method then probes the whole nucleon distribution in the nucleus, as in the hadronic probes. In the Plane Wave Impulse Approximation (PWIA) which assumes that the photoproduction amplitude is merely the sum of the contributions of the elementary amplitudes on each nucleon and that the π^0 exits the nucleus without any final state interaction, the photoproduction cross section is directly proportional to the square of the nucleon density form factor [128]. However, distortions in the exit channel can be significant at energies around the Δ resonance [129, 128]. The coherent π^0-photoproduction is thus rather studied using the Distorted Wave Impulse Approximation (DWIA), which accounts for the pion-nucleus interaction in the final state. As we have already discussed for hadronic probes, the need to simulate the strong interaction increases the uncertainties of the method.

While this experimental method has already been applied as early as the 60's to infer the matter distribution of some nuclei [130, 131], the extraction was hindered by the too poor experimental resolution at the time. More recently, such a measurement has been carried out at the MAinz MIcrotron (MAMI) with a large solid-angle detector system on ^{208}Pb [132]. Their results have been analysed within the DWIA model of Drechsel *et al.* [128, 133], which, in addition to the π^0-nucleus interaction, incorporates a self-energy term for the Δ in-medium propagation. By modelling the proton and neutron densities as two separate 2pF Fermi Dirac distributions, they have extracted the neutron skin thickness of ^{208}Pb and found $\Delta r_{np}^{208} = 0.15 \pm 0.03(\text{stat.})^{+0.01}_{-0.03}(\text{sys.})$ fm. The precision on this measurement has raised a lot of criticisms. Theoretical uncertainties seem to have been largely underestimated since it does not properly quantify the uncertainties due to the poor knowledge of the pion-nucleus interaction and since the model does not include pion charge exchange processes nor medium modifications of nucleon resonances

that could strongly influence the cross section [134].

4.5 Summary

The different results of the extraction of the neutron skin thickness from these selected experiments are compiled in Fig. 4.5. Note that I have chosen to present only the most recent results. For this reason, the contradictory results coming from α-nucleus scattering experiment from the 70's do not appear in this figure. We could be tempted to perform a least square fit on these data by considering each experiment as having the same weight. This provides us with a thickness of $\Delta r_{np}^{208} = 0.156 \pm 0.014$ fm. Note that 1σ and 2σ intervals around the central value are also given.

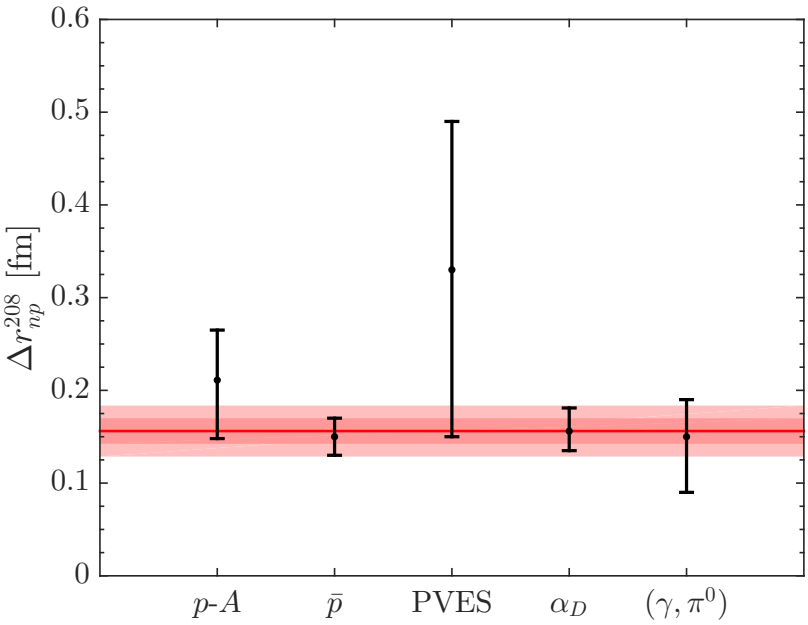

Figure 4.5: Extracted neutron skin thickness of ^{208}Pb from some selected experiments and its least square fit with 1σ and 2σ intervals around the central value if we consider each experiment with the same weight. From left to right: proton-nucleus scattering, α-nucleus scattering, antiprotonic atoms, parity violating electron scattering, electric dipole polarizability, coherent π^0-photoproduction.

As we can see, all these results tend to agree on a thickness of the skin around $\Delta r_{np}^{208} = 0.15$ fm and several methods, namely antipionic atoms, electric dipole polarizability and coherent π^0-photoproduction, even have their central value nearly lined up around this value. It should however be noted that while PVES exhibits a very large error bar, it probably is the only measurement that considers both theoretical and experimental uncertainties. As we have seen, hadron probes suffer from the poor knowledge of the strong interaction. This could also be said about the π^0-photoproduction, in which the final state π-nucleus interaction is simulated by an optical potential which can significantly affect the cross section. Electric dipole polarizability on the other hand, while seemingly clean at first sight, also involves several model-dependencies that are not accounted in this result. All the theoretical uncertainties for these methods are not shown in the error bars of the data shown here and this value of the skin should just be considered as an order of magnitude.

In the recent years, *the importance of including uncertainty estimates in papers involving theoretical calculations of physical quantities* has been highlighted [135] by many authors and notably in the field of neutron skins measurements [136]. With this idea in mind, a cooperative theoretical and experimental effort has been initiated specifically for the coherent π^0-photoproduction method. In order to investigate how large theoretical uncertainties can be and how suited is this method to extract the neutron skin thickness, i.e. how dependent it is on the density, a follow-up experiment using the same experimental setup has been performed on tin isotopes [137] and ^{48}Ca [138]. On the theoretical part, I have developed an advanced reaction code, which is the subject of the next sections.

In Sec. 5, I will describe how coherent π^0-photoproduction cross sections are measured experimentally and I will particularise to the MaMi facility in Mainz in which the recent experiments of Refs. [137, 138] have been performed. In the idea of studying the sensitivity of the process to the details in the density, I will describe different density models in Sec. 6. This section will also allow me to define different nuclear properties that will be needed in Secs. 7 and 8 which detail the implementation of the reaction model. The implementation can be seen as made of two parts. First, in Sec. 7, which discusses the photoproduction process in itself, I will define the formalism in which the model is built and the several simplifying assumptions on which it relies. Second, in Sec. 8, I will discuss how the rescattering of the pion after its production can be taken into account theoretically and numerically. Finally, I will compare the results of my model to previous measurements to validate the implementation of my reaction code in Sec. 9. In this last section, I will also apply this model on a whole range of targets to analyse the sensitivity of photoproduction measurements to the neutron-skin thickness.

5 Experiments on neutral-pion photoproduction

In the π^0-photoproduction process (γ, π^0), an photon γ impinges on a target of mass A and produces a neutral pion π^0. In the case of a coherent process, the target remains in its ground state

$$\gamma + A \to \pi^0 + A \tag{5.1}$$

Because it is short-lived, the produced neutral pion, will decay very quickly. Most of these pions will decay into two photons as the branching ratio for this decay channel has a $\sim 98.8\%$ probability [139]. On an experimental point of view, one hence needs

1. a way to create high energy photons,
2. a reliable way to measure precisely the energy of these photons,
3. a detector that can cover as much of the 4π solid angle around the target as possible in order to measure, in coincidence, the two photons that result from the decay of the pion.

In this section, I will briefly go through some of the experimental details of the recent π^0-photoproduction experiment that I will help analyse.

5.1 The recent measurement at the MaMi facility

The recent experiment of π^0-photoproduction on tin isotopes [137] has been carried out in the A2 hall of the Mainzer Mikrotron (MaMi) facility in the Institut für Kernphysik at the Johannes Gutenberg Universität in Mainz. In this experiment, a beam of electrons is accelerated by several race track microtrons and directed onto a thin copper foil radiator. The interaction of the accelerated electrons with the electrostatic field of the copper nuclei produce bremsstrahlung photons. The momentum of the corresponding electrons are tagged by the Glasgow Photon Tagger so that the momentum of these photons is known with precision. The photons are emitted towards the tin target placed at the center of the Crystal Ball and TAPS setup, an assembly of two spectrometers that cover 97% of the 4π solid angle. The photoproduced π^0 momentum is then reconstructed from the measurement of the two photons that originate from its decay.

In this section, I review some of the components of this experiment in more details.

Mainzer Mikrotron facility

The Mainzer Mikrotron is an intense continuous wave electron accelerator that has been in operation since 1979 (the interested reader is referred to the website of MaMi[1]. In its original stage (MaMi-AI) it was composed of a linear accelerator and one race-track microtron that could deliver electrons with an energy of up to 14 MeV and a maximum intensity of 25 μA. It was upgraded in 1983 (MaMi-AII) by adding a second microtron that increases the maximum energy of the electrons to 183 MeV (which is above threshold for pion photoproduction). A third one was then added in 1990 to push the maximal energy to 855 MeV (MaMi-B) and inspired the logo visible on the right panel of Fig. 5.1.

Race track microtrons basic design is shown on the left panel of Fig. 5.1. A short linear accelerator (LINAC) is placed between two 180° bending magnets that return the

[1] https://www.kernphysik.uni-mainz.de/beschleuniger/mainzer-mikrotron/

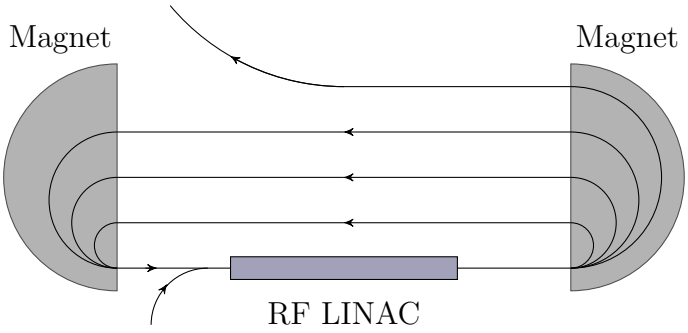

Figure 5.1: Schematic view of a simple race-track microtron (left) and logo of MaMi (right), symbolising three microtrons that are used in series to deliver electrons with energies of up to 855 MeV to the harmonic double-sided microtron.

electrons to their starting position. Thanks to this shape, the field of the magnets can be kept constant. As the electrons pass through the LINAC repeatedly, high energies can be achieved without the need for high accelerations in the LINAC. This also allows the LINAC to be operated in continuous wave mode, making MaMi a 100% duty electron accelerator. By working with continuous wave beams for coincidence measurements, the probability of detecting two or more uncorrelated particles is reduced compared to bunched beams, where the event rate in the bunch can be very high compared to the time resolution of the detector.

However, as the energy of the beam gets larger, the size of the magnets grows in size and weight. To achieve higher energies, the latest stage of MaMi-C has added a harmonic double-sided microtron (HDSM). A schematic view of such machine is reproduced on Fig. 5.2. Rather than having two 180° bending magnets, the HDSM has four 90° bending ones. Between these, two LINACS accelerate the electrons to energies of up to 1.5 GeV. This beam is then directed into one of the four experimental halls. In the case of coherent π^0-photoproduction, to hall A2.

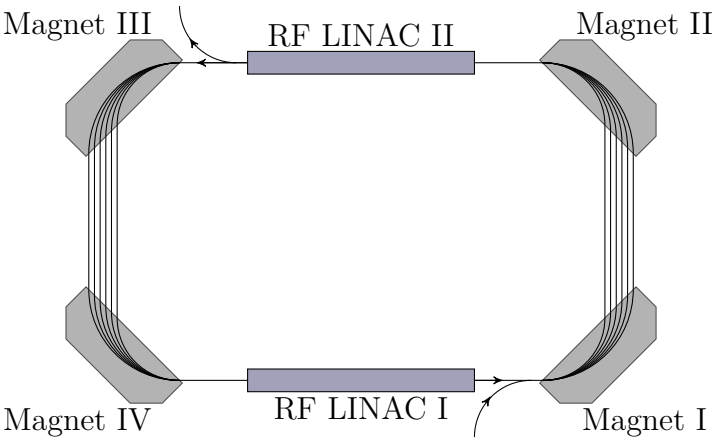

Figure 5.2: Schematics of an harmonic double-sided microtron.

The Glasgow Photon Tagger

After their acceleration, the electrons are directed onto a thin foil of copper which acts as a radiator. When interacting with the electromagnetic field of the copper nuclei, the electrons radiate photons by bremsstrahlung. The energy distribution of these photons hence follows an inverse law in energy and they are produced in a forward cone. To ensure a small beam spot on the target, which reduces the uncertainty on the reaction vertex position, the photon beam is collimated after its passage in the Glasgow Photon Tagger (GPT). The latter is a large momentum acceptance spectrometer that analyses the bremsstrahlung electrons and reconstructs the energy of the incident photon. It is schematically shown on Fig. 5.3. The complete spectrometer can tag photons with an energy of 40 to 800 MeV with an energy resolution between 2 and 8 MeV, depending on the beam energy [140].

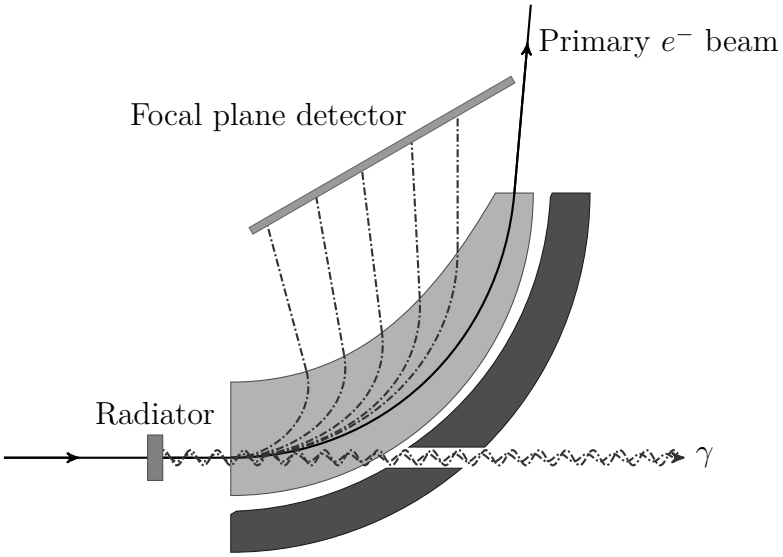

Figure 5.3: Schematics of the Glasgow Photon Tagger. Accelerated electrons impinge on a radiator and radiate photons by bremsstrahlung. The bremsstrahlung electrons are then tagged on the focal plane detector of this spectrometer and the energy of the photon is then deduced.

The Crystal Ball and Taps detectors

The target is located at the center of the Crystal Ball (CB) detector. The CB is shaped as an icosahedron (a polyhedron with 20 triangular faces). Each of these faces (thick black triangles in Fig. 5.4) is divided into 4 smaller triangles (thick red triangles in Fig. 5.4) which each contain 9 modules (smallest triangular shapes in Fig. 5.4). These modules are NaI crystals into which the two photons originating from the π^0 decay deposit their energy. Because the Crystal Ball detector was originally designed for $e^+ - e^-$ colliding beams at the Stanford Linear Acccelerator (SLAC) [141], 24 crystals at each poles have been removed to give space for the passage of the beam and to hold the target (see orange part on Fig. 5.4). In fixed target experiments such as coherent π^0-photoproduction, the reaction products are forward focused in the lab frame and we need to compensate for the forward gap at the pole. For this reason, a second spectrometer is added as a forward

wall: TAPS [142]. TAPS is a highly segmented spectrometer made from 385 hexagonal BaF_2 crystals (see blue part on Fig. 5.4) designed to detect low and high energy single photons. The combination of both these detectors allows to cover 97% of the 4π solid angle. More details can be found in the thesis of M. Ferretti.

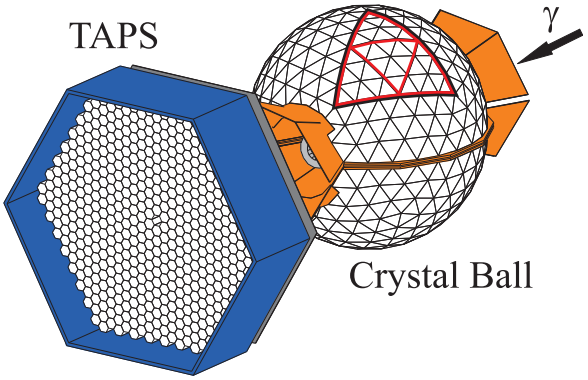

Figure 5.4: Schematics of the Crystal Ball - TAPS detector. Crystal Ball: each triangular face of the icosahedron (thick black triangle) is divided into 4 smaller triangles (thick red) which contain 9 NaI crystals modules (the smallest triangular surfaces). TAPS: hexagonal BaF_2 crystals. Image adapted from Ref. [143].

5.2 GEANT4 simulation and random event generator

The GEANT4 software can be used to determine the experimental resolution of the whole detector setup. It uses Monte Carlo methods to simulate the interaction of the different particles involved in the reaction with the detectors. These simulations hence allow to relate the output of a theoretical model with what is actually measured in the detectors of the experiment. Each reaction can be described by a limited set of variables (e.g. the energy of the photon, the scattering angle of the pion, its azimuthal angle, ...) where each of these variables follows a given statistical distribution in a given experiment. To generate a large set of random events, we need to pick, for each event, a random number for each of these variables.

This section discusses how I built such random event generator. In future works, it can be used to feed the GEANT4 simulation with the theoretical predictions of the coherent π^0-photoproduction of my model. This will be useful to observe how these theoretical cross sections are smeered by the experimental resolution of the detector setup.

In the following, I make the assumption that the pion decays right after its production. This approximation can be tested by calculating the distance travelled by the pion before decaying. For a proper time τ, this distance reads $\Delta x = \gamma\beta c\tau$, where

$$\beta = \frac{\sqrt{(T_\pi + m_\pi)^2 - m_\pi^2}}{T_\pi + m_\pi} \qquad \gamma = \frac{m_\pi + T_\pi}{m_\pi} \tag{5.2}$$

where T_π is the kinetic energy of the emitted pion in the laboratory frame. If we consider pions of energies around $T_\pi = 100$ MeV (which is the order of magnitude of the pion energies encountered in this experiment) and consider that the proper time τ is simply mean lifetime of the pion $\tau = 8.52\ 10^{-17}$s [139], this distance is of the order of 10^{-7} to

10^{-8} m. As it can be seen, this is very small compared to the precision we can expect on the position of the detectors or the target and this assumption is a thus good approximation.

Moreover, we consider the neutral pion to decay only in its most probable decay mode: the double photon channel. Since this channel has a $\sim 98.8\%$ probability [139], this is a very good approximation. In the center of mass frame of the pion, these two photons are emitted back to back and their distribution can be seen as isotropical. The quadri-vectors P''_{γ_1} and P''_{γ_2} read

$$P''_{\gamma 1} = \frac{m_\pi}{2}(1, \cos\xi \sin\eta, \sin\xi \sin\eta, \cos\eta) \tag{5.3}$$

$$P''_{\gamma 2} = \frac{m_\pi}{2}(1, -\cos\xi \sin\eta, -\sin\xi \sin\eta, -\cos\eta) \tag{5.4}$$

where m_π is the mass of the pion. Note that in this system of coordinates, that I will label as $\{\hat{\mathbf{x}}'', \hat{\mathbf{y}}'', \hat{\mathbf{z}}''\}$, this decay can then be described by the two angles $\{\eta, \xi\}$.

The GEANT4 simulation takes these two quadri-vectors in the laboratory frame as input. I hence still need to boost them in this frame. We have, from Eq. (E.16),

$$P^{\text{lab}}_{\gamma i} = R^u_{\theta'} \Lambda_\pi^{-1} P''_{\gamma i} \tag{5.5}$$

where $R^u_{\theta'}$ and Λ_π^{-1} are rotation and boost matrices dependent on $\{\theta, \phi\}$ and defined in App. E. Note that this transformation is done in a "perfect picture" where the photon beam is perfectly collimated, infinitely thin and the target consists of a single nucleus at the center of the Crystal Ball, which I define as the origin of the laboratory axes $\{\hat{\mathbf{x}}, \hat{\mathbf{y}}, \hat{\mathbf{z}}\}$. If I add the angles $\{\theta, \phi\}$ in which the pion is photo-produced and the energy of the incident photon T_γ, I only need five numbers to describe each photoproduction event: $\{\theta, \phi, \eta, \xi, T_\gamma\}$.

Of course, we are not in the ideal situation where the incident photon is purely oriented in the direction $\hat{\mathbf{z}}$. If the incident photon propagates along the direction $\vec{1}_{p_z} = (\cos\varphi \sin\vartheta, \sin\varphi \sin\vartheta, \cos\vartheta)$, this needs to be taken into account. For this, the frame described above has to be rotated along the unit vector $\hat{\vec{w}} = (-\sin\varphi, \cos\varphi, 0)$ by an angle ϑ. In the end, we have

$$P^{\text{lab}}_{\gamma i} = R^w_\vartheta R^u_{\theta'} \Lambda_\pi^{-1} P''_{\gamma i} \tag{5.6}$$

and the pair of angles $\{\vartheta, \varphi\}$ needs to be added to the list of variables.

Finally, let me note that the incident photon does not always interact at the origin of the lab frame. The photon beam has a width and can interact in the entirety of the target, which is of course, not a single nucleus and hence has a thickness. However, this does not change anything to the quadri-vectors of the photons. It's only a translation of the vertex. It will however change the place where the photons are detected in the detector. This can be taken into account just by adding a vertex (X, Y, Z) distributed accordingly to the beam specifications.

To the five variables $\{\theta, \phi, \eta, \xi, T_\gamma\}$ of the "perfect picture", the two angles $\{\vartheta, \varphi\}$ and the three distances $\{X, Y, Z\}$ to describe each photo-production event need to be added.

5.2.1 Random number distributions

Each photo-production event is generated by drawing independently the ten variables $\{\theta, \phi, \eta, \xi, T_\gamma, \vartheta, \varphi, X, Y, Z\}$. The distributions of each of these variables are listed in this section. Note that in the following, I will generate the random numbers from an uniformly distributed distribution. These will then be transformed such as to reproduce any desired distribution. Let me thus define u and v as random numbers distributed uniformly on $[0, 1]$.

Isotropic decay

As we have seen, in the system of coordinates of the center of mass frame of the pion $\{\hat{\mathbf{x}}'', \hat{\mathbf{y}}'', \hat{\mathbf{z}}''\}$, the two photons decay isotropically into the back-to-back directions $\pm\vec{p}_{\gamma 1}$

$$\vec{p}_{\gamma 1} = (\cos\xi \sin\eta, \sin\xi \sin\eta, \cos\eta) \tag{5.7}$$

Each pion decay can thus be described by the pair of angles $\{\eta, \xi\}$. The angle ξ is uniformly distributed over $[0, 2\pi]$ while η is distributed as a sine. If I use the *inversion method* to draw η (see App. F), we have

$$\eta = \arccos(2u - 1) \tag{5.8}$$
$$\xi = 2\pi v \tag{5.9}$$

In Fig. 5.5, the result of $N = 10000$ random draws for ξ and η is displayed.

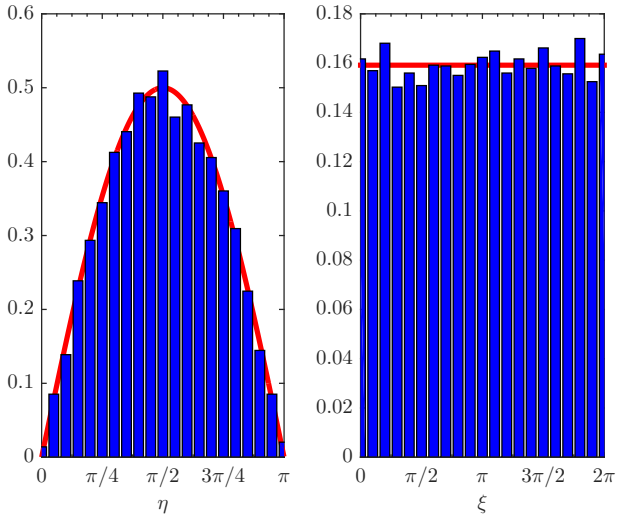

Figure 5.5: ξ and η angles ($N = 10000$) and their distribution in the limit of an infinite number of events in red.

Pion photo-production

Each photo-production event can be described by the energy of the initial photon T_γ and the pair of angles $\{\theta, \phi\}$ of the emitted pion, where θ is the scattering angle and ϕ is the azimutal angle. The distribution that the angles follow is simply the photo-production differential cross section $d\sigma/d\Omega$. In this particular process, this distribution depends solely on θ for symmetry reasons and hence ϕ is distributed uniformly, like ξ above, and can hence be picked such as in Eq. (5.9).

$$\phi = 2\pi v \tag{5.10}$$

The scattering angle θ is distributed as the normalised differential cross section $d\sigma/d\Omega$. In the center-of-mass reference frame of the π-A system, this cross section can be calculated numerically for any given energy and target (see Sec. 9). In the left panel of Fig. 5.6, the

result of drawing $N = 10000$ random angles with the *inversion method* (see App. F) is shown.

In the reactions I am interested in, the energy of the photon T_γ is in the range $[E_0, E_0 + \Delta E]$. These photons are created by bremsstrahlung and their energy distribution has a $1/E$ profile [144]. The right panel of Fig. 5.6 shows the result of $N = 10000$ random draws for T_γ in the bin $[180, 240]$ MeV by also using the *inversion method*.

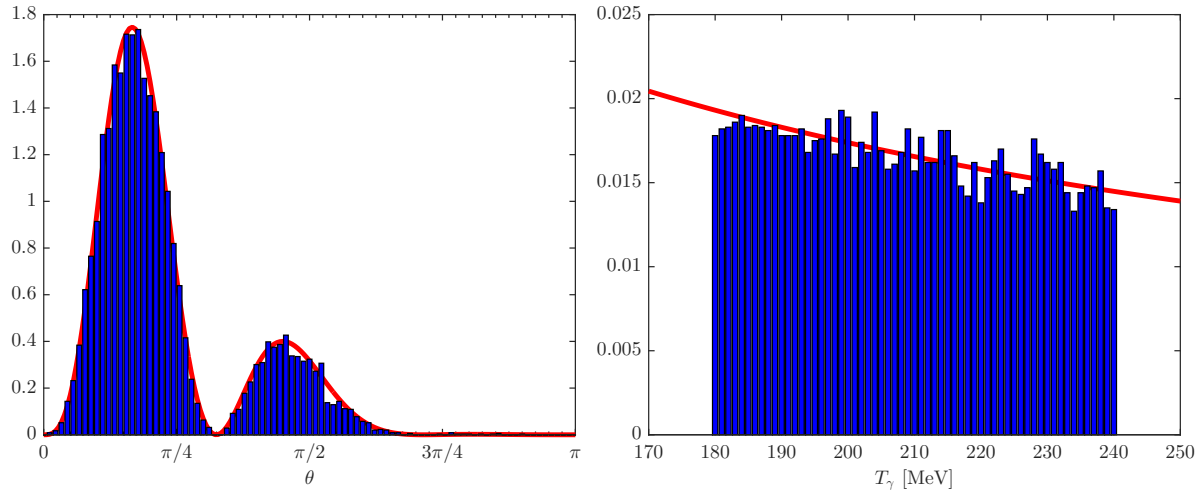

Figure 5.6: Random number generated distribution for the scattering angle θ (left panel) and energy of the incident photon T_γ (right panel) for $N = 10000$ events. In red are the normalised differential cross section (left) and $1/E$ profile (right) which correspond to how these numbers are distributed.

Initial direction of the photon and position of the vertex

As I have said, the photon could be in a direction slightly different than a pure $\hat{\mathbf{z}}$ beam. We could define the direction of the photon as

$$\vec{1}_{p_z} = (\cos\varphi \sin\vartheta, \sin\varphi \sin\vartheta, \cos\vartheta) \tag{5.11}$$

$$= (p_x, p_y, p_z) \tag{5.12}$$

where $\cos\vartheta$ is close to 1. As it can be seen, this direction depends on the pair of angles $\{\vartheta, \varphi\}$. As φ is distributed uniformly, we simply have

$$\varphi = 2\pi v \tag{5.13}$$

The z component of the momentum $p_z = \cos\vartheta$ has been shown to follow a normal distribution of mean $\mu = 1$ and standard deviation $\sigma = 10^{-6}$ but limited to the range $[1 - 2.5\sigma, 1]$ [from discussions with Maria]. We can apply Box-Muller transforms [145] to our uniformly distributed random number u (see App. F) to generate the right distribution for p_z and hence ϑ. The result of $N = 10000$ random draws for $\cos\vartheta$ is shown on the left panel of Fig. 5.7.

In addition to the beam not being perfectly oriented in the $\hat{\mathbf{z}}$ direction, the target is not a single nucleus at the center of the detector. The finite size of the target is modelled by the random numbers $\{X, Y, Z\}$ that represent the position of the vertex inside the target.

The target is considered as a rectangle parallelepiped shape with a thickness of 0.2 cm following axis $\hat{\mathbf{z}}$, and with a height and a length of both 2 cm [private communications with Maria]. We consider the beam to be of Gaussian shape along the $\hat{\mathbf{x}}$ and $\hat{\mathbf{y}}$ axis centered around the origin and of standard deviation $\sigma = 0.5$ cm. If we assume that the photon can interact with uniform probability through the whole thickness of the target, Z simply follows a uniform distribution

$$Z = 0.2\,(2u - 1) \tag{5.14}$$

while X and Y are distributed as a Gaussian and can be generated through Box-Muller transforms [145]. The distribution for $N = 10000$ random choices is shown on the right panel of Fig. 5.7.

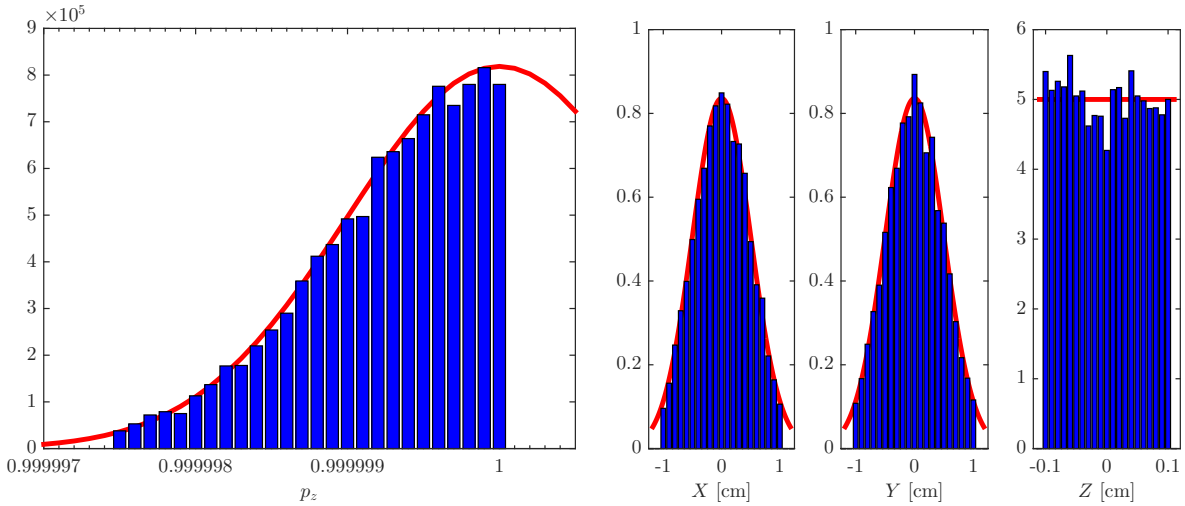

Figure 5.7: Result of $N = 10000$ generated $p_z = \cos\vartheta$ (left) and $\{X, Y, Z\}$ interaction vertices (right) and their respective distribution in red.

6 Nuclear densities

As already discussed in Sec. 4.4, the cross section of coherent neutral-pion photoproduction is a promising observable to study the neutron skin thickness of nuclei and several experiments have been or are being carried on to extract it. As I will discuss in the following sections, this process can involve several-nucleon processes. In the energy region of the experiments considered in this work, one-nucleon and two-nucleon processes are sufficient to describe most of the features of photoproduction cross sections.

In order to study the sensitivity of this observable to the neutron skin thickness and quantify the uncertainties that surround its extraction, it is important to investigate how sensitive it is to the target nucleus model. For one- and two-nucleon processes, the relevant properties of the nucleus are encapsulated in one- and two-nucleon densities, which are the subject of this section.

First, I will properly define these nuclear densities. These will be used throughout the next sections. Most of this section can be found in more details in Refs. [146, 147]. Second, I will describe several different models to calculate these objects. This will allow me to study the model dependence of the extraction of the neutron skin thickness as well as providing with an upper bound on the precision of eventual future experiments.

I will consider six different nuclei in this work: ^{208}Pb, which is studied in the experiment of Ref. [132], ^{116}Sn and ^{124}Sn which are studied in the recent experiment of M. Ferretti [137] and ^{48}Ca [138], which is currently analysed. Additionally, I will consider ^{12}C and ^{40}Ca. While for these nuclei $N = Z$ and the neutron skin is hence nearly non-existent, calculations on these nuclei will allow me to test my model on the data of Krusche *et al.* [129].

6.1 One- and two-nucleon densities

In coordinate space and for A nucleons, the one- and two-nucleon densities can be written respectively as

$$\rho_1(x_1|x_1') = A \sum_{\sigma_2 \dots \sigma_A} \sum_{\tau_2 \dots \tau_A} \int \left(\prod_{i=2}^{A} d\vec{r}_i \right) \Phi^\dagger(x_1', x_2, \dots, x_A) \Phi(x_1, x_2, \dots, x_A) \tag{6.1}$$

and

$$\rho_2(x_1, x_2|x_1', x_2') = A(A-1) \sum_{\sigma_3 \dots \sigma_A} \sum_{\tau_3 \dots \tau_A} \int \left(\prod_{i=3}^{A} d\vec{r}_i \right) \Phi^\dagger(x_1', x_2', x_3, \dots, x_A) \Phi(x_1, x_2, x_3, \dots, x_A) \tag{6.2}$$

where x_i is short for $\{\vec{r}_i, \sigma_i, \tau_i\}$, the position, spin and isospin of each nucleon. Here, $\Phi(x_1, \dots, x_A)$ is the A-body wave function of the nucleus. The spin-isospin sum of these matrices can be seen as the one- and two-nucleon density distributions in coordinate space

$$\rho_1(\vec{r}_1|\vec{r}_1') = \sum_{\sigma_1, \sigma_1'} \sum_{\tau_1, \tau_1'} \rho_1(x_1|x_1') \tag{6.3}$$

$$\rho_2(\vec{r}_1, \vec{r}_2|\vec{r}_1', \vec{r}_2') = \sum_{\sigma_{1,2}, \sigma_{1,2}'} \sum_{\tau_{1,2}, \tau_{1,2}'} \rho_2(x_1, x_2|x_1', x_2') \tag{6.4}$$

Of special importance are the diagonal parts of these densities

$$\rho_1(\vec{r}_1) = \rho_1(\vec{r}_1|\vec{r}_1) = \sum_{\substack{\sigma_1 \\ \sigma_1=\sigma_1'}} \sum_{\substack{\tau_1 \\ \tau_1=\tau_1'}} \rho_1(x_1|x_1) \tag{6.5}$$

$$\rho_2(\vec{r}_1,\vec{r}_2) = \rho_2(\vec{r}_1,\vec{r}_2|\vec{r}_1,\vec{r}_2) = \sum_{\substack{\sigma_{1,2} \\ \sigma_{1,2}=\sigma_{1,2}'}} \sum_{\substack{\tau_{1,2} \\ \tau_{1,2}=\tau_{1,2}'}} \rho_2(x_1,x_2|x_1,x_2) \tag{6.6}$$

They represent the probability to find one nucleon at position $\vec{r}_1$ and two nucleons at positions $\vec{r}_1$ and $\vec{r}_2$ simultaneously, respectively. Note that they are normalised to A and $A(A-1)$, respectively. We can separate the neutron and proton contributions to this density by projecting on the corresponding isospin. For the one-nucleon densities for example, the neutron and proton densities respectively read

$$\rho_1^N(\vec{r}_1) = \sum_{\sigma_1} \rho_1(x_1)\Big|_{\tau_1=-\frac{1}{2}} \tag{6.7}$$

$$\rho_1^Z(\vec{r}_1) = \sum_{\sigma_1} \rho_1(x_1)\Big|_{\tau_1=+\frac{1}{2}} \tag{6.8}$$

They are normalised to N and Z, the number of neutrons and protons, respectively. These can be used to define the neutron skin thickness. For spherically symmetric nuclei, Eq. (4) then reads

$$\Delta r_{np} = \sqrt{\frac{4\pi}{N}\int_0^\infty r^4 \rho_1^N(r) dr} - \sqrt{\frac{4\pi}{Z}\int_0^\infty r^4 \rho_1^Z(r) dr}. \tag{6.9}$$

Of special interest are also the momentum space counter-parts of these quantities, which are defined as

$$\hat{\rho}_1(\vec{q}_1) = \int d\vec{r}_1 e^{i\vec{q}_1\cdot\vec{r}_1} \rho_1(\vec{r}_1) \tag{6.10}$$

$$\hat{\rho}_2(\vec{q}_1,\vec{q}_2) = \int d\vec{r}_1 d\vec{r}_2 e^{i\vec{q}_1\cdot\vec{r}_1} e^{i\vec{q}_2\cdot\vec{r}_2} \rho_2(\vec{r}_1,\vec{r}_2) \tag{6.11}$$

Because of our choice of normalisation in Eqs. (6.1) and Eqs. (6.2), their values at $q_1 = 0$ and at $q_1 = q_2 = 0$ should also be A and $A(A-1)$, respectively.

There are different strategies to obtain these densities. On the one hand, one can directly compute Eqs. (6.1) and (6.2) from the wave functions of the nucleus. These can be obtained for example from mean field or shell model calculations, where the constituting nucleons of the nucleus are subject to a given potential. On the other hand, a simpler solution is to assume some given phenomenological shape. Both these approaches are presented hereafter.

6.2 Mean field and shell model calculations

In mean field and shell model calculations, we consider the nucleons to be subject to a common average field which is produced by the nucleons themselves. In both models, the nucleons inside the nucleus can be seen as moving independently from the others. They are then found in single-particle states.

It is convenient to express the wave-function of the nucleus as a Slater determinant, which naturally satisfies the antisymmetric properties of this fermionic system. The wave function of the nucleus then reads

$$\Phi(x_1,\ldots,x_A) = \frac{1}{\sqrt{A!}}\det\{\psi_{\alpha_i}(\vec{r}_j)\} \tag{6.12}$$

where $\psi_{\alpha_i}(\vec{r}_i)$ are the single-particle states wave function of quantum numbers α_i. The one- and two-nucleon density matrices then respectively read

$$\rho_1(x_1|x_1') = \sum_{i=1}^{A} \psi_{\alpha_i}^\dagger(\vec{r}_1')\psi_{\alpha_i}(\vec{r}_1) \tag{6.13}$$

and

$$\rho_2(x_1, x_2|x_1', x_2') = \sum_{i,j=1}^{A} \left[\psi_{\alpha_i}^\dagger(\vec{r}_1')\psi_{\alpha_j}^\dagger(\vec{r}_2')\psi_{\alpha_i}(\vec{r}_1)\psi_{\alpha_j}(\vec{r}_2) - \psi_{\alpha_i}^\dagger(\vec{r}_1')\psi_{\alpha_j}^\dagger(\vec{r}_2')\psi_{\alpha_i}(\vec{r}_2)\psi_{\alpha_j}(\vec{r}_1)\right] \tag{6.14}$$

$$= \rho_1(x_1|x_1')\rho_1(x_2|x_2') - \rho_1(x_1|x_2')\rho_1(x_2|x_1') \tag{6.15}$$

Note that the two-nucleon density matrix is completely determined by the one-nucleon density matrix. Moreover, the last term of the right hand side is the only one to contribute to exchange effects, i.e. two-body processes where a pair of nucleons exchange their quantum numbers [147].

Let us particularise Eq. (6.5) in both the Florida State University (FSU), which is a mean field model, and in the HO shell model.

6.2.1 Relativistic mean-field calculations (FSU model)

In mean field calculations, the common average field in which the nucleon evolve is calculated from some ansatz on the nucleon wave functions. The field then acts retroactively on these wave functions, which in turn modify the field. The process is repeated iteratively and when (if) convergence is achieved, it finally provides with the wave functions of the nucleons and thus the nucleus [148]. In heavy nuclei which are composed of a large number of nucleons, the assumption that the nucleons evolve in a common average field is a good approximation.

Note that since the movement of the nucleons is relativistic for these nuclei, their description requires a consistent framework that would include these relativistic effects. Relativistic mean-field (RMF) models treat the nuclear systems microscopically by using hadronic (baryon and meson) degrees of freedom phenomenologically. They are usually based on a Lorentz-invariant Lagrangian density and contain only few constants such as meson masses and meson-nucleon coupling strength parameters [149]. The details of such models and their formalism is beyond the scope of this work and the interested reader is referred to Ref. [150] and the references therein for more information.

In Ref. [151], B. G. Todd-Rutel and J. Piekarewicz have introduced the Florida State University model (FSU). By introducing nonlinear couplings between the isoscalar and the isovector mesons they are able to modify the neutron skin thickness of heavy nuclei without changing their isoscalar properties, which are well constrained experimentally. The field equations resulting from this Lagrangian are then solved in the mean-field limit by replacing the meson fields as well as the baryon sources by their expectation values (see Ref. [152] for the details). Single-particle solutions of the Dirac equation are then found and may be written as

$$\psi_{n\varkappa m\tau}(\vec{r}) = \frac{1}{r}\begin{pmatrix} g_{n\varkappa\tau}(r)\mathcal{Y}_{+\varkappa m}(\hat{\vec{r}}) \\ if_{n\varkappa\tau}(r)\mathcal{Y}_{-\varkappa m}(\hat{\vec{r}}) \end{pmatrix}\eta(\tau) \tag{6.16}$$

where n is the principal quantum number. The functions $\mathcal{Y}_{+\varkappa m}$ are spin-spherical harmonics of magnetic quantum number m and generalised angular momentum $\varkappa$. They are defined as

$$\mathcal{Y}_{+\varkappa m}(\hat{\vec{r}}) \equiv [Y_l(\hat{\vec{r}}) \otimes \chi_{1/2}]_{j_\varkappa m} \qquad \text{with} \qquad \begin{cases} j_\varkappa = |\varkappa| - 1/2 \\ l = \begin{cases} \varkappa & \text{if } \varkappa > 0 \\ -1 - \varkappa & \text{if } \varkappa < 0 \end{cases} \end{cases} \tag{6.17}$$

The bound-state wave functions g and f can then be used to compute the one-nucleon densities such that

$$\rho_1(r) = \sum_{n\varkappa}^{\text{occ}} \left(\frac{2j_\varkappa + 1}{4\pi r^2} \right) [g^2_{n\varkappa t}(r) + f^2_{n\varkappa t}(r)] \tag{6.18}$$

I will use densities calculated in this formalism for ^{40}Ca, ^{48}Ca, ^{116}Sn, ^{124}Sn and ^{208}Pb. For all these nuclei, I will study the influence of the skin thickness on the photoproduction cross section. In this perspective, for each of these nuclei, I have been provided with five different densities predicting each a different skin thickness. These were calibrated using various different values of the parameters of the nonlinear couplings of the Lagrangian. They hence correspond to assumed values for the unknown neutron skin thickness of ^{208}Pb. They will be referred to as FSUxxx, with xxx the value of the isoscalar-isovector mixed meson coupling parameter.

I thank Jorge Piekarewicz for sharing with me his calculations.

6.2.2 Shell model and harmonic oscillator

In shell model calculations, the mean field is chosen with some given shape. Among the several different shapes that exist, the harmonic oscillator (HO) has often been used because of its simplicity. Indeed, it has the advantage that the wave functions of the nucleons are analytical and so is the wave function of the nucleus. Note however that the HO reproduces only a few of the magic numbers in the nuclear chart, i.e. the magic numbers of light nuclei. For lighter nuclei, with few nucleons, the mean-field approximation is not as justifiable. It is nonetheless interesting to consider this description because of its simplicity. For these light nuclei, relativistic effects are not as predominant and they can be neglected. Note that I will use densities calculated in this formalism for ^{12}C only.

In the harmonic oscillator shell model, the potential is spherically symmetric. The wave functions $\psi_{\alpha_i}(\vec{r}_i)$ can be written in the form

$$\psi_{\alpha_i}(\vec{r}_i) = \varphi_{n_i l_i m_i}(\vec{r}_i)\chi(\sigma_i)\eta(\tau_i) \tag{6.19}$$

where $\varphi_{n_i l_i m_i}$ is the position part of the wave-function and χ and η the spin and isospin parts. The collection of quantum numbers that characterizes the state of the nucleon α_i are then n_i, the principal quantum number, l_i, the orbital angular momentum quantum number and its projection m_i as well as σ_i and τ_i for the spin and isospin of the nucleon, respectively.

Analytical expressions for the wave functions are easily obtained. In this model, the position part of the nucleon wave-functions (6.19) are given by

$$\varphi_{nlm}(\vec{r}) = R_{nl}(r/a)Y_{lm}(\theta, \varphi) \tag{6.20}$$

where a is the harmonic oscillator parameter and Y_{lm} are the spherical harmonics. The radial part reads

$$R_{nl}(r) = \frac{1}{a^{3/2}}\sqrt{\frac{2n!}{\Gamma(n+l+3/2)}} r^l e^{-\frac{1}{2}r^2} L_n^{l+1/2}(r^2) \tag{6.21}$$

where Γ is the gamma function and $L_n^l(r)$ are the Laguerre polynomials [51].

In the particular case of closed-shell $N = Z = A/2$ nuclei (such as ^{16}O or ^{40}Ca) the one-nucleon density distribution (6.5) in the position space is easily obtained. For these nuclei, the summation on spins and isospins of Eq. (6.13) simply adds a factor 4 and we can then show that it acquires the simple form

$$\rho_1(\vec{r}_1|\vec{r}_1') = 4\sum_i^A \varphi^*_{n_i l_i m_i}(\vec{r}_1')\varphi_{n_i l_i m_i}(\vec{r}_1) \tag{6.22}$$

It should be noted that the ^{12}C nucleus does not fall in the category of closed-shell nuclei however. Indeed, it has its $0s_{1/2}$ and $0p_{3/2}$ shells closed but the $0p_{1/2}$ one remains open. This expression is hence not correct and a proper sum on spins is needed. We can show that the off-diagonal one-nucleon density distribution reads

$$\rho_1(\vec{r}_1|\vec{r}_1') = \frac{4}{\pi^{3/2}a^3}\left[1 + \frac{4}{3}\frac{\vec{r}_1\cdot\vec{r}_1'}{a^2}\right] e^{-\frac{r_1^2+r_1'^2}{2a^2}} \tag{6.23}$$

In the momentum space, the diagonal part then reads

$$\hat{\rho}_1(\vec{q}_1) = \left(12 - \frac{4}{3}a^2q_1^2\right) e^{-\frac{1}{4}a^2q_1^2} \tag{6.24}$$

6.3 Phenomenological and experimental densities

The RMF calculations and the HO shell model ones have the advantage of providing us with the wave-functions of the nucleus. As we will see later, these are needed to build the potential between the impinging particle and the nucleus. At the first order however, only the diagonal part of the one-nucleon density is needed. It is then interesting to resort to densities which shape are built phenomenologically. I will consider two different types of these: the Fermi-Dirac shape densities and the experimental densities, built from a Fourier-Bessel analysis of electron-scattering experiments.

6.3.1 Fermi-Dirac shape (São-Paulo group)

As their name implies, the Fermi-Dirac densities have the shape of a Fermi-Dirac function (see Eq. (3)). This shape is sufficiently simple so that the influence to some of their properties (asymptotic behaviour, neutron skin thickness, etc.) can be tested very easily.

In Ref. [153], an extensive systematisation of proton and neutron densities has been performed by analysing charge distributions extracted from electron scattering experiments as well as theoretical densities derived from mean field models. The proton and neutron densities are then defined as

$$\rho_1^Z(r) \propto \frac{1}{1+\exp\left(\frac{r-R_{0Z}}{a_Z}\right)} \quad \text{and} \quad \rho_1^N(r) \propto \frac{1}{1+\exp\left(\frac{r-R_{0N}}{a_N}\right)} \tag{6.25}$$

which are normalised to Z and N respectively and where the radii and diffusenesses are given by

$$\begin{cases} R_{0Z} = 1.81Z^{1/3} - 1.12 \\ R_{0N} = 1.49N^{1/3} - 0.79 \end{cases} \quad \text{and} \quad \begin{cases} a_Z = 0.47 - 0.00083Z \\ a_N = 0.47 + 0.00046N \end{cases} \tag{6.26}$$

I will refer to these densities as the São Paulo densities (SP).

Note that in this work, instead of the usual Fermi-Dirac shapes, I will rather use the symmetrised form of the Fermi-Dirac shape, which reads

$$\rho_1(r) = \frac{3A}{4\pi R(R^2+\pi^2a^2)}\left[\frac{1}{\exp((r-R)/a)+1} + \frac{1}{\exp(-(r+R)/a)+1} - 1\right], \tag{6.27}$$

$$= \frac{3A}{4\pi R(R^2+\pi^2a^2)}\frac{\sinh(R/a)}{\cosh(r/a)+\cosh(R/a)}, \tag{6.28}$$

This shape has the advantage of being almost indistinguishable from the usual Fermi-Dirac shape while having an analytical Fourier transform which reads

$$\hat{\rho}_1(q) = \frac{3A}{4\pi R(R^2+\pi^2a^2)}\frac{4\pi}{q}\frac{\pi a}{\sinh(\pi qa)}\left[\frac{\pi a\sin(qR)}{\tanh(\pi qa)} - R\cos(qR)\right]. \tag{6.29}$$

These densities can be used for any nucleus, such as ^{12}C, ^{40}Ca, ^{48}Ca, ^{124}Sn and ^{208}Pb.

6.3.2 Experimental density

In this type of densities, the charge density is given as an expansion on spherical Bessel functions. This expansion is model independent and was first used to parametrise the charge distributions in Ref. [154] from electron scattering data.

Charge densities are expanded over a finite domain $[0, R_B]$ and take the form

$$\rho_1^{\text{ch}}(r) = \theta(R_B - r)\sum_{n=1}^{\infty} a_n j_0(q_n r) \tag{6.30}$$

where j_0 is the spherical Bessel functions of zeroth order [51] and $q_n = n\pi/R_B$, where R_B is the truncation radius. The coefficients a_n are then fitted to experiment. Note that this means the Fourier transform of the charge density is analytical and reads

$$\hat{\rho}_1^{\text{ch}}(q) = 4\pi\frac{\sin(qR_B)}{q}\sum_{n=1}^{\infty} a_n\frac{(-1)^n}{q^2-q_n^2} \tag{6.31}$$

In [Atomic data and nuclear data tables 36, 495-536], the charge density Fourier transform measured from several electron-scattering experiments on different nuclei has been parametrised with such an expansion. In Tab. II.1, the coefficients a_n of this Fourier-Bessel analysis (FB) are displayed for ^{12}C and ^{40}Ca nuclei. Note that for both nuclei, the truncation radius is $R_B = 8$ fm.

It should be noted however that only charge densities are available from electron scattering experiments. These still need to be converted to nucleon densities. This can be achieved either by considering that the nucleons are pointlike particles and that the charge densities are equivalent to nucleon densities, or in a less crude way by considering that the proton and neutron have a charge form factor G_p and G_n, respectively. Following

Table II.1: Coefficients of the Fourier-Bessel expansion for ^{12}C and ^{40}Ca charge density

	^{12}C	^{40}Ca		^{12}C	^{40}Ca
a_1	0.15721 10^{-1}	0.44846 10^{-1}	a_9	-0.63568 10^{-3}	-0.39346 10^{-3}
a_2	0.38732 10^{-1}	0.61326 10^{-1}	a_{10}	0.71809 10^{-4}	0.20338 10^{-3}
a_3	0.36808 10^{-1}	-0.16818 10^{-2}	a_{11}	0.18441 10^{-3}	0.25461 10^{-4}
a_4	0.14671 10^{-1}	-0.26217 10^{-1}	a_{12}	0.75066 10^{-4}	-0.17794 10^{-4}
a_5	-0.43277 10^{-2}	-0.29725 10^{-2}	a_{13}	0.51069 10^{-4}	0.67394 10^{-5}
a_6	-0.97752 10^{-2}	0.85534 10^{-2}	a_{14}	0.14308 10^{-4}	-0.21033 10^{-5}
a_7	-0.68908 10^{-2}	0.35322 10^{-2}	a_{15}	0.23170 10^{-5}	–
a_8	-0.27631 10^{-2}	-0.48258 10^{-3}	a_{16}	0.68465 10^{-6}	–

Chandra and Sauer [Phys Rev C13, 245], we can parametrise the proton form factor as a superposition of three Gaussians

$$G_p(q) = 0.506e^{-\frac{0.657^2q^2}{4}} + 0.328e^{-\frac{0.373^2q^2}{4}} + 0.166e^{-\frac{1.235^2q^2}{4}} \tag{6.32}$$

and the neutron form factor as

$$G_n(q) = e^{-\frac{0.685^2q^2}{4}} - e^{-\frac{0.739^2q^2}{4}} \tag{6.33}$$

The Fourier form factor of the nucleon densities are then given as

$$\hat{\rho}_1(q) = \frac{\hat{\rho}_1^{\text{ch}}(q)}{G_p(q) + G_n(q)} \tag{6.34}$$

The densities that consider this form factor renormalisation will be referred to with the acronym *chFF*. Finally, because these two nuclei have an equal number of neutrons and protons $N = Z$, are light and stable, I will consider the neutron and proton distributions to be equal.

6.4 Removal of the center-of-mass motion

It is useful to remove the motion of the nucleus in the reference frame of the reaction we consider. Indeed, in the next sections, we will consider the interaction of a photon or a pion with a nucleus. In the γ-nucleus or π-nucleus centre-of-mass frame, if we denote the momentum of the impinging particle with $\vec{k}^{(\prime)}$ before (after) the reaction, the momentum of the nucleus is then correspondingly given by $-\vec{k}^{(\prime)}$. Let us define the Jacobi coordinates as

$$\begin{cases} \vec{\xi}_{A-1} = \vec{r}_A - \vec{r}_{A-1} \\ \vec{\xi}_{A-2} = \dfrac{\vec{r}_A + \vec{r}_{A-1}}{2} - \vec{r}_{A-2} \\ \quad \vdots \\ \vec{\xi}_2 = \dfrac{\vec{r}_A + \vec{r}_{A-1} + \cdots + \vec{r}_3}{A-2} - \vec{r}_2 \\ \vec{\xi}_1 = \dfrac{\vec{r}_A + \vec{r}_{A-1} + \cdots + \vec{r}_2}{A-1} - \vec{r}_1 \end{cases} \tag{6.35}$$

The Jacobian of such transformation is just 1. These coordinates correspond to the internal degrees of freedom inside the nucleus. If we are interested in one-nucleon processes, we can also define

$$\vec{\xi} = \frac{\vec{r}_2 + \vec{r}_3 + \cdots + \vec{r}_A}{A-1} \tag{6.36}$$

such that

$$\begin{cases} \vec{\xi} - \vec{\xi}_1/A = \dfrac{\sum_{i=1}^{A} \vec{r}_i}{A} \\ \vec{r}_1 = \vec{\xi} - \vec{\xi}_1 \end{cases} \tag{6.37}$$

where $\sum_{i=1}^{A} \vec{r}_i/A$ is the position of the nucleus centre of mass. This allows us to factorise the centre-of-mass motion and write

$$\begin{cases} \Phi_0(x_1, x_2, \ldots, x_A) = e^{-i\vec{k}(\vec{\xi}-\vec{\xi}_1/A)} \phi_{0;\sigma_1\sigma_{2\ldots A};\tau_1\tau_{2\ldots A}}(\vec{\xi}_1, \vec{\xi}_2, \ldots, \vec{\xi}_{A-1}) \\ \Phi_0^\dagger(x'_1, x_2, \ldots, x_A) = e^{+i\vec{k}'(\vec{\xi}-\vec{\xi}'_1/A)} \phi^\dagger_{0;\sigma'_1\sigma_{2\ldots A};\tau'_1\tau_{2\ldots A}}(\vec{\xi}'_1, \vec{\xi}_2, \ldots, \vec{\xi}_{A-1}) \end{cases} \tag{6.38}$$

where $\phi_{0;\sigma_1\sigma_{2\ldots A};\tau_1\tau_{2\ldots A}}$ are the inner wave functions of the nucleus. If instead we are interested in two-nucleon processes, we rather define

$$\vec{\zeta} = \frac{\vec{r}_3 + \vec{r}_4 + \cdots + \vec{r}_A}{A-2} \tag{6.39}$$

such that

$$\begin{cases} \vec{\zeta} - \vec{\xi}_1/A - \vec{\xi}_2/(A-1) = \dfrac{\sum_{i=1}^{A} \vec{r}_i}{A} \\ \vec{r}_1 = \vec{\zeta} - \vec{\xi}_1 - \vec{\xi}_2/(A-1) \\ \vec{r}_2 = \vec{\zeta} - \vec{\xi}_2 \end{cases} \tag{6.40}$$

and which allows us to write

$$\begin{cases} \Phi_0(x_1, x_2, x_3, \ldots, x_A) = e^{-i\vec{k}(\vec{\zeta}-\vec{\xi}_1/A-\vec{\xi}_2/(A-1))} \phi_{0;\sigma_1\sigma_2\sigma_{3\ldots A};\tau_1\tau_2\tau_{3\ldots A}}(\vec{\xi}_1, \vec{\xi}_2, \vec{\xi}_3, \ldots, \vec{\xi}_{A-1}) \\ \Phi_0^\dagger(x'_1, x'_2, x_3, \ldots, x_A) = e^{+i\vec{k}'(\vec{\zeta}-\vec{\xi}'_1/A-\vec{\xi}'_2/(A-1))} \phi^\dagger_{0;\sigma'_1\sigma'_2\sigma_{3\ldots A};\tau'_1\tau'_2\tau_{3\ldots A}}(\vec{\xi}'_1, \vec{\xi}'_2, \vec{\xi}_3, \ldots, \vec{\xi}_{A-1}) \end{cases} \tag{6.41}$$

In both cases, we are then left with an inner wave function that depends only on the internal coordinates $\vec{\xi}_i$ and a plane wave term representing the centre-of-mass motion of the nucleus. Very similarly to Eqs. (6.1) and (6.2), we can define densities from these internal wave functions such as

$$\rho_1(\tilde{x}_1|\tilde{x}'_1) = A \sum_{\sigma_2\ldots\sigma_A} \sum_{\tau_2\ldots\tau_A} \int \left(\prod_{i=2}^{A-1} d\vec{\xi}_i \right) \phi^\dagger_{0;\sigma'_1\sigma_{2\ldots A};\tau'_1\tau_{2\ldots A}}(\vec{\xi}'_1, \vec{\xi}_2, \ldots, \vec{\xi}_A) \phi_{0;\sigma_1\sigma_{2\ldots A};\tau_1\tau_{2\ldots A}}(\vec{\xi}_1, \vec{\xi}_2, \ldots, \vec{\xi}_A) \tag{6.42}$$

and

$$\rho_2(\tilde{x}_1, \tilde{x}_2|\tilde{x}'_1, \tilde{x}'_2) = A(A-1) \sum_{\sigma_3\ldots\sigma_A} \sum_{\tau_3\ldots\tau_A} \int \left(\prod_{i=3}^{A} d\vec{\xi}_i \right) \phi^\dagger_{0;\sigma'_1\sigma'_2\sigma_{3\ldots A};\tau'_1\tau'_2\tau_{3\ldots A}}(\vec{\xi}'_1, \vec{\xi}'_2, \vec{\xi}_3, \ldots, \vec{\xi}_{A-1}) \phi_{0;\sigma_1\sigma_2\sigma_{3\ldots A};\tau_1\tau_2\tau_{3\ldots A}}(\vec{\xi}_1, \vec{\xi}_2, \vec{\xi}_3, \ldots, \vec{\xi}_{A-1}) \tag{6.43}$$

where $\tilde{x}_i = \{\vec{\xi}_i, \sigma_i, \tau_i\}$. Similarly to Eqs. (6.3) and (6.4), we can define

$$\rho_1(\vec{\xi}_1|\vec{\xi}_1') = \sum_{\sigma_1,\sigma_1'} \sum_{\tau_1,\tau_1'} \rho_1(\tilde{x}_1|\tilde{x}_1') \tag{6.44}$$

$$\rho_2(\vec{\xi}_1,\vec{\xi}_2|\vec{\xi}_1',\vec{\xi}_2') = \sum_{\sigma_{1,2},\sigma_{1,2}'} \sum_{\tau_{1,2},\tau_{1,2}'} \rho_2(\tilde{x}_1,\tilde{x}_2|\tilde{x}_1',\tilde{x}_2') \tag{6.45}$$

where the diagonal parts $\rho_1(\vec{\xi}_1)$ and $\rho_2(\vec{\xi}_1,\vec{\xi}_2)$ correspond to $\tilde{x}_1' = \tilde{x}_1$ and $\tilde{x}_2' = \tilde{x}_2$ similarly to Eqs. (6.5) and (6.6). Their momentum space counter-parts read

$$\hat{\rho}_1(\vec{q}_1) = \int d\vec{\xi}_1 e^{i\vec{q}_1\cdot\vec{\xi}_1} \rho_1(\vec{\xi}_1) \tag{6.46}$$

$$\hat{\rho}_2(\vec{q}_1,\vec{q}_2) = \int d\vec{\xi}_1 d\vec{\xi}_2 e^{i\vec{q}_1\cdot\vec{\xi}_1} e^{i\vec{q}_2\cdot\vec{\xi}_2} \rho_2(\vec{\xi}_1,\vec{\xi}_2) \tag{6.47}$$

and are often referred to as the nuclear form factors. These expressions will become handy later. Note that as we have seen previously, the wave functions are not always available. This means that removing the centre-of-mass motion is not always feasible properly.

It should be noted that additionally to the centre-of-mass motion discussed above and due to the change of reference frame, an additional motion has to be considered when calculating the nuclear wave functions in mean field or in shell model calculations. In these computations, the potential is assumed to have a fixed origin. By convenience, the individual motion of the nucleons are then given relative to the centre of this potential. This is especially true for shell model calculations. In reality, the origin should depend on the mean position of the nucleons and the wave function of the system should thus be a function only of the relative coordinates of the constituent nucleons [155]. In the case of the HO, for example, this causes the centre-of-mass to oscillate unphysically around the origin.

The removal of this motion is not always possible. In the case of the HO however, it is done relatively simply for example with the correction of Tassie and Barker, which can be found in Ref. [156]. For the FSU densities on the contrary, this removal cannot be done in a model-independent way [157]. The São Paulo density and the experimental one intrinsically remove this motion.

In summary, the diagonal part of the nuclear density Eqs. (6.44) and its Fourier transform (6.46) are available for all densities except the RMF ones. Note however that RMF calculations are made only for heavy nuclei. Fortunately, the effect of this correction is smaller as the target becomes heavier [157]. I will thus neglect it for RMF densities.

6.5 Comparison of the different densities

It is interesting to have a look at the different densities to see what are the main differences that exist between them. This will help us pinpoint the main characteristics of the densities that influence the behaviour of the pion photoproduction cross section. This will be particularly handy for the heavier targets.

The ^{12}C nucleon densities are displayed on Fig. 6.1. These are shown for the different models discussed above, i.e. the HO model (dash-dotted) without (black) and with (blue) centre-of-mass correction, the São Paulo model (solid), the FB analysis (dashed) without (black) and with (blue) charge form factor renormalisation. As discussed earlier, for ^{12}C, $\rho_1^N = \rho_1^Z$ for all densities except the São Paulo ones. For this model, the neutron density is shown in red.

On the left panel of Fig. 6.1, these densities are displayed in linear scale. It should be noted how after the centre-of-mass and the charge form factor corrections for the HO and FB densities, respectively, the internal part of the densities are very similar. On the right one, the densities are displayed in log scale. It should be noted that the Fourier Bessel densities become negative past $r = 7$ fm. This does not cause any issue in momentum space however. The HO densities have a very different asymptotic behaviour to the SP ones, as the former have a gaussian decay, while the latter an exponential one.

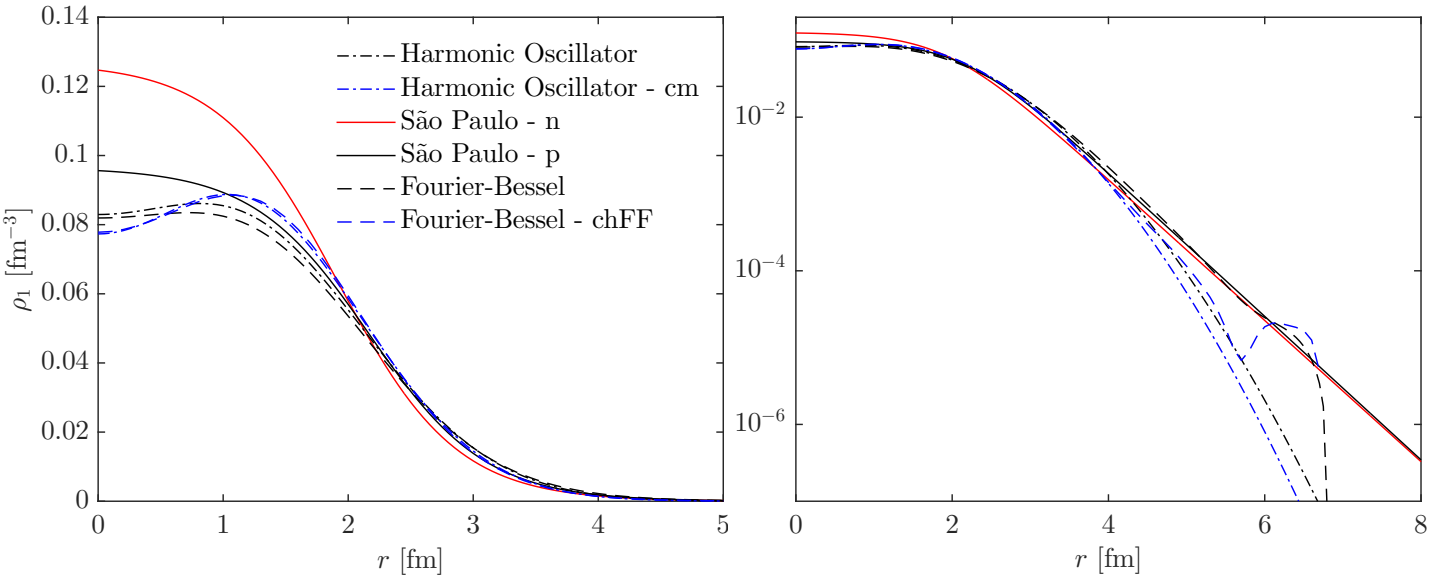

Figure 6.1: ^{12}C nucleon densities. See text for details.

The ^{40}Ca nucleon densities are displayed on Fig. 6.2. These are shown on the left panel for the different models discussed above, i.e. the FSU model (dash-dotted), the São Paulo model (solid), the FB analysis (dashed) without (black) and with (blue) charge form factor renormalisation. As discussed earlier, for ^{40}Ca, $\rho_1^N = \rho_1^Z$ for the Fourier-Bessel analysis but not for the São Paulo and FSU models. The proton densities are shown in black while the neutron ones are shown in red for these two models.

In the sake of conciseness, only one of the FSU densities is displayed on the left panel. Four other FSU densities are shown on the right panel of Fig. 6.2. These are obtained by varying the isoscalar-isovector mixed meson coupling parameter (see Sec. 6.2.1). Note that the blue one is the same density that is displayed on the left panel. The differences between the FSU curves are small, especially in the region $r \sim 3 - 4$ fm. This is also visible on Fig. 6.3, where the FSU densities and the SP ones are displayed in log scale. The exponential decay of the FSU densities are nearly superimposed and no significant changes are visible. What can be seen however is the clearly different asymptotic behaviour of the neutron and proton densities as well as the differences that exist between the SP and FSU densities.

Even though the skin thickness Δr_{np} is expected to be very small and its impact on the pion photoproduction cross section will not be studied on this nucleus, it can be interesting to actually compute it for these densities. Δr_{np} is given in the first line of Tab. II.2 for the densities that exhibit a skin. In this table, it should be noted how the neutron skin thickness is negative for this nucleus. This is to be expected because for

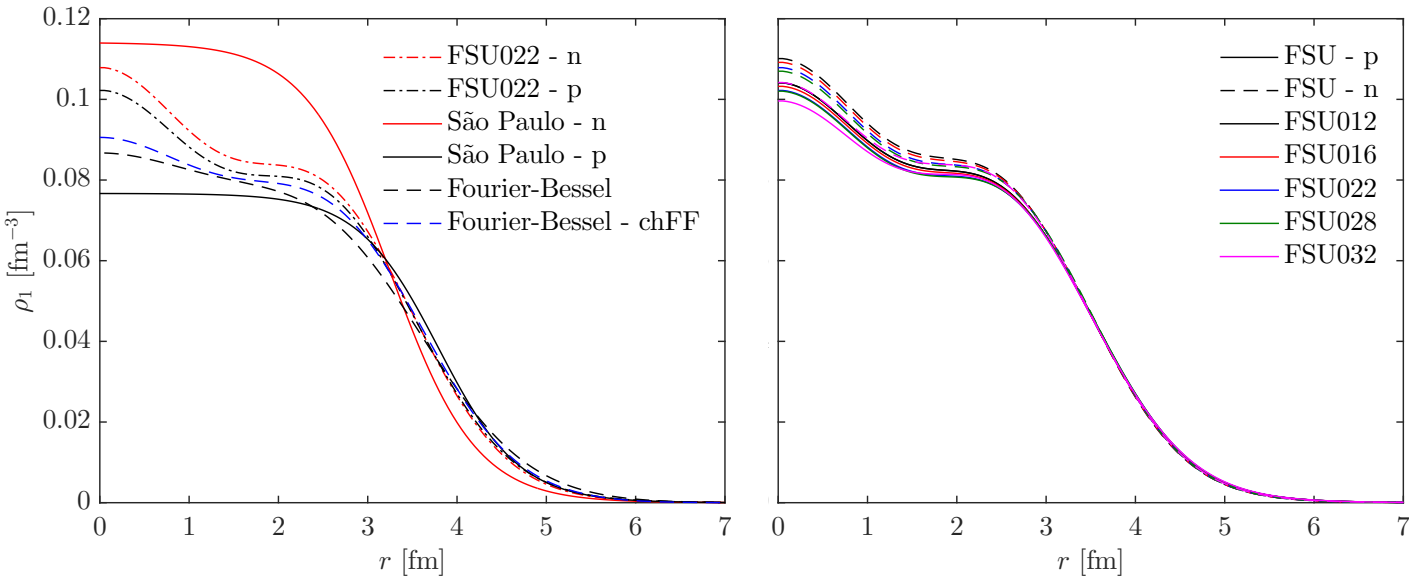

Figure 6.2: ^{40}Ca nucleon densities. See text for details.

$N = Z$ nuclei, the Coulomb interaction pushes the protons out relative to the neutrons. Note however that the neutron skin reproduced by the SP densities is almost a factor 10 larger (or rather... smaller since it is negative) compared to the ones reproduced by FSU, which do not vary much. This thickness is probably not physical but illustrates the differences in Δr_{np} that can be obtained by using a different model. This will help me analyse its influence on the photoproduction cross section later.

Table II.2: Neutron skin thicknesses for the different densities that exhibit a skin for ^{40}Ca and ^{48}Ca.

Δr_{np} [fm]	São Paulo	FSU012	FSU016	FSU022	FSU028	FSU032
^{40}Ca	-0.301	-0.052	-0.052	-0.052	-0.050	-0.048
^{48}Ca	0.017	0.147	0.167	0.197	0.232	0.244

Similarly to Fig. 6.2, the ^{48}Ca nucleon densities are displayed on Fig. 6.4, linearly on the left panel and in log scale on the right one. The proton (dashed) and neutron (solid) densities are shown for the São Paulo model (with a dot) and FSU ones (without dot). Like for ^{40}Ca, five different FSU densities have been calculated. As was to be expected from the fact that ^{48}Ca has 8 extra neutrons compared to its number of protons, the neutron densities extend significantly farther than the proton ones. This is clearly visible both in linear scale and in log scale. Contrary to the case of ^{40}Ca, variations in the isoscalar-isovector mixed meson coupling parameter have a stronger impact on the neutron densities but leave the proton ones nearly untouched however.

The neutron skin thickness reproduced by these densities are shown in the second line of Tab. II.2. While in the case of SP, Δr_{np} is close to 0, it ranges from 0.15 fm to 0.24 fm for FSU. While these are larger than the 0.12—0.15 fm range predicted by recent *ab initio* calculations [158], they provide with a large range of values (0.1 fm!), which will help me quantify the effects of the thickness on the pion photoproduction cross section.

The same figures as Fig. 6.4 but for ^{116}Sn, ^{124}Sn and ^{208}Pb are displayed in Figs. 6.5,

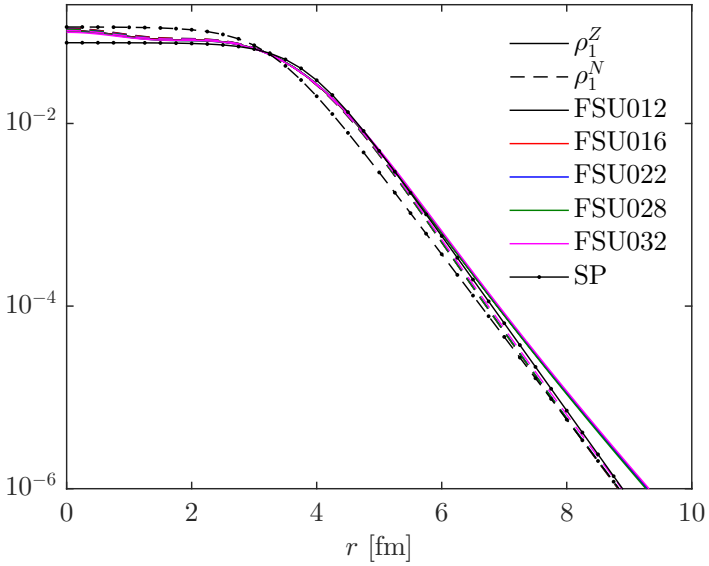

Figure 6.3: ^{40}Ca nucleon densities in log scale. All FSU densities as well as the São Paulo ones are displayed.

6.6 and 6.7, respectively. It should be noted that I only have the two extreme FSU densities for ^{116}Sn. The conclusions we can draw from these figures are similar to the ones I have made for ^{48}Ca. First, the neutron densities extend farther than the proton ones, giving rise to a neutron skin that is clearly visible. Second, the proton densities vary much less than the neutron ones for changes in the isoscalar-isovector mixed meson coupling parameter. Additionally, it should be noted how the density in the interior is pretty much constant, which nicely illustrates the saturation properties of nuclear matter already discussed in the introduction and more particularly in Fig. 2.

The neutron skin thicknesses of these densities are shown in the first, second and third line of Tab. II.3, for ^{116}Sn, ^{124}Sn and ^{208}Pb, respectively. It should be noted that the range of isoscalar-isovector mixed meson coupling parameters explored here generate a wide range of values of the slope L and intercept J of the symmetry energy at saturation density (see Eq.(4.3)). These reproduce the whole range of previous neutron skin measurements on tin isotopes (see Fig. 17 of Ref. [9]).

Like for ^{48}Ca, the neutron skin thickness reproduced by SP is much thinner than the ones of FSU (it is even negative for ^{116}Sn). But contrary to ^{48}Ca, the influence of the isoscalar-isovector mixed meson coupling parameter on the neutron skin thickness of ^{116}Sn, ^{124}Sn and ^{208}Pb seems to be opposite. Rather than seeking an explanation of this effect (which I leave to projects related to these type of calculations), the important message of these tables is the large span of thicknesses that these densities reproduce. The range of skins thicknesses reproduced by FSU is 0.02 fm, 0.03 fm and 0.11 fm, for ^{116}Sn, ^{124}Sn and ^{208}Pb, respectively. These different ranges represent relative changes of roughly 50% in the thickness of the skin for all these nuclei. The influence of Δr_{np} on the photoproduction cross section will be studied in Sec. 9.

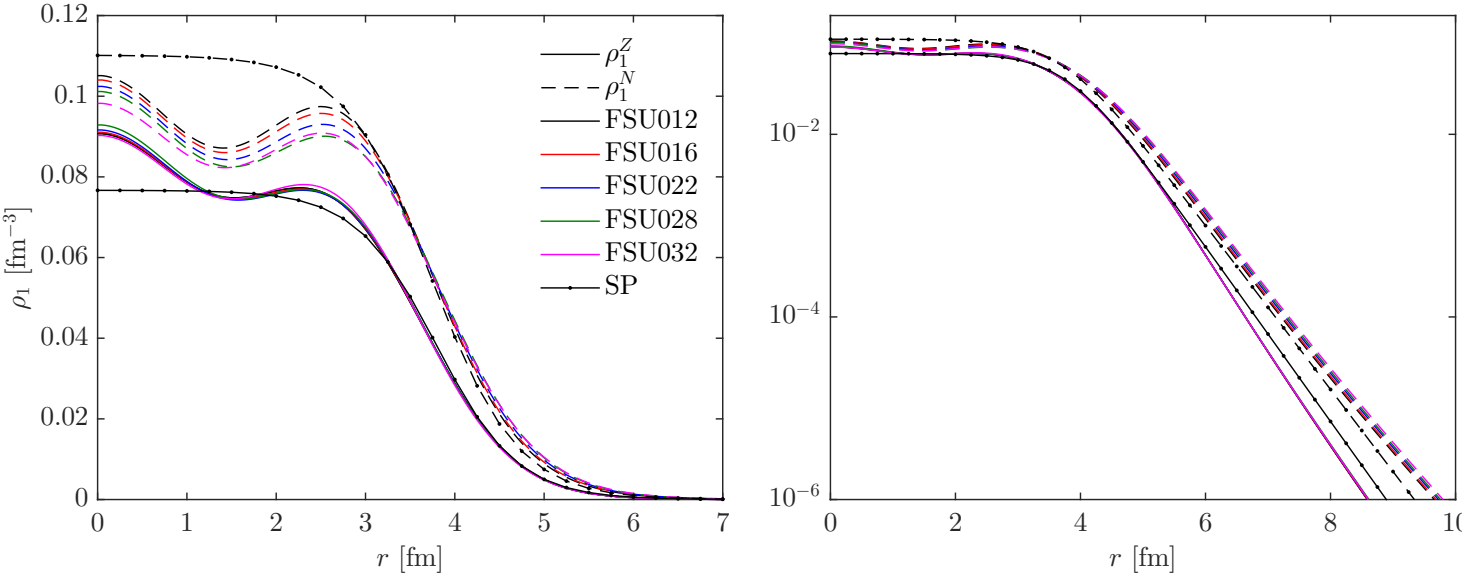

Figure 6.4: ^{48}Ca nucleon densities. See text for details.

Table II.3: Neutron skin thicknesses for ^{124}Sn and ^{208}Pb.

Δr_{np} [fm]	São Paulo	FSU000	FSU010	FSU020	FSU030	FSU040
^{116}Sn	-0.035	0.048	–	–	–	0.029
^{124}Sn	0.013	0.080	0.074	0.068	0.061	0.053
^{208}Pb	0.101	0.286	0.261	0.234	0.207	0.176

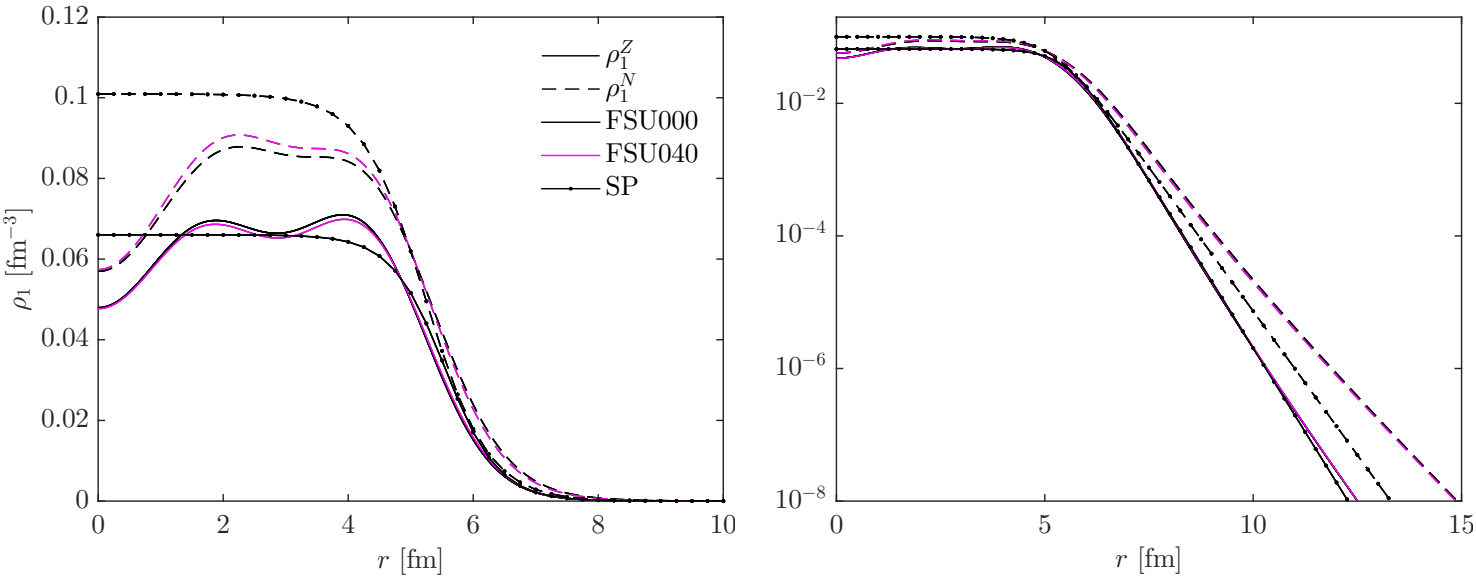

Figure 6.5: ^{116}Sn nucleon densities. See text for details.

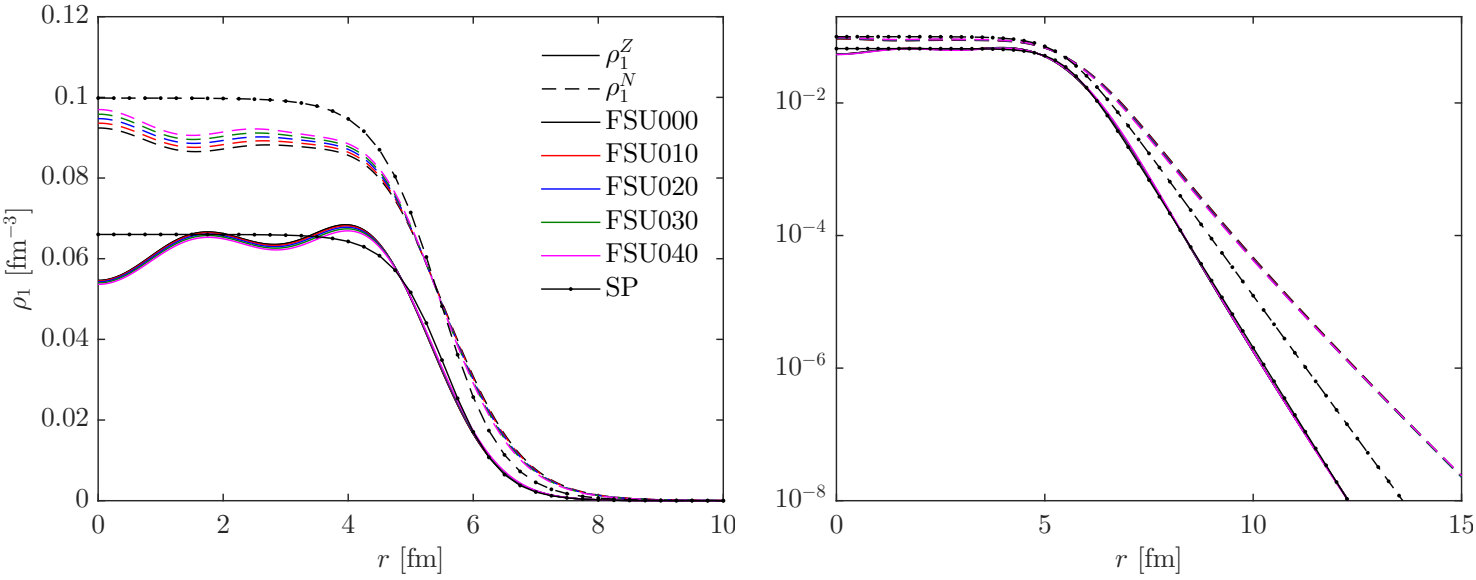

Figure 6.6: ^{124}Sn nucleon densities. See text for details.

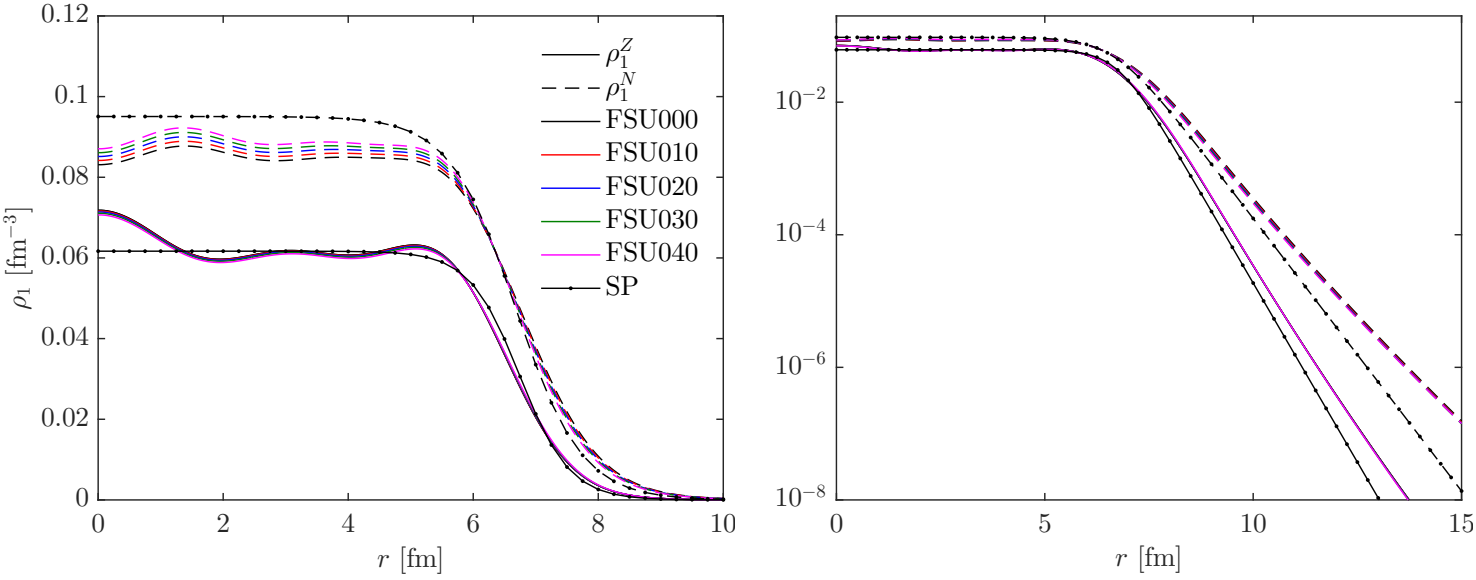

Figure 6.7: ^{208}Pb nucleon densities. See text for details.

7 Pion-nucleus interaction in the Kerman-McManus-Thaler formalism

7.1 The Kerman-McManus-Thaler formalism

The Kerman, McManus and Thaler (KMT) formalism [159] is often used to describe the scattering of a particle from a system of A identical particles in a given state (i.e. the A nucleons of a nucleus in its ground state). This multiple scattering formalism is shortly discussed here and is used throughout this work. I will particularise it to the case of π-A scattering. Some of the final expressions are also extended to photoproduction processes. It should be noted that in the following, I will adopt the convention $\hbar = c = 1$.

Let us suppose that the pion of mass m_π is impinging with a momentum $\vec{k}_0$ on a nucleus of mass m_A made up of A nucleons of (free) mass m_N. The internal A-body Hamiltonian of this nucleus is given by H_N. The eigenstates of this Hamiltonian satisfy

$$H_N \left|\Phi_i\right\rangle = \mathcal{E}_i \left|\Phi_i\right\rangle \tag{7.1}$$

where Φ_i includes the bound states as well as the continuum states of the target nucleus (i can thus be seen as a "continuous" label of the state in which the nucleus is found). Here I will consider the target in its ground state Φ_0 of energy $\mathcal{E}_0$ which I will consider as nil, i.e. $\mathcal{E}_0 = 0$. The energies $\mathcal{E}_i$ are thus the excitation energies of the target for $i > 0$.

Let me define the interaction potential between the pion and the nucleus by V and the kinetic energy operator of the incident pion as $\hat{K}_0$. The Hamiltonian of the total system H is then given by

$$\begin{aligned} H &= H_N + \hat{K}_0 + V_{\pi A} && (7.2)\\ &= H_0 + V_{\pi A} && (7.3) \end{aligned}$$

where H_0 is the $A+1$-body Hamiltonian of a non-interacting pion-nucleus (π-A) system. The eigenfunctions of H_0 satisfy

$$H_0 \left|\Xi_i\right\rangle = E_i \left|\Xi_i\right\rangle \tag{7.4}$$

where $E_i = \mathcal{E}_i + K_0$ is the sum of the nuclear energy and the kinetic energy of the incident pion. These wave functions correspond to the case where the interaction between the pion and the nucleus is turned off. The relative π-A motion should thus be in a plane wave and we thus have

$$\Xi_i(\vec{r}_0, \vec{r}_1, \ldots, \vec{r}_A) = \frac{e^{i\vec{k}_0\vec{r}_0}}{(2\pi)^{3/2}} \Phi_i(\vec{r}_1, \ldots, \vec{r}_A) \tag{7.5}$$

The wave function of the total system when the interaction is turned on is noted $\Psi_{i,k}$ and obeys the Schrödinger equation

$$\left[(H_0 - E) + V_{\pi A}\right] \Psi_{i,k} = 0 \tag{7.6}$$

where i is the index of the state Φ_i in which the nucleus is found and k is the momentum of the pion. Because the nucleus has an internal structure, we could further write V in the explicit form

$$V_{\pi A} = \sum_{i=1}^{A} v(\vec{r}_0, \vec{r}_i) = \sum_i v_i \tag{7.7}$$

Here, v_i is the two-body interaction between the incident pion at $\vec{r}_0$ and a bound nucleon of the target at $\vec{r}_i$. For antisymmetric nuclear states, the matrix element $\langle \Phi_n | \, v_i \, | \Phi_{n'} \rangle$ should not be dependent on the index i and can thus be removed [159]. Because the π-A potential is non-local (see later), its treatment is easier in momentum space. We can then re-write the Schrödinger equation formally as the Lippmann-Schwinger equation

$$T_{\pi A} = V_{\pi A} + V_{\pi A} \frac{1}{E - H_0 + i\varepsilon} T_{\pi A} \tag{7.8}$$

where we see the non-interacting π-A propagator $(E - H_0 + i\varepsilon)^{-1}$ appear and where we introduce the scattering matrix $T_{\pi A}$. The cross section for the process of a pion in the initial momentum $\vec{k}_0$ impinging on a target in its groundstate Φ_0 and scattered to the final momentum $\vec{k}$, leaving it in the state Φ_i is given in terms of the matrix elements of this matrix such that

$$\frac{d\sigma}{d\Omega} = (2\pi)^4 \left| -\mu_{\pi A} \sqrt{\frac{k}{k_0}} \, \langle \Psi_{i,k'} | \, T_{\pi A} \, | \Psi_{0,k} \rangle \right|^2 \tag{7.9}$$

where $\mu_{\pi A}$ is the π-A reduced mass (note that here, because of the light mass of the pion compared to the mass of the nucleus, we have $\mu_{\pi A} \simeq m_\pi$).

We can use Eq. (7.7) to write [159]

$$T_{\pi A} = Av \left(1 + \frac{\mathscr{A}}{E - \hat{K}_0 - H_N + i\varepsilon} T_{\pi A} \right) \tag{7.10}$$

where $\mathscr{A}$ is the antisymmetrization operator. Let us also define the transition operator on a single bound nucleon [Annals of Physics 8, 551]

$$\tau_{\pi N} = v \left(1 + \frac{\mathscr{A}}{E - K_0 - H_N + i\varepsilon} \tau_{\pi N} \right) = v \left(1 + \frac{1}{\alpha} \tau_{\pi N} \right) \tag{7.11}$$

where I have written the propagator more concisely as

$$\frac{1}{\alpha} = \frac{\mathscr{A}}{E - \hat{K}_0 - H_N + i\varepsilon} \tag{7.12}$$

For later, it is interesting to also define α_i

$$\frac{1}{\alpha_i} = \frac{\mathscr{A}}{E - \hat{K}_0 - \mathcal{E}_i + i\varepsilon} \tag{7.13}$$

which can be understood as the π-A propagator for a given state Φ_i of the nucleus. It should be noted that $\tau_{\pi N}$ is *not* the free pion-nucleon scattering operator $t_{\pi N}$, which is defined as

$$t_{\pi N} = v \left(1 + \frac{1}{E - \hat{K}_0 - \hat{K}_1 + i\varepsilon} t_{\pi N} \right) = v \left(1 + \frac{1}{h} t_{\pi N} \right) \tag{7.14}$$

in which only the kinetic operator of the free nucleon $\hat{K}_1$ appears in the propagator and not the full nuclear A-body Hamiltonian H_N. We can show (see App. C) that $T_{\pi A}$ can then be related to $\tau_{\pi N}$ by the following equation

$$T_{\pi A} = A \tau_{\pi N} \frac{1}{1 - (A-1)\frac{1}{\alpha} \tau_{\pi N}} \tag{7.15}$$

If we define the auxiliary matrix

$$T'_{\pi A} = \frac{A-1}{A} T_{\pi A} \tag{7.16}$$

and

$$V^{(0)}_{\pi A} = (A-1)\tau_{\pi N} \tag{7.17}$$

we can finally re-write the Lippmann-Schwinger equation in terms of $T'_{\pi A}$ and $V^{(0)}_{\pi A}$ as

$$T'_{\pi A} = V^{(0)}_{\pi A} + V^{(0)}_{\pi A} \frac{1}{\alpha} T'_{\pi A} \tag{7.18}$$

It is interesting to expand this equation into the series expansion

$$T'_{\pi A} = V^{(0)}_{\pi A} + V^{(0)}_{\pi A} \frac{1}{\alpha} V^{(0)}_{\pi A} + \dots \tag{7.19}$$

The first term can be seen as the single scattering part, the second as the double scattering, etc. We should keep in mind that this equation is a set of coupled integral equations. As such it involves all the target excited states. When considering ground state elastic scattering for example, we have

$$\left\langle \Psi_{0,k'} \right| T'_{\pi A} \left| \Psi_{0,k_0} \right\rangle = \left\langle \Psi_{0,k'} \right| V^{(0)}_{\pi A} \left| \Psi_{0,k_0} \right\rangle + \sum\!\!\!\!\!\!\int_{i,k''} \left\langle \Psi_{0,k'} \right| V^{(0)}_{\pi A} \left| \Psi_{i,k''} \right\rangle \frac{1}{\alpha_i} \left\langle \Psi_{i,k''} \right| V^{(0)}_{\pi A} \left| \Psi_{0,k_0} \right\rangle + \dots \tag{7.20}$$

The first term consists of the ground-state diagonal part of $V^{(0)}_{\pi A}$. The second term consists in the scattering to any nuclear state Φ_i (that could be the ground state) by the first $V^{(0)}_{\pi A}$ (on the right) then a re-scattering to the ground state by the second $V^{(0)}_{\pi A}$ term (on the left). For $i > 0$, it then consists in the product of two off-diagonal terms. At low energies and for low mass projectiles such as the pion the diagonal elements of $V^{(0)}_{\pi A}$ should have a larger contribution than the off-diagonal ones. It would then be handy to separate $V^{(0)}_{\pi A}$ into its different terms. In order to do so, we introduce the projectors

$$\begin{cases} \mathbb{P}_0 = |\Phi_0\rangle\langle\Phi_0| \\ \mathbb{Q}_0 = \sum_{i\neq 0} |\Phi_i\rangle\langle\Phi_i| \end{cases} \qquad \text{and hence} \qquad \mathbb{P}_0 + \mathbb{Q}_0 = \sum_i |\Phi_i\rangle\langle\Phi_i| = \mathbb{1} \tag{7.21}$$

which project on the nucleus ground-state $|\Phi_0\rangle$ and excited states $|\Phi_{i>0}\rangle$. We can rewrite $T'_{\pi A}$ as (see App. C)

$$T'_{\pi A} = \frac{1}{1 - V^{(0)}_{\pi A} \frac{1}{\alpha} \mathbb{Q}_0} V^{(0)}_{\pi A} \left(1 + \frac{1}{\alpha} \mathbb{P}_0 T'_{\pi A}\right) \tag{7.22}$$

$$= \bar{V}_{\pi A} \left(1 + \frac{1}{\alpha} \mathbb{P}_0 T'_{\pi A}\right) \tag{7.23}$$

where we will call $\bar{V}_{\pi A}$ the potential matrix. This equation is much simpler than Eq. (7.18). Indeed, $\bar{V}_{\pi A}$ contains all the effects due to the nuclear excited states. Because of the ground-state projector, the transition amplitude $T'_{\pi A}$ is suppressed for any transition other than to the ground state. We can thus see $\bar{V}_{\pi A}$ as an effective single-particle optical potential for the Lippmann-Schwinger equation. All the complexity arising from the

many-body aspect of the scattering is thus encapsulated in this optical potential. As an example, the ground state elastic scattering T' matrix obeys

$$\langle \Psi_{0,k} | T'_{\pi A} | \Phi_{0,k_0} \rangle = \left\langle \Psi_{0,k} \right| \bar{V}_{\pi A} \left| \Psi_{0,k_0} \right\rangle + \int_{k'} \left\langle \Psi_{0,k} \right| \bar{V}_{\pi A} \left| \Psi_{0,k'} \right\rangle \frac{1}{\alpha_0} \langle \Psi_{0,k'} | T'_{\pi A} | \Psi_{0,k_0} \rangle \quad (7.24)$$

where as we have seen in Eq. (7.13), α_0 can be understood as the propagator of a free-pion-nucleus system where the nucleus remains in its groundstate. Note also that because of the presence of the projector to the ground state in Eq. (7.23), any transition to an excited state will be dependent on the ground-state diagonal auxiliary matrix element $\langle \Psi_{0,k} | T'_{\pi A} | \Psi_{0,k_0} \rangle$.

$$\langle \Psi_{n,k} | T'_{\pi A} | \Psi_{0,k_0} \rangle = \left\langle \Psi_{n,k} \right| \bar{V}_{\pi A} \left| \Psi_{0,k_0} \right\rangle + \int_{k'} \left\langle \Psi_{n,k} \right| \bar{V}_{\pi A} \left| \Psi_{0,k'} \right\rangle \frac{1}{\alpha_0} \langle \Psi_{0,k'} | T'_{\pi A} | \Psi_{0,k_0} \rangle \quad (7.25)$$

Let us see what is the form of the potential matrix $\bar{V}_{\pi A}$. From Eq. (7.22), we know it obeys a Lippmann-Schwinger type equation

$$\bar{V}_{\pi A} = V^{(0)}_{\pi A} + V^{(0)}_{\pi A} \frac{1}{\alpha} \mathbb{Q}_0 \bar{V}_{\pi A} \quad (7.26)$$

which we can expand at first and second order as

$$\bar{V}_{\pi A} = V^{(0)}_{\pi A} + V^{(0)}_{\pi A} \frac{1}{\alpha} \mathbb{Q}_0 V^{(0)}_{\pi A} + \dots \quad (7.27)$$

If we inject this expansion in Eqs. (7.23) and use Eqs. (7.16) and (7.17), we finally have

$$T_{\pi A} = \left[A\tau_{\pi N} + A(A-1)\tau_{\pi N} \frac{1}{\alpha} \mathbb{Q}_0 \tau_{\pi N} \right] + \frac{A-1}{A} \left[A\tau_{\pi N} + A(A-1)\tau_{\pi N} \frac{1}{\alpha} \mathbb{Q}_0 \tau_{\pi N} \right] \frac{1}{\alpha} \mathbb{P}_0 T_{\pi A} \quad (7.28)$$

which, if we define the term between brackets as V_{opt}

$$\bar{V}_{\pi A,\text{opt}} = A\tau_{\pi N} + A(A-1)\tau_{\pi N} \frac{1}{\alpha} \mathbb{Q}_0 \tau_{\pi N} \quad (7.29)$$

can be written more concisely as

$$T_{\pi A} = \bar{V}_{\pi A,\text{opt}} + \frac{A-1}{A} \bar{V}_{\pi A,\text{opt}} \frac{1}{\alpha} \mathbb{P}_0 T_{\pi A} \quad (7.30)$$

which is a Lippmann-Schwinger type equation for the scattering of a pion off a nucleus by the effective potential $\bar{V}_{\pi A,\text{opt}}$.

7.1.1 The impulse approximation

A significant difficulty of many-body scattering comes from the choice of $\bar{V}_{\pi A,\text{opt}}$ and hence from the calculation of $\tau_{\pi N}$. We can show (see App. C), that $t_{\pi N}$ and $\tau_{\pi N}$ are related through the equation

$$\tau_{\pi N} = t_{\pi N} + t_{\pi N} \left(\frac{1}{\alpha} - \frac{1}{h} \right) \tau_{\pi N} \quad (7.31)$$

but this equation is as difficult to solve as the Lippmann-Schwinger one. In order to ease the problem, let us make a simplifying assumption: the *impulse approximation*.

In the impulse approximation, that I will sometimes refer to as IA, we assume two things. The first one is that the single nucleon amplitude $\tau_{\pi N}$ can simply be considered as the amplitude for the free scattering $t_{\pi N}$. The second is to consider that the nuclear Hamiltonian H_N contained in the propagator α is set to $E_0 = 0$, such that $\alpha = \alpha_0$. Because of these two assumptions, the nucleons could be seen as free nucleons unbound to the nucleus. The effective optical potential for the scattering of the impinging pion with the nucleus is then approximated by the expression

$$\bar{V}_{\pi A,\text{opt}} = A t_{\pi N} + A(A-1) t_{\pi N} \frac{1}{\alpha_0} \mathbb{Q}_0 t_{\pi N} \tag{7.32}$$

In this work, I will take the ground-state averages of these operators

$$V_{\pi A,\text{opt}} = \left\langle \Phi_0 \right| \bar{V}_{\pi A,\text{opt}} \left| \Phi_0 \right\rangle \tag{7.33}$$

$$= A \left\langle \Phi_0 \right| t_{\pi N} \left| \Phi_0 \right\rangle + A(A-1) \sum_{i>0} \left\langle \Phi_0 \right| t_{\pi N} \left| \Phi_i \right\rangle \frac{1}{\alpha_0} \left\langle \Phi_i \right| t_{\pi N} \left| \Phi_0 \right\rangle \tag{7.34}$$

It should be noted that the KMT formalism avoids double counting on the pion re scattering on the same nucleon, as visible from the $A-1$ factor of the second term.

This formalism can be extended to π-photoproduction, such that the photoproduction T-matrix for this process $T_{\gamma\pi}$ reads [160]

$$T_{\gamma\pi} = \sum_{i=1}^{A} \tau_{\gamma\pi,i} + \sum_{j\neq i}^{A} \sum_{i=1}^{A} \tau_{\pi N,j} \frac{1}{\alpha} \tau_{\gamma\pi,i} + \sum_{k\neq i,j}^{A} \sum_{j\neq i}^{A} \sum_{i=1}^{A} \tau_{\pi N,k} \frac{1}{\alpha} \tau_{\pi N,j} \frac{1}{\alpha} \tau_{\gamma\pi,i} + \dots \tag{7.35}$$

where the sum is on all nucleons. The operators $\tau_{\gamma\pi}$ correspond to the pion photoproduction operator, also on bound nucleons. In the impulse approximation, the operators on free nucleons $t_{\pi N}$ are used instead of the $\tau_{\pi N}$ and $\alpha = \alpha_0$. The equation above can thus be rewritten as an integral equation

$$T_{\gamma\pi} = V_{\gamma\pi} + \frac{A-1}{A} T_{\pi A} \frac{1}{\alpha_0} \mathbb{P}_0 V_{\gamma\pi} \tag{7.36}$$

where $T_{\pi A}$ is the pion-nucleus scattering T-matrix already encountered in Eq.(7.30) and where the photoproduction amplitude $V_{\gamma\pi}$ reads

$$V_{\gamma\pi} = \sum_{i=1}^{A} t_{\gamma\pi,i} = A t_{\gamma\pi} \tag{7.37}$$

Note that as seen in Eq. (7.10), the index i can be dropped due to the fact that we are interested only in antisymmetric matrix elements and we consider isospin symmetry.

The right-hand side of Eq. (7.36) is composed of two terms. In what could be seen as the "first order" term, the pion does not further interact with the nucleus after its production. Its wave function is hence a plane wave. For this reason, the approximation that neglects the second term is commonly referred to as the Plane Wave Impulse Approximation (or PWIA). The second term is the term that simulates the rescattering of the pion with the nucleus. In what could be called a "second order" of the reaction, the pion wave function is distorted by its interaction with the nucleus. The full expression Eq. (7.36) will be referred to as the Distorted Wave Impulse Approximation (or DWIA).

From Eqs. (7.35)–(7.37), it should be noted that only the dominant one-body mechanism of the photoproduction is considered: the neutral pion is produced on a single

nucleon [see Fig. 7.1(a)]. Two-body processes, in which a charged pion is produced on a first nucleon and then charge exchanges into a neutral pion [see Fig. 7.1(b)], are thus not considered in this approximation. The influence of this effect on the photoproduction cross section has been recently investigated in Ref. [161]. While it is relatively small, it could affect the quality of the extraction of the neutron skin thickness. In my work, the intermediate states of the reaction in the DWIA are assumed to contain no other particle than the nucleus and a neutral pion. Two-body processes are hence not considered here. It should be noted however that the elementary process on a single nucleon $t_{\gamma\pi}$ may still contain charge exchange processes as well as rescattering terms. These happen however on the same nucleon and are not two-body processes.

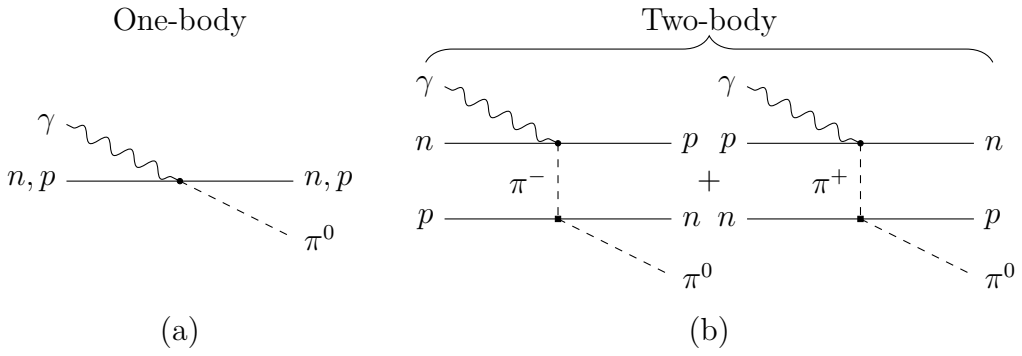

Figure 7.1: One-body (left) and two-body (right) processes for the photoproduction of a neutral pion.

It should be noted that for an impinging on-shell momentum k_0 of the pion, the non-relativistic propagator α_0^{-1} for a pion with momentum k reads

$$\frac{1}{\alpha_0(k)} = \frac{1}{\frac{k_0^2}{2\mu_{\pi A}} - \frac{k^2}{2\mu_{\pi A}} + i\varepsilon} \tag{7.38}$$

where the momentum dependence of α_0 has been written explicitly. It is useful to define a non-relativistic Green operator

$$G_0(k) \equiv \frac{1}{2\mu_{\pi A}\alpha_0(k)} = \frac{1}{k_0^2 - k^2 + i\varepsilon} \tag{7.39}$$

and to define

$$\tilde{T}_\beta = -\frac{2\mu_{\pi A}}{4\pi} T_\beta \tag{7.40}$$

where β refers to the different processes defined above (such as πA, $\gamma\pi$, etc.). In the example of the π-A scattering, the cross section Eq. (7.9) for a pion going from momentum k_0 to k reads simply

$$\frac{d\sigma}{d\Omega} = (2\pi)^3 \frac{k}{k_0} \left|\tilde{T}(\vec{k}, \vec{k}_0)\right|^2 \tag{7.41}$$

Similarly, by defining

$$U_\beta = -\frac{2\mu_{\pi A}}{4\pi} V_\beta \tag{7.42}$$

Eq. (7.30) can be rewritten as

$$\tilde{T}_{\pi A} = U_{\pi A,\text{opt}} - 4\pi \frac{A-1}{A} U_{\pi A,\text{opt}} G_0 \mathbb{P}_0 \tilde{T}_{\pi A} \tag{7.43}$$

Likewise, Eq. (7.36) reads

$$\tilde{T}_{\gamma\pi} = U_{\gamma\pi} - 4\pi \frac{A-1}{A} \tilde{T}_{\pi A} G_0 \mathbb{P}_0 U_{\gamma\pi} \tag{7.44}$$

If we wish to correct the propagator for relativity, the energies are calculated relativistically and the π-A reduced mass $\mu_{\pi A}$ can be replaced by a relativistic equivalent of the reduced mass. In Ref. [128], the latter is defined as $\mathcal{M}$, which has the form

$$\mathcal{M}(k) = \frac{E_\pi(k) E_A(k)}{E_\pi(k) + E_A(k)} \tag{7.45}$$

where $E_\pi(k)$ and $E_A(k)$ are the relativistic energies of the pion and the target, respectively and the non-relativistic Green operator Eq. (7.39) then becomes

$$G(k) \equiv \frac{1}{2\mathcal{M}(k)} \frac{1}{E(k_0) - E(k) + i\varepsilon} \tag{7.46}$$

where $E(k) = E_\pi(k) + E_A(k)$ is the sum of the pion and nucleus energies. The explicit expressions of these energies will be given in next section.

For reasons that will become clear in Sec. 8.3, when the Lippmann-Schwinger equation is actually solved, it is useful to rewrite it in terms of the non-relativisctic propagator G_0. In this alternative form, we have

$$G(k) = \frac{2\widetilde{\mathcal{M}}(k)}{2\mathcal{M}(k)} \frac{1}{k_0^2 - k^2 + i\epsilon} \tag{7.47}$$

where

$$2\widetilde{\mathcal{M}}(k) = \frac{[E(k) + E(k_0)][E_\pi(k)E_A(k) + E_\pi(k_0)E_A(k_0)]}{E^2(k) + E^2(k_0)} \tag{7.48}$$

In the limit $k \to k_0$, $\widetilde{\mathcal{M}}(k) \to \mathcal{M}(k)$ such that $G(k) \to G_0(k)$. The explicit expressions for the PWIA amplitude $V_{\gamma\pi}$ and DWIA amplitude $T_{\gamma\pi}$ and the explicit expressions for the elementary amplitudes $t_{\gamma\pi}$ are detailed in the next two sections.

7.2 Elementary pion-photoproduction

The elementary pion-photoproduction is the process of a photon being absorbed by a single free nucleon and producing a pion. In the pion-nucleon (π-N) centre-of-mass frame, the kinematics of this process are reproduced on Fig. 7.2. It should be noted that I will note the kinematic variables in the π-N frame with a tilde, to clearly dissociate them from the pion-nucleus variables that we will encounter in next section.

By definition, in the π-N frame, the momentum of the free struck nucleon before the reaction $\tilde{\vec{p}}$ is opposite to the momentum of the impinging photon $\tilde{\vec{k}}_\gamma$, i.e. $\tilde{\vec{p}} = -\tilde{\vec{k}}_\gamma$. Similarly, the momentum of the nucleon after the reaction $\tilde{\vec{p}}'$ is opposite to the momentum of the outgoing pion $\tilde{\vec{k}}_\pi$, i.e. $\tilde{\vec{p}}' = -\tilde{\vec{k}}_\pi$. Because all particles are on-shell, the pion and nucleon energies read

$$\tilde{E}_\pi = \sqrt{m_\pi^2 + \tilde{k}_\pi^2} \qquad \tilde{E}_N = \sqrt{m_N^2 + \tilde{p}^2} \qquad \tilde{E}'_N = \sqrt{m_N^2 + \tilde{p}'^2} \tag{7.49}$$

where I remind the reader that m_π and m_N are the pion and free nucleon masses, respectively. I will consider the photon momentum to be aligned with the $\hat{\mathbf{z}}$ axis. The scattering

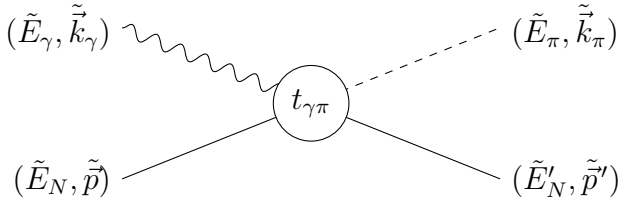

Figure 7.2: Kinematics of the elementary pion-photoproduction reaction. The quadrivectors of the photon, the initial free nucleon, the pion and the final nucleon correspond to the index γ, N, π and N', respectively.

angle, i.e. the angle between the direction of the outgoing pion and the $\hat{\mathbf{z}}$ axis, is defined as $\tilde{\theta}$. For a given lab energy of the photon T_γ, the total energy of the system is well defined and is given by

$$W_{\gamma N} = \sqrt{m_N^2 + 2T_\gamma m_N} \tag{7.50}$$

From energy conservation, the momentum of the pion can be calculated to be

$$\tilde{k}_\pi = \frac{\sqrt{(W_{\gamma N}^2 - m_N^2 - m_\pi^2)^2 - 4m_N^2 m_\pi^2}}{2W_{\gamma N}} \tag{7.51}$$

If we define J^μ as the nucleon electromagnetic current, the T-matrix for the elementary photoproduction process from a state i to a state f is given by

$$t_{\gamma\pi,fi} = \left\langle \tilde{p}' \tilde{k}_\pi \right| \varepsilon_\mu J^\mu \left| \tilde{p} \right\rangle \tag{7.52}$$

where ε_μ is the photon polarisation quadrivector. It is convenient to express the matrix element in the π-N centre-of-mass system in terms of Pauli matrices and two-component spinors χ_i and χ_f, the initial γ-N and final π-N' states. This allows to use the angular momentum properties of photoproduction. The quantity $\mathcal{F}$ (known as the CGLN amplitudes [162], see also Ref. [163] for their explicit form) is introduced such that the elementary t-matrix reads

$$t_{\gamma\pi,fi} = \chi_f^\dagger \mathcal{F} \chi_i \tag{7.53}$$

and $\mathcal{F}$ reads [163]

$$\mathcal{F} = i(\vec{\sigma}\cdot\vec{\varepsilon})\mathcal{F}_1 + (\vec{\sigma}\cdot\hat{\vec{k}}_\pi)(\vec{\sigma}\cdot(\hat{\vec{k}}_\gamma \times \vec{\varepsilon}))\mathcal{F}_2 + i(\vec{\sigma}\cdot\hat{\vec{k}}_\gamma)(\hat{\vec{k}}_\pi\cdot\vec{\varepsilon})\mathcal{F}_3 + i(\vec{\sigma}\cdot\hat{\vec{k}}_\pi)(\hat{\vec{k}}_\pi\cdot\vec{\varepsilon})\mathcal{F}_4 \tag{7.54}$$

where $\hat{\vec{x}}$ is a unit vector in the direction of $\vec{x}$ and $\vec{\sigma}$ are the Pauli spin operators. The pion photoproduction amplitudes are usually expressed in terms of the electric (E_{lj}) and magnetic (M_{lj}) multipoles, l being the pion-nucleon angular momentum and j is the total spin, resulting from the coupling between l and $s = 1/2$, the intrinsic spin of the nucleon. For $l > 0$, the total spin is further abbreviated to $\pm$, depending on whether $j = l \pm 1/2$. This eases the analysis of experimental data and allows to study the baryon resonances

individually. In this expansion, the amplitudes read

$$\mathcal{F}_1 = E_{0+} + \sum_{l>0} \left[l M_{l+} + E_{l+} \right] P'_{l+1}(\cos\tilde{\theta}) + \left[(l+1) M_{l-} + E_{l-} \right] P'_{l-1}(\cos\tilde{\theta}) \tag{7.55}$$

$$\mathcal{F}_2 = \sum_{l\geq 1} \left[(l+1) M_{l+} + l M_{l-} \right] P'_l(\cos\tilde{\theta}) \tag{7.56}$$

$$\mathcal{F}_3 = \sum_{l\geq 1} \left[E_{l+} - M_{l+} \right] P''_{l+1}(\cos\tilde{\theta}) + \left[E_{l-} + M_{l-} \right] P''_{l-1}(\cos\tilde{\theta}) \tag{7.57}$$

$$\mathcal{F}_4 = \sum_{l\geq 2} \left[M_{l+} - E_{l+} - M_{l-} - E_{l-} \right] P''_l(\cos\tilde{\theta}) \tag{7.58}$$

where P'_l and P''_l are the first and second order derivatives of the Legendre polynomials of order l and where the multipoles depend on the $W_{\gamma N}$ energy. Note that in this work, I will consider these matrices calculated in MAID, an Unitary Isobar Model (UIM) [164, 165]. An example of the calculation of total photoproduction cross section on a single free nucleon is shown in App. D. On Fig. 7.3, the result of this calculation for the total photoproduction as a function of T_γ is displayed for two reactions: $\gamma + p \to \pi^0 + p$ (circles in black for the data, solid green line) and $\gamma + p \to \pi^+ + n$ (circles in blue for the data, solid red line). As we can see, the data is well reproduced in the Δ resonance region and around.

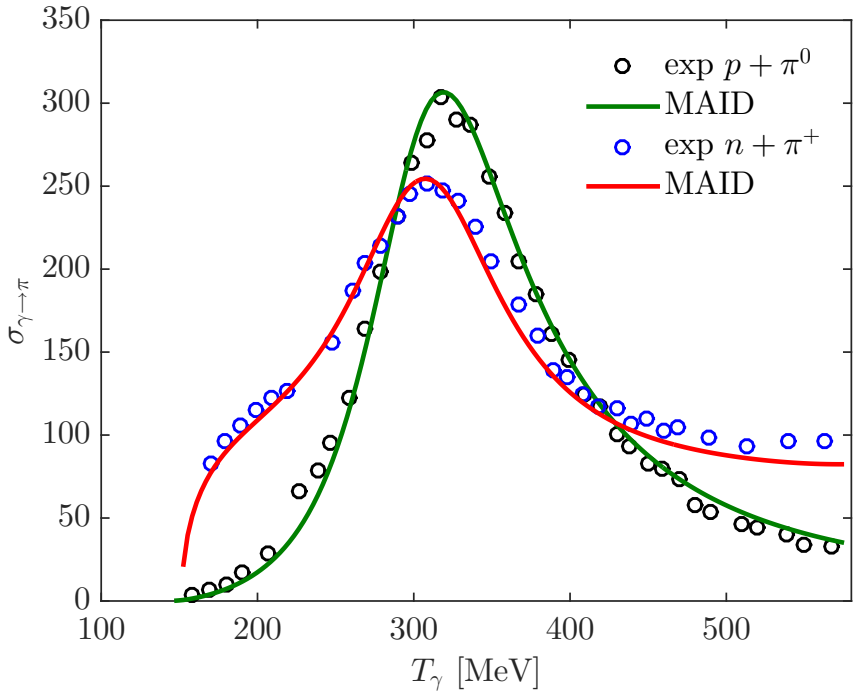

Figure 7.3: Calculated total photoproduction as a function of energy of the photon in the lab frame for two channels: $\gamma + p \to \pi^0 + p$ (in black) and $\gamma + p \to \pi^+ + n$ (in blue). Comparison to experiment taken from the compilation of Fujii et al., [166] and Menze et al., [167]

It should be noted that the form of Eq. (7.54) has a crucial advantage. As already discussed in Sec. 7.1, in the impulse approximation, the photoproduction amplitude can be seen as the sum of the amplitudes on each nucleon. In this work, because the nucleus

has no spin, it is useful to rewrite the matrix $\mathcal{F}$ (7.54) in order to include this hypothesis. One of the results of App. D is that the second term of the right-hand side of Eq. (7.54) can be rewritten as

$$(\vec{\sigma}\cdot\hat{\vec{k}}_\pi)(\vec{\sigma}\cdot(\hat{\vec{k}}_\gamma\times\vec{\varepsilon})) = (\vec{\varepsilon}\cdot(\hat{\vec{k}}_\pi\times\hat{\vec{k}}_\gamma)) + i(\vec{\sigma}\cdot\hat{\vec{k}}_\gamma)(\hat{\vec{k}}_\pi\cdot\vec{\varepsilon}) - i(\hat{\vec{k}}_\pi\cdot\hat{\vec{k}}_\gamma)(\vec{\sigma}\cdot\vec{\varepsilon}) \tag{7.59}$$

where spin dependent and spin independent parts of $\mathcal{F}_2$ can be separated. The first term on the right hand side of this expression is the only component of the whole matrix $\mathcal{F}$ that is independent on spin. For the spin 0 nuclei that will be considered in this work, all components excepts the spin-independent part of the amplitude can thus be dropped. This much simplifies the problem and provides with a spin-average of the photoproduction amplitude

$$\bar{\mathcal{F}} = \vec{\varepsilon}\cdot(\hat{\vec{k}}_\pi\times\hat{\vec{k}}_\gamma)\mathcal{F}_2 \tag{7.60}$$

which is the only component that will be needed in this work.

While I will not go into details of the UIM model MAID, it should be noted that it considers two different contributions to the amplitudes $\mathcal{F}_2$. First, background contributions, composed of Born and vector mesons exchange terms, and that are calculated by evaluation of the Feynman diagrams derived from an effective Lagrangian density [164]. And second, resonant contributions, that are calculated by assuming that the relevant resonant multipoles have a Breit-Wigner shape. At the energies considered in this work, the M_{1+} multipole which corresponds to the Δ resonance, gives the largest contribution to $\mathcal{F}_2$. It is parametrised as [128]

$$M_{1+} = f_{\gamma N\Delta}(W_{\gamma N})\frac{M_\Delta\Gamma_\Delta(W_{\gamma N})e^{i\phi_{\pi N}(W_{\gamma N})}}{M_\Delta^2 - W_{\gamma N}^2 - iM_\Delta\Gamma_\Delta(W_{\gamma N})}f_{\pi N\Delta}(W_{\gamma N}) \tag{7.61}$$

where $f_{\gamma N\Delta}$ and $f_{\pi N\Delta}$ are the $\gamma N\Delta$ and $\pi N\Delta$ vertex functions, respectively. It has a Breit-Wigner form that describes the decay of the Δ resonance of energy M_Δ and with total width $\Gamma_\Delta(W_{\gamma N})$. If we consider the single-pion branching ratio to be 1, the energy dependence of the total width of the Δ resonance reads [164]

$$\Gamma_\Delta(W_{\gamma N}) = \Gamma_0\left(\frac{\tilde{k}_\pi}{\tilde{k}_{\pi,\Delta}}\right)^3\left(\frac{\Lambda^2+k_{\pi,\Delta}^2}{\Lambda^2+k_\pi^2}\right)\frac{M_\Delta}{W_{\gamma N}} \tag{7.62}$$

where Γ_0 and $\tilde{k}_{\pi,\Delta}$ are the total width and the center-of-mass pion momentum at the resonance peak. According to the PDG [139] M_Δ= 1232 MeV and Γ_0 = 117 MeV. Λ is a damping parameter chosen as 500 MeV.

In Eq. (7.61), the phase-shift $\phi_{\pi N}(W_{\gamma N})$ is a unitary phase that adjusts the phase of the total multipole (background as well as resonance) to the corresponding π-N scattering phase $\delta_{\pi N}$, in accordance with the Fermi-Watson theorem [168]. An expression of the parametrisation of this phase is given in Ref. [164]. Note however that this procedure becomes necessary for photon energies well above the Δ resonance energy [164]

7.3 Pion-photoproduction on a nucleus

The pion-photoproduction on a nucleus is the process of a photon being absorbed by a nucleus and producing a pion. As already discussed in Sec. 7.1.1, I will consider the photon to interact with only one bound nucleon. No multiple-body processes will be considered

here and the neutral pion is hence produced on a single nucleon. In the photon-nucleus (γ-A) and pion-nucleus (π-A) centre-of-mass frames, which are equivalent, the kinematics are reproduced on Fig. 7.4. It should be noted that I will note the kinematic variables in the γ-A/π-A frame without a tilde, to clearly dissociate them from their equivalent in the pion-nucleon centre-of-mass frame that have been encountered in previous section.

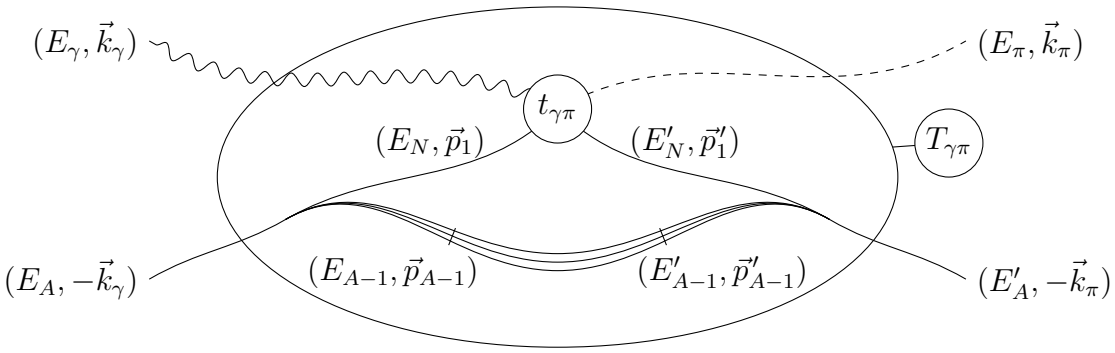

Figure 7.4: Kinematics of the pion-photoproduction reaction on a nucleus in the γ-A/π-A centre-of-mass frame. The quadrivectors of the photon, the nucleus before the reaction, the pion and the nucleus after the reaction correspond to the indices γ, A, π and A', respectively. Inside of the nucleus, the quadrivectors of the struck nucleon before and after the reaction read $(E_N, \vec{p}_1)$ and $(E'_N, \vec{p}'_1)$, respectively, while the quadrivectors for the spectator nucleons read $(E_{A-1}, \vec{p}_{A-1})$ and $(E'_{A-1}, \vec{p}'_{A-1})$, respectively.

By definition, in the γ-A frame, the momentum of the nucleus before the reaction is opposite to the momentum of the impinging photon $\vec{k}_\gamma$. Similarly, the momentum after the photoproduction is opposite to the momentum of the outgoing pion $\vec{k}_\pi$. I will suppose the photon to have a momentum oriented in the $\hat{\boldsymbol{z}}$ direction. The angle between $\hat{\boldsymbol{z}}$ and the direction of $\vec{k}_\pi$ is defined as the scattering angle θ.

Because these particles are on-shell, the energies of the nucleus before and after the reaction and the pion energy are unambiguously defined and read, respectively

$$E_A = \sqrt{m_A^2 + k_\gamma^2} \qquad E'_A = \sqrt{m_A^2 + k_\pi^2} \qquad E_\pi = \sqrt{m_\pi^2 + k_\pi^2} \tag{7.63}$$

For a given lab energy of the photon T_γ, the total energy of the system (in the π-A frame) is

$$E_{\text{tot}} = E_\gamma + E_A = \sqrt{m_A^2 + 2T_\gamma m_A} \tag{7.64}$$

and the photon momentum is hence

$$k_\gamma = \frac{m_A T_\gamma}{E_{\text{tot}}} \tag{7.65}$$

in this frame.

From energy conservation, the momentum of the on-shell pion reads

$$k_\pi = \frac{\sqrt{(E_{\text{tot}}^2 - m_A^2 - m_\pi^2)^2 - 4m_A^2 m_\pi^2}}{2E_{\text{tot}}} \tag{7.66}$$

The energy of the γ-N system in the γ-A centre-of-mass frame is given by

$$W_{\gamma N} = \sqrt{(E_N + E_\gamma)^2 - (\vec{p}_1 + \vec{k}_\gamma)^2} \tag{7.67}$$

before the reaction and in the π-A centre-of-mass frame

$$W_{\pi N} = \sqrt{(E'_N + E_\pi)^2 - (\vec{p}'_1 + \vec{k}_\pi)^2} \tag{7.68}$$

after the reaction, where $\vec{p}_1$ ($\vec{p}'_1$) is the struck nucleon momenta before (after) the reaction and E_N (E'_N) is its energy. Note that the choice of nucleon energy is not unambiguous and different prescriptions will be studied in Sec. 7.3.2.

7.3.1 Plane Wave Impulse Approximation (PWIA)

In the PWIA and for a photon polarisation $\lambda = \pm 1$, the photoproduction cross-section is given by [133]

$$\frac{d\sigma^{\gamma\pi}}{d\Omega} = \frac{k_\pi}{k_\gamma}\frac{1}{2}\sum_\lambda \left|U^{(\lambda)}_{\gamma\pi}(\vec{k}_\pi, \vec{k}_\gamma)\right|^2 \tag{7.69}$$

where, from Eq. (7.37), the matrix element of the amplitude $U^{(\lambda)}_{\gamma\pi}$ averaged on the nucleus ground-state simply reads in momentum space

$$U^{(\lambda)}_{\gamma\pi}(\vec{k}_\pi, \vec{k}_\gamma) = \left\langle k_\pi \right| U^{(\lambda)}_{\gamma\pi} \left| k_\gamma \right\rangle = A \left\langle k_\pi \right| \left\langle \Phi_0 \right| t^{(\lambda)}_{\gamma\pi} \left| \Phi_0 \right\rangle \left| k_\gamma \right\rangle \tag{7.70}$$

Explicitly, previous equation takes the form

$$\begin{aligned} U^{(\lambda)}_{\gamma\pi}(\vec{k}_\pi, \vec{k}_\gamma) = A \int \left(\prod_{i=1}^{A} dx_i\right) dx'_1 \frac{d\vec{p}'_1}{(2\pi)^3}\frac{d\vec{p}_1}{(2\pi)^3} e^{i(\vec{p}'_1\vec{r}'_1 - \vec{p}_1\vec{r}_1)} \\ \Phi^\dagger_0(x'_1, x_2, \ldots, x_A) \left\langle \vec{k}_\pi, \vec{p}'_1 \right| t^{(\lambda)}_{\gamma\pi} \left| \vec{k}_\gamma, \vec{p}_1 \right\rangle \Phi_0(x_1, x_2, \ldots, x_A) \end{aligned} \tag{7.71}$$

where $x_i = \{\vec{r}_i, \sigma_i, \tau_i\}$ and $\int dx_i \equiv \sum_{\sigma_i\tau_i} \int d\vec{r}_i$ and where the bra-ket is a short notation for the matrix elements of the elementary photoproduction transition amplitude

$$\left\langle \vec{k}_\pi, \vec{p}'_1 \right| t^{(\lambda)}_{\gamma\pi} \left| \vec{k}_\gamma, \vec{p}_1 \right\rangle = (2\pi)^3 \delta(\vec{k}_\pi + \vec{p}'_1 - \vec{k}_\gamma - \vec{p}_1) t^{(\lambda)}_{\gamma\pi}(W_{\gamma N}, \tilde{\theta}) \tag{7.72}$$

It should be noted that until now, no choice has been made on the prescription for the calculation of the energy of the γ-N system. As we will see later, for some prescriptions, the energy and the scattering angle can depend on the momenta of the four particles involved in the process. For this reason, I will rather write previous equation as

$$\left\langle \vec{k}_\pi, \vec{p}'_1 \right| t^{(\lambda)}_{\gamma\pi} \left| \vec{k}_\gamma, \vec{p}_1 \right\rangle = (2\pi)^3 \delta(\vec{k}_\pi + \vec{p}'_1 - \vec{k}_\gamma - \vec{p}_1) t^{(\lambda)}_{\gamma\pi}(\vec{k}_\pi, \vec{p}'_1; \vec{k}_\gamma, \vec{p}_1) \tag{7.73}$$

where the dependencies on the momenta of the produced pion, final nucleon, impinging photon and initial nucleon is made explicit.

Let me define the transfer momentum as

$$\vec{q} = \vec{k}_\pi - \vec{k}_\gamma \tag{7.74}$$

of modulus

$$q = \sqrt{k_\pi^2 + k_\gamma^2 - 2k_\pi k_\gamma \cos\theta} \tag{7.75}$$

where I remind that θ is the scattering angle. We can then shift the integration variables $\vec{p}_1 = \vec{p} + \vec{q}/2$ and $\vec{p}'_1 = \vec{p}' - \vec{q}/2$ as this change will simplify the expressions of $U^{(\lambda)}_{\gamma\pi}(\vec{k}_\pi, \vec{k}_\gamma)$

in later steps. Note also that the momentum conservation delta intrinsically contained in the bra-ket cancels the integral over $\vec{p}_1'$. We have

$$U_{\gamma\pi}^{(\lambda)}(\vec{k}_\pi,\vec{k}_\gamma) = A\int\left(\prod_{i=1}^{A}dx_i\right)dx_1'\frac{d\vec{p}}{(2\pi)^3}e^{i(\vec{p}-\vec{q}/2)\vec{r}_1'-i(\vec{p}+\vec{q}/2)\vec{r}_1}$$
$$\Phi_0^\dagger(x_1',x_2,\ldots,x_A)\Phi_0(x_1,x_2,\ldots,x_A)t_{\gamma\pi}^{(\lambda)}(\vec{k}_\pi,\vec{p}-\vec{q}/2;\vec{k}_\gamma,\vec{p}+\vec{q}/2) \tag{7.76}$$

As we have seen in Sec. 6, we can factorize the nuclear recoil and centre-of-mass movement from the wave function. If we apply the change to the internal coordinates $\vec{\xi}_i$ described by Eqs. (6.35) and (6.36) and inject Eq. (6.38) in the expression above, we have

$$U_{\gamma\pi}^{(\lambda)}(\vec{k}_\pi,\vec{k}_\gamma) = A\sum_{\sigma_1,\sigma_1'}\sum_{\tau_1,\tau_1'}\sum_{\sigma_2\ldots\sigma_A}\sum_{\tau_2\ldots\tau_A}\int\left(\prod_{i=1}^{A-1}d\vec{\xi}_i\right)d\vec{\xi}d\vec{\xi}_1'\frac{d\vec{p}}{(2\pi)^3}e^{i(\vec{p}-\vec{q}/2)(\vec{\xi}-\vec{\xi}_1')}e^{-i(\vec{p}+\vec{q}/2)(\vec{\xi}-\vec{\xi}_1)}$$
$$e^{i\vec{k}_\pi(\vec{\xi}-\vec{\xi}_1'/A)}e^{-i\vec{k}_\gamma(\vec{\xi}-\vec{\xi}_1/A)}\phi^\dagger_{0;\sigma_1'\sigma_2\ldots A;\tau_1'\tau_2\ldots A}(\vec{\xi}_1',\vec{\xi}_2,\ldots,\vec{\xi}_{A-1})$$
$$\phi_{0;\sigma_1\sigma_2\ldots A;\tau_1\tau_2\ldots A}(\vec{\xi}_1,\vec{\xi}_2,\ldots,\vec{\xi}_{A-1})t_{\gamma\pi}^{(\lambda)}(\vec{k}_\pi,\vec{p}-\vec{q}/2;\vec{k}_\gamma,\vec{p}+\vec{q}/2) \tag{7.77}$$

Since the other nucleons are spectator of the reaction, this can be further simplified if we use the one-body density matrix defined in Eq. (6.42). We then have

$$U_{\gamma\pi}^{(\lambda)}(\vec{k}_\pi,\vec{k}_\gamma) = \sum_{\sigma_1,\sigma_1'}\sum_{\tau_1,\tau_1'}\int\frac{d\vec{p}}{(2\pi)^3}d\vec{\xi}d\vec{\xi}_1d\vec{\xi}_1'\;e^{i\left\{[\vec{q}-(\vec{k}_\pi-\vec{k}_\gamma)]\vec{\xi}+[-(\vec{p}-\vec{q}/2)-\vec{k}_\pi/A]\vec{\xi}_1'+[(\vec{p}+\vec{q}/2)+\vec{k}_\gamma/A]\vec{\xi}_1\right\}}$$
$$\rho_1(\vec{\xi}_1|\vec{\xi}_1')t_{\gamma\pi}^{(\lambda)}(\vec{k}_\pi,\vec{p}-\vec{q}/2;\vec{k}_\gamma,\vec{p}+\vec{q}/2) \tag{7.78}$$

Note that the integral on the first term of the exponential is simply the momentum-conserving delta. The argument of the exponential can then be re-written by injecting the alternative definitions $\vec{k}_\gamma = \vec{k}_\gamma/2+(\vec{k}_\pi-\vec{q})/2$ and $\vec{k}_\pi = \vec{k}_\pi/2+(\vec{k}_\gamma+\vec{q})/2$. We then have

$$U_{\gamma\pi}^{(\lambda)}(\vec{k}_\pi,\vec{k}_\gamma) = \sum_{\sigma_1,\sigma_1'}\sum_{\tau_1,\tau_1'}\int\frac{d\vec{p}}{(2\pi)^3}d\vec{\xi}_1d\vec{\xi}_1'\;e^{i\left\{\vec{p}(\vec{\xi}_1-\vec{\xi}_1')+\frac{\vec{k}_\pi+\vec{k}_\gamma}{2A}(\vec{\xi}_1-\vec{\xi}_1')+\frac{A-1}{2A}\vec{q}(\vec{\xi}_1+\vec{\xi}_1')\right\}}$$
$$\rho_1(\vec{\xi}_1|\vec{\xi}_1')t_{\gamma\pi}^{(\lambda)}(\vec{k}_\pi,\vec{p}-\vec{q}/2;\vec{k}_\gamma,\vec{p}+\vec{q}/2) \tag{7.79}$$

Because of the exponent, we can shift variables again $\vec{p}\to\vec{p}-(\vec{k}_\gamma+\vec{k}_\pi)/2A$ to simplify these expression so that we finally have

$$U_{\gamma\pi}^{(\lambda)}(\vec{k}_\pi,\vec{k}_\gamma) = \sum_{\sigma_1,\sigma_1'}\sum_{\tau_1,\tau_1'}\int\frac{d\vec{p}}{(2\pi)^3}d\vec{\xi}_1d\vec{\xi}_1'\;e^{-i\vec{p}(\vec{\xi}_1'-\vec{\xi}_1)}\;e^{i\frac{A-1}{2A}\vec{q}(\vec{\xi}_1+\vec{\xi}_1')}$$
$$\rho_1(\vec{\xi}_1|\vec{\xi}_1')t_{\gamma\pi}^{(\lambda)}(\vec{k}',\vec{p}-\vec{q}/2-(\vec{k}_\gamma+\vec{k}_\pi)/2A;\vec{k}_\gamma,\vec{p}+\vec{q}/2-(\vec{k}_\gamma+\vec{k}_\pi)/2A) \tag{7.80}$$

This is the expression of the photoproduction amplitude in the PWIA that includes the recoil of the nucleus. It should be noted that an integral on p, representing the Fermi averaging, is involved. Such integral is difficult and model dependent. In order to simplify this integral, I will make another assumption: the *factorisation approximation* [169, 170].

In this approximation, the $t_{\gamma\pi}$ matrix is considered to be a slowly varying function of $\vec{p}$. It is then evaluated at $p = 0$ to simplify the expressions, such that

$$t_{\gamma\pi}^{(\lambda)}\left(\vec{k}', \vec{p} - \frac{\vec{q}}{2} - \frac{\vec{k}_\gamma + \vec{k}_\pi}{2A}; \vec{k}_\gamma, \vec{p} + \frac{\vec{q}}{2} - \frac{\vec{k}_\gamma + \vec{k}_\pi}{2A}\right) = (2\pi)^3\delta(\vec{p})t_{\gamma\pi}^{(\lambda)}\left(\vec{k}', -\frac{\vec{q}}{2} - \frac{\vec{k}_\gamma + \vec{k}_\pi}{2A}; \vec{k}_\gamma, \frac{\vec{q}}{2} - \frac{\vec{k}_\gamma + \vec{k}_\pi}{2A}\right) \tag{7.81}$$

After integration on $\vec{p}$, the expression of $U_{\gamma\pi}(\vec{k}_\pi, \vec{k}_\gamma)$ finally reads

$$U_{\gamma\pi}^{(\lambda)}(\vec{k}_\pi, \vec{k}_\gamma) = \sum_{\sigma_1,\sigma_1'}\sum_{\tau_1,\tau_1'}\int d\vec{\xi}_1\, e^{i\frac{A-1}{A}\vec{q}\vec{\xi}_1}\rho_1(\vec{\xi}_1|\vec{\xi}_1)t_{\gamma\pi}^{(\lambda)}\left(\vec{k}', -\frac{\vec{q}}{2} - \frac{\vec{k}_\gamma + \vec{k}_\pi}{2A}; \vec{k}_\gamma, \frac{\vec{q}}{2} - \frac{\vec{k}_\gamma + \vec{k}_\pi}{2A}\right) \tag{7.82}$$

$$= t_{\gamma\pi}^{(\lambda)}\left(\vec{k}', -\frac{\vec{q}}{2} - \frac{\vec{k}_\gamma + \vec{k}_\pi}{2A}; \vec{k}_\gamma, \frac{\vec{q}}{2} - \frac{\vec{k}_\gamma + \vec{k}_\pi}{2A}\right) \times \hat{\rho}_1\left(\tilde{q}\right) \tag{7.83}$$

where $\tilde{q} = (A-1)/Aq$ and we see the nuclear form factor $\hat{\rho}_1$ appear (6.46). For medium heavy and heavy nuclei, $(A-1)/A \simeq 1$ and $\tilde{q} \simeq q$ and these can be interchanged without any visible impact. This expression is usually called the $t\rho$ form, for obvious reasons. Note that by making the factorisation approximation, we assign fixed values of the momenta to the nucleons before and after the reaction. These can be seen as effective momenta, as these simulate the Fermi motion inside the nucleus. They take into account the recoil of the nucleus and can be re-written in the more usual way as

$$\vec{p}_{1,\text{eff}} = -\frac{\vec{k}_\gamma}{A} + \frac{A-1}{2A}(\vec{k}_\pi - \vec{k}_\gamma) = -\frac{A+1}{2A}\vec{k}_\gamma + \frac{A-1}{2A}\vec{k}_\pi \tag{7.84}$$

$$\vec{p}'_{1,\text{eff}} = -\frac{\vec{k}_\pi}{A} - \frac{A-1}{2A}(\vec{k}_\pi - \vec{k}_\gamma) = -\frac{A+1}{2A}\vec{k}_\pi + \frac{A-1}{2A}\vec{k}_\gamma \tag{7.85}$$

It should be noted that the $t\rho$ form is only a first order term. Higher order terms coming from the dependence in p of $t_{\gamma\pi}^{(\lambda)}$ have been explored for example in [170, 171]. Such calculations are however cumbersome and I will not consider them here.

The amplitude $t_{\gamma\pi}^{(\lambda)}$ should now be evaluated in the γ-A center-of-mass frame. Going back to the notation of Sec. 7.2 and in the γ-N centre-of-mass frame, the amplitude matrix element has the simple form (7.60)

$$t_{\gamma\pi}^{(\lambda)}(\tilde{\vec{k}}_\pi, \tilde{\vec{k}}_\gamma) = \mathcal{F}_2(\tilde{\vec{k}}_\pi, \tilde{\vec{k}}_\gamma; W_{\gamma N})\left[\hat{\tilde{\vec{k}}}_\pi \times \hat{\tilde{\vec{k}}}_\gamma\right] \cdot \vec{\varepsilon}_\lambda \tag{7.86}$$

Let me link the momenta in the γ-N frame with those in the γ-A frame by a Lorentz transformation

$$\tilde{\vec{k}}_{\gamma(\pi)} = \vec{k}_{\gamma(\pi)} + \alpha_{\gamma(\pi)}\vec{P} \tag{7.87}$$

where $\vec{P} = \vec{k}_\gamma + \vec{p}_1$ $(= \vec{k}_\pi + \vec{p}'_1)$ is the total momentum of the γ-N system (π-N system) evaluated in the γ-A (π-A) centre-of-mass frame and where α reads

$$\alpha_\gamma = \frac{1}{W_{\gamma N}}\left(\frac{\vec{P}\cdot\vec{k}_\gamma}{E_\gamma + E_N + W_{\gamma N}} - E_\gamma\right) \qquad \alpha_\pi = \frac{1}{W_{\pi N}}\left(\frac{\vec{P}\cdot\vec{k}_\pi}{E_\pi + E'_N + W_{\pi N}} - E_\pi\right) \tag{7.88}$$

By plugging the expressions (7.84) and (7.85) and Eq.(7.87) in Eq. (7.86), we have

$$\tilde{\vec{k}}_\pi \times \tilde{\vec{k}}_\gamma = \frac{1}{\tilde{k}_\pi \tilde{k}_\gamma} \left(\vec{k}_\pi + \alpha_\pi A_-(\vec{k}_\gamma + \vec{k}_\pi)\right) \times \left(\vec{k}_\gamma + \alpha_\gamma A_-(\vec{k}_\gamma + \vec{k}_\pi)\right) \tag{7.89}$$

$$= \frac{1}{\tilde{k}_\pi \tilde{k}_\gamma} \left(1 + A_-(\alpha_\gamma + \alpha_\pi)\right) \left[\vec{k}_\pi \times \vec{k}_\gamma\right] \tag{7.90}$$

where $A_\pm = (A \pm 1)/2A$. The elementary amplitude in the γ-A center-of-mass frame hence reads

$$t^{(\lambda)}_{\gamma\pi}(\vec{k}_\pi, \vec{k}_\gamma) = \frac{k_\pi k_\gamma}{\tilde{k}_\pi \tilde{k}_\gamma} \left(1 + A_-(\alpha_\gamma + \alpha_\pi)\right) \mathcal{F}_2(\tilde{\vec{k}}_\pi, \tilde{\vec{k}}_\gamma; W_{\gamma N}) \left[\hat{\vec{k}}_\pi \times \hat{\vec{k}}_\gamma\right] \cdot \vec{\varepsilon}_\lambda \tag{7.91}$$

Finally, I will use the phase-space factor $\mathcal{W}_A$ defined in Ref. [128].

$$\mathcal{W}_A = \frac{W_{\gamma N}}{E_{\text{tot}}} \sqrt{\frac{E_A E'_A}{E_N E'_N}} \tag{7.92}$$

to link the amplitude in these two frames. The PWIA amplitude for the coherent photoproduction of neutral pions on spin-isospin zero nuclei then has the form

$$U^{(\lambda)}_{\gamma\pi}(\vec{k}_\pi, \vec{k}_\gamma) = \frac{-i\lambda e^{i\phi\lambda}}{\sqrt{2}} \mathcal{W}_A \frac{k_\pi k_\gamma}{\tilde{k}_\pi \tilde{k}_\gamma} \left(1 + A_-(\alpha_\gamma + \alpha_\pi)\right) \left[\hat{\vec{k}}_\pi \times \hat{\vec{k}}_\gamma\right] \mathcal{F}_2(\tilde{\vec{k}}_\pi, \tilde{\vec{k}}_\gamma; W_{\gamma N}) \hat{\rho}_1(q) \tag{7.93}$$

where ϕ is the azimuthal angle. More compactly, this expression reads

$$U^{(\lambda)}_{\gamma\pi}(\vec{k}_\pi, \vec{k}_\gamma) = F^{(\lambda)}(\theta) \hat{\rho}_1(q) \tag{7.94}$$

where

$$F^{(\lambda)}(\theta) = \frac{-i\lambda e^{i\phi\lambda}}{\sqrt{2}} \mathcal{W}_A \frac{k_\pi k_\gamma}{\tilde{k}_\pi \tilde{k}_\gamma} \left(1 + A_-(\alpha_\gamma + \alpha_\pi)\right) \sin\theta \mathcal{F}_2(\tilde{\vec{k}}_\pi, \tilde{\vec{k}}_\gamma; W_{\gamma N}) \tag{7.95}$$

where the cross product has been replaced by the sine of the scattering angle.

This expression for the photoproduction amplitude calls for a general comment. It should be noticed how in the PWIA, the photoproduction cross section is directly proportional to the square modulus of the density form factor $\hat{\rho}_1$. This illustrates the interest of the coherent photoproduction of neutral pions in the study of the neutron skin thickness. Indeed, because of this direct proportionality, we can expect, within the assumptions of the PWIA and the factorisation approximations, to extract the nuclear (or matter) density directly from the measurement of such observable. If we then know the proton distribution (from electron scattering measurements, for example) we can directly deduce the neutron distribution and hence the neutron skin thickness. In this regard, coherent neutral pion photoproduction should be a rather clean way to extract Δr_{np} (see Sec. 5).

In order to show the variations of the cross section due to changes in the target density, the target is described by three different Fermi-Dirac densities (see Sec. 6.3.1): the first one (black) uses roughly the same parameters of the São Paolo while the second (red) and third (blue) have the same parameters but respectively a radius and a diffuseness increased by respectively 10% and 30%. These densities are displayed in Fig. 7.5.

On Fig. 7.6, the two factors of Eq. (7.94) are displayed for a photoproduction process involving a photon of incident kinetic energy of 180 MeV in the laboratory frame on

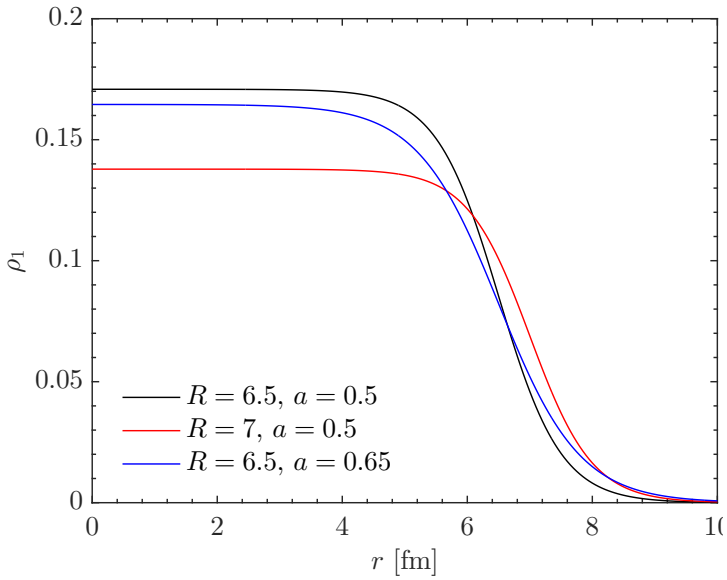

Figure 7.5: The nuclear density of the target described by three different Fermi-Dirac densities.

a ^{208}Pb target. On the left panel, the modulus of $F^{(\lambda)}$ is shown as a function of the scattering angle (in the γ-A centre of mass frame). As it should be noted, the function $F^{(\lambda)}$ resembles a sine function. This is to be expected from its form Eq. (7.93). The Fourier transform of the three densities are shown in log scale on the right panel. Note that the solid part of the curves corresponds to the transferred momenta that contribute to the cross section while the dashed ones do not (see Eq. (7.75)).

As we can see from the right panel of Fig. 7.6, the Fourier transform of the densities $\hat{\rho}_1$ are peaked at $q = 0$ and are normalised to $A = 208$. As the radius of the density increases, the width of the peak at $q = 0$ decreases (compare the red and black curves). A similar observation can be done when the diffuseness increases, although less pronounced (compare the blue and black curves). This has the impact of pushing the zeros of $\hat{\rho}_1$ towards $q = 0$, i.e. towards forward angles. Because in the PWIA, the cross section is proportional to the square of Eq. (7.94), these main characteristics of the densities are directly visible on the photoproduction cross section, displayed in Fig. 7.7. Indeed, we can very clearly observe the shifts of the zeros of the cross section with changes in R and a. Additionally, we can see how the width of the density peak around $q = 0$ has a strong impact on the height of the first peak of the photoproduction cross section. From this very basic analysis, we see which changes in the cross section we can expect from simple variations of the density.

In a similar fashion to what is done in Ref. [128], I will choose $\mathcal{F}_2$ as the isospin average of the elementary amplitudes on neutrons and protons

$$\mathcal{F}_2\rho_1(q) \to \frac{N\mathcal{F}_2^n\rho_1^N(q) + Z\mathcal{F}_2^p\rho_1^Z(q)}{A} \tag{7.96}$$

where the nucleon density has been separated into its contributions from the proton density $\rho_1^Z(q)$ and neutron density $\rho_1^N(q)$.

It should be noted that the choice of prescription for the γ-N energy $W_{\gamma N}$ has not yet been discussed. The calculations shown here have been made within one prescription

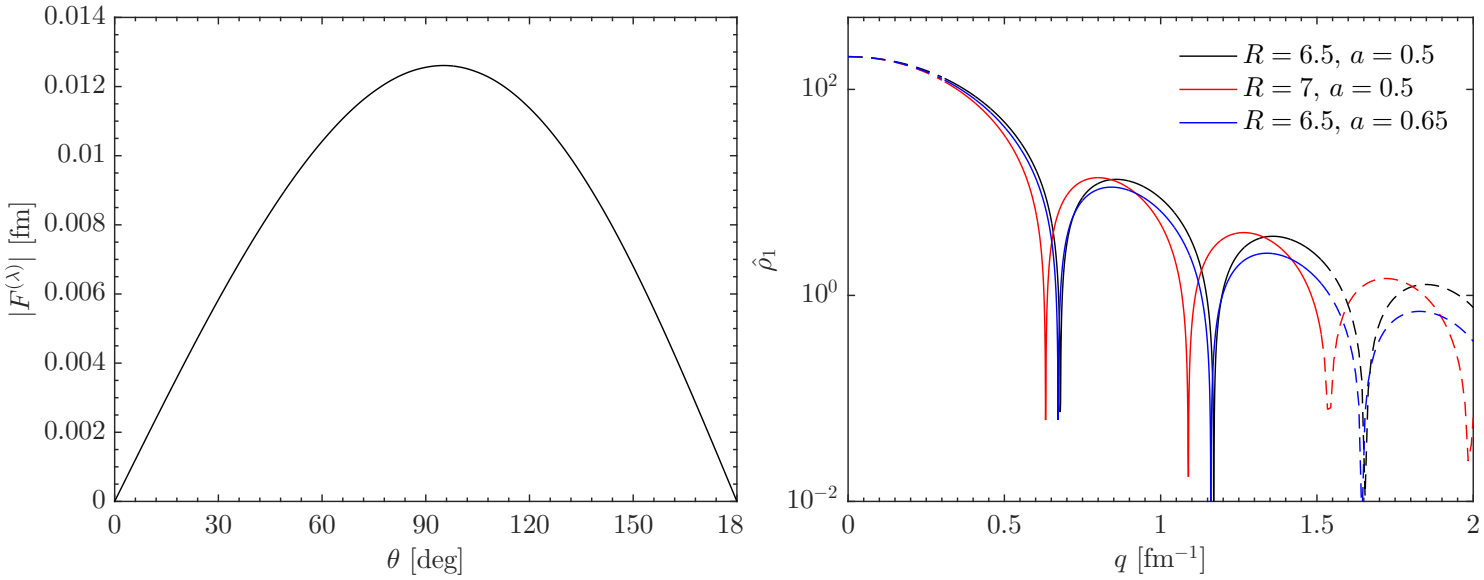

Figure 7.6: The function $|F^{(\lambda)}|$ (see Eq. (7.95)) (left) is displayed for a photoproduction process involving a photon of incident kinetic energy of 180 MeV in the laboratory frame on a ^{208}Pb target. The target is described by three different Fermi-Dirac densities (right, see text for details).

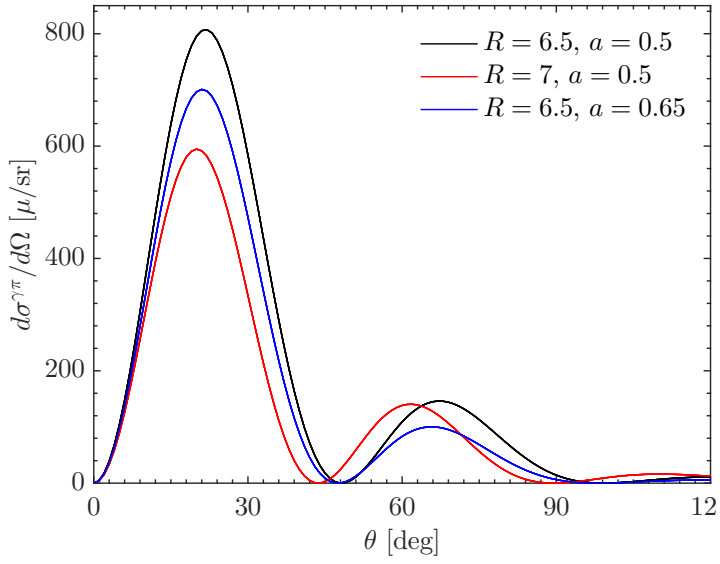

Figure 7.7: Photoproduction cross section for a photon of incident kinetic energy of 180 MeV in the laboratory frame on ^{208}Pb for the three densities shown on Fig. 7.5.

and it is interesting to see how dependent are the photoproduction cross sections on this choice. This is the subject of next section.

7.3.2 Energy of the active photon-nucleon system

It should be noted that in the case of a photoproduction on a nucleus, there are several prescriptions for the choice of the nucleon energy $E_N^{(\prime)}$ in Eqs. (7.67) and (7.68). Contrary to the elementary process, this choice is not unambiguous. This affects the energy of the γ-N active system but also the phase-space factor $\mathcal{W}_A$ (7.92). Following the definitions of Ref. [172], we can try three different prescriptions for the nucleon energy.

Blankenbecler-Sugar choice **(BS)**

In this prescription, the total energy of the target is distributed equally between all the nucleons before the reaction $W_{\gamma N}^{\mathrm{BS}}$ and after $W_{\pi N}^{\mathrm{BS}}$. In other words, the mass of the nucleon is $1/A$ the mass of the target. The mass of the remaining $A-1$ nucleons is then $\frac{(A-1)}{A} m_A$

$$E_N^{(\prime)\,2} - p_1^{(\prime)\,2} = \left(\frac{m_A}{A}\right)^2 \qquad \text{and} \qquad E_{A-1}^{(\prime)\,2} - (\vec{p}_1^{\,(\prime)} + \vec{k}_\gamma)^2 = \left((A-1)\frac{m_A}{A}\right)^2 \tag{7.97}$$

By injecting $E_{A-1}^{(\prime)} = E_A^{(\prime)} - E_N^{(\prime)}$ in the second equation, we find for $E_N^{(\prime)}$

$$E_N^{(\prime)} = \frac{1}{E_A^{(\prime)}} \left[A \left(\frac{m_A}{A}\right)^2 - \vec{p}_1^{\,(\prime)} \cdot \vec{k}_{\gamma(\pi)} \right] \tag{7.98}$$

and hence

$$W_{\gamma N}^{\mathrm{BS}} = \sqrt{\left(\frac{1}{E_A} \left[A \left(\frac{m_A}{A}\right)^2 - \vec{p}_1 \cdot \vec{k}_\gamma \right] + E_\gamma \right)^2 - (\vec{p}_1 + \vec{k}_\gamma)^2} \tag{7.99}$$

and similarly

$$W_{\pi N}^{\mathrm{BS}} = \sqrt{\left(\frac{1}{E'_A} \left[A \left(\frac{m_A}{A}\right)^2 - \vec{p}'_1 \cdot \vec{k}_\pi \right] + E_\pi \right)^2 - (\vec{p}'_1 + \vec{k}_\pi)^2} \tag{7.100}$$

Active nucleon on-shell **(N)**

In this prescription, the struck nucleon is assumed to be on-shell before the reaction $W_{\gamma N}^{\mathrm{N}}$ and after $W_{\pi N}^{\mathrm{N}}$. In other words:

$$E_N^{(\prime)} = \sqrt{m_N^2 + p_1^{(\prime)\,2}} \tag{7.101}$$

and hence

$$W_{\gamma N}^{\mathrm{N}} = \sqrt{\left(\sqrt{m_N^2 + p_1^2} + E_\gamma \right)^2 - (\vec{p}_1 + \vec{k}_\gamma)^2} \tag{7.102}$$

and similarly

$$W_{\pi N}^{\mathrm{N}} = \sqrt{\left(\sqrt{m_N^2 + p_1'^2} + E_\pi \right)^2 - (\vec{p}'_1 + \vec{k}_\pi)^2} \tag{7.103}$$

***Spectator core on-shell* (S)**

In this prescription, the $A-1$ spectator nucleus to which the struck nucleon is bound is assumed on-shell before the reaction $W^{\mathrm{S}}_{\gamma N}$ and after $W^{\mathrm{S}}_{\pi N}$. In other words:

$$E_{A-1} = \sqrt{m^2_{A-1} + (\vec{p}_1 + \vec{k}_\gamma)^2} \tag{7.104}$$

and hence

$$W^{\mathrm{S}}_{\gamma N} = \sqrt{\left(E_A - \sqrt{m^2_{A-1} + (\vec{p}_1 + \vec{k}_\gamma)^2} + E_\gamma\right)^2 - (\vec{p}_1 + \vec{k}_\gamma)^2} \tag{7.105}$$

and similarly

$$W^{\mathrm{S}}_{\pi N} = \sqrt{\left(E'_A - \sqrt{m^2_{A-1} + (\vec{p}'_1 + \vec{k}_\pi)^2} + E_\pi\right)^2 - (\vec{p}'_1 + \vec{k}_\pi)^2} \tag{7.106}$$

In all these prescriptions, the momentum of the struck nucleon $\vec{p}_1$ still needs to be chosen. To take the Fermi motion into account, I use the results of the *factorisation approximation*, already discussed in previous section 7.3.1. While the energies before and after the reaction should be the same, it will not always be the case in all prescriptions because of this assumption. By taking again $A_\pm = (A \pm 1)/2A$, the momenta (7.84) and (7.85) read

$$\vec{p}_1 = -A_+\vec{k}_\gamma + A_-\vec{k}_\pi \tag{7.107}$$

$$\vec{p}'_1 = -A_+\vec{k}_\pi + A_-\vec{k}_\gamma \tag{7.108}$$

and such that the expressions derived above become

$$W^{\mathrm{BS}}_{\gamma N} = \sqrt{\left(\frac{1}{E_A}\left\{\left(\frac{m_A}{A}\right)^2 A - \left[-A_+k^2_\gamma + A_-\vec{k}_\gamma\cdot\vec{k}_\pi\right]\right\} + E_\gamma\right)^2 - A^2_-(\vec{k}_\gamma + \vec{k}_\pi)^2} \tag{7.109}$$

$$W^{\mathrm{BS}}_{\pi N} = \sqrt{\left(\frac{1}{E'_A}\left\{\left(\frac{m_A}{A}\right)^2 A - \left[-A_+k^2_\pi + A_-\vec{k}_\gamma\cdot\vec{k}_\pi\right]\right\} + E_\pi\right)^2 - A^2_-(\vec{k}_\gamma + \vec{k}_\pi)^2} \tag{7.110}$$

$$W^{\mathrm{N}}_{\gamma N} = \sqrt{\left(\sqrt{m^2_N + \left[A^2_+k^2_\gamma + A^2_-k^2_\pi - 2A_-A_+\vec{k}_\gamma\cdot\vec{k}_\pi\right]} + E_\gamma\right)^2 - A^2_-(\vec{k}_\gamma + \vec{k}_\pi)^2} \tag{7.111}$$

$$W^{\mathrm{N}}_{\pi N} = \sqrt{\left(\sqrt{m^2_N + \left[A^2_+k^2_\pi + A^2_-k^2_\gamma - 2A_-A_+\vec{k}_\gamma\cdot\vec{k}_\pi\right]} + E_\pi\right)^2 - A^2_-(\vec{k}_\gamma + \vec{k}_\pi)^2} \tag{7.112}$$

$$W^{\mathrm{S}}_{\gamma N} = \sqrt{\left([E_A + E_\gamma] - \sqrt{m^2_{A-1} + A^2_-(\vec{k}_\gamma + \vec{k}_\pi)^2}\right)^2 - A^2_-(\vec{k}_\gamma + \vec{k}_\pi)^2} \tag{7.113}$$

$$= \sqrt{\left([E'_A + E_\pi] - \sqrt{m^2_{A-1} + A^2_-(\vec{k}_\gamma + \vec{k}_\pi)^2}\right)^2 - A^2_-(\vec{k}_\gamma + \vec{k}_\pi)^2} \tag{7.114}$$

Note that the Blankenbecler-Sugar and active nucleon on-shell prescriptions are different if we calculate the energy before (the prior case) or after (the post case) the reaction. However, this difference is not big if we make the factorisation approximation. On the

other hand, within the factorisation approximation, the energy in the spectator on-shell prescription is identical in the prior and post forms.

In a similar fashion to what has been done in Ref. [172], we can quantify the kinematically accessible energies of the γ-N and π-N systems by studying their dependence on the momentum of the struck nucleon. To have a rough idea of the impact of the Fermi motion on $W_{\gamma N}$ and $W_{\pi N}$, let us suppose a Fermi gas model behaviour for the momentum of the nucleons inside the nucleus. The momentum $\vec{p}_1$ is then the sum of the average nucleon momentum in the nucleus $-\vec{k}_\gamma/A$ and some momentum $\vec{p}$ which magnitude ranges from 0 to p_F and whose direction is uniformly distributed

$$\vec{p}_1 = -\frac{\vec{k}_\gamma}{A} + \vec{p} \tag{7.115}$$

Following Ref. [173], we can consider the Fermi momentum p_F to be pretty much constant around 260 MeV/c for all nuclei. I will do these calculations both on a light target and a heavy one, to see how it impacts this range of energies.

On the left panel of Fig. 7.8, I display the minimal (when $\vec{k}_\gamma$ is aligned with $\vec{p}$) and maximal (when they are in opposite direction) energies available in the $\gamma - N$ system as a function of the initial momentum of the struck nucleon for the reaction on a ^{12}C target at an incident photon kinetic energy $T_\gamma = 180$ MeV in the lab frame . While the BS (black) and S (blue) prescription remain close to each other throughout the whole range of momenta in the Fermi gas-like approximation, they present a sizeable difference with the N (red) prescription. This difference is visible both in the magnitude of the energy, which is globally larger for N, but also in the behaviour of its momentum dependence, which grows (and decays) linearly for N, while it presents a maximum for the two other prescriptions. It should be noted that there is a slight difference in energy in the prior case (solid lines) and in the post case (dashed) for the BS and N prescritions. These differences are the largest in the BS prescription. For the S however, the prior and post cases are superimposed.

In thick lines, I also display the energies obtained when making the factorisation approximation. Note that in the latter case, the variation of energy is solely due to the production angle of the pion, with small and large angles corresponding to lower and higher energies, respectively. We observe that the range of energies in the factorisation approximation does not correspond to the whole range of Fermi momenta. This is expected since the factorisation approximation attributes effective momentum and direction to the struck nucleon. Only a tiny portion of the energies otherwise available in the Fermi gas-like model are then available in this approximation. It should also be noted that the differences between the prior and post cases are much smaller when making the factorisation approximation. Also, both the BS (black) and S (blue) prescriptions are superimposed in this approximation. Finally, the difference between the N and other prescriptions seems to exist only in magnitude. Depending on the angle at which the pion is photoproduced, the difference goes from around 8 MeV at low angles to nearly 20 MeV at larger ones.

The same kind of calculations are done on a ^{208}Pb target and displayed on the right panel of Fig. 7.8. On heavier targets, the discrepancies between the prior and post cases are much smaller. Moreover, the differences between the BS and S prescriptions is then nearly imperceptible. The discrepancies with the N prescription remain as large as for the light target, however.

Because of these sizeable differences between the different prescriptions, one should expect an important difference in the photoproduction cross sections for these various

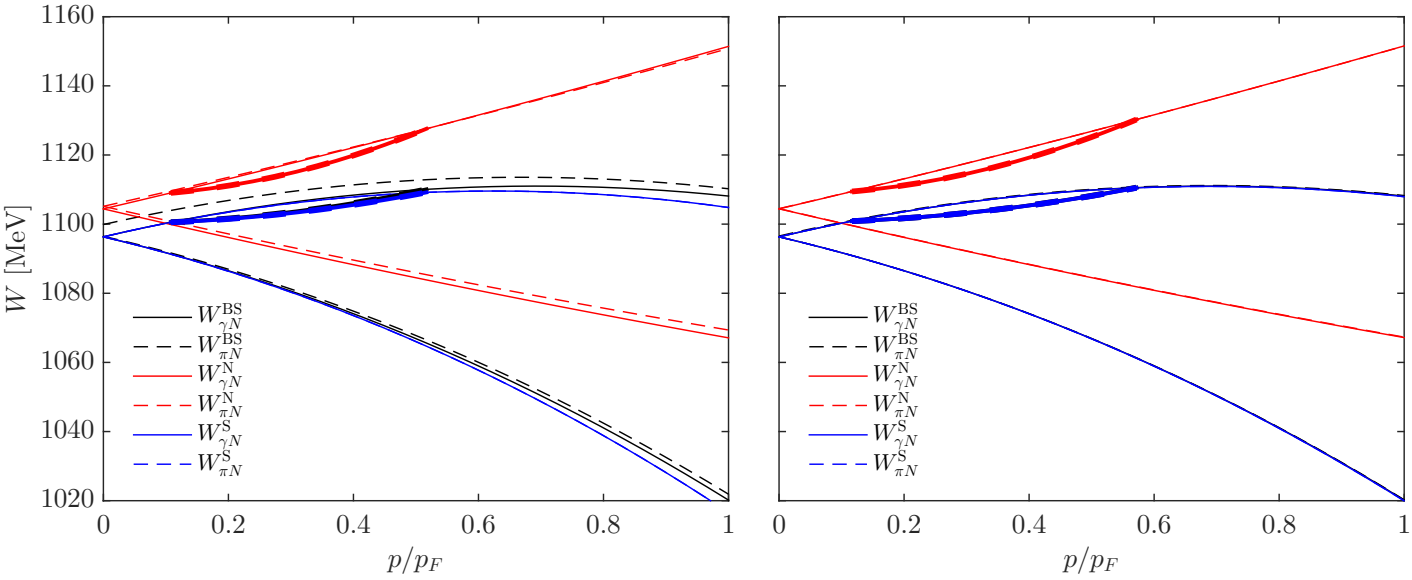

Figure 7.8: Whole range of kinematically possible energies available in the $\gamma - N$ system as a function of p in the different prescriptions when considering the whole range of momenta in the Fermi gas model for p in Eq. (7.115). The reaction photoproduction takes place on a ^{12}C target (left) or a ^{208}Pb one (right) at an incident photon kinetic energy of 180 MeV in the lab frame. Thick lines correspond to the energies available in the factorisation approximation.

prescriptions. On Fig. 7.9, this dependence is tested by comparing photoproduction cross sections in the PWIA for both targets at an incident photon kinetic energy of 180 MeV in the lab. As expected, the N prescription (red) is significantly different than the BS (black) and S (blue) ones. Here, only the prior calculations are shown, as the post ones are nearly identical to their corresponding prior.

From these results, we see that the choice of the energy of the active γN system has a significant influence on the photoproduction cross sections. *A priori*, there is no clear reason to choose one prescription over the other and these will have to be compared to actual data to determine which one fits best. Note that because the BS and S prescriptions are nearly identical and because the prior and post forms do not induce much variations on the cross sections, I will consider, in the sake of conciseness, only the N and S prescriptions in the prior form in the next sections.

7.3.3 Distorted Wave Impulse Approximation (DWIA)

While we can expect the PWIA to be a nice approximation at low energies, distortion has a significant impact on the photoproduction cross section at energies around the delta resonance energy. The effect of the rescattering of the pion by the nucleus can be taken into account in the Distorted Wave Impulse Approximation (DWIA), which adds a second term to the photoproduction cross section (Eq. (7.36)).

When considering the final-state interactions, the photoproduction cross section in the distorted wave impulse approximation (DWIA) reads [133, 128]

$$\frac{d\sigma^{\gamma\pi}}{d\Omega} = \frac{k_\pi}{k_\gamma}\frac{1}{2}\sum_\lambda \left| U^{(\lambda)}_{\gamma\pi}(\vec{k}_\pi, \vec{k}_\gamma) + D^{(\lambda)}_{\gamma\pi}(\vec{k}_\pi, \vec{k}_\gamma) \right|^2 \tag{7.116}$$

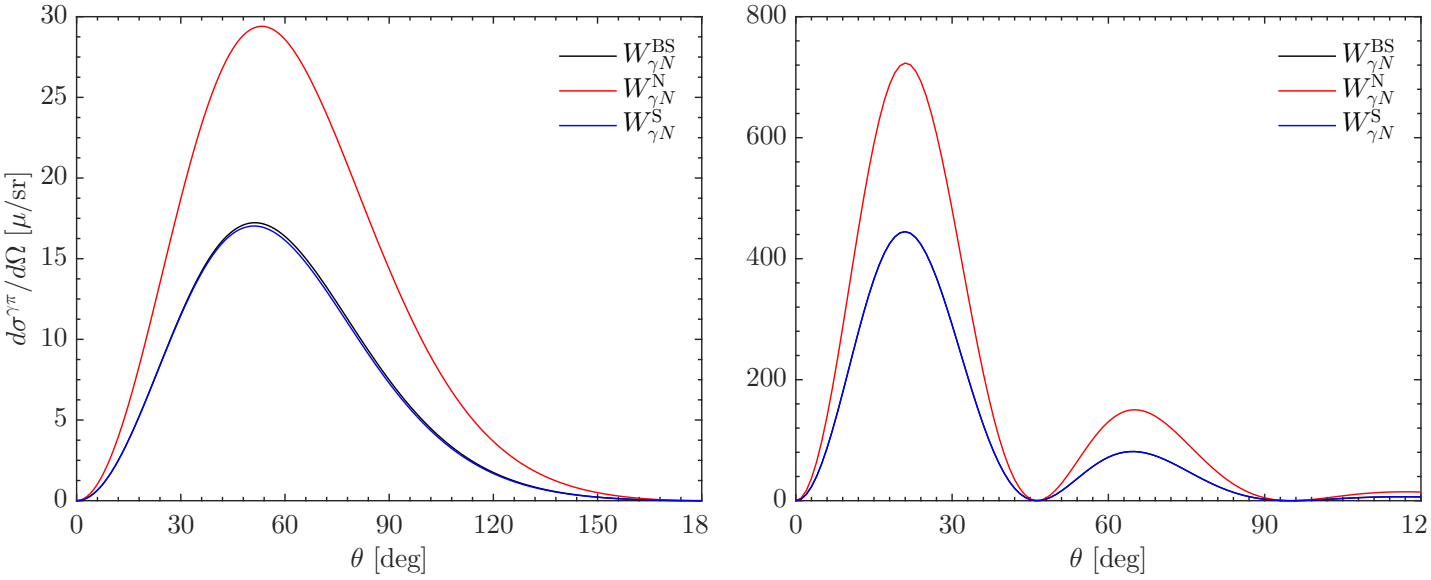

Figure 7.9: Pion photoproduction cross section in the PWIA on a ^{12}C target (left) and a ^{208}Pb one (right) at an incident photon kinetic energy of 180 MeV in the lab. BS (black), N (red) and S (blue) prescriptions are displayed in the prior form.

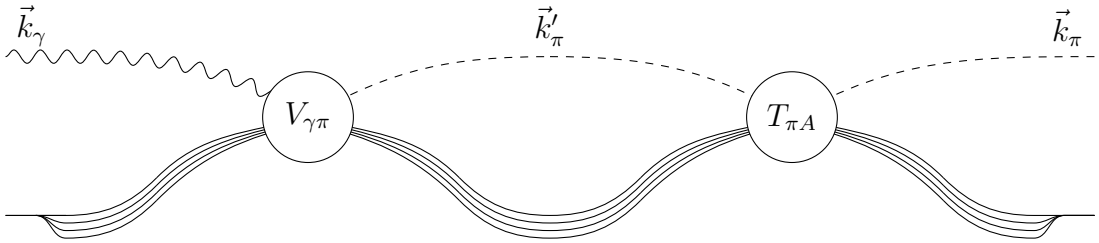

Figure 7.10: Kinematics of the photoproduction of a pion on a single nucleon in a nucleus in the center-of-mass frame of the γ-A system.

where the additional $D^{(\lambda)}_{\gamma\pi}$ term coming from the right hand side of Eq. (7.36) has the form

$$D^{(\lambda)}_{\gamma\pi}(\vec{k}_\pi, \vec{k}_\gamma) = -4\pi \frac{A-1}{A} \int d\vec{k}'_\pi \tilde{T}_{\pi A}(\vec{k}_\pi, \vec{k}'_\pi) G(\vec{k}'_\pi) U^{(\lambda)}_{\gamma\pi}(\vec{k}'_\pi, \vec{k}_\gamma) \tag{7.117}$$

where $\tilde{T}_{\pi A}$ is the T-matrix of the scattering of a pion from k'_π to k_π momentum (see Eq. (7.44)). More on this matter and the way to solve the T-matrix for the scattering of a pion on a nucleus will be discussed in Sec. 8.3.

It should be noted that in Eq. (7.117), the amplitude $U^{(\lambda)}_{\gamma\pi}$ is needed at off-shell momenta. All the developments of Sec. 7.3.1 have been made with the idea that the produced pion is on-shell however. Moreover, the Lorentz transformations defined in Eq. (7.87) are only defined for on-shell values of the pion momentum. As it has been done in Ref. [128], I will consider that the Lorentz transformation still holds even for off-shell momenta.

Additionally, I will multiply the photoproduction amplitude by a dipole-like form factor

$$g(\tilde{k}_\pi; \tilde{k}_{\pi,0}) = \left(\frac{\Lambda^2 + \tilde{k}_{\pi,0}^2}{\Lambda^2 + \tilde{k}_\pi^2} \right)^2 \tag{7.118}$$

where $\tilde{k}_{\pi,0}$ is the on-shell value of the momentum of the pion in the π-N centre-of-mass frame and where Λ is a cut-off parameter which I will fix to 450 MeV, like in Ref. [128]. For off-shell values of the pion momentum, the photoproduction amplitude hence reads

$$U_{\gamma\pi}^{(\lambda)}(\vec{k}'_\pi, \vec{k}_\gamma) = U_{\gamma\pi}^{(\lambda)}(\vec{k}'_{\pi,0}, \vec{k}_\gamma) g(\tilde{k}'_\pi; \tilde{k}_{\pi,0}) \tag{7.119}$$

where $\vec{k}'_{\pi,0}$ is a vector in the same direction as $\vec{k}'_\pi$ but of magnitude $k'_{\pi,0}$, the on-shell momentum of the pion.

8 Modeling the final state interactions

As we have seen in Sec. 7.3.3, the rescattering of the pion after its production should be accounted for. In order to model these final state interactions, we need the T-matrix of the π-A scattering process and hence, we need a potential that correctly simulates this interaction.

As we have seen in Sec. 7.1.1, this potential can be built from the the much simpler elementary pion-nucleon interaction. In this section and in a very similar fashion as I have done in previous Sec. 7.3 for photoproduction, I will start by describing the pion-nucleon interaction, with the help of a partial wave expansion. From this potential, I will then build the π-A potential.

After this potential has been defined, I will discuss how to calculate the T-matrix through the resolution of the Lippmann-Schwinger equation. The numerical methods used to solve such equation will be discussed later in this section.

8.1 Elementary pion-nucleon interaction

The elementary pion-nucleon scattering is the process of a pion interacting with a free nucleon. The kinematic variables of this process in the π-N centre-of-mass frame are shown on Fig. 8.1. Like in Sec. 7.2, the tilde reminds us that we are in the π-N centre-of-mass frame, in order to clearly dissociate them from the pion-nucleus variables that we will encounter in next section.

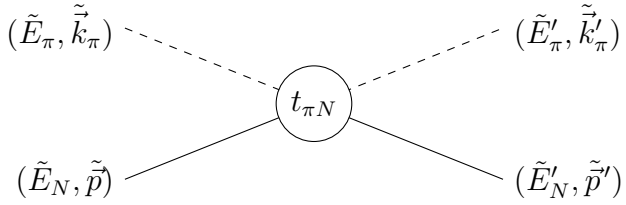

Figure 8.1: Kinematics of the elementary pion-nucleon scattering. The quadrivectors of the initial (final) pion and nucleons correspond to the index $\pi^{(\prime)}$ and $N^{(\prime)}$, respectively.

By definition, in the π-N frame, the nucleon initial (final) momentum $\tilde{\vec{p}}^{(\prime)}$ is opposite to the pion one $\tilde{\vec{k}}_\pi^{(\prime)}$, i.e. $\tilde{\vec{p}}^{(\prime)} = -\tilde{\vec{k}}_\pi^{(\prime)}$. Because all particles are on-shell, the pion and nucleon energies read

$$\tilde{E}_\pi^{(\prime)} = \sqrt{\tilde{k}_\pi^{(\prime)\,2} + m_\pi^2} \qquad \text{and} \qquad \tilde{E}_N^{(\prime)} = \sqrt{\tilde{k}_\pi^{(\prime)\,2} + m_N^2} \tag{8.1}$$

where I remind the reader that m_π and m_N are the pion and free nucleon masses, respectively. The total energy of the reaction is defined as $\tilde{E}_{\pi N} = \tilde{E}_\pi + \tilde{E}_N$. I will consider the initial pion momentum to be aligned with the $\hat{\boldsymbol{z}}$ axis. The scattering angle, i.e. the angle between the final and initial pion momenta is defined as $\tilde{\theta}$.

In the π-N centre-of-mass frame, the scattering amplitude to final momentum $\tilde{\vec{k}}'_\pi$ can be expanded in the most general way into a spin non-flip and spin-flip part. Each of these parts is a function of the total energy $\tilde{E}_{\pi N}$ and the scattering angle $\tilde{\theta}$. The scattering amplitude reads

$$f_{\pi N}(\tilde{\vec{k}}'_\pi, \tilde{\vec{k}}_\pi) = g\left(\tilde{E}_{\pi N}, \tilde{\theta}\right) + ih\left(\tilde{E}_{\pi N}, \tilde{\theta}\right) \vec{\sigma} \cdot \vec{n} \tag{8.2}$$

where $\vec{n}$ is the unit vector $\tilde{\vec{k}}_\pi \times \tilde{\vec{k}}'_\pi / \sin\tilde{\theta}$ and $\vec{\sigma}$ is the nucleon spin vector. Since both the orbital and total angular momenta, l and j, and the total isospin T are conserved, it is convenient to expand this in partial waves and into its isospin components as [174]

$$f_{\pi N}(\tilde{\vec{k}}'_\pi, \tilde{\vec{k}}_\pi) = \sum_{T=\frac{1}{2},\frac{3}{2}} \hat{Q}_T \sum_l (2l+1) \sum_j \hat{Q}_{l,j} P_l(\cos\tilde{\theta}) f^l_{2T,2j} \tag{8.3}$$

where $\hat{Q}_T$ is the projector on a total isostpin T and $\hat{Q}_{l,j}$ is a projector on a π-N state of orbital angular momentum l and total angular momentum j (with $\vec{j}$ being the result of the coupling of $\vec{l}$ with the spin of the nucleon $\vec{\sigma}$). Their expressions read, respectively

$$\begin{cases} \hat{Q}_{T=\frac{1}{2}} = \dfrac{1}{3}\left(1 - \hat{t}_\pi \cdot \hat{\tau}_N\right) \\ \hat{Q}_{T=\frac{3}{2}} = \dfrac{1}{3}\left(2 + \hat{t}_\pi \cdot \hat{\tau}_N\right) \end{cases} \tag{8.4}$$

where $\vec{t}_\pi$ and $\vec{t}_N = \vec{\tau}_N/2$ are the pion and nucleon isospin vectors and

$$\begin{cases} \hat{Q}_{l,j=|l-\frac{1}{2}|} \equiv \hat{Q}_{l,-} = \dfrac{l - \vec{\sigma}\cdot\vec{l}}{2l+1} \\ \hat{Q}_{l,j=|l+\frac{1}{2}|} \equiv \hat{Q}_{l,+} = \dfrac{l+1+\vec{\sigma}\cdot\vec{l}}{2l+1} \end{cases} \tag{8.5}$$

where $\vec{l}$ is the orbital angular momentum and $\vec{\sigma}$ is the spin vector. Note that since the application of $\vec{\sigma}\cdot\vec{l}$ on a Legendre polynomial gives [174]

$$\left(\vec{\sigma}\cdot\vec{l}\right) P_l(\cos\theta) = -i\left(\vec{\sigma}\cdot\vec{n}\right) P'_l(\cos\theta)\sin\theta \tag{8.6}$$

The different terms of Eq. (8.3) can then be regrouped such that the scattering amplitude can thus be expanded as

$$f_{\pi N}(\tilde{\vec{k}}'_\pi, \tilde{\vec{k}}_\pi) = \sum_l \left[f^l_0 + f^l_1\left(\hat{t}_\pi\cdot\hat{\tau}_N\right)\right] P_l(\cos\tilde{\theta}) + \sum_l \left[f^l_2 + f^l_3\left(\hat{t}_\pi\cdot\hat{\tau}_N\right)\right]\left(\vec{\sigma}\cdot\vec{n}\right) P'_l(\cos\tilde{\theta})\sin\tilde{\theta} \tag{8.7}$$

where

$$\begin{cases} f^l_0 = \dfrac{1}{3}\left[l(f^l_{1,|2l-1|} + 2f^l_{3,|2l-1|}) + (l+1)(f^l_{1,2l+1} + 2f^l_{3,2l+1})\right] \\ f^l_1 = \dfrac{1}{3}\left[l(f^l_{3,|2l-1|} - f^l_{1,|2l-1|}) + (l+1)(f^l_{3,2l+1} - f^l_{1,2l+1})\right] \\ f^l_2 = \dfrac{i}{3}\left[(f^l_{1,|2l-1|} + 2f^l_{3,|2l-1|}) - (f^l_{1,2l+1} + 2f^l_{3,2l+1})\right] \\ f^l_3 = \dfrac{i}{3}\left[(f^l_{3,|2l-1|} - f^l_{1,|2l-1|}) - (f^l_{3,2l+1} - f^l_{1,2l+1})\right] \end{cases} \tag{8.8}$$

The partial wave amplitudes $f^l_{2T,2j}$ are energy dependent (through their momentum dependence). They can be expressed through the π-N scattering phase shifts in the different channels $\delta^l_{2T,2j}$ as [174]

$$f^l_{2T,2j}(\tilde{k}_\pi) = \frac{e^{i\delta^l_{2T,2j}}\sin(\delta^l_{2T,2j}}{\tilde{k}_\pi} \tag{8.9}$$

These phase shifts have been determined at several energies and have also been parametrized. An example of such parametrisation is given in Refs. [175, 176], which we will later refer to as the SAID parametrization. In this parametrisation, the partial-wave amplitudes and resonances have been extracted and parametrised from an extensive partial-wave analysis of $\pi^{\pm}$-p elastic scattering and charge-exchange data on a range of energies going from threshold to nearly 3 GeV in the laboratory pion kinetic energy.

At low and intermediate energies the only resonant phase is the one associated with the Δ resonance (P_{33}). At the energies we will consider here, the s and p waves are dominant [174]. We can thus further reduce this expression by introducing the following parameters

$$\begin{cases} b_0 \equiv f_0^0 = \dfrac{1}{3}\left(f_{1,1}^0 + 2f_{3,1}^0\right) \\ b_1 \equiv f_1^0 = \dfrac{1}{3}\left(f_{3,1}^0 - f_{1,1}^0\right) \end{cases} \quad \text{and} \quad \begin{cases} c_0 \equiv \dfrac{f_0^1}{\tilde{k}_\pi^2} = \dfrac{1}{3\tilde{k}_\pi^2}\left(f_{1,1}^1 + 2f_{3,1}^1 + 2f_{1,3}^1 + 4f_{3,3}^1\right) \\ c_1 \equiv \dfrac{f_1^1}{\tilde{k}_\pi^2} = \dfrac{1}{3\tilde{k}_\pi^2}\left(f_{3,1}^1 - f_{1,1}^1 + 2f_{3,3}^1 - 2f_{1,3}^1\right) \\ d_0 \equiv \dfrac{f_2^1}{\tilde{k}_\pi^2} = \dfrac{i}{3\tilde{k}_\pi^2}\left(f_{1,1}^1 + 2f_{3,1}^1 - f_{1,3}^1 - 2f_{3,3}^1\right) \\ d_1 \equiv \dfrac{f_3^1}{\tilde{k}_\pi^2} = \dfrac{i}{3\tilde{k}_\pi^2}\left(f_{3,1}^1 - f_{1,1}^1 - f_{3,3}^1 + f_{1,3}^1\right) \end{cases} \tag{8.10}$$

such that the scattering amplitude reads

$$f_{\pi N}(\tilde{\vec{k}}'_\pi, \tilde{\vec{k}}_\pi) = b_0 + b_1(\vec{t}_\pi \cdot \vec{\tau}_N) + \left[c_0 + c_1(\vec{t}_\pi \cdot \vec{\tau}_N)\right](\tilde{\vec{k}}'_\pi \cdot \tilde{\vec{k}}_\pi) + i\left[d_0 + d_1(\vec{t}_\pi \cdot \vec{\tau}_N)\right]\vec{\sigma} \cdot (\tilde{\vec{k}}'_\pi \times \tilde{\vec{k}}_\pi) \tag{8.11}$$

The parameters b_i, c_i and d_i are complex energy dependent scalars. The most significant ones are b_0 and c_0, which are found in the isospin-independent part of the interaction, as well as b_1, the s-wave isospin-dependent parameter. Their energy-dependence is represented on Fig. 8.2. The other parameters have a much less important role. As later, the scattering is considered on a nucleus of spin nil, d_0 and d_1 will have no influence at all and the spin dependent part can hence be neglected.

It should be noted that at the energies we are interested in (below 100 MeV), most of these parameters are very slowly varying functions of the energy, with the exception of Re$[b_0]$ and Im$[b_0]$. Also, s-wave parameters are repulsive (their real part is negative) while p-wave ones are attractive up to the resonance.

Finally, the π-N interaction in the π-N center-of-mass frame is given by

$$f_{\pi N}(\tilde{\vec{k}}'_\pi, \tilde{\vec{k}}_\pi; \tilde{E}_{\pi N}) = b_0 + b_1(\vec{t}_\pi \cdot \vec{\tau}_N) + \left[c_0 + c_1(\vec{t}_\pi \cdot \vec{\tau}_N)\right](\tilde{\vec{k}}'_\pi \cdot \tilde{\vec{k}}_\pi) \tag{8.12}$$

where I have added the energy dependence of the amplitude explicitly in the arguments of $f_{\pi N}$. The transition matrix evaluated in the π-N centre of mass frame can then be constructed from the simple relation [177]

$$t_{\pi N}^{\pi N}(\tilde{\vec{k}}'_\pi, \tilde{\vec{k}}_\pi; \tilde{E}_{\pi N}) = -\frac{4\pi}{2\bar{\omega}_{\pi N}} f_{\pi N}(\tilde{\vec{k}}'_\pi, \tilde{\vec{k}}_\pi; \tilde{E}_{\pi N}) \tag{8.13}$$

where, the πN "exponent" marks the centre-of-mass frame in which this expression is valid, i.e. the π-N centre-of-mass frame here. Similarly to Eq. (7.45), $\bar{\omega}_{\pi N}$ is a reduced energy for the π-N system which reads

$$\bar{\omega}_{\pi N} = \frac{\tilde{E}_\pi \tilde{E}_N}{\tilde{E}_{\pi N}} \tag{8.14}$$

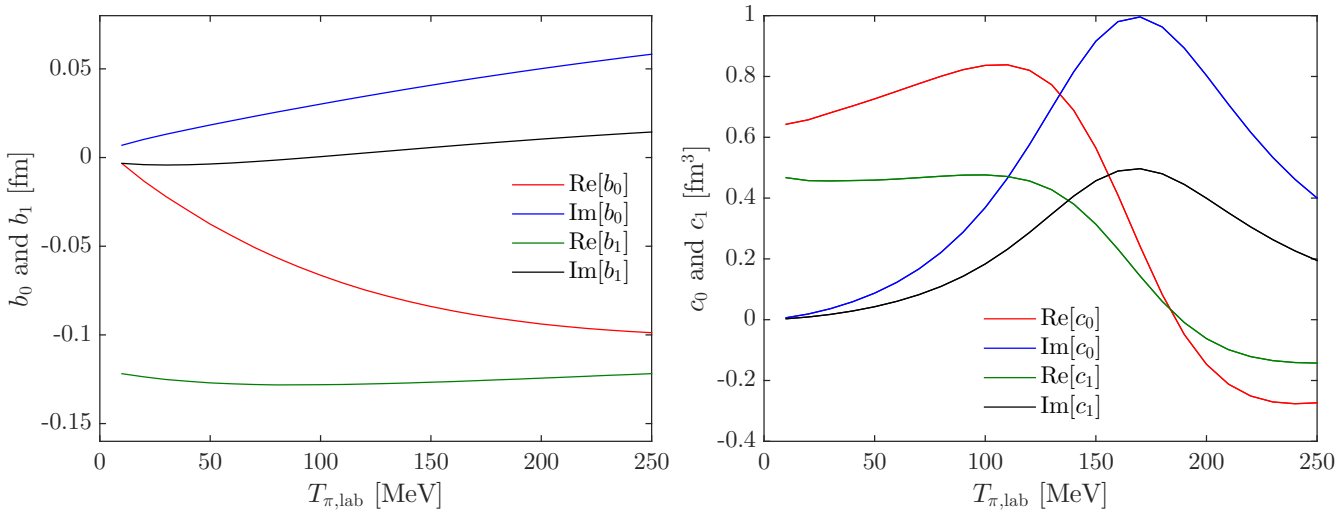

Figure 8.2: Real and imaginary parts of b_0 and b_1 (left) and c_0 and c_1 (right) as a function of the laboratory pion energy. Coefficients are calculated from the phaseshifts Eq. (8.9) which are extracted from the web interface of SAID http://gwdac.phys.gwu.edu/

8.2 Interaction of a pion with a nucleus

As we have seen in Sec. 7.1, the KMT formalism allows me to build an optical potential for the pion-nucleus interaction from the t-matrix of the elementary process on a single nucleon. In the impulse approximation discussed in Sec. 7.1.1, only one-body mechanisms are considered and the elementary t-matrix are considered on a free nucleon. From Eq. (7.32), we see that this potential contains first order and second order scattering. Both orders are described in the next two sections. The first order describes the scattering of a pion on one single nucleon. Correspondingly, the second order describes the scattering and subsequent rescattering of a pion on two different nucleons.

In the KMT formalism and in the expressions derived above, a pion can always be found in the intermediate state. This comes from the fact that no real absorption can take place in an elementary pion-nucleon process. Indeed, due to energy and momentum conservation, several nucleons must be involved for a true absorption to happen. In a nucleus, true absorption is possible as the kinetic and mass energy of the pion can then be shared among the bound nucleons of the nucleus. One should then also consider this process in the π-A potential. Because the absorption process seems to be dominated by two-nucleon processes [178, 179, 180, 181].

As we will see, the two-nucleon density matrix Eq. (6.47) is needed to build the second order and absorptive part of the potential. This can cause some issues, especially for the phenomenological and experimental densities of Sec. 6.3, for which the two-nucleon density matrix is not known. Because I will need a potential that allows me to use such densities, I will finally present the MSU potential. This potential has also been derived in the KMT formalism but makes some further simplifying assumptions which I will briefly discuss.

8.2.1 First order of the interaction

The first order of this potential describes the scattering of a pion on a single nucleon. The useful kinematic variables of the reaction are shown on Fig. 8.3. In the plane wave impulse

approximation, the first-order potential matrix element for this reaction then reads in the momentum space (see Eq. (7.34))

$$V^{\text{1st}}_{\pi A,\text{opt}}(\vec{k}'_\pi, \vec{k}_\pi) = \left\langle k'_\pi \right| V^{\text{1st}}_{\pi A,\text{opt}} \left| k_\pi \right\rangle = A \left\langle k'_\pi \right| \left\langle \Phi_0 \right| t_{\pi N} \left| \Phi_0 \right\rangle \left| k_\pi \right\rangle \tag{8.15}$$

This expression is the equivalent of Eq. (7.70) for π-N scattering. Correspondingly, in a very similar fashion to what has been done for photoproduction to get to Eq. (7.83), I will apply the factorisation approximation such that previous expression can be written in the $t\rho$ form

$$V^{\text{1st}}_{\pi A,\text{opt}}(\vec{k}'_\pi, \vec{k}_\pi) = t_{\pi N}\left(\vec{k}'_\pi, -\frac{\vec{q}}{2} - \frac{\vec{k}_\pi + \vec{k}'_\pi}{2A}, \vec{k}_\pi, \frac{\vec{q}}{2} - \frac{\vec{k}_\pi + \vec{k}'_\pi}{2A}\right) \times \hat{\rho}_1\left(\frac{A-1}{A} q\right) \tag{8.16}$$

where the momentum transfer for π-A scattering is

$$\vec{q} = \vec{k}'_\pi - \vec{k}_\pi \tag{8.17}$$

and where $\hat{\rho}_1$ is the Fourier transform of the density Eq. (6.46). It should be reminded that in this expression, there is an implicit summation on spins and isospins in the integral. In coherent processes on a spin nil nucleus, where the nucleus remains in its ground state, $\sigma_1 = \sigma'_1$ and $\tau_1 = \tau'_1$. Only the spin non-flip part of the potential will hence contribute (the coefficients b_0 and c_0). Finally, effective nucleon momenta $\vec{p}$ and $\vec{p}'$ can be attributed to the initial and final nucleon momenta. These are defined in a very similar fashion as in Eqs. (7.84) and (7.85) and read

$$\vec{p} = -\frac{A+1}{2A}\vec{k}_\pi + \frac{A-1}{2A}\vec{k}'_\pi \tag{8.18}$$

$$\vec{p}' = -\frac{A+1}{2A}\vec{k}'_\pi + \frac{A-1}{2A}\vec{k}_\pi \tag{8.19}$$

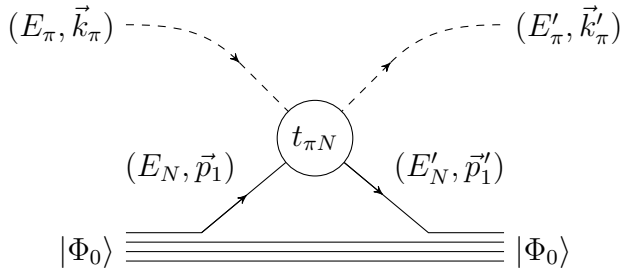

Figure 8.3: Relevant kinematic variables of the reaction of first order scattering of a pion with momentum $\vec{k}_\pi$ and scattered to final momentum $\vec{k}'_\pi$ on a nucleon with initial and final momenta momentum $\vec{p}_1$ and $\vec{p}'_1$, respectively.

It should be noted that we still need the expression of the t-matrix in the π-A centre-of-mass frame. To do so, let me define the total centre-of-mass energy of the π-N system before (after) the reaction as

$$W^{(\prime)}_{\pi N} = \sqrt{E^{(\prime)\,2}_{\pi N} - P^{(\prime)\,2}} \tag{8.20}$$

where the total energy $E^{(\prime)}_{\pi N}$ is the sum of the pion and nucleon energies $E^{(\prime)}_{\pi}+E^{(\prime)}_{N}$ and where the total momentum of the π-N system before (after) the reaction $\vec{P}^{(\prime)} = \vec{k}_\pi+\vec{p}(= \vec{k}'_\pi+\vec{p}')$. The same Lorentz transform Eq. (7.87) can then be used for scattering, *mutatis mutandis*.

For on-shell initial and final momenta the t-matrix for the π-N scattering in the π-A centre-of-mass frame reads [177]

$$t^{\pi A}_{\pi N}(\vec{k}'_\pi, \vec{k}_\pi; W_{\pi N}) = \sqrt{\frac{\tilde{E}_\pi \tilde{E}'_\pi \tilde{E}_N \tilde{E}'_N}{E_\pi E'_\pi E_N E'_N}}\; t^{\pi N}_{\pi N}(\tilde{\vec{k}}'_\pi, \tilde{\vec{k}}_\pi; \tilde{E}_{\pi N}) \tag{8.21}$$

where the πA "exponent" marks the centre-of-mass frame in which this expression is valid, i.e. the π-A one. In this expression, the energies of the pion and the nucleon read

$$\tilde{E}^{(\prime)}_\pi = \frac{E^{(\prime)}_\pi E^{(\prime)}_{\pi N} - \vec{k}^{(\prime)}_\pi \cdot \vec{P}^{(\prime)}}{W^{(\prime)}_{\pi N}} \qquad \text{and} \qquad \tilde{E}^{(\prime)}_N = \frac{E^{(\prime)}_N E^{(\prime)}_{\pi N} - \vec{p}^{(\prime)} \cdot \vec{P}^{(\prime)}}{W^{(\prime)}_{\pi N}} \tag{8.22}$$

To be consistent with what has been done for photoproduction, the same energy prescription for the π-N energy must be chosen.

It should be noted that in the DWIA form of the pion photoproduction Eq. (7.117), the T-matrix for the π-A scattering is needed at off-shell momenta. This is also the case in the resolution of the Lippmann-Schwinger equation (see later in Sec. 8.3). However, all the developments of this section have been made with the idea that the impinging and scattered pion are on-shell. The Lorentz transformations defined in Eq. (7.87) are only defined for on-shell values of the pion and nucleon momenta. As it has been done in Ref. [128] and for photoproduction, I will consider that this transformation still holds even for off-shell momenta

It is useful to symmetrise the expression of the reduced πN energy Eq. (8.14) into

$$\bar{\omega}_{\pi N} = \sqrt{\frac{\tilde{E}_\pi \tilde{E}_N}{\tilde{E}_{\pi N}} \frac{\tilde{E}'_\pi \tilde{E}'_N}{\tilde{E}'_{\pi N}}} \tag{8.23}$$

With this definition and Eqs. (8.13) and (8.21) the $t_{\pi N}$ matrix in the π-A center-of-mass frame reads

$$t^{\pi A}_{\pi N}(\vec{k}'_\pi, \vec{k}_\pi; W_{\pi N}) = -4\pi \sqrt{\frac{\tilde{E}_{\pi N}}{2E_\pi E_N} \frac{\tilde{E}'_{\pi N}}{2E'_\pi E'_N}}\, f_{\pi N}(\tilde{\vec{k}}'_\pi, \tilde{\vec{k}}_\pi; \tilde{E}_{\pi N}) \tag{8.24}$$

$$= -4\pi \mathcal{W}^{\pi A}_{\pi N}\, f_{\pi N}(\tilde{\vec{k}}'_\pi, \tilde{\vec{k}}_\pi; \tilde{E}_{\pi N}) \tag{8.25}$$

As discussed in Ref. [182], the kinematical factor introduced in Eq. (8.25) should be a reasonable approximation. This is further supported by the fact that the finite nuclear size contained in the optical potential through the product with the density (see Eq. (8.16)) significantly dampens the influence of far off-shell scattering. Moreover, the factorisation approximation greatly reduces the importance of unphysical scattering angles [180].

Finally, by injecting this expression in Eq. (8.16) and because of the implicit summation on isospins already discussed, the first-order potential then reads

$$V^{\text{1st}}_{\pi A,\text{opt}}(\vec{k}'_\pi, \vec{k}_\pi) = -4\pi \mathcal{W}^{\pi A}_{\pi N} \left[b_0 + c_0(\tilde{\vec{k}}'_\pi \cdot \tilde{\vec{k}}_\pi)\right] \hat{\rho}_1(\vec{q}) \tag{8.26}$$

where the scalar product should be transformed according to Eq. (7.87).

8.2.2 Second order of the interaction and absorption

The second order of the potential describes the scattering of a pion on a single nucleon to an excited state of the nucleus and its re-scattering on a different nucleon, the target going back to the ground state of the nucleus. The kinematics of the reaction are shown on Fig. 8.4.

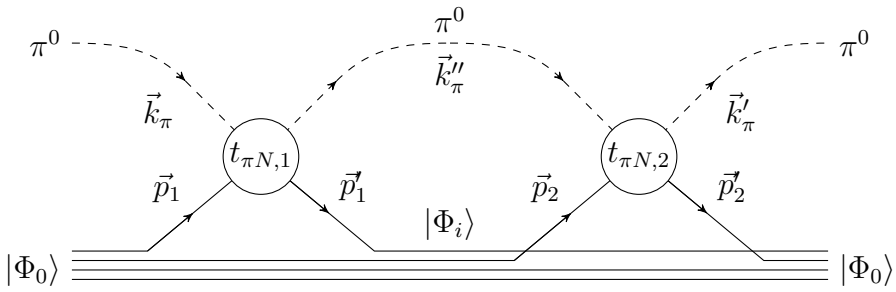

Figure 8.4: Kinematics of the reaction of second order scattering of a pion with momentum $\vec{k}_\pi$ and scattered with final momentum $\vec{k}'_\pi$ on two different nucleons, that go from initial momentum $\vec{p}_{1,2}$ to final $\vec{p}'_{1,2}$. The momentum of the intermediate state of the pion is $\vec{k}''_\pi$.

We can replace the $\mathbb{Q}_0$ operator by $\mathbb{1} - \mathbb{P}_0$ in Eq. (7.32) so that second order reads

$$\begin{aligned} V^{\text{2nd}}_{\pi A,\text{opt}}(\vec{k}'_\pi, \vec{k}_\pi) &= \left\langle \vec{k}'_\pi \right| V^{\text{2nd}}_{\pi A,\text{opt}} \left| \vec{k}_\pi \right\rangle \\ V^{\text{2nd,1}}_{\pi A,\text{opt}}(\vec{k}'_\pi, \vec{k}_\pi) + V^{\text{2nd,2}}_{\pi A,\text{opt}}(\vec{k}'_\pi, \vec{k}_\pi) &= A(A-1) \Big[\langle k'_\pi | \langle \Phi_0 | t_{\pi N,2} \frac{1}{\alpha_0} t_{\pi N,1} | \Phi_0 \rangle | k_\pi \rangle \\ &\quad - \langle k'_\pi | \langle \Phi_0 | t_{\pi N,2} | \Phi_0 \rangle \frac{1}{\alpha_0} \langle \Phi_0 | t_{\pi N,1} | \Phi_0 \rangle | k_\pi \rangle \Big] \end{aligned} \tag{8.27}$$

where I have added the indices 1 and 2 on the πN elementary t-matrices refer to denote the first and second nucleon struck, respectively.

If we develop this expression and use similar approximations as for the first order (see the derivation in App. H.1), we can show that the first term of this second order potential reads (Eq. (H.22))

$$\begin{aligned} V^{\text{2nd}}_{\pi A,\text{opt}}(\vec{k}'_\pi, \vec{k}_\pi) = \int \frac{d\vec{k}''_\pi}{(2\pi)^3} \frac{1}{\alpha_0(k''_\pi)} t_{\pi N} \left(\vec{k}'_\pi, -\frac{\vec{q}_2}{2} - \frac{\vec{k}'_\pi + \vec{k}_\pi}{2(A-1)}; \vec{k}''_\pi, \frac{\vec{q}_2}{2} - \frac{\vec{k}_\pi + \vec{k}'_\pi}{2(A-1)} \right) \\ t_{\pi N} \left(\vec{k}''_\pi, -\frac{\vec{q}_1}{2} - \frac{\vec{k}_\pi + \vec{k}'_\pi}{2A}; \vec{k}_\pi, \frac{\vec{q}_1}{2} - \frac{\vec{k}_\pi + \vec{k}'_\pi}{2A} \right) \times \hat{\rho}_2(\vec{q}_1, \vec{q}_2) \end{aligned} \tag{8.28}$$

where $\vec{q}_1$ and $\vec{q}_2$ read

$$\begin{cases} \vec{q}_1 = \vec{k}''_\pi - \vec{k}_\pi \\ \vec{q}_2 = \vec{k}'_\pi - \vec{k}''_\pi \end{cases} \tag{8.29}$$

Note that there remains an implicit summation on spins and isospins in this expression, which I will not discuss here. I refer the reader to App. H for more on this matter.

What should be noted is that this first term involves the Fourier transform of the 2-body density matrix $\hat{\rho}_2$ [see Eq. (6.47)]. As already mentioned before, this object cannot be calculated for all the densities presented in Sec. 6 especially for the phenomenological and experimental densities of Secs. 6.3. The absorptive part of the potential suffers from the same issue.

While a proper understanding of how a pion is absorbed by a nucleus has not yet been achieved, the absorption mechanism seems to be dominated by two-nucleon absorption at low energy and for low-mass nuclei [178, 179, 180, 181]. Because considering processes involving more than two nucleons would turn intractable, I will consider here that true absorption is only due to two-nucleon processes.

As a first step, the pion is seen as scattering on a first nucleon and then absorbed by a second one. After the propagation of this pion-less state, the pion is re-emitted. A schematic diagram of such process is given on Fig. 8.5. This correction term can hence be thought of a fourth order term. However, the large imaginary part (which removes flux in the elastic channel) of this term will significantly contribute to the scattering amplitude, especially at low energies, for which the imaginary parts of the other terms of the π-N potential are small.

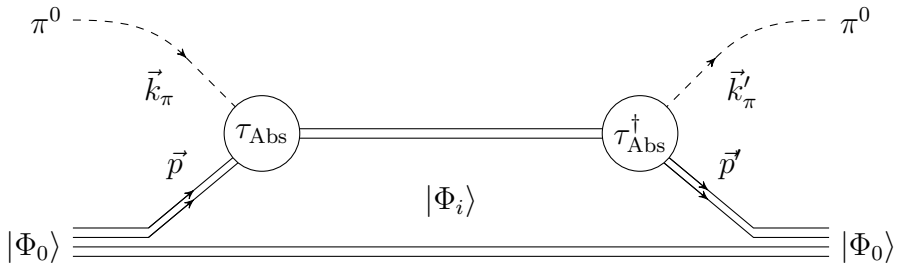

Figure 8.5: Schematics of the reaction of true absorption and emission of a pion from momentum $\vec{k}$ to final momentum $\vec{k}'$ as a two-nucleon process.

Following Refs. [183, 184], if we consider the true absorption amplitude to have a similar shape to the isospin non-flip part of the π-N potential, the absorptive part of the potential reads

$$f_{\text{Abs}}(\tilde{\tilde{\vec{k}}}'_\pi, \tilde{\tilde{\vec{k}}}_\pi; \tilde{\tilde{E}}_{\pi NN}) = B_0 + C_0(\tilde{\tilde{\vec{k}}}'_\pi \cdot \tilde{\tilde{\vec{k}}}_\pi) \tag{8.30}$$

where the double tilde denotes the variables calculated in the πNN centre-of-mass frame and where the energy $E_{\pi NN}$ is the sum of the energies of the π and the two nucleons. Calculations of the parameters B_0 and C_0 have been done in Ref. [185] in an infinite nuclear matter Fermi-gas model by assuming that true absorption is dominated by two-body absorption and is mediated by the exchange of π and ρ mesons. In Ref. [186] a different approach is chosen. These parameters are considered as free and are fitted to $\pi^\pm$-^{12}C data at low energies ($T_{\pi,\text{lab}} \leq 250$ MeV) by imposing that their value at 0 energy is in agreement with meso-atomic data.

After the transformation of this amplitude into the π-A center-of-mass frame, we can expect a similar form as Eq. (8.26). Since it's a two-nucleon process however, the one-body density is replaced by the two-body one and thus will resemble

$$V^{\text{Abs}}_{\pi A,\text{opt}}(\vec{k}'_\pi, \vec{k}_\pi) \propto \left[B_0 + C_0(\tilde{\tilde{\vec{k}}}'_\pi \cdot \tilde{\tilde{\vec{k}}}_\pi)\right] \times \hat{\rho}_2(q, q) \tag{8.31}$$

As we can see, like for the second order of the potential, absorption involves the Fourier transform of the 2-body density matrix. This form of the absorptive part of the potential is hence not suited for the use of such densities.

Because this form of the second order and absorptive part of the potential are not suited for the use of such densities, I will discuss a different form for this potential, i.e. the MSU π-A potential, which is the subject of next section. The expressions derived in App. H for the second order of the potential will not be used in this work. I refer the reader to the thesis of V. Tsaran where such expressions are particularised to ^{12}C in the HO model. Some of the developments in this model are given in Sec. H.2 of this appendix. These can serve as a starting point for future works.

8.2.3 MSU total potential

The two-nucleon densities of the target ρ_2 (or more precisely their Fourier transforms $\hat{\rho}_2$) are thus needed to build the second order and the absorptive parts of the optical potential. As we have seen in Sec. 6.2, the wave functions of the nucleons inside the nucleus which are needed to obtain ρ_2 can be obtained from mean field or shell model calculations. However, if one wants to use phenomenological or experimental densities such as the São Paulo densities (see Sec. 6.3.1) or the Fourier Bessel ones (see Sec. 6.3.2), these wave functions cannot be obtained.

In the PhD of K. Stricker-Bauer [187] and in a series of papers on the derivation of a π-A optical potential in the KMT formalism [188, 189, 184], the two-nucleon density matrix ρ_2 is simply replaced by the square of the one-nucleon density ρ_1 such that its Fourier transform reads

$$\hat{\rho}_2(q) = \mathscr{F}[\rho_1^2](q) \tag{8.32}$$

where instead of putting a hat, which could lead to some confusion as to when the square is taken, I define $\mathscr{F}[f](q)$ as the Fourier transform of some function f. In addition to this assumption, the density in the second order terms is sometimes replaced by its Thomas Fermi approximation[2] in the mathematically involved developments. Within these approximations, calculations then become much simpler and can be performed analytically. This constant density is then switched back to a coordinate dependent density ρ_1 in the final steps of the development. The details of this derivation can be found in Ref. [187].

In the end, the final form of the nuclear optical potential for a charged pion, which I will refer to as the MSU potential[3], reads

$$V^{\text{MSU}}_{\pi A,\text{opt}}(\vec{k}'_\pi, \vec{k}_\pi) = -4\pi \left(p_1 b(q) + p_2 B(q) + (\vec{k}_\pi \cdot \vec{k}'_\pi)\mathcal{L}(q) - \left[p'_1 c(q) + p'_2 C_0(q) \right] q^2 \right) \tag{8.33}$$

where

$$b(q) = \bar{b}_0 \hat{\rho}_1(q) \mp b_1 \mathscr{F}[\delta\rho_1](q) \tag{8.34}$$
$$B(q) = B_0 \hat{\rho}_2(q) \mp B_1 \mathscr{F}[\rho_1 \delta\rho_1](q) \tag{8.35}$$
$$c(q) = c_0 \hat{\rho}_1(q) \mp c_1 \mathscr{F}[\delta\rho_1](q) \tag{8.36}$$
$$C(q) = C_0 \hat{\rho}_2(q) \mp C_1 \mathscr{F}[\rho_1 \delta\rho_1](q), \tag{8.37}$$

[2]The Thomas Fermi approximation consists in considering the density in momentum space to be constant up to some chosen momentum $k_F \simeq 1.4$ fm^{-1} known as the Fermi momentum.

[3]Michigan State University, i.e. the location where she did her thesis.

where the $\mp$ sign corresponds to a pion of charge ± 1 and is simply 0 for a neutral pion and where $\delta\rho_1$ is the neutron-proton density difference. The function $\mathcal{L}$ reads

$$\mathcal{L}(q) = \mathscr{F}\left[\frac{L}{1+\frac{4\pi}{3}\lambda L}\right](q) \tag{8.38}$$

where λ is the Lorenz-Lorentz-Ericson-Ericson (LLEE) parameter (more on this later) and where

$$L(r) = p_1^{-1}\left(c_0\rho_1(r) \mp c_1\delta\rho_1(r)\right) + p_2^{-1}\left(C_0\rho_1^2(r) \mp C_1\rho_1(r)\delta\rho_1(r)\right). \tag{8.39}$$

$p_1^{(\prime)}$ and $p_2^{(\prime)}$ are kinematic factors which expressions are defined as

$$p_1 = \frac{1+\varepsilon}{1+\varepsilon/A} \qquad p_2 = \frac{1+\varepsilon/2}{1+\varepsilon/2A} \tag{8.40}$$

$$p_1' = \frac{1}{2}(1-p_1^{-1}) \qquad p_2' = \frac{1}{2}(1-p_2^{-1}) \tag{8.41}$$

and where $\varepsilon = \sqrt{k_{\pi,0}^2 + m_\pi^2}/m_N$.

It should be noted that the s-wave terms of this MSU potential are very similar to the s-wave part of Eq. (8.26), except for the kinematical factors, which are different. However, because of the assumptions made to arrive at this expression, the s-wave part of the second order is also proportional to the density. This tends to modify the value of b_0 of Eq. (8.26) to an effective value $\bar{b}_0$

$$\bar{b}_0 = b_0 - \frac{3k_F}{2\pi}(b_0^2 + 2b_1^2) \tag{8.42}$$

where we recognise the $(b_0^2+2b_1^2)$ factor also present in Eq. (H.32) and coming from nucleon correlations.

For the p-wave part on the contrary, several other terms appear that have no equivalent in Eqs. (8.26) and Eq. (8.31). First, let us observe how there appears a term proportional to q^2. This term arises from the Lorentz transformation of the scalar product present in Eq. (8.26). Moreover, in the term proportional to the scalar product $\vec{k}_\pi' \cdot \vec{k}_\pi$, the c_0 and C_0 constants are replaced by a complex function $\mathcal{L}$. This term is usually called the Ericson-Ericson, or Lorenz-Lorentz-Ericson-Ericson (LLEE) effect[4]. It simulates higher-order terms of the scattering and was first derived for a zero-range interaction and in the low-energy limit in Ref. [183]. It arises from the inclusion of short-range correlations between nucleons and effectively reduces p-wave scattering. The extent of this reduction is determined by the parameter λ or LLEE parameter, and is the strongest as λ approaches 1. It should be noted that this parameter is model dependent. Here, it is chosen equal to 1.4 [184]. The p-wave term of the absorptive part of the potential is also included in the LLEE effect.

While the initial hypotheses used for the derivation of this potential are the same as the ones shown in Secs. 8.1 and 8.2, the additional assumptions used in the development leading to Eq. (8.33) refrain us from using the SAID values of the parameters b_i, c_i, ... without further adjustment. In Ref. [184], the parameters of the potential are fitted to

[4]This *Lorenz-Lorentz* addition comes from the fact that this term induces a non-linear dependence on the density, which is analogous to the Lorenz-Lorentz effect in electromagnetism.

elastic scattering data on several different nuclei ranging from ^{12}C to ^{208}Pb at low energy (from T_π=0, i.e. pionic atoms, to T_π=50 MeV, both in the laboratory frame).

Because only the one-nucleon density is needed to build this potential, the π-A scattering can be computed even for phenomenological densities. Moreover, as it has been fitted on a wide range of nuclei and at energies close to the ones of interest of this work, I will use this form of the potential in the following.

8.3 Resolution of the Lippmann-Schwinger equation

Now that I have defined the effective potential that I will use to model the π-A interaction, I can use it to find $\tilde{T}_{\pi A}$, i.e. the T-matrix for the π-A scattering process, and calculate the impact of the distortion in Eq. (7.117). As we have seen in Sec. 7.1, the T-matrix is obtained by solving a Lippmann-Schwinger equation. For a non-relativistic process it reads (7.43)

$$\tilde{T}_{\pi A} = U_{\pi A,\text{opt}} - 4\pi\frac{A-1}{A}U_{\pi A,\text{opt}}G_0\mathbb{P}_0\tilde{T}_{\pi A} \tag{8.43}$$

Since this section concerns π-A scattering and these matrices all concern π-A processes, I will remove the indices and rewrite this equation in a more concise way as

$$\tilde{T} = U - \eta_0 U G_0 \mathbb{P}_0 \tilde{T} \tag{8.44}$$

where the indices have disappeared, $\eta_0 = 4\pi(A-1)/A$ and the non-relativistic propagator is defined in Eq. (7.39).

In order to solve this equation, note that we can separate the free particle's Green operator into the sum [190]

$$G_0(k) = \mathcal{P}\left(\frac{1}{k_{\pi,0}^2 - k_\pi^2}\right) - i\pi\frac{1}{2k_{\pi,0}}\delta(k_{\pi,0} - k_\pi) \tag{8.45}$$

where $\mathcal{P}$ denotes the Cauchy principal value. Note that since all momenta encountered in this section are pion momenta, I will remove the π indices on all momenta in the following in the sake of conciseness. The first term corresponds to the *off-shell* part $G_{\text{OFF}}(k)$ of the propagator while the second corresponds to its *on-shell* part $G_{\text{ON}}(k)$. Eq. (8.43) can thus be written

$$\tilde{T} = U - \eta_0 U G_{\text{OFF}}\tilde{T} - \eta_0 U G_{\text{ON}}\tilde{T} \tag{8.46}$$

We can separate the problem and define the K-matrix

$$K \equiv (1 + \eta_0 U G_{\text{OFF}})^{-1} U \tag{8.47}$$

This matrix also satisfies a Lippmann-Schwinger type equation

$$K = U - \eta_0 U G_{\text{OFF}} K \tag{8.48}$$

This last equation reads explicitly, in term of matrix elements

$$K(\vec{k}', \vec{k}) = U(\vec{k}', \vec{k}) - \eta_0 \mathcal{P}\left(\int \frac{d\vec{k}''}{(2\pi)^3}\frac{U(\vec{k}', \vec{k}'')K(\vec{k}'', \vec{k})}{k_0^2 - k''^2}\right), \tag{8.49}$$

and is the equation we will solve. Note that in the plane-wave basis, which will be used in this work, these matrix elements are the simple Fourier transform of the operators. In order to obtain $\tilde{T}$ from K, we just need to insert Eq. (8.48) back in (8.46)

$$\tilde{T} = K - \eta_0 K G_{\text{ON}} \tilde{T}, \tag{8.50}$$

and which explicitly reads

$$\tilde{T}(\vec{k}', \vec{k}) = K(\vec{k}', \vec{k}) + \eta_0 \frac{i}{k_0} K(\vec{k}', \vec{k}_0) \tilde{T}(\vec{k}_0, \vec{k}) \tag{8.51}$$

If we solve this for $\tilde{T}(\vec{k}_0, \vec{k})$, we finally have

$$\tilde{T}(\vec{k}', \vec{k}) = K(\vec{k}', \vec{k}) + \eta_0 \frac{i}{k_0} K(\vec{k}', \vec{k}_0) \left[1 - \eta_0 \frac{i}{k_0} K(\vec{k}_0, \vec{k}_0)\right]^{-1} K(\vec{k}_0, \vec{k}) \tag{8.52}$$

We thus see that by solving Eq. (8.49), we get access to the T matrix which can then be used to calculate the impact of the distortion in Eq. (7.117).

As already discussed in Sec. 7.1, in relativistic processes, the π-A reduced mass $\mu_{\pi A}$ can be replaced by $\mathcal{M}$, a relativistic equivalent of the reduced mass and which is defined in Eq. (7.45). The propagator then becomes the relativistically corrected one Eq. (7.47). If one used this propagator instead, Eq. (8.49) becomes

$$K(\vec{k}', \vec{k}) = U(\vec{k}', \vec{k}) - \eta_0 \mathcal{P} \left(\int \frac{d\vec{k}''}{(2\pi)^3} \frac{\widetilde{\mathcal{M}}(k'')}{\mathcal{M}(k'')} \frac{U(\vec{k}', \vec{k}'') K(\vec{k}'', \vec{k})}{k_0^2 - k''^2} \right), \tag{8.53}$$

In the sake of conciseness, I will define

$$\eta(k) = \begin{cases} \eta_0 & \text{non-relativistic} \\ \eta_0 \dfrac{\widetilde{\mathcal{M}}(k)}{\mathcal{M}(k)} & \text{relativistic} \end{cases} \tag{8.54}$$

so that Eq. (8.53) becomes

$$K(\vec{k}', \vec{k}) = U(\vec{k}', \vec{k}) - \mathcal{P} \left(\int \frac{d\vec{k}''}{(2\pi)^3} \eta(k'') \frac{U(\vec{k}', \vec{k}'') K(\vec{k}'', \vec{k})}{k_0^2 - k''^2} \right), \tag{8.55}$$

and is now valid for both non-relativistic and relativistic approaches. It should be noted that for $k \to k_0$, we have $\eta(k) \to \eta_0$. In the following, in order to be consistent with the relativistic treatment of photoproduction, I will use the relativistic propagator.

8.3.1 Partial wave decomposition

In order to solve Eq. (8.55), I will decompose U and K in partial waves

$$K(\vec{k}', \vec{k}) = \sum_l (4\pi)(2l+1) K_l(k', k) P_l(\cos\theta'), \tag{8.56}$$

where the expression of $K_l(k', k)$ reads

$$K_l(k', k) = \frac{1}{4\pi} \frac{1}{2} \int_{-1}^{1} d\cos\theta' P_l(\cos\theta') K(\vec{k}', \vec{k}) \tag{8.57}$$

and where $\cos\theta'$ is the cosine of the angle between $\vec{k}'$ and $\vec{k}$ (see Fig. 8.6). Because $\vec{k}$, $\vec{k}'$ and $\vec{k}''$ are not always coplanar, the angle between $\vec{k}'$ and $\vec{k}''$ can be more easily expressed from the directions that define it. In order to keep notations simple for all angles, I will write the cosine of an angle θ' as the scalar product of the directions that define it, i.e. $\cos\theta' = \mathbf{k}\cdot\mathbf{k}'$, where $\mathbf{k}^{(\prime)}$ denotes a unit vector of direction $\vec{k}^{(\prime)}$. The Lippmann-Schwinger Eq. (8.55) can then be rewritten as

$$\sum_l (4\pi)(2l+1)\left(K_l(k',k) - U_l(k',k)\right) P_l(\mathbf{k}\cdot\mathbf{k}') = \\ -\sum_{ll'}(4\pi)^2(2l+1)(2l'+1)\mathcal{P}\left(\int_0^\infty \frac{dk''}{(2\pi)^3}\eta(k'')\frac{k''^2 U_l(k',k'')K_{l'}(k'',k)}{k_0^2-k''^2}\right) \\ \times \int_0^{2\pi} d\phi'' \int_{-1}^{1} d(\mathbf{k}\cdot\mathbf{k}'')P_l(\mathbf{k}''\cdot\mathbf{k}')P_{l'}(\mathbf{k}\cdot\mathbf{k}'') \tag{8.58}$$

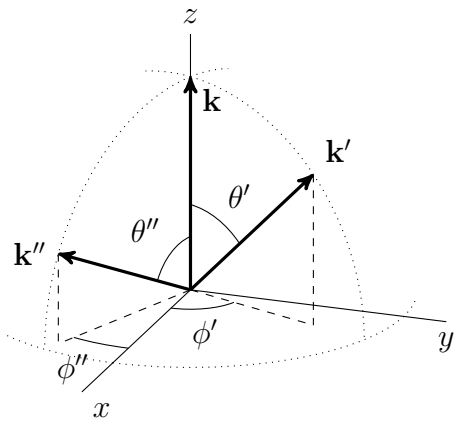

Figure 8.6: Definition of angles characterising the vectors $\vec{k}$, $\vec{k}'$ and $\vec{k}''$. Note that here $\mathbf{k}$, $\mathbf{k}'$ and $\mathbf{k}''$ denote unit vectors.

We see in the last expression a 4π-integral on the product of two Legendre polynomials. If we decompose the Legendre polynomial in spherical harmonics as in

$$P_l(\mathbf{k}'\cdot\mathbf{k}'') = \frac{4\pi}{2l+1}\sum_{m=-l}^{l} Y_{lm}(\theta',\phi')Y^*_{lm}(\theta'',\phi'') \tag{8.59}$$

and we plug this decomposition in the $4\pi-$integral we have

$$\int_0^{2\pi} d\phi'' \int_{-1}^{1} d(\mathbf{k}\cdot\mathbf{k}'')P_l(\mathbf{k}''\cdot\mathbf{k}')P_{l'}(\mathbf{k}\cdot\mathbf{k}'') \\ = \frac{(4\pi)^2}{(2l+1)(2l'+1)}\sum_m\sum_{m'} Y_{lm}(\theta',\phi')Y^*_{l'm'}(0,0)\underbrace{\int_0^{2\pi} d\phi'' \int_{-1}^{1} d(\mathbf{k}\cdot\mathbf{k}'')Y_{lm}(\theta'',\phi'')Y^*_{l'm'}(\theta'',\phi'')}_{\delta_{ll'}\delta_{mm'}} \\ = \frac{4\pi}{2l+1}P_l(\mathbf{k}'\cdot\mathbf{k})\delta_{ll'} \tag{8.60}$$

and the Lippmann-Schwinger Eq. (8.55) can be written as

$$K_l(k',k) = U_l(k',k) - \frac{2}{\pi}\mathcal{P}\left(\int_0^\infty dk''\eta(k'')k''^2\frac{U_l(k',k'')K_l(k'',k)}{k_0^2-k''^2}\right) \tag{8.61}$$

In order to evaluate this integral numerically we use the fact that the principal value $\mathcal{P}(\int dk''/(k_0^2 - k''^2))$ is 0. This term can thus be added to the right-hand side of the equation. This amounts to add $1/(k_0^2 - k''^2)$ in the integrand of the principal value. In particular, this term can be multiplied by the constant factor $k_0^2 U_l(k', k_0)K_l(k_0, k)$, so that the equation can be rewritten as

$$K_l(k', k) = U_l(k', k) - \frac{2}{\pi}\mathcal{P}\left(\int_0^\infty dk'' \frac{\eta(k'')k''^2 U_l(k', k'')K_l(k'', k) - \eta_0 k_0^2 U_l(k', k_0)K_l(k_0, k)}{k_0^2 - k''^2}\right). \tag{8.62}$$

The integrand has now a finite limit for $k'' = k_0$ and we can hence drop the Cauchy principal value

$$K_l(k', k) = U_l(k', k) - \frac{2}{\pi}\int_0^\infty dk'' \frac{\eta(k'')k''^2 U_l(k', k'')K_l(k'', k) - \eta_0 k_0^2 U_l(k', k_0)K_l(k_0, k)}{k_0^2 - k''^2} \tag{8.63}$$

8.3.2 Numerical resolution

Now that the pole has been removed and the integrand is smooth, we can evaluate it with numerical method routines. I will do it with a Gauss-Legendre quadrature [191] of N_k abscissas k_i'' and weights w_i''. These are generated from the Gauss-Legendre abscissas x_i and weights w_i that are then non-linearly mapped following

$$k_i'' = c\tan\left(\frac{\pi}{4}(1 + x_i)\right) \tag{8.64}$$

$$w_i'' = c\frac{\pi}{4}\sec^2\left(\frac{\pi}{4}(1 + x_i)\right) w_i \tag{8.65}$$

where c is a constant that will be discussed later. We then have

$$K_l(k_i', k) = U_l(k_i', k) - \frac{2}{\pi}\sum_{j=1}^{N_k} w_j'' \frac{\eta(k_j'')k_j''^2 U_l(k_i', k_j'')K_l(k_j'', k) - \eta_0 k_0^2 U_l(k_i', k_0)K_l(k_0, k)}{k_0^2 - k_j''^2} \tag{8.66}$$

The grids $\{k_i'\}$ and $\{k_j''\}$ are chosen identical.

In order to solve this equation, I will try to cast it as a matrix system of the type

$$A_{ij}X_j = B_i \tag{8.67}$$

Let us note however that k_0 is not necessarily in this grid (and we will generally try to avoid that it is). On the right side of the equation we are thus left with a term $K_l(k_0, k)$ that is not on the grid and impedes us from casting this equation directly in this form.

This issue can be solved in three ways :

1. Add a point to the grid : k_0. This is the first option we will discuss.

2. By Lagrange interpolation [192]: we express $K_l(k_0, k)$ as a weighted sum of the values of $K_l(k_j'', k)$ on the grid, which allows us to put the last term of the equation on the left hand side.

3. Iteratively: we first approximate $K_l(k_0, k) = U_l(k_0, k)$ (the Born approximation) on the right hand side and then solve the system. If we want to refine the solution, we then replace $K_l(k_0, k)$ by an interpolation of the solution we have obtained for $K_l(k_j, k)$. We then repeat this process until convergence is achieved.

Note that the c constant above can have a significant impact depending on the method that we use. The two most important characteristics are the position of k_0 compared to the grid and the proximity of the different points of the grid to k_0. We can estimate these two quantities by defining two numbers: p and d. The first defines the portion of points of the grid that are smaller than k_0. If we define the grid points around k_0 as k_m and k_{m+1} we can then define d as the number that satisfies

$$k_0 = k_m(1-d) + dk_{m+1} \tag{8.68}$$

If d is close to 0, k_0 is close to the m^{th} point of the grid. On the contrary, if d is close to 1, k_0 is close to the $m+1$ one. An illustration of these characteristics is given in Fig. 8.7, with the different points of the grid given as a function of their index. Note that the values of k are in a logarithmic scale. As should be noted, the points in the grid can thus grow to values of several thousands of fm^{-1}. In the case of low energy scattering for which k_0 lies below or around 1 fm^{-1}, these points of the grid are not very useful. Indeed, because of the density dependence of the potential, large values of k are significantly suppressed. A cut-off is thus usually applied around $k \sim 10$ fm^{-1} to avoid unnecessary calculations. Note that this is also true for small values of k for which the number of points at very low k values is high in this type of grid.

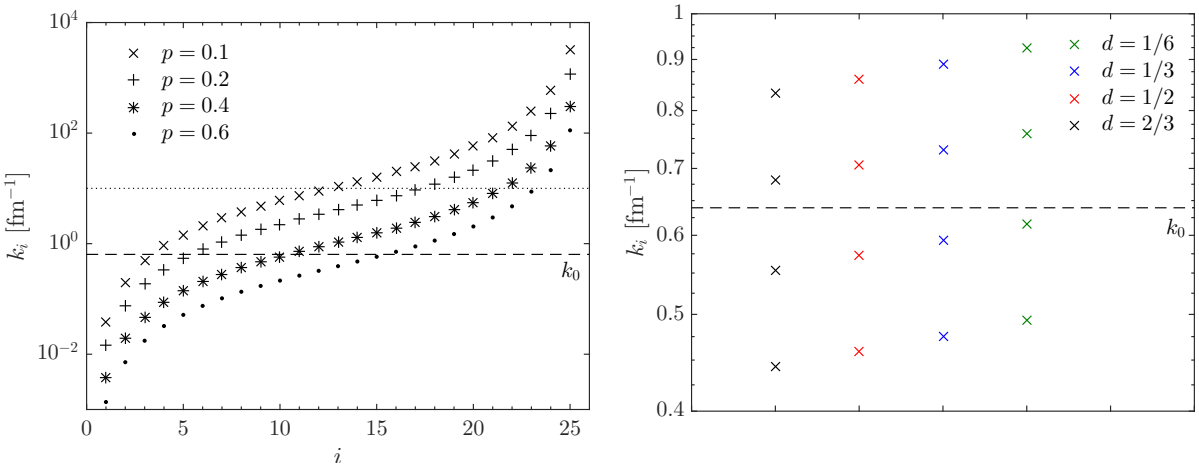

Figure 8.7: Left: grids $\{k_i\}$ of $N_k = 25$ points for the different values of p and the influence on the position of the grid points around k_0 (dashed line). Dotted line is an example of cut-off of the grid around $k \sim 10$ fm^{-1}. Right: influence of d on the proximity of the grid points to k_0.

Option 1 : adding a point to the grid ($N_k + 1$)

Let us consider a $N_k + 1^{\text{th}}$ point in the grid $k_{N_k+1} = k_0$. If we replace k_0 in the terms U_l and K_l (not in the propagator!). This allows us to write the integral (8.66) as

$$K_l(k'_i,k) = U_l(k'_i,k) - \sum_{j=1}^{N_k} \frac{2}{\pi}\left[\frac{w''_j\eta(k''_j)k''^2_j}{k_0^2 - k''^2_j}\right] U_l(k'_i,k''_j)K_l(k''_j,k) \tag{8.69}$$

$$+ \frac{2}{\pi}\left[\sum_{j=1}^{N_k} \frac{w''_j\eta_0 k_0^2}{k_0^2 - k''^2_j}\right] U_l(k'_i,k''_{N_k+1})K_l(k''_{N_k+1},k) \tag{8.70}$$

where i can thus also take the values from 1 to $N_k + 1$. This expression can be simplified by renaming the terms in the square brackets with

$$W_j = \begin{cases} -\frac{2}{\pi} \frac{w''_j \eta(k''_j) k''^2_j}{k_0^2 - k''^2_j} & j \neq N_k + 1 \\ \frac{2}{\pi} \sum_{n=1}^{N_k} \frac{w''_n \eta_0 k_0^2}{k_0^2 - k''^2_n} & j = N_k + 1 \end{cases} \tag{8.71}$$

such that we can write

$$K_l(k'_i, k) = U_l(k'_i, k) + \sum_{j=1}^{N_k+1} W_j U_l(k'_i, k''_j) K_l(k''_j, k) \tag{8.72}$$

We should keep in mind here that W_{N_k+1} corresponds to the term $\mathcal{P}(\int dk''/(k_0^2 - k''^2))$ that I have added in Eq. (8.62). Numerically, this might actually not be equal to 0 depending on the grid that is chosen. This term actually compensates for the pole of the integrand. I will come back to that later.

If last expression is rewritten in a matrix form by taking the sum to the left, we get the $(N_k + 1) \times (N_k + 1)$ system

$$\sum_{j=1}^{N_k+1} \left[\delta_{ij} - W_j U_l(k'_i, k''_j) \right] K_l(k''_j, k) = U_l(k'_i, k) \tag{8.73}$$

$$\sum_{j=1}^{N_k+1} \tilde{F}_{ij} K_l(k''_j, k) = U_l(k'_i, k) \tag{8.74}$$

where δ_{ij} is the Kronecker delta.

In the end, we have replaced the principal value of Eq. (8.55) by a sum of $N_k + 1$ terms, the sum of the first N_k gives the result that we would have obtained by just making a Gauss-quadrature and the last term one compensates for the possible divergence. Note finally that the resolution of the $(N_k + 1) \times (N_k + 1)$ system provides us with $K_l(k'_i, k)$ at the N_k values of the grid as well as the value $K_l(k_0, k)$.

Option 2 : Lagrange polynomials (Lag.)

A different approach which does not need the adding of another point to the grid is to use the N_k Lagrange polynomials $\hat{f}_j(k)$ associated to the grid and calculated at $k = k_0$ and their corresponding weights $\hat{\lambda}_j$ [193]

$$f_j(x) = (-1)^{N_k - j} \left(\frac{1 - x_j^2}{2} \right)^{1/2} \frac{P_{N_k}(x)}{x - x_j} \tag{8.75}$$

$$\lambda_j = \frac{2}{N_k^2} \frac{(1 - x_i^2)}{P_{N_k - 1}(x_i)^2} \tag{8.76}$$

Note that since the grid of Gauss-Legendre $\{x_i\}$ is mapped onto $\{k_i\}$ with $(-1, 1) \to (t^{-1}(-1), t^{-1}(1))$ and $t^{-1}(x) = c \tan\left(\frac{\pi}{4}(1 + x_i)\right)$, we need to transform these functions and weights as

$$\hat{f}_i(k) = [t'(k)]^{1/2} f_i(t(k)) \tag{8.77}$$

$$\hat{\lambda}_i = \lambda_i / t'(k_i) \tag{8.78}$$

where $t'(k)$ is the derivative of t. Here we have

$$t(x) = \arctan\left(\frac{x}{c}\right)\frac{4}{\pi} - 1 \tag{8.79}$$

$$\Rightarrow t'(x) = \frac{4}{\pi}\frac{c}{c^2+x^2} \tag{8.80}$$

We can then write $K_l(k_0,k)$ as a sum of these polynomials

$$K_l(k_0,k) = \sum_{j=1}^{N_k} \hat{\lambda}_j^{1/2} K_l(k'_j,k)\hat{f}_j(k_0) \tag{8.81}$$

$$= \sum_{j=1}^{N_k} l_j(k_0) K_l(k'_j,k) \tag{8.82}$$

If we plug this in Eq. (8.66) and use the same definition of the first N_k W_j in Eq. (8.71) and of b_j in Eq. (8.90), we have

$$\sum_{j=1}^{N_k}\left[\delta_{ij} - \left(-\frac{2}{\pi}\frac{w''_j\eta(k''_j)k''^2_j}{k_0^2-k''^2_j}\right)U_l(k'_i,k''_j)\right]K_l(k''_j,k) = U_l(k'_i,k) + \left(\frac{2}{\pi}\sum_{j=1}^{N_k}\frac{w''_j\eta_0 k_0^2}{k_0^2-k''^2_j}\right)U_l(k'_i,k_0)K_l(k_0,k) \tag{8.83}$$

$$\sum_{j=1}^{N_k}\left[\delta_{ij} - W_j U_l(k'_i,k''_j)\right]K_l(k''_j,k) = U_l(k'_i,k) - b_i\sum_{j=1}^{N_k} l_j(k_0)K_l(k''_j,k) \tag{8.84}$$

$$\sum_{j=1}^{N_k}\left[\delta_{ij} - W_j U_l(k'_i,k''_j) + b_i l_j(k_0)\right]K_l(k''_j,k) = U_l(k'_i,k) \tag{8.85}$$

$$\sum_{j=1}^{N_k}\hat{F}_{ij}K_l(k''_j,k) = U_l(k'_i,k) \tag{8.86}$$

which is a $N_k \times N_k$ system. Its resolution provides us with the values of $K_l(k_m,k)$ at the N_k values of the grid $\{k_m\}$. We then can of course also calculate $K_l(k_n,k)$ at any other value k_n thanks to expression

$$K_l(k_n,k) = \sum_{j=1}^{N_k}\hat{\lambda}_j^{1/2}K_l(k'_j,k)\hat{f}_j(k_n). \tag{8.87}$$

Option 3 : by iteration

A third and last method to cast Eq. (8.66) as a matrix system in order to invert it is to proceed by iteration. Let me first rewrite it as

$$\sum_{j=1}^{N_k}\left[\delta_{ij} + \frac{2}{\pi}w''_j\eta(k''_j)\frac{k''^2_j U_l(k'_i,k''_j)}{k_0^2-k''^2_j}\right]K_l(k''_j,k) = U_l(k'_i,k) + \frac{2}{\pi}\sum_{j=1}^{N_k} w''_j\eta(k''_j)\frac{k_0^2 U_l(k'_i,k_0)K_l(k_0,k)}{k_0^2-k''^2_j} \tag{8.88}$$

which can be written into the form

$$\sum_{j=1}^{N_k} F_{ij}K_l(k''_j,k) = U_l(k'_i,k) - \left[-\frac{2}{\pi}\sum_{j=1}^{N_k} w''_j\eta(k''_j)\frac{k_0^2 U_l(k'_i,k_0)}{k_0^2-k''^2_j}\right]K_l(k_0,k) \tag{8.89}$$

$$= U_l(k'_i,k) - b_i K_l(k_0,k). \tag{8.90}$$

Note that in order to write this equation in this form we have had to split the sum Eq. (8.66) into two terms. In Eq. (8.62), the second term of the sum appears precisely to smooth out the integrand. By splitting it in two, have we really won anything? This will be discussed in next section.

In order to cast it as a solvable system, we can at first consider the Born approximation, which reads $K_l(k_0, k) \simeq U_l(k_0, k)$. This can be called the *zero-th* order of the resolution $K_l^{(0)}(k_0, k)$. At the first iteration, we then have to solve the system

$$F_{ij} K_l^{(1)}(k_j'', k) = U_l(k_i', k) - b_i K_l^{(0)}(k_0, k) \tag{8.91}$$

$$= U_l(k_i', k) - b_i U_l(k_0, k) \tag{8.92}$$

It should be noted however that this provides with the values only at the grid points. The value $K_l^{(1)}(k_0, k)$ then has to be calculated through interpolation (for example with Lagrange polynomials see previous method). We can then calculate any higher order m by solving

$$F_{ij} K_l^{(m)}(k_j'', k) = U_l(k_i', k) - b_i K_l^{(m-1)}(k_0, k). \tag{8.93}$$

Comparison of the solving methods

In each of these methods, we solve a system of the type

$$A_{ij} X_j = B_i \tag{8.94}$$

where the matrix A_{ij} is the $(N_k + 1) \times (N_k + 1)$ matrix $\tilde{F}_{ij}$ (Eq. (8.74)), the $N_k \times N_k$ matrix $\hat{F}_{ij}$ (Eq. (8.86)) or the $N_k \times N_k$ matrix F_{ij} (Eq. (8.90)) depending on the method.

The precision of the solution will of course depend on the number of points of the grid N_k. An example of converged solution for a high number of points ($N_k = 60$) is given on Fig. 8.8 (left), where the elastic scattering cross section of a π^0 of 50 MeV laboratory energy on a ^{12}C target is calculated on a $N_k = 60$ grid. The convergence of the cross section is studied on the right panel by analysing the relative error for some selected angles as a function of the number of points of the grid. The cross section for $N_k = 60$ is considered as fully converged. Note how even for a limited number of points in the grid $N_k \ll 60$, the relative error is at least at the percent level.

The precision of the resolution will also depend on how these points are distributed around k_0 and thus on c and thus finally on p and d. I have found that the best value of d lies around 0.5. This is specially true for the iterative method. This is illustrated on Fig. 8.9. While for the $N_k + 1$ and Lagrange methods, no visible changes occur when d is varied, the iterative method gives significantly different results. This comes from the fact that contrarily to what is done in the two other methods, the iterative solution splits the integral of Eq. (8.63) into two parts. The divergence of the argument of the integral is then better absorbed when the points of the grid are distributed symmetrically around k_0. For this reason, I will take $d = 0.5$ in the grid in the following. The portion p also does impact the resolution by reducing the amount of points needed in the grid as illustrated on right panel of Fig. 8.9. The convergence is faster with a low portion p. This however means that a higher portion of points are not used in the resolution.

It should be noted that the choice of N_k, d and p will depend on the problem considered. And there is no general rule to quantify which values are best beforehand. This study rather serves as an illustration of the influence of these parameters.

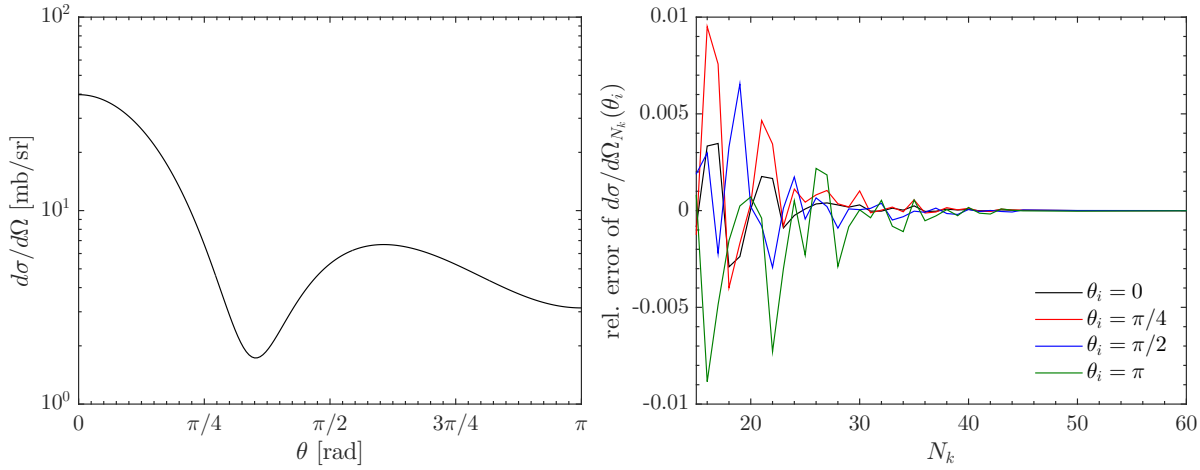

Figure 8.8: Elastic scattering cross section of a π^0 of 50 MeV lab energy on a ^{12}C target calculated on a $N_k = 60$ grid (left). Convergence of the cross section at selected angles as a function of the number of points of the grid (right).

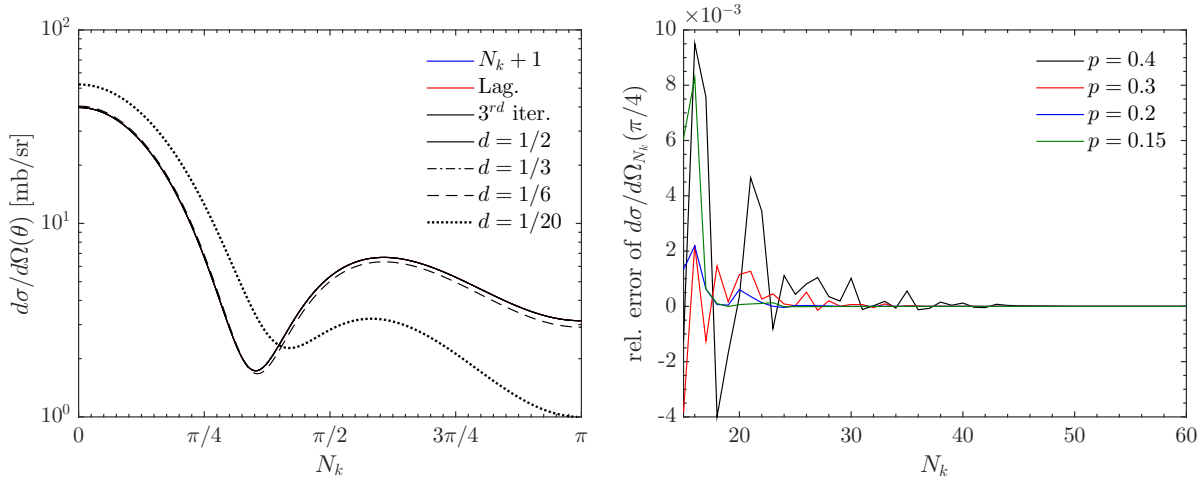

Figure 8.9: Left: Influence of d on the resolution for the three different methods on the elastic scattering cross section of a π^0 of 50 MeV lab energy on a ^{12}C target. The first and second method (labeled $N_k + 1$ and Lag.) lie under the black solid curve and are not visible. These do not show any visible influence on the value taken for d. The solution found by the iterative method (black lines) on the contrary is significantly impacted by this choice. Right: influence of p on the number of points needed in the grid to attain convergence for the iterative method.

8.3.3 Comparison to pion-nucleus elastic scattering data

Throughout this section, I have shown how to solve the Lippmann-Schwinger equation. As we have seen, two methods are nearly equivalent, i.e. the $N_k + 1$ and Lagrange methods. While there is no clear reason on why to prefer one over the other, I will rather use the one which uses Lagrange polynomials as it naturally allows for interpolations of the different matrix elements involved in the calculations.

This method can be tested on actual pion-nucleus elastic scattering data. My model will be used at low kinetic energies of the impinging photon, i.e. from 170 MeV to 220 MeV [private communication with Maria]. The corresponding energies of the emitted pion are then roughly 50 MeV.

Unfortunately, because of the very short life time of the neutral pion, there does not exist any data on π^0-A scattering and one needs to resort to charged pion elastic scattering experiments. This means that we need a way to include the Coulomb interaction in the potential. This interaction is well known and has a very simple form.

The pointlike Coulomb potential between a pion of charge π_C and a nucleus of charge Z can be written as

$$V_C(r) = \pi_C \frac{Z\alpha}{r} \tag{8.95}$$

where α is the fine-structure constant. The matrix elements of this interaction on a plane-wave basis then read in momentum space

$$V_C(\vec{k}', \vec{k}) = \pi_C Z\alpha \frac{4\pi}{q^2} \tag{8.96}$$

where as before, $\vec{q} = \vec{k}' - \vec{k}$. As seen previously, these elements can be expanded in partial waves following Eq. (8.57),

$$V_{C,l}(k', k) = \pi_C \frac{Z\alpha}{2} \int_{-1}^{1} d\cos\theta' \frac{P_l(\cos\theta')}{k^2 + k'^2 - 2kk'\cos\theta'} \tag{8.97}$$

They are clearly singular at $k = k'$.

Because of its long-range behaviour, the treatment of the Coulomb interaction in momentum space is hence not straightforward. While in most of the cases, there is no way yet to account for this interaction properly, some approximate methods exist. One of these is to screen the Coulomb potential [194]. More information on this method is given in App. G. It should be noted however that this method is limited to nuclear dominated processes, i.e. on light nuclei such as ^{12}C. For heavier nuclei, the Coulomb dominance of the reaction causes this approximation to lapse.

Because of the limitations of the method exposed in App. G, I choose to compare to elastic scattering data on ^{12}C. At the energy of 50 MeV, five groups have measured such cross sections [195, 196, 197, 198, 199]. On Figs. 8.10, these cross sections for the reaction of a positive pion (left) and a negative pion (right) are displayed and compared to the data. The potential I use is the MSU one, which I have discussed in Sec. 8.2.3.

As we can see, the agreement is not perfect, especially below 60 deg. It should be noted that the density used for the target does not have much of an influence on the cross section. This shows that most of the disagreement actually comes from the potential itself. The agreement is however fair and reproduces correctly the order of magnitude of the data as well as its global shape. By plugging in Eq. (7.117) the solution to the Lippmann-Schwinger Eq. (8.43) obtained with the Lagrange method and with the MSU potential, the distortion is now correctly included in the photoproducion cross sections. In next section, I will apply this model.

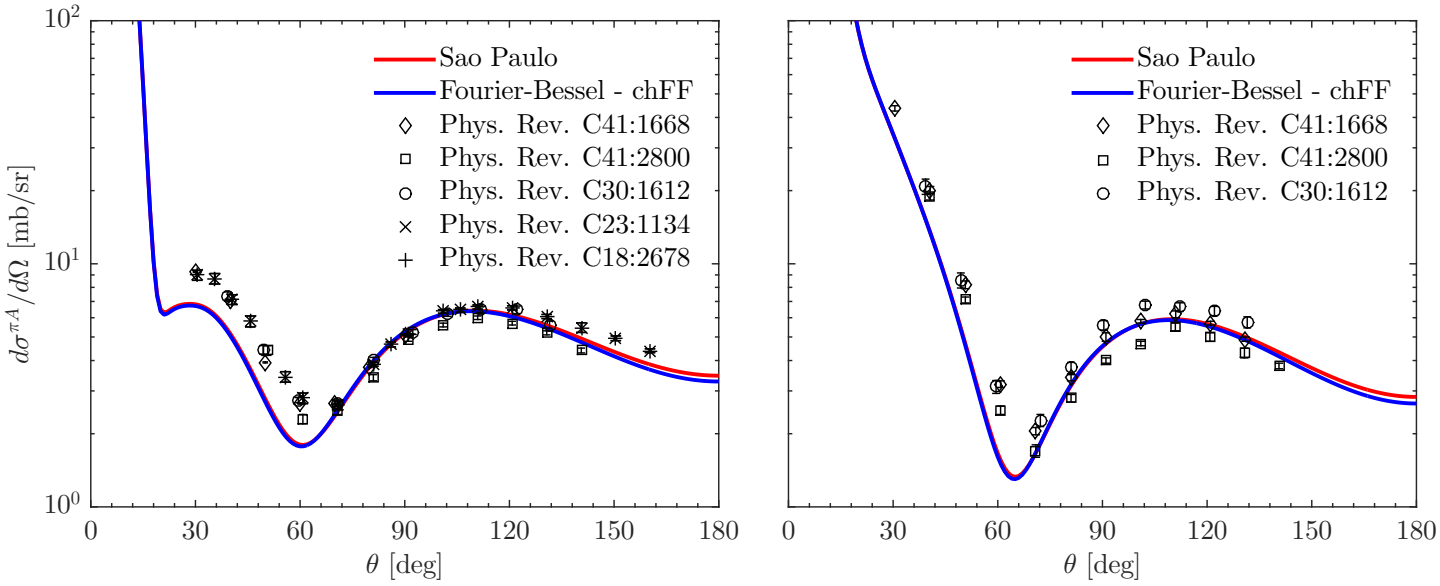

Figure 8.10: Elastic scattering cross section of a π^+ (left) or a π^- (right) of 50 MeV lab energy on a ^{12}C target. The density of the target is the São Paulo density (red) and the Fourier-Bessel one corrected for the charge form factor (blue). Data from Refs. [195, 196, 197, 198, 199]

9 Detailed analyses of experimental π^0-photoproduction

Very fortunately, there exist recent and precise data on coherent π^0-photoproduction at the energies of interest to the present work. These have been reported in Krusche *et al.* [129], who have measured the differential cross section for this process on ^{12}C, ^{40}Ca and ^{208}Pb. These measurements have been carried out at MaMi using the same set-up as presented in Sec. 5 for an impinging photon kinetic energy of 200 MeV in the laboratory frame. At this energy of the photon, the re-scattering of the pion after its production occurs at an energy that would be equivalent to a pion impinging on a nucleus at a kinetic energy of around 65 MeV in the laboratory frame. While this is slightly above the 50 MeV at which the MSU potential has been fitted [see Sec. 8.2.3], I will consider that this potential is still valid.

Now that all the ingredients of the model have been presented, let me apply my model to directly compare the results of my calculations to the cross-sections reported in Ref. [129]. This comparison will allow me to validate my model and its implementation. This will also allow me to discriminate between the different prescriptions for the choice of energy of the γ-N interacting system described in Sec. 7.3.2. Also, for each of these nuclei, I will be able to explore the dependence of my cross sections on the density used to describe the target nucleus and compare these differences to the experimental uncertainty. I will also see how important is the effect of the distortion. All this will allow me to infer qualitatively how sensitive this observable is to the neutron skin thickness. This will be particularly relevant on ^{208}Pb, which exhibits a thick neutron skin.

In future works, this model will provide a quantitative tool to analyse future experiments performed at MaMi. Recently, two different measurements on coherent π^0-photoproduction have been carried out at MaMi. These aim at extracting the neutron skin of several isotopes on the isotopic chain of tin [137] and of the ^{48}Ca nucleus [138]. I will thus also perform calculations on these targets.

9.1 Comparison to previous data: ^{12}C, ^{40}Ca and ^{208}Pb

^{12}C

The π^0 photoproduction cross sections of Ref. [129] on a ^{12}C target at an incident photon kinetic energy of 200 MeV in the lab frame are displayed on Fig. 9.1 as black dots[5] as a function of the scattering angle in the π-A centre-of-mass frame. Are also shown the results of my calculations in the PWIA (left panel) and DWIA (right panel). These are displayed in the active nucleon on-shell prescription $W^N_{\gamma N}$ (black) and in the spectator on-shell one $W^N_{\gamma N}$ (red). The density used in my calculations is the Fourier-Bessel density corrected for the charge form factor of the nucleons [see Sec. 6.3.2].

As already noted in Sec. 7.3.2 at a lower energy, there is a factor around 1.5 and 2 between the nucleon on-shell and spectator on-shell prescriptions. The former seems to work better than the latter. This is true both in the PWIA and DWIA cases. Notably, the choice of prescription impacts mainly the magnitude of the curve. Indeed, both prescriptions provide me with a cross section that is very similarly shaped with its maximum

[5] Note that these data are extracted directly from Fig. 4 of Ref. [129]. For some of these data points, the error bars on the data are not visible in the figure as they are occulted by the dots representing the data. For these points, I have made the conservative hypothesis that the data uncertainty is as large as the size of the dots.

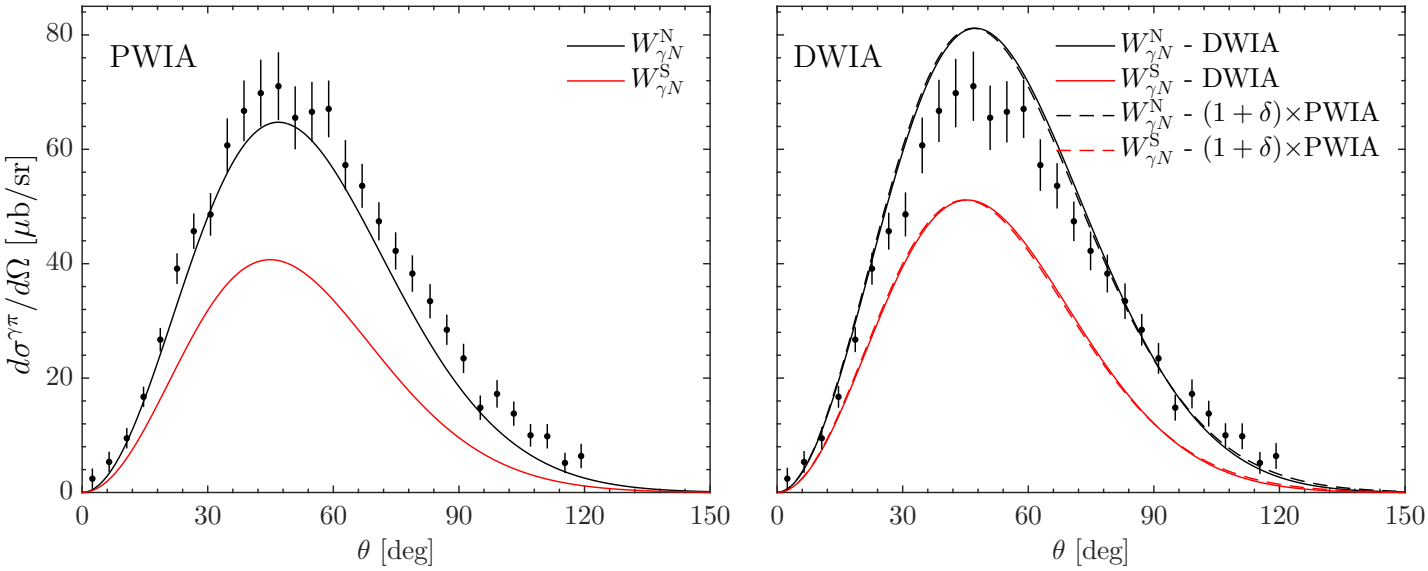

Figure 9.1: Coherent π^0 photoproduction cross sections data of Ref. [129] (dots) on a ^{12}C target at an incident photon kinetic energy of 200 MeV in the lab frame. PWIA (left panel) and DWIA (right panel) calculations are shown in the active nucleon on-shell prescription $W^{N}_{\gamma N}$ (black) and the spectator on-shell one $W^{N}_{\gamma N}$ (red). The density used here for the calculations is the Fourier Bessel corrected for the charge form factor of the nucleons. On the right panel, the agreement of the approximation Eq. (9.1) with the DWIA cross section is also evaluated.

nearly at the exact same angle. A more careful analysis of these curves shows that at larger angles, this is not totally true. However, the magnitude of the cross section at those angles is very small and such tiny effects cannot be discriminated using experimental data (nor are these angles even measured).

The distortion increases the photoproduction cross section equally for both prescriptions. The DWIA cross sections are 25% higher than the PWIA in both cases. Moreover, as it was the case when switching from one energy prescription to the other, the distortion seems to influence only the magnitude of the cross section. There is no significant effect on the shape of these curves and the angle of the maximum remains the same with and without distortion. This is reminiscent of what has been observed in Ref. [200], where the effect of distortion on coherent π^0 photoproduction has been analysed for light targets and at energies near threshold, i.e. below 200 MeV. The distortion was observed to have a scaling effect on the PWIA cross section. In the region of the peak, the DWIA cross section can be approximated by the expression

$$\frac{d\sigma}{d\Omega}(\text{DWIA}) \simeq (1+\delta)\frac{d\sigma}{d\Omega}(\text{PWIA}) \tag{9.1}$$

where the constant δ, which does not depend on the angle, corresponds to the relative change induced by the distortion. From what has been observed above, we can expect δ to be around 0.25 in this case. There are different ways to obtain this parameter. It could for example be chosen such as to make both the DWIA integrated cross section and its approximation coincide, or such as to minimise the χ^2 between Eq. (9.1) and the data,

or even such as to reproduce the magnitude of the DWIA cross section at any angle of interest. Here, I will use the latter way as it is the easiest and fix the value of δ such that the maximum of the DWIA and its approximation have exactly the same value.

To test if the approximation Eq. (9.1) is in a good agreement with the DWIA calculations, it has also been plotted on the right panel of Fig. 9.1 as dashed lines. For both energy prescriptions, it should be observed how the difference between the DWIA calculation and its approximation Eq. (9.1) are very small. In the angular region of the peak, Eq. (9.1) is hence an excellent approximation. δ is nearly identical for both prescriptions (δ=0.254 and for the active nucleon on-shell and δ=0.256 for the spectator-core on-shell one).

It is interesting to study the effect of the choice of density on these calculations to see if it can explain the observed disagreement with the data. The π^0-photoproduction cross sections displayed in Fig. 9.2 are calculated in the PWIA (left) and DWIA (right) for the different densities of Fig. 6.1 [see Sec. 6.5], i.e. the São Paulo (SP, solid), Fourier-Bessel (FB, dashed) and harmonic oscillator (HO, dash-dotted). The Fourier-Bessel densities with (chFF) and without the correction for the charge form factor of the nucleons are displayed in blue and black, respectively. The former (blue) is the density already used in Fig. 9.1. The HO density with centre-of-mass corrections (HO - cm) and without it are displayed in blue and black, respectively. Because the nucleon on-shell prescription seems to work better, only results calculated using this prescription are displayed.

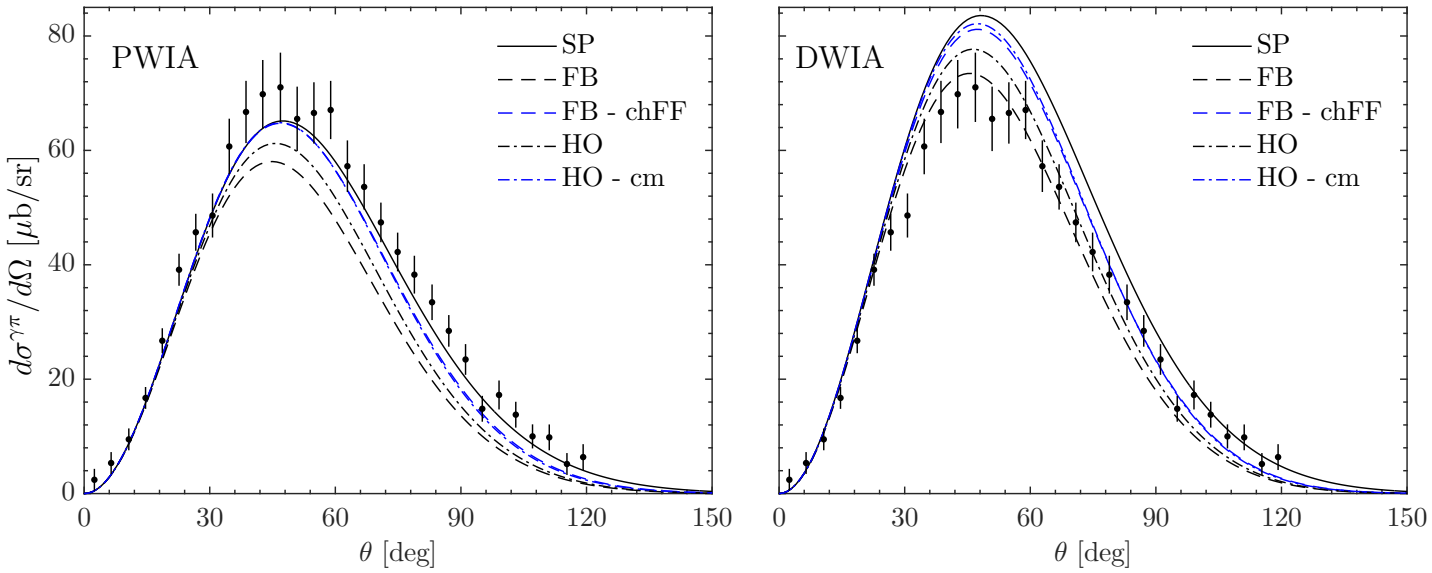

Figure 9.2: Coherent π^0 photoproduction cross sections data of Ref. [129] (circles) on a ^{12}C target at an incident photon kinetic energy of 200 MeV in the lab frame. PWIA (left panel) and DWIA (right panel) calculations are shown in the active nucleon on-shell prescription $W^N_{\gamma N}$ for the different densities of Fig. 6.1.

At the very forward angles, my model predicts the same cross sections for all these densities. This is to be expected since these angles correspond to low values of the transferred momentum q. At low q, all the density form factors are close to one another (since they are normalised to A at $q = 0$). This is depicted on Fig. 9.3, where the Fourier transforms of the densities of Fig. 6.1 are displayed. At low angles, the PWIA is

hence a good (but rather expensive) method to measure the target mass number A. The differences between the different curves start to be visible above 30°. This fortunately corresponds to the region around the angle of the maximum.

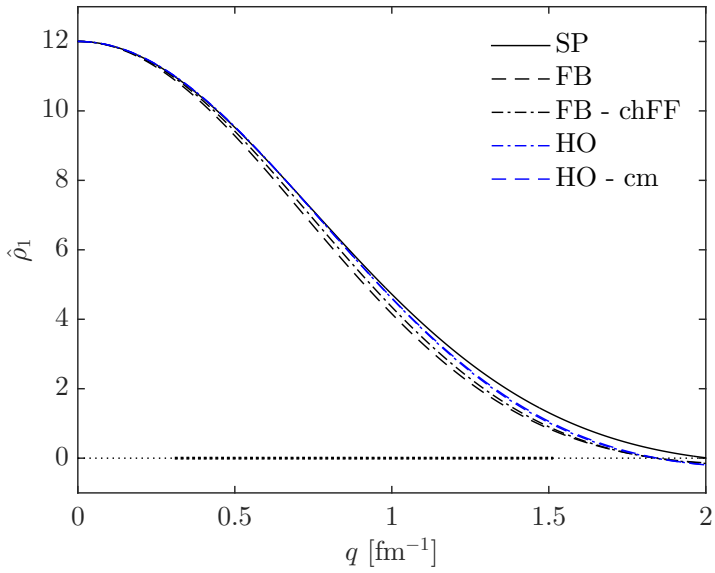

Figure 9.3: Density form factor (6.10) for the different densities of Fig. 6.1. The thick dotted line represents the range of transferred momenta that contribute to the PWIA cross section [see also Eq. (7.75)].

The magnitude of the peak exhibits variations of around 10%, both in the PWIA and in the DWIA. This difference is smaller than the uncertainty on the data which is of around 15% in the region of the peak (see Fig. 4 in Ref. [129]). Moreover, a careful analysis of these curves shows that the position of the maximum changes by about 2° with the density. Again, this difference is less than the uncertainty on the angle coming from the experiment which bins are of around 4°.

Finally, as previously observed for the Fourier-Bessel density on Fig. 9.1, the effect of the distortion does not seem to affect the shape of the cross section up to 100°. Below that angle, the effect of the distortion is a simple scaling [see Eq. (9.1)] of the curve and the magnitude of this effect is close to 25% for all densities (δ is contained in the range 0.254–0.283). Above 100°, nonlinear effects come into action but these will be discussed later on heavier targets such as lead, where they are more visible.

While the agreement between the calculations and the data is not perfect, the order of magnitude and the shape of the cross section are well reproduced in the DWIA. The height of the maximum is slightly overestimated in the DWIA nearly for all densities, but globally, the agreement is fair.

^{40}Ca

Similarly to the case of a carbon target, the π^0 photoproduction cross sections measured in Ref. [129] on a ^{40}Ca target at an incident photon kinetic energy of 200 MeV in the lab frame are displayed on Fig. 9.4 as black dots. Are also shown the results of my calculations in the PWIA (left panel) and DWIA (right panel). These are displayed in the active nucleon on-shell prescription $W_{\gamma N}^{N}$ (black) and in the spectator on-shell one

$W^N_{\gamma N}$ (red). The density used in my calculations is the Fourier-Bessel density corrected for the charge form factor of the nucleons [see Sec. 6.3.2 and see Fig. 6.2]. Additionally, the approximation Eq. (9.1) is also displayed on the right panel.

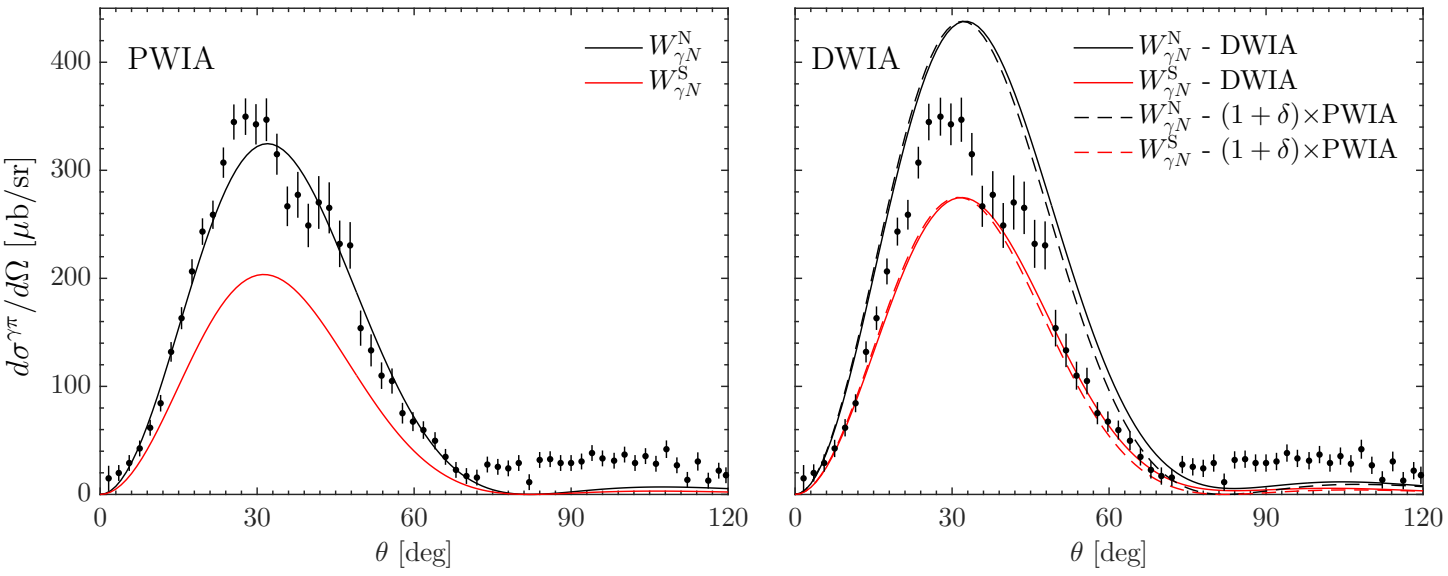

Figure 9.4: Same as Fig. 9.1 for a ^{40}Ca target. The density used here is also the Fourier-Bessel corrected for the charge form factor of the nucleons [see Fig. 6.2]. Data from Ref. [129].

Since the target is heavier, the curves are pushed towards the forward angle region. This is due to the larger extent of the nucleus. The Fourier form factor of the density is then more sharply peaked and the maximum appears at more forward angle. This is depicted on Fig. 9.5, where the SP densities for ^{12}C (black), ^{40}Ca (red) and ^{208}Pb (blue) are displayed in coordinate space on the left panel and their Fourier transform normalised to A are displayed on the right panel. This also means that the zeros of the density Fourier transform appear at smaller q, and hence smaller angles [see Eq. (7.75)] than for lighter targets. While no zero is visible for ^{12}C on Fig. 9.1, the first zero of the Fourier transform of the ^{40}Ca is clearly visible around 80° on the left panel of Fig. 9.4. A second maximum is hence also visible past this zero. It is however much smaller in comparison to the first peak.

As already noted for a carbon target, there is a factor around 1.5 and 2 between the nucleon on-shell and spectator on-shell prescriptions. Also, like for the lighter target, the former seems to work better than the latter in the PWIA. This time however, when distortion is added, both prescriptions cannot reproduce the data. The choice of prescription seems to impact mainly the magnitude of the curve. Indeed, both prescriptions provide with a cross section that is very similarly shaped with its maximum nearly at the exact same angle. At larger angles, after the first minimum (around 80°) and in the range of the second maximum (around 110°), this remains true, although the cross sections are too small to observe much.

Like for the ^{12}C target, the distortion increases the photoproduction cross section equally for both prescriptions (δ=0.349 and 0.350). This effect is thus stronger than in the case of carbon where δ has its value around 0.25. The distortion influences only the

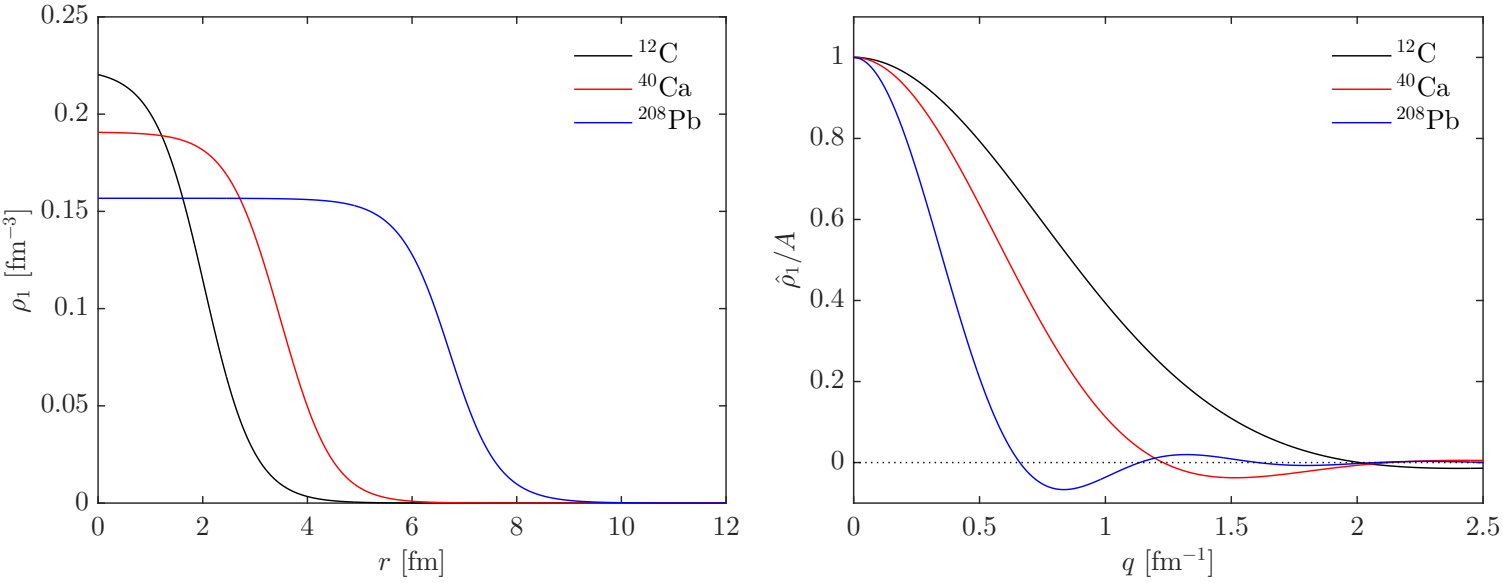

Figure 9.5: SP densities for ^{12}C (black), ^{40}Ca (red) and ^{208}Pb (blue) are displayed in coordinate space on the left panel and their Fourier transform normalised to A are displayed on the right panel. The larger extent of the target nucleus in coordinate space means a sharper peak in momentum space and hence zeros that appear at smaller transferred momenta q.

magnitude of the cross section in the region of the first peak. This is confirmed by looking at the dashed curve, which is a simple scaling of the PWIA cross section [see Eq. (9.1)]. There is hence no significant effect on the shape of the peak and the angle of its maximum remains nearly the same with and without distortion. At larger angles however, in the region of the first minimum and the second peak, the effect of the distortion is stronger. It should be observed how the first zero of the PWIA (corresponding to first zero of the density form factor) is filled in the DWIA, as if it was smeered. However, this effect is not strong enough to explain the plateau observed in the experimental data past the minimum. Discussions with the lead author who published the data [129] have revealed however that separating the coherent and incoherent processes has been difficult for the ^{40}Ca nucleus. There is hence a high probability that the data is significantly contaminated by incoherent processes. This could also explain why the minimum of my DWIA calculations does not reproduce the minimum of the data.

To analyse the effect of the choice of density on these cross sections I perform the calculations for the different densities of Fig. 6.2 [see Sec. 6.5], i.e. the São Paulo (solid), Fourier-Bessel (dashed) and FSU densities (dash-dotted). These are displayed on Fig. 9.6, in the PWIA (left) and DWIA (right). The Fourier-Bessel densities with the correction for the charge form factor of the nucleons and without it are displayed in blue and black, respectively. The different FSU densities are displayed in the same color code as in the right panel of Fig. 6.2. Because for ^{12}C, the nucleon on-shell prescription worked better than the spectator core on-shell one, results calculated only in the former are displayed.

As was to be expected from the results on ^{12}C, at very forward angles the cross sections for all these densities are superimposed since in this region, they are directly linked to the target mass. The differences between the different curves start to be visible above 20° in

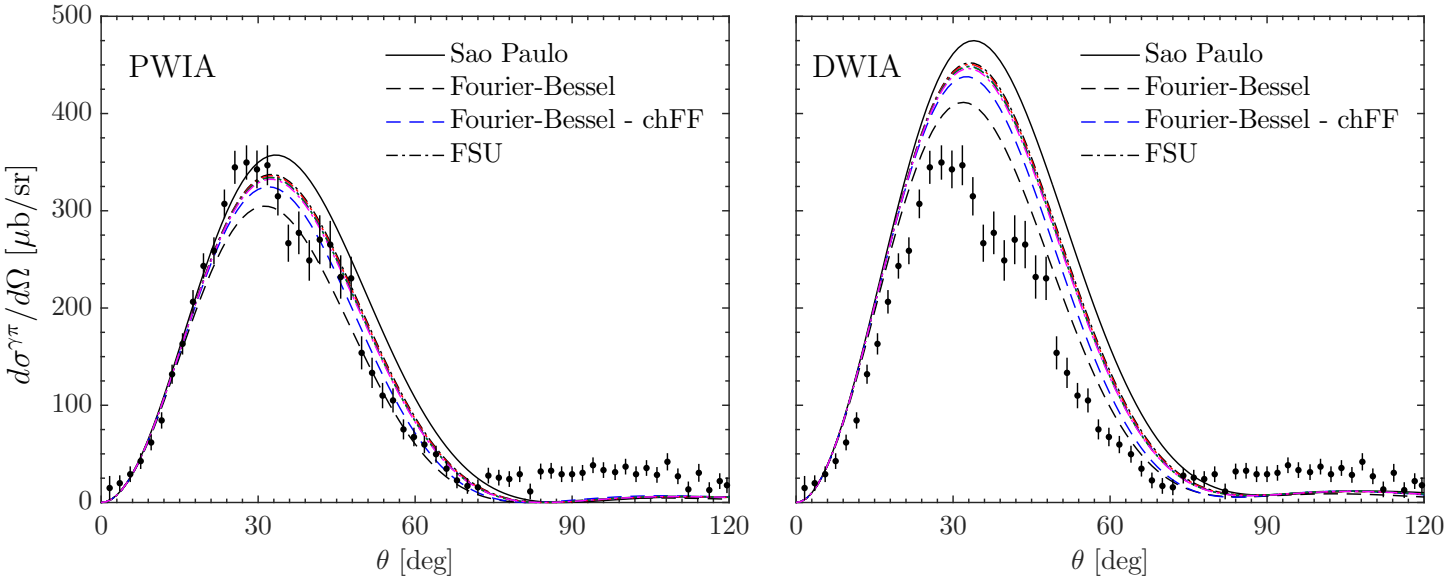

Figure 9.6: Same as Fig. 9.2 for a ^{40}Ca target. The densities are the ones from Fig. 6.2. The different FSU densities are displayed in the same color code as in the right panel of Fig. 6.2. Data from Ref. [129].

the angular region of the maximum.

The maximum of the peak exhibits variations of around 15%, both in the PWIA and in the DWIA. Contrary to the case of ^{12}C, this difference is larger than the uncertainty on the data which is slightly above 10%. The angles of the maximum of each density exhibit at most a 2° difference. Contrary to the case of carbon, this difference is similar to the angular uncertainty of the data. Note however that if we look only at the FSU densities, these differences are of a mere 1.5%, nearly ten times smaller than the uncertainty on the data. There is hence no way to discriminate between these FSU densities.

Finally, Eq. (9.1) is valid for all densities. The scaling being $\delta \simeq 0.35$ for all densities (δ is equal to 0.329 for SP, 0.350 and 0.349 for FB and FB chFF and in the range 0.341-0.343 for all the FSU densities). Beyond the minimum however, nonlinear effects start to appear although the cross sections are too small to observe these effects experimentally.

The agreement between the calculations and the data is not good, especially beyond the first minimum. As already discussed, this can be caused by the contamination of incoherent processes in the data.

^{208}Pb

Finally, the π^0 photoproduction cross sections of Ref. [129] on a ^{208}Pb target at an incident photon kinetic energy of 200 MeV in the lab frame are displayed on Fig. 9.7 as black dots. Are also shown the results of my calculations in the PWIA (left panel) and DWIA (right panel). These are displayed in the active nucleon on-shell prescription $W_{\gamma N}^{N}$ (black) and in the spectator on-shell one $W_{\gamma N}^{N}$ (red). The density used in my calculations is the FSU030 density [see Sec. 6.2.1 and Fig. 6.7]. Additionally, the approximation Eq. (9.1) is also displayed on the right panel as dashed lines.

Because of the much larger mass of the target, the peak is pushed towards forward

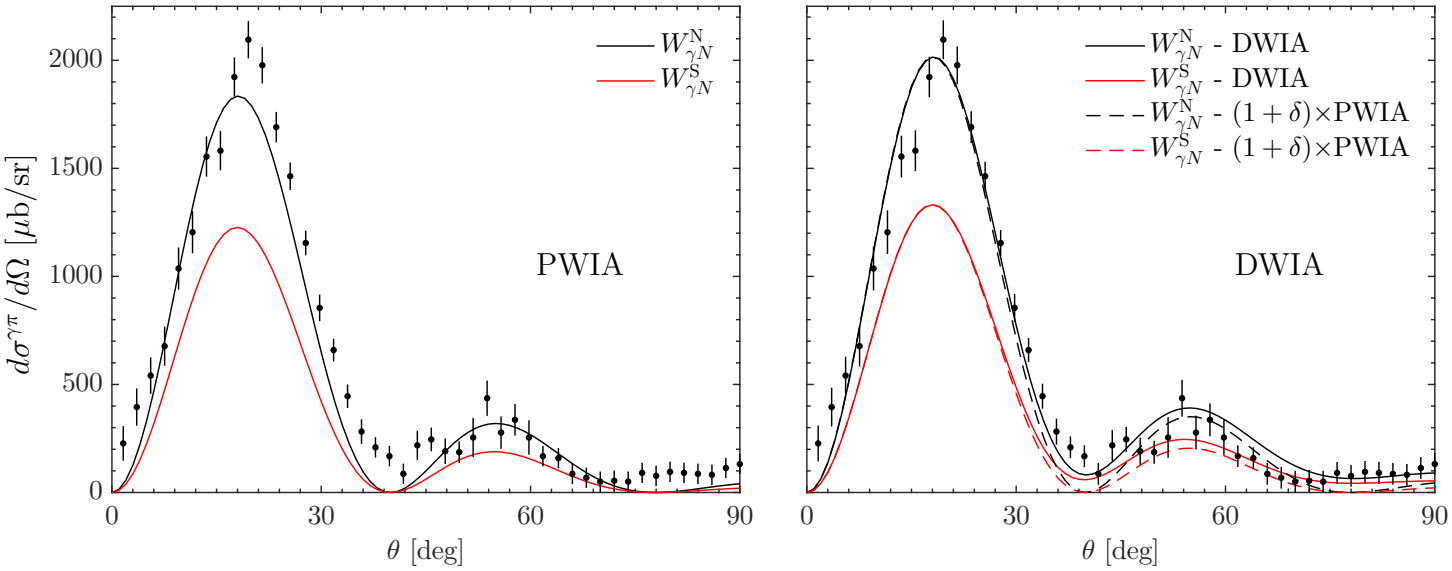

Figure 9.7: Same as Fig. 9.1 for a ^{208}Pb target. The density used here is the FSU030 one [see Fig. 6.7]. Data from Ref. [129].

angles and has now its maximum at an angle around 20°. Additionally, we clearly see the first two minima of the density Fourier form factor at around 40° and 80° as well as a marked second peak between them [see also Fig. 9.5].

In the first peak and similarly to lighter targets, the magnitude of the active nucleon on-shell prescription is 1.5 times larger than that of the spectator on-shell one, the former hence working much better than the latter. Contrary to ^{40}Ca however, this is clearly the case also in the DWIA, where the nucleon on-shell prescription works spectacularly well. As already observed for carbon and calcium, the choice of prescription impacts the PWIA cross section nearly only in its magnitude. Both curves are hence similarly shaped and the angles of the different maxima and zeros are the same.

When distortion is switched on, the DWIA cross section agrees spectacularly well with the data. This is true not only in the region of the first peak but also in the region of the minimum. In the region of the second peak, my results slightly overestimate the data. Up to 35°, near the minimum, the scaling Eq. (9.1) reproduces nearly perfectly the DWIA cross section. Note that the effect of the distortion is nearly identical for both prescriptions but are much smaller than for ^{12}C and ^{40}Ca (δ is 0.099 and 0.086 for the active nucleon on-shell $W^N_{\gamma N}$ and the spectator on-shell $W^N_{\gamma N}$, respectively). Beyond the first peak, non-linear effects become visible, such as the smeering of the first (and second) zeros as well as the flattening of the third maximum (around 90°). At these large angles, the scaling Eq. (9.1) is then not a good approximation as the cross section main contribution comes from the distortion which varies non linearly with the density.

The effect of the density on these cross sections is displayed on Fig. 9.8 in the PWIA (left) and DWIA (right) for the São Paulo (solid) and the FSU model (dash-dotted). Because the nucleon on-shell prescription seems to work spectacularly, only results calculated in this prescription are displayed. At very forward angles once again, the cross sections for all these densities are superimposed and differ only beyond 10°, in the angular region of the maximum of the first peak.

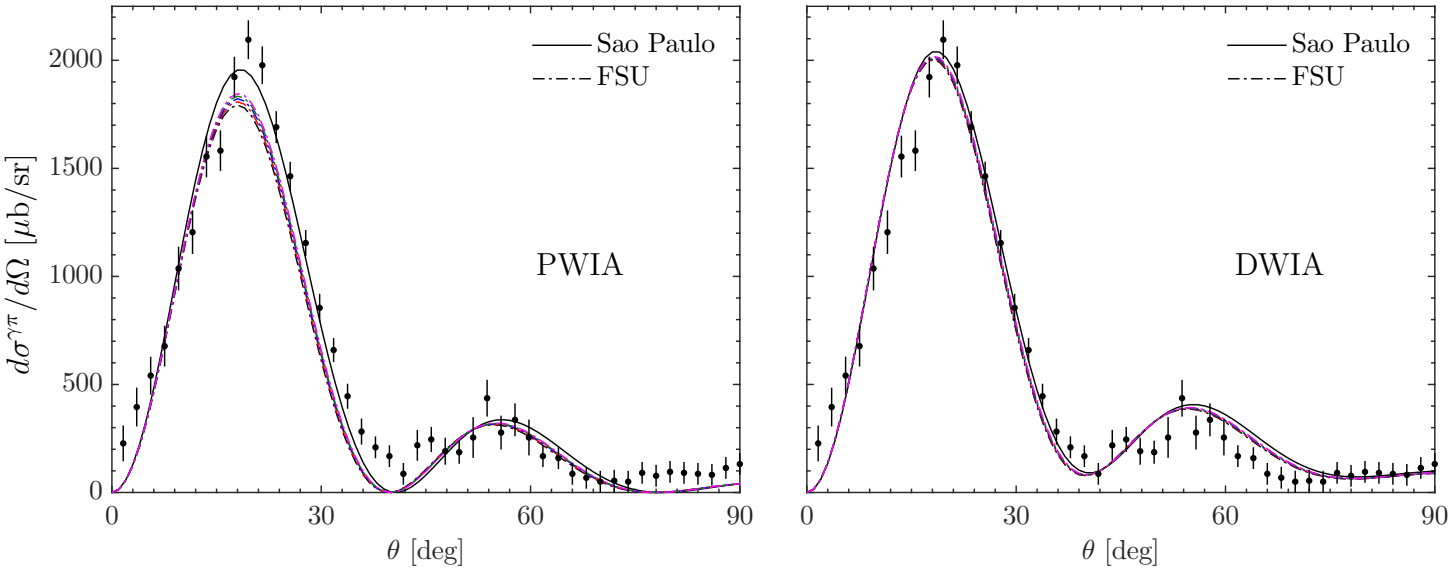

Figure 9.8: Same as Fig. 9.2 for a ^{208}Pb target. The densities are the ones from Fig. 6.7. The different FSU densities are displayed in the same color code as in the right panel of Fig. 6.7. Data from Ref. [129].

In the PWIA, the magnitude at the maximum of the peak exhibits variations smaller than the 10% experimental uncertainty and the position of the maximum varies by less than 0.5°, nearly 4 times less the angular uncertainty of the data. The relative discrepancies between the different density curves in the region of the second maximum remain roughly the same, below the 10% mark, well below the 30% uncertainty of the experimental data. Moreover, the angular shift that can be observed between the positions of their second maximum is at most of 1°, which is well below the angular uncertainty of the data.

While the distortion simply scales the PWIA curve in the region of the first peak as in Eq. (9.1), this scaling is much more density dependent in the case of lead than it is for lighter targets (δ=0.043 for the SP density and goes from 0.117 to 0.094 for the FSU000–FSU040 ones). Interestingly, this tends to reduce the discrepancies between the different densities even more (around 2%). Similarly, adding the distortion reduces the angular shift that exists between these curves. The agreement between the calculations and the data is very good in this case, especially in the first peak and in the region of the first minimum, but all densities reproduce the data and it is nearly impossible to discriminate between them.

Summary of the comparison on all targets

The agreement of my calculations to the data of Ref. [129] varies between targets. For ^{12}C, the agreement is fair but my DWIA calculations slightly overestimate the data at the peak for all densities. For ^{40}Ca, the agreement is not good since the data cannot be reproduced in the DWIA with any density, although it could be caused by the contamination of incoherent events. For ^{208}Pb, the agreement is perfect for all of them at the DWIA. For these three nuclei, this comparison seems to confirm that the best prescription is the

active nucleon on-shell [see Sec. 7.3.2]. From private communications with the authors of Ref. [129], this result was also observed in their analysis of the data. Therefore, I will use only this prescription in the following.

In the region of the first peak, the effect of the distortion is mostly to change the magnitude of the PWIA cross section. Correspondingly, the DWIA cross section can be approximated with a good accuracy by Eq. (9.1). This works particularly well for all targets up to the angle of the first minimum. If this remains true for medium heavy nuclei such as tin, this might make the interpretation of the data easier because the first peak is thus directly proportional to the Fourier transform of the density. It should be noted however that while the scaling approximation works well, there is (yet) no way to predict the value of δ beforehand. Also, while δ is not density dependent on carbon and calcium, it is on heavier targets. This, on the contrary, is not desirable. Moreover, the differences between the DWIA cross sections predicted for the different densities is usually smaller or at least comparable in size to the uncertainty on the data. This is especially true for ^{208}Pb, for which the relative differences between the DWIA cross sections are smaller than the experimental uncertainty by up to one order of magnitude.

The results on the ^{208}Pb target call for a general comment. As it is visible from Fig. 9.8, variations of the skin thickness of around 0.11 fm for the different FSU densities (see Tab. II.3) have a very small impact on the DWIA cross section. The relative differences at the maximum of the peak are indeed lower than 1%. Adding the São Paulo density to this comparison enlarges these discrepancies by a factor 2, to 2% but it also increases the variations of the skin thickness by the same factor of 2, to roughly 0.2 fm. The angular shifts originating from these changes in the density are also below the degree. It hence seems that discerning between these densities would require measurements with a very high precision both in angle and in magnitude. This disagrees with the very high precision of the recent measurement of Ref. [132], which quotes a neutron skin thickness of $\Delta r_{np}^{208} = 0.15 \pm 0.03(\text{stat.})^{+0.01}_{-0.03}(\text{sys.})$ fm, even though their uncertainty on the data at the first peak is around 10%.

9.2 Recent experiments: Sn isotopic chain and ^{48}Ca

Because tin exhibits the largest stable chain of isotopes in the nuclear chart, a recent measurement has been carried out at MaMi (see also Sec. 5.1) on the three different isotopes ^{116}Sn, ^{120}Sn and ^{124}Sn [137]. Out of these three isotopes, the analysis of the measurements has been started only for the lightest and heaviest ones, i.e. ^{116}Sn and ^{124}Sn. In this section, I will apply my reaction code to these two isotopes.

While the measurements have been carried out at energies in a range of energies between 140 MeV and 300 MeV for the laboratory photon energy, the extraction of coherent events is best done at a bin energy between 180 MeV and 190 MeV [private communications with Maria]. I will thus compute the cross sections at these energies, which fortunately are compatible with the use of the MSU potential [see Sec. 8.2.3].

Additionally, I will run these calculations for a ^{48}Ca target. While being much lighter than the tin isotopes, it has an 8-neutron excess compared to protons and should thus exhibit a neutron skin. Recent measurements [138] have been carried out on this nucleus and my calculations could be helpful in the analysis of the data. I will make calculations in the same range of energies as for tin.

^{116}Sn and ^{124}Sn

On Figs. 9.9 and 9.10, the photoproduction cross sections are displayed for the ^{116}Sn and ^{124}Sn targets, respectively. These are calculated in the PWIA (left panel) and in the DWIA (right panel) at a photon energy of 185 MeV in the laboratory frame. For the sake of clarity, only three different densities are shown. These are the FSU000 and FSU040 [see Sec. 6.2.1] as well as the São Paulo one [see Sec. 6.3.1]. As discussed in Sec. 6.5, these two FSU densities correspond to those that reproduce the most extreme thicknesses of the neutron skin [see also Tab. II.3 and Figs. 6.5 and 6.6].

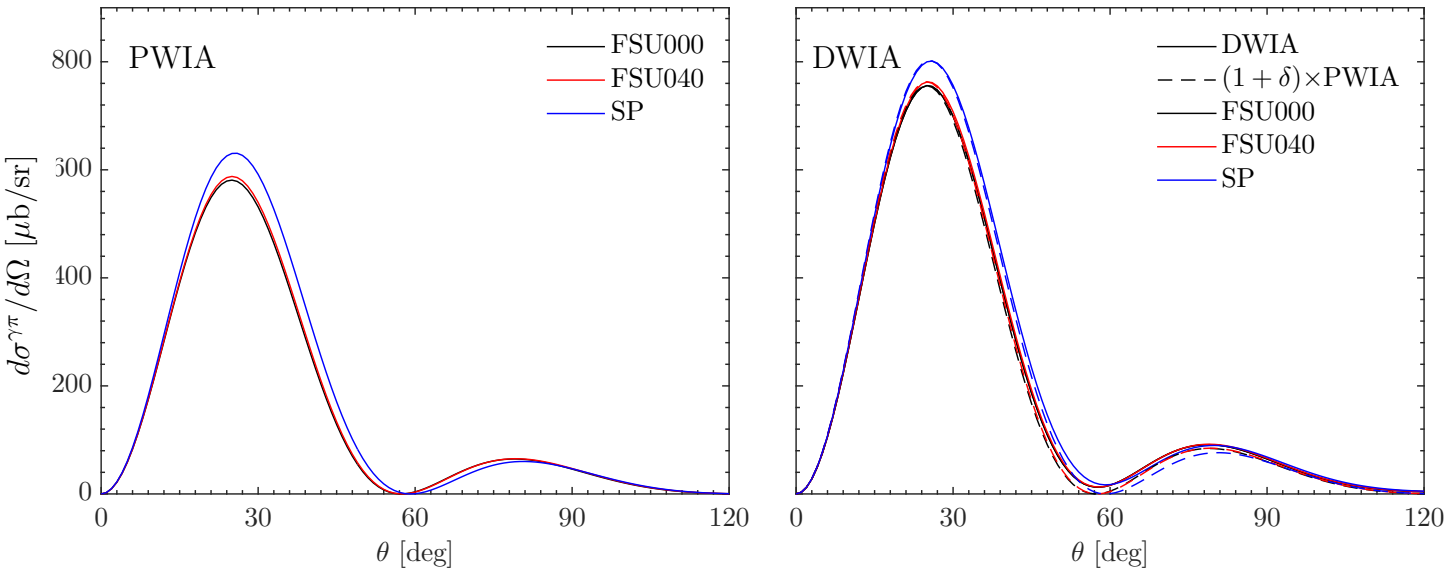

Figure 9.9: Coherent π^0 photoproduction cross sections on a ^{116}Sn target at an incident photon kinetic energy of 185 MeV in the laboratory frame. PWIA (left panel) and DWIA (right panel) calculations are shown in the active nucleon on-shell prescription $W^N_{\gamma N}$. The densities correspond to the FSU densities that reproduce the most extreme thicknesses of the neutron skin [see Fig. 6.5 and Tab. II.3]. On the right panel, the agreement of the approximation Eq. (9.1) with the DWIA cross section is also evaluated.

Several of the characteristics already observed in Sec. 9.1 are also visible on these figures. First, the zeros of the PWIA cross section are clearly visible on the left panels. These correspond to the zeros of the Fourier transform of the density. Second, these zeros are pushed towards the forward angle region as the target mass increases (compare the left panels of Figs. 9.9 and 9.10). This is due to the larger extent of the nucleus in position space and hence to the Fourier form factor of the density being more sharply peaked in momentum space. This means that the zeros appear at smaller angles than for lighter targets. Note however that when comparing two nuclei with a relatively similar number of nucleons such as ^{116}Sn and ^{124}Sn, this effect is small. Here, this shift is about 1°. By comparing the zeros of the two isotopes, one could thus hope to gain information about the distribution of these excess neutrons inside of the nucleus. The extraction of such information is however hindered by the distortion which tends to smeer the cross section in the angular range of the PWIA zero, which becomes a local minimum (see

right panels). As already observed before, the DWIA cross section (solid) can be well approximated by scaling the PWIA cross section as in Eq. (9.1) (dashed). In the region of the first peak, these are indeed in a very good agreement. It is interesting to note that δ is slightly dependent on the density (on ^{116}Sn, δ=0.301 and 0.298 for the FSU000 and FSU040 densities and 0.271 for the SP one) but that these values of δ are nearly identical on both targets (on ^{124}Sn, δ=0.300 and 0.298 for the FSU000 and FSU040 densities and 0.268 for the SP one). At larger angles and in the region of the second maximum however, the DWIA and its approximation Eq. (9.1) do not coincide. As already observed in the previous section, this confirms that the angular region of the first zero and of the second peak are influenced non-linearly by the distortion. We should expect this to hinder the clean extraction of a neutron-skin thickness.

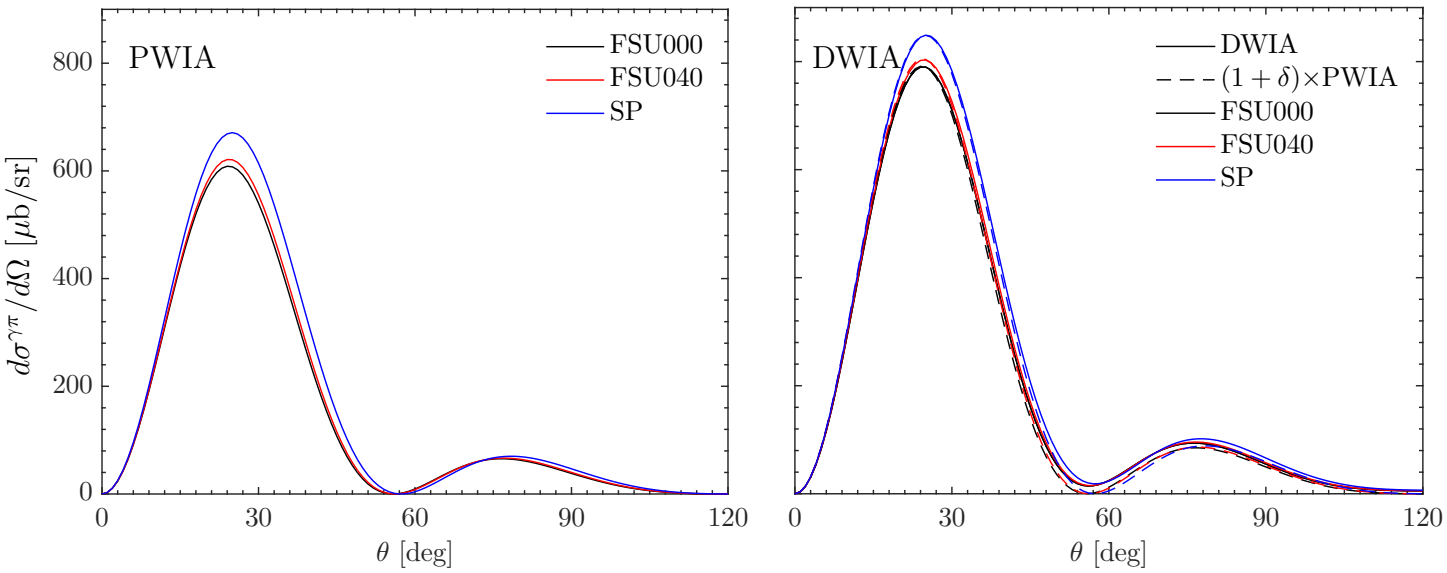

Figure 9.10: Same as Fig. 9.9 for a ^{124}Sn target.The densities correspond to the FSU densities that reproduce the most extreme thicknesses of the neutron skin [see Fig. 6.6 and Tab. II.3]

For both isotopes, the discrepancies observed at the peak for the different densities are slightly smaller than 10% for the PWIA, while they lie around 6% for the DWIA. This decrease in the sensitivity to the density is reminiscent of what has been observed for a ^{208}Pb target. If we only consider the realistic FSU densities, these drop to around 1–1.5% for both the PWIA and DWIA cross sections. In order to realise how these differences compare to experiment, let me plot these curves alongside preliminary data of the measurement [137]. These have been given to me by M. Ferretti, who is working on their analysis.

On Fig. 9.11, the preliminary data on coherent pion photoproduction are shown for both targets (on the left panel, for ^{116}Sn, on the right for ^{124}Sn). The PWIA and DWIA cross sections shown above are also displayed. Note however that because the data are largely overestimated by my calculations, I have scaled these by some arbitrary factor (0.45 for both targets) so that they fall approximately on top of the measurements. As these data are preliminary, there is no way yet to know if my predictions are off or if some normalising factor is missing in the data analysis. Note however that the results of

previous Sec. 9.1 on ^{12}C and ^{208}Pb seem to suggest the latter. What can be compared however are the shapes of the data with the predictions of my model, as well as the order of magnitude of the precision on this data with the discrepancies induced by the theoretical changes in density.

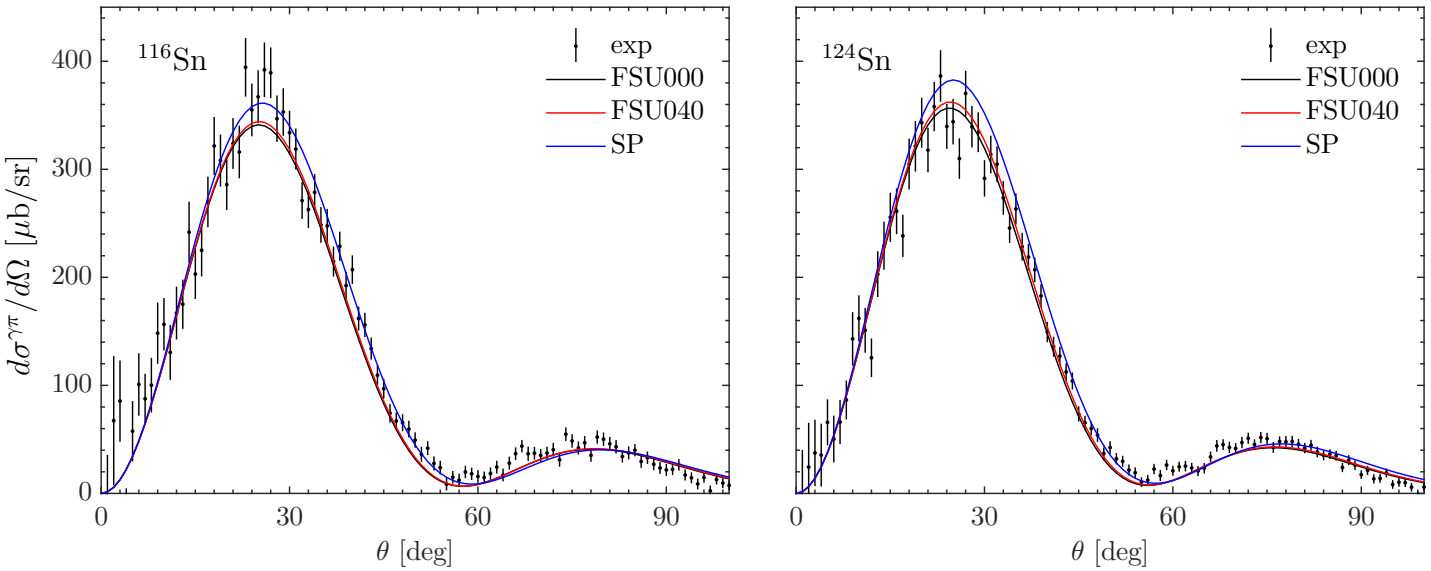

Figure 9.11: Comparison of preliminary data on π^0 photoproduction cross sections on ^{116}Sn (left) and ^{124}Sn (right) targets with my theoretical DWIA calculations. The incident photon energy is taken in the 180-190 MeV range of energies in the laboratory frame. Cross sections are calculated in the nucleon on-shell prescription for three densities: the FSU000 (black), FSU040 (red) and São Paulo (blue). Note that my theoretical calculations have been arbitrarily scaled by a factor of 0.45 for both targets so that they are approximately on top of the data.

The shape of my (scaled) theoretical predictions reproduces the shape of these preliminary data quite well. This is especially true in the angular region of the first peak. Additionally, on the one hand, the positions of the first peak and of the minimum as well as the magnitude of the minimum seem to correspond to ones of the data for both targets. On the other hand, the position of the second DWIA peak seems to be slightly shifted towards larger angles and looks wider than the preliminary data. It should be noted however that the uncertainty on the data is much larger than the discrepancies between the different densities. This is particularly visible in the first peak, where the relative uncertainty of the data at the maximum lies between 10 and 15% for both targets, which is twice the differences between the SP and FSU curves, and around 10 times larger than between the two FSU ones. At the position of the second peak, where the distortion has the largest effect, this experimental uncertainty grows to 20%, therefore hindering significantly the extraction of valuable information from these angles. These results seem to suggest that the extraction of the neutron skin from these measurements will be difficult if the uncertainty on the data remains at the level shown here.

^{48}Ca

On Fig. 9.12, the coherent π^0 photoproduction cross sections are displayed for a ^{48}Ca target. These are calculated in the PWIA (left panel) and in the DWIA (right panel) at a photon energy of 185 MeV in the laboratory frame. For the sake of clarity, only three different densities are shown. These are the FSU012 and FSU032 [see Sec. 6.2.1] as well as the São Paulo one [see Sec. 6.3.1]. As discussed in Sec. 6.5, these two FSU densities correspond to those that reproduce the most extreme thicknesses of the neutron skin [see also Tab. II.2 and Fig. 6.4].

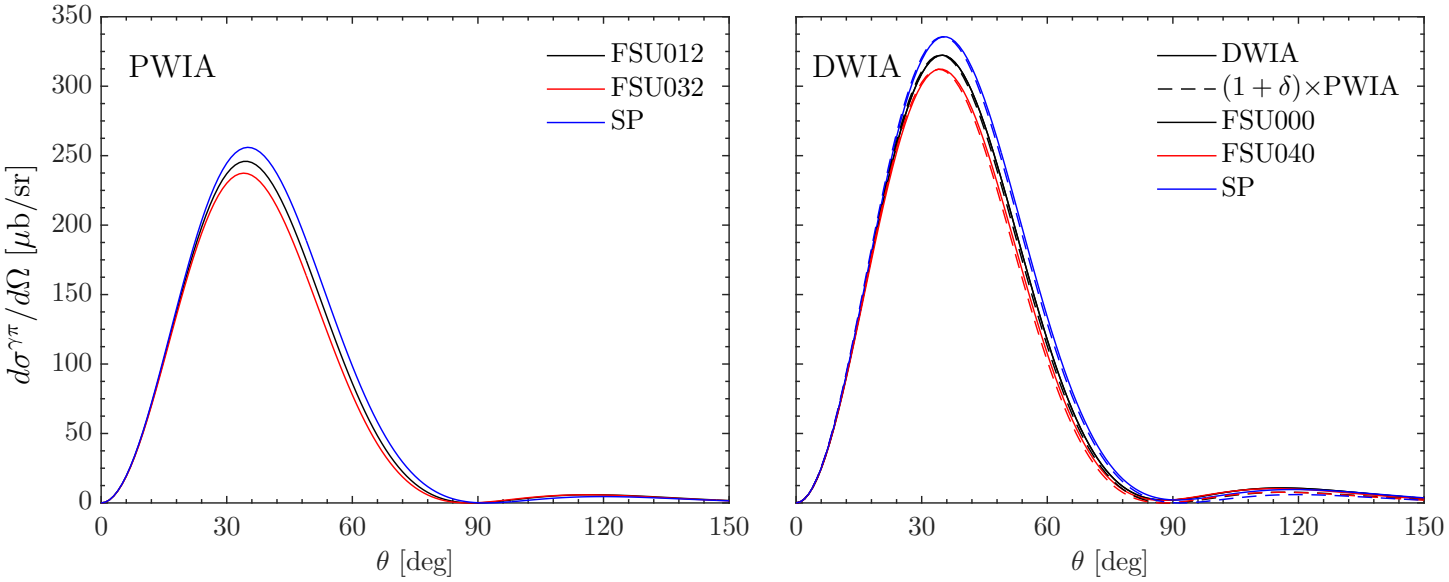

Figure 9.12: Coherent π^0 photoproduction cross sections on a ^{48}Ca target at an incident photon energy of 185 MeV in the lab frame. PWIA (left panel) and DWIA (right panel) calculations are shown in the active nucleon on-shell prescription $W^N_{\gamma N}$. The densities correspond to the FSU densities that reproduce the most extreme thicknesses of the neutron skin [see Fig. 6.4 and Tab. II.2]. On the right panel, the agreement of the approximation Eq. (9.1) with the DWIA cross section is also evaluated.

Several of the characteristics already observed for ^{40}Ca are also visible for ^{48}Ca. First, the shape of these cross sections are very similar to what has been observed on Fig. 9.4 for the lighter ^{40}Ca isotope. Indeed, they both exhibit a very small second peak comparatively to the first, both in the PWIA and the DWIA. From my calculations, we see that a very high precision would thus be required beyond the angle of the first minimum in the actual data taking to observe anything. Also, similarly to what has been observed on Fig. 9.4, the effect of the distortion is to simply scale the PWIA cross section in the angular region of the first peak, according to Eq. (9.1). Similary to ^{40}Ca, the scaling affects the PWIA cross section by more than 30%. Contrary to the results of Fig. 9.6 however, this scaling is nearly identical for all densities (δ ranges from 0.311 to 0.315 for the FSU densities and equals 0.311 for the SP one).

The changes induced by variations in the density are very small, with relative differences below 7% in the region of the first peak. These are even twice as small when we only

consider the FSU densities. If we compare these differences to the skin thicknesses Δr_{np} that these densities reproduce [see Tab. II.2], we see that the precision on the coherent π^0 photoproduction measurement that is needed to be able to discriminate Δr_{np} at the 0.1 fm level is already *very* high.

9.3 Summary and prospects of this model

In the previous sections, I have compared my model for coherent π^0-photoproduction on the data of Krusche *et al.* [129] who measured this process on several targets, i.e. ^{12}C, ^{40}Ca and ^{208}Pb, at energies of the impinging photon of 200 MeV.

The first result of these comparisons is that for all these targets, the active nucleon on-shell prescription $W_{\gamma N}^{N}$ [see Sec. 7.3.2] works best and seems to be the right choice for future works. In this prescription, the quality of the agreement of my calculations with the data depends on the target. For the light targets, ^{12}C and ^{40}Ca, my DWIA predictions overestimate the data [see Figs. 9.1 and 9.4]. This overestimation is however significant only in the case of ^{40}Ca, for which the data might be contaminated with incoherent processes. For ^{12}C, the agreement is actually still fair. For the heaviest target ^{208}Pb finally, my DWIA calculations fall directly on top of the data [see Fig. 9.7]. The agreement is therefore spectacular without any adjustment of the MSU potential.

In the region of the first peak, the distortion has a simple scaling effect on the PWIA cross section. With a good agreement, the DWIA cross section can then be approximated by Eq. (9.1), i.e. the product of a constant factor $(1 + \delta)$ with the PWIA cross section, where δ is the rate of increase of the cross section induced by the distortion [see Figs. 9.1, 9.4 and 9.7 at 200 MeV and Figs. 9.9, 9.10 and 9.12 at 185 MeV]. The knowledge of this factor could help greatly in the analysis of experimental cross sections as we would then have access to the PWIA cross section (at least in the first peak), which is directly proportional to the Fourier transform of the density. The value of δ is displayed in Fig. 9.13 for all the targets and densities analysed in past sections. Note that these values are calculated for a π^0 photoproduction reaction at 200 MeV photon energy in the laboratory frame for all targets. These are regrouped in the four density families that have been used in this work: the São Paulo one (asterisks) [see Sec. 6.3.1], the Fourier-Bessel ones (squares) [see Sec. 6.3.2], harmonic oscillator ones (plus sign) [see Sec. 6.2.2] and FSU ones (cross) [see Sec. 6.2.1]. While there is currently no way to predict δ beforehand, we can observe from Fig. 9.13 that it decreases with A. This is a good news since the cross section is then closer to its PWIA, which is directly proportional to the Fourier transform of the density. However, while for light nuclei, the dependence of δ on the density is rather small, it increases with A. This is visible in Fig. 9.13 from the range of values taken by δ for a given isotope. This has the unfortunate effect of reducing the differences between the cross sections calculated for different densities [see for example Fig. 9.8], thereby increasing the precision needed on experimental data taking.

In the large angle region, past the first minimum (for targets heavier than ^{12}C that exhibit a minimum), the effect of the distortion is not linear. At these angles, the distortion tends to smeer the minimum and to flatten the second maximum [see Fig. 9.8]. For these angles, the approximation Eq. (9.1) is no longer good and calculations need to be done in the DWIA to correctly take the distortion into account.

Finally, on ^{12}C, ^{40}Ca and ^{208}Pb targets for which I have access to the uncertainty on the π^0 photoproduction cross section data, the effect of the density is rather small [see Figs. 9.2, 9.6 and 9.8]. In particular, for ^{208}Pb, the differences induced by changes in the

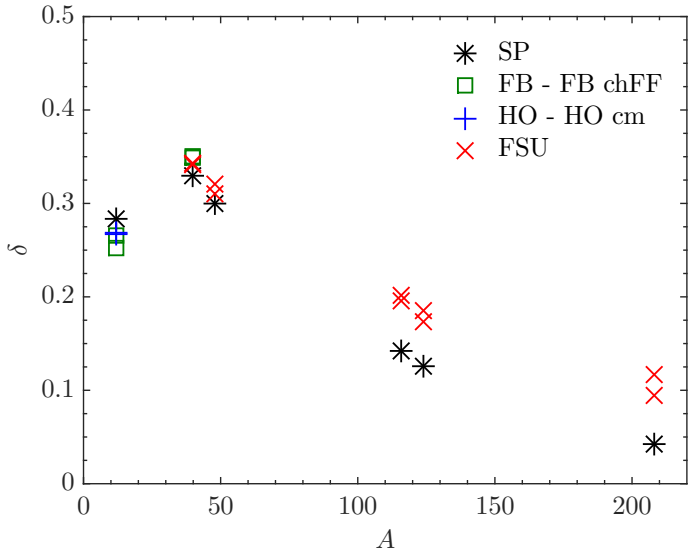

Figure 9.13: Value of δ, the linear increase due to distortion [see Eq. (9.1)] as a function of the target mass number A. The values of δ (calculated for a coherent π^0 photoproduction at a photon energy of 200 MeV in the laboratory frame) are regrouped in the different families of densities encountered in this work, i.e. the São Paulo one (asterisks) [see Sec. 6.3.1], the Fourier-Bessel ones (squares) [see Sec. 6.3.2], harmonic oscillator ones (plus sign) [see Sec. 6.2.2] and FSU ones (cross) [see Sec. 6.2.1]. Note that for the FSU densities, only the ones that correspond to the largest and thinnest skin thicknesses are displayed.

density can even be as small as a tenth of the corresponding experimental uncertainty. While the data on tin isotopes are still preliminary, these observations also seem to be valid. We should expect a similar behaviour on ^{48}Ca. If we consider the changes of neutron-skin thickness Δr_{np} that these different densities reproduce [see Tabs. II.2 and II.3], we can safely conclude that with the current experimental resolution, the coherent π^0-photoproduction cross section is not very sensitive to Δr_{np}. The precision of future experiments that rely on this process should thus be at the percent level, at the least, to discriminate between such neutron-skin thicknesses.

Note however that if one gets to this level of experimental precision, there remains another uncertainty that needs to be quantified: the sensitivity to the π-A potential itself. As discussed in Sec. 8.2.3, the one used in this work has been fitted on pion-nucleus elastic scattering data at one single energy on a whole range of targets. The shape of this potential can be affected by the different simplifying assumptions used to build it (especially at the second order [see Sec. 8.2.3]) as well as from the inevitable uncertainty that exists on its fitted parameters. One of the natural prospects of this work is the systematic study on the impact of the potential used for the π-A interaction.

To get a foretaste of what one could expect from such study, I have slightly modified some of the parameters of the MSU potential [see Sec. 8.2.3] and analysed the effect of this change on the DWIA coherent π^0 photoproduction cross section. Here, I have slightly modified the values of the $\bar{b}_0$ and c_0 parameters of the MSU potential [see Eqs. (8.33),

(8.34) and (8.36)] by a mere 5% separately[6]. In order to check if this change is not too drastic, its effect on the π^+-^{12}C elastic scattering cross section (calculated at a pion kinetic energy of 50 MeV in the laboratory frame) is shown on the left panel of Fig. 9.14 as a grey area and compared to the elastic scattering cross section for the original values of the potential (red) and to data on this cross section [see also Sec. 8.10]. On the right panel, the effect of varying these parameters on the DWIA coherent π^0 photoproduction cross section is shown for a ^{124}Sn target described by the FSU040 density at an incident photon kinetic energy of 185 MeV in the lab frame (grey area). These are compared to DWIA calculations that use the original MSU potential and a FSU040 (red), a FSU000 (black) and a SP density (blue) [these curves are the ones displayed in solid lines on the right panel of Fig. 9.10]. Note that the top right panel of Fig. 9.14 is a zoom on the maximum of the peak while the bottom right panel is a zoom in the angular region of the minimum and second maximum.

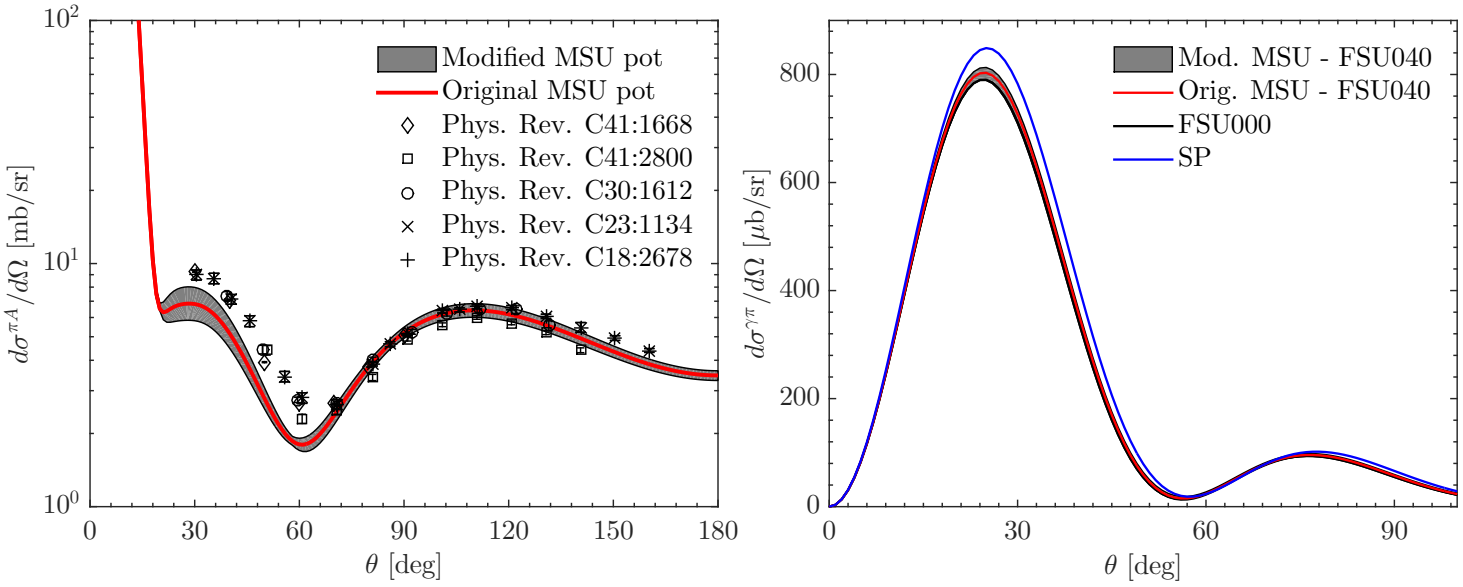

Figure 9.14: Effect of slight variations of the parameters of the MSU potential on the π^+-^{12}C elastic scattering cross section at a pion kinetic energy of 50 MeV in the laboratory frame (left) and on the DWIA coherent π^0 photoproduction cross section on a ^{124}Sn target at an incident photon kinetic energy of 185 MeV in the lab frame (right). Details in the text.

The left panel of Fig. 9.14 shows that the variations of $\bar{b}_0$ and c_0 by 5% are not too drastic. Indeed, the grey band around the original elastic scattering cross section (red) has a similar width as the uncertainty on the data of the different experiments displayed here. These changes on $\bar{b}_0$ and c_0 should therefore be a good order of magnitude of the uncertainty on the MSU potential (at least for ^{12}C). The impact of these variations on the coherent π^0-photoproduction calculated at the DWIA on the right panel of Fig. 9.14,

[6]Note that in a proper systematic study, these two complex parameters (four real ones) would have to be modified separately and simultaneously such as to span the whole four-dimensional parameter space. This however increases significantly the number of parameters combinations and hence the calculation time. Here, as I aim only at a mere foretaste of what one could obtain in a more systematic study, I will just change them separately.

also shown as a grey band, are significant. Let us note how at the first maximum (for which a zoom is given in the top panel of Fig. 9.15), the uncertainty on the MSU potential translates into variations of the cross section that are twice as big as the difference between the FSU000 and FSU040 already observed in Fig. 9.10. Similar observations can be made in the region of the minimum and the second maximum (for which a zoom is given in the bottom panel of Fig. 9.15).

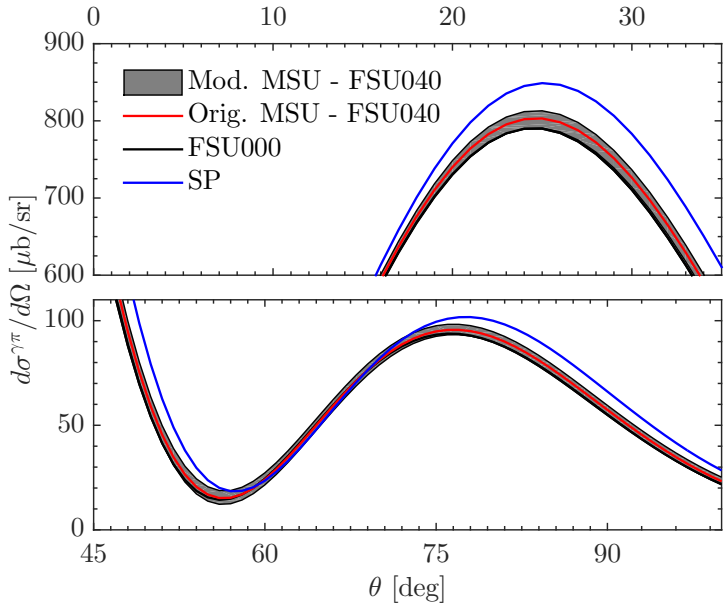

Figure 9.15: Zoom of the plot on the right panel of Fig. 9.14. Top: zoom on the first maximum. Bottom: zoom on the region of the first minimum and the second maximum.

While this does not qualify as a proper systematic study of the sensitivity to the π-A potential, the results of these calculations show that the theoretical uncertainties of the model should be accounted for. These uncertainties include the values of the parameters of the potential but also its shape [see the assumptions made to build the second order in Sec. 8.2.3]. The building of a π-A potential that could allow this sensitivity study in a systematic way is currently ongoing and will be discussed in the PhD thesis of V. Tsaran. Finally, the effect of the inclusion of two-body processes in the photoproduction amplitude [see Fig. 7.1] should also be taken into account. Such study has been conducted in Ref. [161] and found that the influence of these processes on the photoproduction cross section can be as large as 5% for a ^{208}Pb target.

Conclusion

The equation of state of nuclear matter governs the properties of nuclear systems in a whole range of scales, from the microscopic scale of the nucleus to the macroscopic scale of neutron stars [8, 9]. However, the ingredients of this equation are not well known because of how different are the conditions in which nuclear matters appears on Earth or in neutron stars. By studying the structure of nuclei and how their properties evolve as we cover the whole chart of nuclides and go from stability to extreme instability, in the laboratory or by watching distant stars, nuclear physicists hope to better constrain this equation.

One of the most important ingredients of the equation of state of nuclear matter is the symmetry energy, which makes the bridge between the properties of the rather symmetric systems ($N \gtrsim Z$) that we find on Earth and the extremely asymmetric neutron stars ($N \ggg Z$) found in our universe [8, 9]. But even if this asymmetry is small, its effects are still visible on medium-heavy and heavy nuclei. Indeed, for these nuclei, the excess neutrons tend to form a thick layer around the nucleus: the neutron skin. The thickness of this skin seems to be highly correlated with the symmetry energy and more particularly its density dependence. The measure of this thickness to attempt at constraining the symmetry energy are one of the hot topics of today's nuclear physics.

The advent of radioactive ion beams has opened the exploration of the nuclear chart far from stability [3]. Close to the driplines, very peculiar nuclear structures have been discovered: halo nuclei. While most nuclei are usually seen as a compact system of bound nucleons, some radioactive nuclei have been observed to be unusually large [14]. For these exotic nuclei, one nucleon extends farther out of the range of the nuclear interaction and forms a diffuse halo, which gives them their name. Because the nucleon of the halo spends most of its time far from the nucleus to which it is bound, halo nuclei can be seen as a compact core around which "orbits" one valence nucleon. The halo phenomenon questions the traditional vision of nuclei close to stability and the validity of nuclear structure models far from stability. By studying such systems, nuclear physicists hope to better understand how the nuclear interaction works and hence improve their description of nuclear matter. They are studied experimentally through reactions [19], such as elastic scattering [35] and breakup [36]. The information on the structure of their halo that can be extracted from these collisions is however reaction and model dependent [44]. This dependence arises from the mechanisms involved in the collision as well as from the uncertainties on the core-target interactions, which are usually poorly known, especially when the core is radioactive [45].

My thesis comes within the scope of these two hot topics of today's nuclear physics and more particularly on the tools that are used in these fields. On the one hand, my work aims at the investigation of a new technique for the analysis of one-neutron halo nuclei, i.e. the ratio method [38]. Originally thought for the reaction of one-neutron halo nuclei at high energies, I have tested if it works at low energies, that would make the measurement appropriate to facilities such as SPIRAL2 (GANIL, Caen, France) and ReA12 at FRIB (Michigan State University), as well as for proton halos. On the other hand, my work strives to develop a new reaction code that attempts to estimate the neutron-skin thickness Δr_{np} of heavy nuclei from recent coherent neutral-pion photoproduction measurements at MaMi [137, 138] and to study the sensitivity of this process to Δr_{np}.

For neutron halos, such as ^{11}Be, the archetypical one-neutron halo nucleus, the angular distributions of elastic scattering and breakup reactions at intermediate and high energies exhibit very similar features, which do not carry much information about the structure of

the halo [44]. Correspondingly, by taking the ratio of cross sections of these two processes $\mathcal{R}_{\text{sum}}$, we are left with an observable that removes most of these features [38]. This result can be explained within the Recoil Excitation and Breakup model (REB) [37], in which the collision is considered adiabatic—or sudden—and the halo-target interaction can be neglected compared to the core-target one. In this model, the elastic scattering and angular breakup cross sections factorise into a projectile-structure part and a reaction-dynamics part. By taking their ratio in the REB, we completely remove the part that depends on the mechanism of the reaction and are then left with a form factor $|F_{E,0}|^2$ that depends only on the wave functions of the projectile. As such, by measuring this observable, we can hope to extract valuable information about the structure of the halo that are much less marred by the reaction mechanism. At high energies, that satisfy the adiabatic hypothesis of the REB, the ratio observable still exhibits some remnant oscillations that are due to the elastic scattering and breakup angular distributions not being perfectly in phase. These oscillations are however small and follow the REB form factor closely. Correspondingly, $\mathcal{R}_{\text{sum}}$ has been shown to be nearly independent of the reaction mechanism and insensitive to the core-target interaction while still being very sensitive to the structure of the halo of the projectile [38]. These interesting properties led to the idea that in an actual experiment, valuable information could be extracted by directly comparing the form factor to $\mathcal{R}_{\text{sum}}$ calculated from the data instead of comparing the results of cumbersome calculations to the cross sections for the individual processes. This is known as the ratio method.

In this work, I have explored the validity of this method for one-neutron halos at low energy and on proton halos at intermediate energy by studying the reactions of ^{11}Be at 20 MeV/nucleon and ^{8}B, the archetypical one-proton halo nucleus, at 44 MeV/nucleon. These results have led to the publications of Refs. [71] and [81], respectively. For these two reactions, my calculations have revealed that the remnant oscillations of the dynamical ratio (which were observed at higher energy and are not predicted by the REB) were aggravated in comparison to the ratio calculated for a reaction at high energy. Also, the agreement between $\mathcal{R}_{\text{sum}}$ and $|F_{E,0}|^2$ at small angles, where the reaction is Coulomb dominated, is poorer. These effects are due to the adiabatic assumptions of the REB being less well satisfied on these reactions. For ^{11}Be, this is caused by the lower energy of the reaction, which extends the importance of the Coulomb interaction on the cross section further out in angle. Similarly, for ^{8}B, this originates from the charge of the halo. The interaction of the valence-proton with the target has an infinite range which does not comply with the sudden assumption of the REB and which exacerbates the importance of Coulomb in comparison to neutron halos. Also, for ^{8}B, because of the addition of Coulomb, the valence-target interaction can hardly be neglected in comparison to the core-target one. This leads to increased remnant oscillations compared to the case of neutron halos at the same energy. For both projectiles however, these effects are rather small on light targets, for which the nuclear interaction still dominates. The agreement between $\mathcal{R}_{\text{sum}}$ and $|F_{E,0}|^2$ is not as convincing as for neutron halos at high energies but remains fair on light targets. Nevertheless, this agreement deteriorates significantly on heavy targets, for which the Coulomb interaction dominates. In the idea of applying the ratio method to other proton-halo candidates, I have also explored the reliability of the ratio method on several proton-rich nuclei. In the particular case of ^{27}P, the agreement of the ratio with its REB prediction is surprisingly good on a light target at high energy.

In an extensive study of the reliability of the ratio method and its sensitivity to the projectile structure and to the reaction model, I have shown that the ratio keeps

its sensitivity to the single-particle structure of the projectile, especially to the orbital angular momentum l_0 in which the halo is bound and its binding energy E_0. Changes in these two quantities induce significant variations in shape and in magnitude of the ratio and also influence how well the ratio can be approximated by its REB prediction. The agreement between $\mathcal{R}_{\rm sum}$ and $|F_{E,0}|^2$ has also been shown to be better when the projectile is loosely-bound and in a low orbital angular momentum, i.e. for s and p waves. Moreover, the ratio has been shown to keep its independence of the potential used to simulate the core-target interaction as well as the reaction model used for the calculations. It seems from these interesting properties that albeit less accurate than for neutron halos at high energy, the ratio could still enable experimentalists to infer pertinent structure information from the analysis of actual data. From the results discussed above, however, the ratio can be applied in its *strict* application, i.e. the one suggested in Refs. [38], only to ^{27}P, a possible proton-halo nucleus bound by 0.8 MeV in the s-wave. In a more *approximate* application of the ratio, only the order of magnitude and general shape of the experimental ratio would be confronted to $|F_{E,0}|^2$. This application makes use of the strong sensitivity in shape and magnitude of $\mathcal{R}_{\rm sum}$ to the projectile structure. Small differences in the ANC cannot be distinguished in this variant. However, it could still provide with a good estimate of the orbital angular momentum and binding energy, which are difficult to measure directly far from stability. This approximate application could be done at intermediate energy on ^{8}B or at lower energies on ^{11}Be. Finally, in the *dynamical* variant, measurements are compared not to $|F_{E,0}|^2$, but to the results of state-of-the-art dynamical reaction calculations like CDCC or DEA. The gain in this case over the more usual analysis of cross sections for individual reactions lies in the complete independence of the ratio to the reaction mechanism. Also, because it is the ratio of two cross sections, this observable is not sensitive to normalisation, which is a valuable experimental quality. This third variant would be applicable to any nucleus that exhibits a clear single-particle structure but is more computationally involved.

Because the major part of the disagreement between the REB form factor and the dynamical ratio comes from the interaction between the halo fragment and the target, a natural prospect of this work would be to account for the valence-nucleon-target interaction, e.g., at the first order of the perturbations. This might improve the REB prediction and open the *strict* application to ^{8}B at intermediate energy and to ^{11}Be at low energy.

The measurement of the neutron skin thickness carried out at MaMi relies on the process of coherent neutral-pion photoproduction. In order to interpret the recent data measured on tin isotopes and ^{48}Ca [137, 138] and extract the neutron-skin thickness from these experiments, I have built a reaction code that models this process. Moreover, this code will help me properly quantify the uncertainty that exists on the extraction of the neutron-skin thickness in this type of measurements. This is done by including the possibility to calculate this collision for realistic nuclear densities.

Within the impulse approximation which is one of the main assumptions of my model, the photoproduction on a nucleus is seen as the coherent sum of the contributions of the elementary process on each of the nucleons of the target. In the plane wave impulse approximation in which the produced pion exits the target unscattered after its production, the pion-photoproduction cross section is then directly proportional to the Fourier transform of the nuclear density [128], which is an interesting property. In reality, the pion scatters off the nucleus after its production. The contribution of this process is taken into account in the distorted wave impulse approximation. The pion-nucleus interaction

is then simulated by a potential which I have chosen from the literature [184]. This potential is built within the same formalism as the photoproduction from parametrising the elementary pion-nucleon scattering potential. The parameters of this elementary process are then adjusted such as to reproduce the elastic scattering cross sections on a nucleus on a wide range of targets and at a low scattering energy [184].

While the energy at which the photoproduction reaction takes place is well defined in the photoproduction process on a single and free nucleon, this is no longer the case on a nucleus. My calculations show that the choice of prescription for this energy actually has a very strong impact on the photoproduction cross sections. From the comparison of my predictions to the data of Ref. [129], in which this reaction has been measured on ^{12}C, ^{40}Ca and ^{208}Pb targets, the best results are obtained by considering the struck nucleon to be on-shell. In the particular case of ^{208}Pb target, the agreement of my model with the data is spectacular. Additionally, my calculations confirm the significant impact that distortion has in this process [128], therefore emphasising the need for a π-nucleus potential that correctly reproduces the scattering of the pion after its production. Finally, since the energy at which this experiment is measured are similar to the conditions of the recent experiments on tin and ^{48}Ca of Refs. [137, 138], these calculations performed on several realistic nuclear densities have also served as a test of the sensitivity of the process to the fine details of the description of the target.

Although distortion causes changes that are less significant in magnitude for heavy nuclei than for light nuclei, these changes become increasingly dependent on the density of the target as the target mass grows. Unfortunately, this has actually the effect of deteriorating the sensitivity of the pion-photoproduction process to the density. In the particular case of a ^{208}Pb nucleus, which exhibits the largest skin of the nuclei considered in this work, variations of the neutron-skin thickness Δr_{np} of around 0.1 fm have been shown to impact the photoproduction cross section at the percent level, which is up to ten times less than the size of the experimental error. These results, although less dramatic, hold for the tin targets, for which preliminary data exist and ^{48}Ca.

Finally, as a foretaste to a proper analysis of the sensitivity of these cross sections to the uncertainty on the parameters of the pion-nucleus potential, I have explored the influence of slight changes in those parameters. This brief study seems to suggest that the uncertainty on the potential can have a visible effect on the photoproduction cross section, therefore further hindering the extraction of the neutron-skin thickness.

In the light of all these results, the sensitivity of coherent neutral-pion photoproduction to the neutron-skin thickness is rather low. This process does not seem to be suited in the study of the neutron-skin thickness. This conclusion goes in contrast to the results of Ref. [132], in which the neutron-skin thickness of ^{208}Pb was reported with a remarkable precision, both on the statistics and the systematics.

In future works, my code could be used as a starting point to a proper systematic study of the sensitivity of these cross sections to the model of the reaction itself and hence to a proper quantification of the theoretical uncertainties on the extraction of the neutron-skin thickness that are induced by the model. In addition to the uncertainty on the parameters of the pion-nucleus potential briefly explored in this work, one could also be interested in quantifying the effect of changing the assumptions that lead to the shape of this potential, e.g. by deriving a new form for this potential. Some of the paths that could help for such derivation have also been explored very briefly. These will be more thoroughly investigated in the PhD thesis of V. Tsaran. Finally, one could be interested in the influence of including the possibility of charge exchange processes in the description

of the photoproduction. Although not studied systematically, this sensitivity has been explored in Ref. [161].

Appendices

A The completeness relation of the REB form factor

In this section, I will demonstrate that the denominator of expression (3.3), is equal to 1, that is, that

$$|F_{0,0}(\mathbf{Q})|^2 + \int |F_{E',0}(\mathbf{Q})|^2 \, dE' = 1. \tag{A.1}$$

Let me first write explicitly the form factors, as given in expressions (2.60) and (2.62) in Dirac notations

$$|F_{0,0}(\mathbf{Q})|^2 = \frac{1}{2j_0+1} \sum_{m_0} \left| \langle \phi_0 | \, e^{i\boldsymbol{Q}\cdot\boldsymbol{r}} \, | \phi_0 \rangle \right|^2, \tag{A.2}$$

$$|F_{E,0}(\mathbf{Q})|^2 = \frac{1}{2j_0+1} \sum_{m_0} \sum_{ljm} \left| \langle \phi_0 | \, e^{i\mathbf{Q}\cdot\mathbf{r}} \, | \phi_{ljm}(E) \rangle \right|^2. \tag{A.3}$$

The left hand side of expression (A.1) then reads

$$\frac{1}{2j_0+1} \sum_{m_0} \left[\left| \langle \phi_0 | \, e^{i\boldsymbol{Q}\cdot\boldsymbol{r}} \, | \phi_0 \rangle \right|^2 + \int \sum_{ljm} \left| \langle \phi_0 | \, e^{i\mathbf{Q}\cdot\mathbf{r}} \, | \phi_{ljm}(E') \rangle \right|^2 \, dE' \right]. \tag{A.4}$$

The term between brackets can be written more explicitly as

$$\langle \phi_0 | \, e^{i\boldsymbol{Q}\cdot\boldsymbol{r}} \, | \phi_0 \rangle \, \langle \phi_0 | \, e^{-i\boldsymbol{Q}\cdot\boldsymbol{r}} \, | \phi_0 \rangle + \int \sum_{ljm} \langle \phi_0 | \, e^{i\mathbf{Q}\cdot\mathbf{r}} \, | \phi_{ljm}(E') \rangle \, \langle \phi_{ljm}(E') | \, e^{-i\mathbf{Q}\cdot\mathbf{r}} \, | \phi_0 \rangle \, dE'. \tag{A.5}$$

We can then change the order of the summations and the integrals to find

$$\langle \phi_0 | \, e^{i\boldsymbol{Q}\cdot\boldsymbol{r}} \left[| \phi_0 \rangle \, \langle \phi_0 | + \int \sum_{ljm} | \phi_{ljm}(E') \rangle \, \langle \phi_{ljm}(E') | \, dE' \right] e^{-i\boldsymbol{Q}\cdot\boldsymbol{r}} \, | \phi_0 \rangle \, . \tag{A.6}$$

where the term between brackets is clearly the unity operator. Indeed, it consists of the sum of every projector on every possible state of the projectile. As these states are orthonormal to each other, the term between brackets is 1, by the completeness relation. The expression (A.6) is thus simply $\langle \phi_0 | \phi_0 \rangle = 1$. If we put this result back in Eq. (A.4), we finally have that

$$|F_{0,0}(\mathbf{Q})|^2 + \int |F_{E',0}(\mathbf{Q})|^2 \, dE' = \frac{1}{2j_0+1} \sum_{m_0} 1 = 1, \tag{A.7}$$

as stated in Eq. (A.1).

B Fresco

Fresco is a free program developed by Ian Thompson over the period 1983 - 2006, to perform coupled channels calculations in nuclear reaction physics. It uses Fortran 90 or Fortran 95. This is the program that has been used to solve the Schrödinger equation for coupled channels Eq. (2.26). In this section I will explain the basics of the program in a user point of view. I will obviously focus on CDCC calculations for breakup reactions.

All relevant information about Fresco, including a public version of the code, can be found on the website www.fresco.org.uk.

B.1 Input file

In this section, I will explain most of the content of the input file. An example of the input file for breakup CDCC calculations is visible on Fig. B.1. Unimportant parameters have been shaded and will not be discussed deeply here. An explanation of their impact on calculations can be found in the documentation.

The input file begins with a **heading**, simply describing the reaction we are dealing with. This line is not considered by Fresco. It can be seen as a memo to the user, that here reminds us that ^{11}Be is impinging on a ^{12}C target, with a beam energy of 67 MeV/nucleon. After this heading line, four different namelists gather the parameters used by Fresco. These namelists are *CDCC, nucleus, bin* and *potential*. Let us look at their use.

CDCC

The CDCC namelist introduces all parameters that will be involved in the calculation (numerical parameters and reaction parameters) as well as the output options.

Among the numerical parameters, we find **hcm** and **accrcy**, that control the step of integration and the accuracy of the piecewise step length respectively. The matching radius, at which the calculated wave function of the projectile is matched to its asymptotic behaviour is given by **rmatch**. But here, as should be noted, its value is negative. This tells the code to integrate the coupled equation up to **rmatch** numerically and then match them with the coupled-channel Coulomb functions up to **rasym**. This allows to include the effects of coupling out to large distances due to the long-range Coulomb interaction without having to integrate them over a large radius. The **cutr** parameter will be explained later. **thmax** and **thinc** simply indicate the span of the scattering/breakup angle and the step to be held into account.

Among the reaction parameters, we find **elab**, that determines the energy of the projectile beam and **jbord** and **jump** that control the number of projectile-target ($P-T$) partial waves included in the calculation. Many $P-T$ partial waves have to be included for the couplings and including partial waves up to $J = 5000$ can sometimes be necessary, J being the projectile-target total spin. In order to avoid calculating them one by one, an interpolation on the scattering amplitudes is done with **jbord** and **jump**. In our input file example, we start from $J = 0$ up to $J = 200$ by steps of one, then from $J = 200$ to $J = 300$ by steps of 10 and finally from $J = 300$ to $J = 2000$ by steps of 50. The **absend** parameter can be used to limit the number of partial wave calculated. Once the absorption of three successive J sets is smaller than the value of **absend** in millibarns, no more $P - T$ partial wave is added. Here, **absend** value is negative, which means

```
CDCC 11Be+12C 67MeV/nucleon

 &CDCC
   hcm=0.01 accrcy=0.001
   rmatch= -60 rasym=1000 cutr=-20
   thmax=10 thinc=0.05

   elab=737
   jbord= 0 200 300 2000 jump= 1 10 50 absend=-50
   ncoul=0 reor=0 q=2

   smats=2 xstabl=1/


 &NUCLEUS part='Proj' name='11Be' charge=4 mass=11
     spin=0 parity=+1 be=0.503 n=2 l=0 j=0/
 &NUCLEUS part='Core' name='10Be' charge=4 mass=10 /
 &NUCLEUS part='Valence' name='neutron' charge=0
     mass=1 spin=0 /
 &NUCLEUS part='Target' name='12C' charge=6 mass=12
     spin=0 /


 &BIN spin=0 parity=+1 start=0.001 step=0.25 end=15
     energy=T l=0 j=0 /
 &BIN /


 &POTENTIAL part='Proj' /
 &POTENTIAL part='Core' a1=1 rc=5.33 v=123 vr0=3.33
     a=0.8 w=65 wr0=3.47 aw=0.8 /
 &POTENTIAL part='Valence' a1=1 v=30.9 vr0=2.75
     a=0.623 w=7.82 wr0=3.18 aw=0.667/
 &POTENTIAL part='Gs' a1=1 v=62.52 vr0=2.585 a=0.6
     vso=5.25 rso0=2.585 aso=0.6 /
```

Figure B.1: Input file example for the breakup CDCC calculation of ^{11}Be on ^{12}C. In a clarity purpose, uninteresting parameters of the file have been shaded.

that every $P-T$ partial wave from **jbord/jump** is taken into account. When such amount of partial waves is considered, the strong Coulomb repulsion at small radii can cause numerical instabilities. The **cutr** parameter avoids this problem by setting a radial cutoff. If its value is negative, the cutoff is done inside the Coulomb turning point. **ncoul** determines whether only the Coulomb interaction or only the nuclear interaction or both two must be taken into account, the latter being the case here, **reor** determines whether including or not off-diagonal couplings and **q** is the multipole order of the deforming

potential.

Finally, the ouput options are **smats** and **xstabl**, which, when increased, increase the amount of printed files and variable details. The parameter **IPCGS** can also be added to print the wavefunction of the ground state.

Note that many of these parameters are default parameters and that a great amount of other parameters exist.

Nucleus

The nucleus namelist introduces all different partitions of the problem. We recognise here the projectile, its core, the valence neutron and the target as the different partitions. Each partition has a **name**, a **charge** and a **mass**. The state j^π of the impinging projectile is described by the parameters **spin** and **parity**.

Normally, the ^{11}Be in its ground state should be characterised by the set of quantum numbers {**n**, **l**, **j** ; **spin**, **parity**} = $\{n, l, s; j, \pi\} = \{2, 0, 1/2; 1/2, +1\}$ with a bound-state energy of **be**=0.503 MeV. But we have decided here to neglect the spin orbit interaction and hence set the spin of the neutron to 0.

Bin

The bin namelist will contain all the continuum discrete excited states. The parameters describe the quantum numbers of the different energies excited states of the projectile : j^π (with the parameters **spin** and **parity**) as well as the orbital angular momentum l and total spin j (with the parameters $\boldsymbol{l}$ and $\boldsymbol{j}$).

The different energy binnings are described by the parameters **start**, **end** and **step**, the first two defining the span of the continuum that is considered and the latter defining the width of each bin.

The last parameter is **energy**, which can take the values T (for true) or F (for false) and that defines the type of binning. In the case of T, each bin has the same width, defined by the **step** parameter. There is thus (**end-start**)/**step** bins. In the case of F, the binning is made in the k space. The number of bins is still (**end-start**)/**step** but the bins have now equal size in the k-span. This type of binning allows a finer grid at low energies of the continuum and a coarser grid at high energies as $E \propto k^2$. The energy width of the bins will thus vary for this type of binning but in the sake of conciseness, we will still refer the parameter step as the width ΔE of the bin. The interest of this type of binning will be illustrated later.

Multiple bin namelists can be added, in order to describe different excited states, of other quantum numbers. Here, in the example given on Fig. B.1, only the $l = 0$ partial wave of the projectile (the s state) has been discretised. Some other parameters can be added but I will not explain them here.

Potential

This last namelist provides all the parameters needed to define the interaction potentials used to model our problem. Different shapes can be used, but the Woods-Saxon shape is set by default. The part 'Core' describes the interaction between the core and the target, the part 'Valence' the interaction of the neutron valence with the target and the 'GS'

part (which stands for *Ground State*) is the interaction potential between the core and the valence neutron.

As seen before, the optical potentials used to simulate the nuclear interactions are usually described by a Woods-Saxon shape, Eq. (2.66), while the Coulomb interaction has the form Eq. (2.63).

v, **vr0** and **a** are the parameters for the Woods-Saxon shape of the real volume component (respectively V_r, r_r and a_r).

w, **wr0** and **aw** are the parameters for the Woods-Saxon shape of the imaginary volume component (respectively W_i, r_i and a_i).

wd, **wdr0** and **awd** are the parameters for the Woods-Saxon shape of the imaginary surface component (respectively W_D, r_D and a_D).

vso, **rso** and **aso** are the parameters for the Woods-Saxon shape of the spin-orbit component (respectively V_{so}, r_{so} and a_{so}).

rc is the Coulomb radius (r_C).

It sould be noted that fresco considers all radii **vr0**, **wr0**, **rso** and **rc** as a reduced radii. They are then rescaled as it is done in Eq. (2.64). However, a parameter **a1** can be added to avoid any rescaling if needed. By assigning it the value 1, the radii $R_j = r_j \cdot \boldsymbol{a1}^{1/3}$ are then equal to their reduced radii equivalent.

Note finally that Fresco's treatment of the potentials given as input can sometimes be obscure. Indeed, Fresco may change the depth of the core-valence neutron potential to fit the energy of the bound state given in input. Moreover, the potential conventions and forms I have defined in Sec. 2.5 could be different from the ones used in the previous works from which I have chosen my parameters, and could even be different from the conventions of Fresco. In order to verify that all my results are based on the same interactions and that hence I analyse the same cross sections, the results obtained on elastic scattering with Fresco have been compared to a third method, based on the partial wave expansion method. This has ensured that all problems treated are indeed the same. The computations based on this method have been carried out with a code written by D. Baye, which I would like to thank.

B.2 Output files

The output files depend mostly on the output parameters defined in the CDCC namelist but only some of them are relevant to our study and will be mentioned.

fort.13 contains breakup cross sections energy distributions for each partial wave.

fort.16 contains angular distributions of the breakup cross sections for each energy bin.

fort.44 contains the bin phase shifts as functions of the energy of the bin. This file can be used to characterise the eventual resonances.

fort.58 contains the bin wavefunctions.

fort.201 contains the elastic cross section angular distribution. Since it diverges at small angles, the cross section is actually divided by Rutherford's cross section.

C KMT

We can rewrite Eq. (7.10) as

$$T = Av\left(1 + \frac{1}{\alpha}T\right) \tag{C.1}$$

$$\Leftrightarrow \quad \left(1 - Av\frac{1}{\alpha}\right)T = Av \tag{C.2}$$

This can then be solved formally for T in two ways. Either "on the right", as in

$$T = \frac{1}{1 - Av\frac{1}{\alpha}}Av \tag{C.3}$$

where we see that v multiplies the fraction on the right hand side, or "on the left" as in

$$\left(1 - Av\frac{1}{\alpha}\right)T = Av\left(1 - \frac{1}{\alpha}Av\right)\frac{1}{1 - \frac{1}{\alpha}Av} \tag{C.4}$$

$$\Leftrightarrow \quad \left(1 - Av\frac{1}{\alpha}\right)T = \left(Av - Av\frac{1}{\alpha}Av\right)\frac{1}{1 - \frac{1}{\alpha}Av} \tag{C.5}$$

$$\Leftrightarrow \quad \left(1 - Av\frac{1}{\alpha}\right)T = \left(1 - Av\frac{1}{\alpha}\right)Av\frac{1}{1 - \frac{1}{\alpha}Av} \tag{C.6}$$

$$\Leftrightarrow \quad T = Av\frac{1}{1 - \frac{1}{\alpha}Av} \tag{C.7}$$

where it multiplies it on the left hand side. In the end, we formally have

$$T = \frac{1}{1 - Av\frac{1}{\alpha}}Av = Av\frac{1}{1 - \frac{1}{\alpha}Av} \tag{C.8}$$

Similarly, for v we have from Eq. (7.11)

$$v = \frac{1}{1 + \tau\frac{1}{\alpha}}\tau = \tau\frac{1}{1 + \frac{1}{\alpha}\tau} \tag{C.9}$$

where τ is either on the right or on the left of the fraction.

If I inject the "on the left" solution for v into the respective "on the left" solution for T, we have

$$T = A\tau\frac{1}{1 + \frac{1}{\alpha}\tau}\frac{1}{1 - \frac{1}{\alpha}A\tau\frac{1}{1+\frac{1}{\alpha}\tau}} \tag{C.10}$$

$$= A\tau\frac{1}{\left(1 + \frac{1}{\alpha}\tau\right) - \left(1 + \frac{1}{\alpha}\tau\right)\frac{1}{\alpha}A\tau\frac{1}{1+\frac{1}{\alpha}\tau}} \tag{C.11}$$

$$= A\tau\frac{1}{\left(1 + \frac{1}{\alpha}\tau\right) - \left(A\frac{1}{\alpha}\tau\frac{1}{1+\frac{1}{\alpha}\tau} + A\frac{1}{\alpha}\tau\frac{1}{\alpha}\tau\frac{1}{1+\frac{1}{\alpha}\tau}\right)} \tag{C.12}$$

$$= A\tau\frac{1}{\left(1 + \frac{1}{\alpha}\tau\right) - A\frac{1}{\alpha}\tau\left(\frac{1}{1+\frac{1}{\alpha}\tau} + \frac{1}{\alpha}\tau\frac{1}{1+\frac{1}{\alpha}\tau}\right)} \tag{C.13}$$

$$= A\tau\frac{1}{\left(1 + \frac{1}{\alpha}\tau\right) - A\frac{1}{\alpha}\tau\left(1 + \frac{1}{\alpha}\tau\right)\frac{1}{1+\frac{1}{\alpha}\tau}} \tag{C.14}$$

$$= A\tau\frac{1}{1 - (A-1)\frac{1}{\alpha}\tau} \tag{C.15}$$

and similarly, on the right

$$T = \frac{1}{1-(A-1)\tau\frac{1}{\alpha}} A\tau \tag{C.16}$$

This equation can be cast into the form

$$T - (A-1)\tau\frac{1}{\alpha}T = A\tau \tag{C.17}$$

$$\frac{A-1}{A}T = (A-1)\tau + (A-1)\tau\frac{1}{\alpha}\frac{A-1}{A}T \tag{C.18}$$

The auxiliary matrix $T' = \frac{A-1}{A}T$ (7.16) and $V^{(0)} = (A-1)\tau$ (7.17) and the projectors (7.21) allow me to re-write this equation as

$$T' = V^{(0)} + V^{(0)}\frac{1}{\alpha}(\mathbb{P}_0 + \mathbb{Q}_0)T' \tag{C.19}$$

$$\Leftrightarrow \quad \left(1 - V^{(0)}\frac{1}{\alpha}\mathbb{Q}_0\right)T' = V^{(0)}\left(1 + \frac{1}{\alpha}\mathbb{P}_0 T'\right) \tag{C.20}$$

$$\Leftrightarrow \quad T' = \frac{1}{1 - V^{(0)}\frac{1}{\alpha}\mathbb{Q}_0} V^{(0)}\left(1 + \frac{1}{\alpha}\mathbb{P}_0 T'\right) \tag{C.21}$$

Relation between τ and t From the definitions of t and τ in Eqs. (7.14) and (7.11) and from Eq. (C.9) we see that

$$\begin{cases} v = \tau\dfrac{1}{1+\frac{1}{\alpha}\tau} \\ v = \dfrac{1}{1+t\frac{1}{h}}t \end{cases} \quad \Rightarrow \quad \tau\frac{1}{1+\frac{1}{\alpha}\tau} = \frac{1}{1+t\frac{1}{h}}t \tag{C.22}$$

$$\Leftrightarrow \quad \left(1 + t\frac{1}{h}\right)\tau = t\left(1 + \frac{1}{\alpha}\tau\right) \tag{C.23}$$

$$\Leftrightarrow \quad \tau = t + t\left(\frac{1}{\alpha} - \frac{1}{h}\right)\tau \tag{C.24}$$

D Photoproduction of a pion on a single free nucleon

In the following, I will consider a photon of momentum k impinging on a free nucleon and photoproducing a pion of momentum q. I will evaluate these momenta in the π-N center-of-mass frame. I will drop the tilde and indices for conciseness (except when it's needed). The pion photoproduction differential cross section from a $\gamma - N$ initial Pauli spinor state ξ_i to a $\pi - N'$ final state ξ_f is given by

$$\frac{d\sigma^{i\to f}}{d\Omega} = \frac{q}{k} \left|\langle \xi_i | \mathcal{F} | \xi_f \rangle\right|^2 \tag{D.1}$$

where $\mathcal{F}$ reads [163]

$$\mathcal{F} = i(\vec{\sigma}\cdot\vec{\varepsilon})\mathcal{F}_1 + (\vec{\sigma}\cdot\hat{\vec{q}})(\vec{\sigma}\cdot(\hat{\vec{k}}\times\vec{\varepsilon}))\mathcal{F}_2 + i(\vec{\sigma}\cdot\hat{\vec{k}})(\hat{\vec{q}}\cdot\vec{\varepsilon})\mathcal{F}_3 + i(\vec{\sigma}\cdot\hat{\vec{q}})(\hat{\vec{q}}\cdot\vec{\varepsilon})\mathcal{F}_4 \tag{D.2}$$

where $\hat{x}$ is a unit vector and ε is the polarization of the photon. Note that the second term can be rewritten in Einstein summation indices form as

$$(\vec{\sigma}\cdot\vec{q})(\vec{\sigma}\cdot(\vec{k}\times\vec{\varepsilon})) = \sigma_i q_i k_k \varepsilon_l \varepsilon_{klj}\sigma_j \tag{D.3}$$

$$= q_i k_k \varepsilon_l \varepsilon_{klj}\sigma_i\sigma_j \tag{D.4}$$

where ε_{ijk} is the Levi-Civita symbol. I can use the fact that $\sigma_i\sigma_j = \delta_{ij} + i\varepsilon_{ijm}\sigma_m$ to rewrite this as

$$(\vec{\sigma}\cdot\vec{q})(\vec{\sigma}\cdot(\vec{k}\times\vec{\varepsilon})) = q_i k_k \varepsilon_l \varepsilon_{kli} + i q_i k_k \varepsilon_l \varepsilon_{klj}\varepsilon_{ijm}\sigma_m \tag{D.5}$$

Using the properties of the Levi-Civita symbol, namely $\varepsilon_{klj}\varepsilon_{mij} = \delta_{km}\delta_{li} - \delta_{ki}\delta_{lm}$, I can write this as

$$(\vec{\sigma}\cdot\vec{q})(\vec{\sigma}\cdot(\vec{k}\times\vec{\varepsilon})) = q_i k_k \varepsilon_l \varepsilon_{kli} + i q_i k_k \varepsilon_i \sigma_k - i q_i k_i \varepsilon_l \sigma_l \tag{D.6}$$

$$= (\vec{\varepsilon}\cdot(\vec{q}\times\vec{k})) + i(\vec{\sigma}\cdot\vec{k})(\vec{q}\cdot\vec{\varepsilon}) - i(\vec{q}\cdot\vec{k})(\vec{\sigma}\cdot\vec{\varepsilon}) \tag{D.7}$$

I thus have

$$\mathcal{F} = i(\vec{\sigma}\cdot\vec{\varepsilon})\mathcal{F}_1 + \vec{\varepsilon}\cdot(\vec{q}\times\vec{k})\mathcal{F}_2 + i(\vec{\sigma}\cdot\vec{k})(\vec{q}\cdot\vec{\varepsilon})[\mathcal{F}_2+\mathcal{F}_3] - i(\vec{q}\cdot\vec{k})(\vec{\sigma}\cdot\vec{\varepsilon})\mathcal{F}_2 + i(\vec{\sigma}\cdot\vec{q})(\vec{q}\cdot\vec{\varepsilon})\mathcal{F}_4 \tag{D.8}$$

It should already be noted at this point that the second term on the right hand side is the only component that does not depend on spin. In the case that the polarisation of the initial and final nucleons is not measured, and all possible polarisations of the photon $\lambda(=\pm1)$ are considered we have

$$\frac{d\sigma_{\gamma\to\pi}}{d\Omega} = \frac{q}{k}\left(\frac{1}{2}\sum_{\lambda}\right)\left(\frac{1}{2}\sum_{m_i}\right)\sum_{m_f}\langle\xi_i|\mathcal{F}^{(\lambda)\dagger}|\xi_f\rangle\langle\xi_f|\mathcal{F}^{(\lambda)}|\xi_i\rangle \tag{D.9}$$

$$= \frac{q}{4k}\sum_{m_i,\lambda}\langle\xi_i|\mathcal{F}^{(\lambda)\dagger}\mathcal{F}^{(\lambda)}|\xi_i\rangle \tag{D.10}$$

In $\{\vec{e}_x, \vec{e}_y, \vec{e}_z\}$ axis and for circular polarization, we can write both polarization vectors of the photon as

$$\vec{\varepsilon}_\lambda = \frac{1}{\sqrt{2}}(\vec{e}_x + i\lambda\vec{e}_y) \tag{D.11}$$

For $\vec{k}$ oriented in the z direction and $\hat{\vec{q}} = (\sin\theta\cos\phi, \sin\theta\sin\phi, \cos\theta)$, we have

$$\begin{aligned}
\mathcal{F}^{(\lambda)} =& \frac{i}{\sqrt{2}}(\sigma_x + i\lambda\sigma_y)\mathcal{F}_1 && \text{(D.12)}\\
&+ \frac{\sin\theta}{\sqrt{2}}(\sin\phi - i\lambda\cos\phi)\mathcal{F}_2 && \text{(D.13)}\\
&+ i\frac{\sin\theta}{\sqrt{2}}(\cos\phi + i\lambda\sin\phi)\sigma_z[\mathcal{F}_2 + \mathcal{F}_3] && \text{(D.14)}\\
&- i\frac{\cos\theta}{\sqrt{2}}(\sigma_x + i\lambda\sigma_y)\mathcal{F}_2 && \text{(D.15)}\\
&+ \frac{i}{\sqrt{2}}\Big[\cos\theta\sin\theta(\cos\phi + i\lambda\sin\phi)\sigma_z + \sin^2\theta\cos\phi(\cos\phi + i\lambda\sin\phi)\sigma_x && \text{(D.16)}\\
&\qquad + \sin^2\theta\sin\phi(\cos\phi + i\lambda\sin\phi)\sigma_y\Big]\mathcal{F}_4 && \text{(D.17)}\\
=& \frac{i}{\sqrt{2}}\Big[(\sigma_x + i\lambda\sigma_y)\mathcal{F}_1 - \lambda\sin\theta e^{i\lambda\phi}\mathcal{F}_2 + \sin\theta e^{i\lambda\phi}\sigma_z[\mathcal{F}_2 + \mathcal{F}_3] - \cos\theta(\sigma_x + i\lambda\sigma_y)\mathcal{F}_2 && \text{(D.18)}\\
&+ e^{i\lambda\phi}(\cos\theta\sin\theta\sigma_z + \sin^2\theta\cos\phi\sigma_x + \sin^2\theta\sin\phi\sigma_y)\mathcal{F}_4\Big] && \text{(D.19)}
\end{aligned}$$

Let me use the ladder operators $\sigma_\pm$ defined as

$$\sigma_\pm = \sigma_x \pm i\sigma_y \quad (= \sigma_\mp^\dagger) \tag{D.20}$$

$$\Leftrightarrow \begin{cases} \sigma_x = \dfrac{1}{2}(\sigma_+ + \sigma_-) \\ \sigma_y = \dfrac{1}{2i}(\sigma_+ - \sigma_-) \end{cases} \tag{D.21}$$

and which have the properties

$$\begin{cases} \sigma_+ |-\rangle = 2\,|+\rangle \\ \sigma_- |+\rangle = 2\,|-\rangle \\ \sigma_+ |+\rangle = \sigma_- |-\rangle = 0 \\ \sigma_z\sigma_\pm = \pm\sigma_\pm \\ \sigma_\pm\sigma_z = \mp\sigma_\pm \end{cases} \tag{D.22}$$

to write

$$\begin{aligned}
\mathcal{F}^{(\lambda)} =& \frac{i}{\sqrt{2}}\Big[\sigma_\lambda\mathcal{F}_1 + \Big(\sin\theta e^{i\lambda\phi}\{\sigma_z - \lambda\} - \cos\theta\sigma_\lambda\Big)\mathcal{F}_2 + \sin\theta e^{i\lambda\phi}\sigma_z\mathcal{F}_3 && \text{(D.23)}\\
&+ e^{i\lambda\phi}\left(\cos\theta\sin\theta\sigma_z + \frac{\sin^2\theta}{2}e^{-i\phi}\sigma_+ + \frac{\sin^2\theta}{2}e^{i\phi}\sigma_-\right)\mathcal{F}_4\Big] && \text{(D.24)}
\end{aligned}$$

and since $\sigma_{\pm\lambda}^\dagger = \sigma_{\mp\lambda}$, its complex conjugate reads

$$\begin{aligned}
\mathcal{F}^{(\lambda)\dagger} =& \frac{-i}{\sqrt{2}}\Big[\sigma_{-\lambda}\mathcal{F}_1^\dagger + \Big(\sin\theta e^{-i\lambda\phi}\{\sigma_z - \lambda\} - \cos\theta\sigma_{-\lambda}\Big)\mathcal{F}_2^\dagger + \sin\theta e^{-i\lambda\phi}\sigma_z\mathcal{F}_3^\dagger && \text{(D.25)}\\
&+ e^{-i\lambda\phi}\left(\cos\theta\sin\theta\sigma_z + \frac{\sin^2\theta}{2}e^{i\phi}\sigma_- + \frac{\sin^2\theta}{2}e^{-i\phi}\sigma_+\right)\mathcal{F}_4^\dagger\Big] && \text{(D.26)}
\end{aligned}$$

By noting that $\sigma_z\sigma_{\pm\lambda} = -\sigma_{\pm\lambda}\sigma_z = \pm\lambda\sigma_{\pm\lambda}$, we can write $\mathcal{F}^{(\lambda)\dagger}\mathcal{F}^{(\lambda)}$ in the following form

$$2\mathcal{F}^{(\lambda)\dagger}\mathcal{F}^{(\lambda)} = \sigma_{-\lambda}\sigma_\lambda|\mathcal{F}_1|^2 + \left[2\sin^2\theta(1-\lambda\sigma_z) + \cos^2\theta\sigma_{-\lambda}\sigma_\lambda\right]|\mathcal{F}_2|^2 + \sin^2\theta|\mathcal{F}_3|^2 + \sin^2\theta|\mathcal{F}_4|^2 \tag{D.27}$$

$$- \cos\theta\sigma_{-\lambda}\sigma_\lambda(\mathcal{F}_1^*\mathcal{F}_2 + \mathcal{F}_1\mathcal{F}_2^*) \tag{D.28}$$

$$+ \lambda\sin\theta\left(e^{i\lambda\phi}\sigma_{-\lambda}\mathcal{F}_1^*\mathcal{F}_3 + e^{-i\lambda\phi}\sigma_\lambda\mathcal{F}_3^*\mathcal{F}_1\right) \tag{D.29}$$

$$+ \sin\theta e^{i\lambda\phi}\left(\lambda\cos\theta\sigma_{-\lambda} + \frac{\sin\theta}{2}e^{-i\phi}\sigma_{-\lambda}\sigma_+ + \frac{\sin\theta}{2}e^{i\phi}\sigma_{-\lambda}\sigma_-\right)\mathcal{F}_1^*\mathcal{F}_4 \tag{D.30}$$

$$+ \sin\theta e^{-i\lambda\phi}\left(\lambda\cos\theta\sigma_\lambda + \frac{\sin\theta}{2}e^{i\phi}\sigma_-\sigma_\lambda + \frac{\sin\theta}{2}e^{-i\phi}\sigma_+\sigma_\lambda\right)\mathcal{F}_4^*\mathcal{F}_1 \tag{D.31}$$

$$+ \left(\sin^2\theta(1-\lambda\sigma_z) - \lambda e^{i\lambda\phi}\sin\theta\cos\theta\sigma_{-\lambda}\right)\mathcal{F}_2^*\mathcal{F}_3 \tag{D.32}$$

$$+ \left(\sin^2\theta(1-\lambda\sigma_z) - \lambda e^{-i\lambda\phi}\sin\theta\cos\theta\sigma_\lambda\right)\mathcal{F}_3^*\mathcal{F}_2 \tag{D.33}$$

$$+ \Big[\sin^2\theta\cos\theta(1-\lambda\sigma_z) - \lambda\cos^2\theta\sin\theta e^{i\lambda\phi}\sigma_{-\lambda} \tag{D.34}$$

$$+ \frac{\sin^3\theta}{2}\{e^{-i\phi}(1-\lambda)\sigma_+ - e^{i\phi}(1+\lambda)\sigma_-\} \tag{D.35}$$

$$- \frac{\sin^2\theta\cos\theta}{2}e^{i\lambda\phi}\sigma_{-\lambda}\{\sigma_- e^{i\phi} + \sigma_+ e^{-i\phi}\}\Big]\mathcal{F}_2^*\mathcal{F}_4 \tag{D.36}$$

$$+ \Big[\sin^2\theta\cos\theta(1-\lambda\sigma_z) - \lambda\cos^2\theta\sin\theta e^{-i\lambda\phi}\sigma_\lambda \tag{D.37}$$

$$+ \frac{\sin^3\theta}{2}\{e^{i\phi}(1-\lambda)\sigma_- - e^{-i\phi}(1+\lambda)\sigma_+\} \tag{D.38}$$

$$- \frac{\sin^2\theta\cos\theta}{2}e^{-i\lambda\phi}\{e^{-i\phi}\sigma_+ + e^{i\phi}\sigma_-\}\sigma_\lambda\Big]\mathcal{F}_4^*\mathcal{F}_2 \tag{D.39}$$

$$+ \sin^2\theta\left(\cos\theta + \frac{\sin\theta}{2}\{e^{-i\phi}\sigma_+ - e^{i\phi}\sigma_-\}\right)\mathcal{F}_3^*\mathcal{F}_4 \tag{D.40}$$

$$+ \sin^2\theta\left(\cos\theta + \frac{\sin\theta}{2}\{e^{i\phi}\sigma_- - e^{-i\phi}\sigma_+\}\right)\mathcal{F}_4^*\mathcal{F}_3 \tag{D.41}$$

I need to sum this expression over the initial spin of the nucleon and over all polarizations. Note that

$$\langle m|\,\sigma_{-\lambda}\sigma_\lambda\,|m\rangle = 2\delta_{\lambda(-m)}\,\langle m|\,\sigma_m\,|-m\rangle = 4\delta_{\lambda(-m)} \tag{D.42}$$

$$\langle m|\,\sigma_z\,|m\rangle = m \tag{D.43}$$

$$\langle m|\,\sigma_{\pm\lambda}\,|m\rangle = 2\delta_{\lambda(\mp m)}\,\langle m|\,-m\rangle = 0 \tag{D.44}$$

$$\langle m|\,\sigma_{-\lambda}\sigma_\pm\,|m\rangle = 2\delta_{m(\mp1)}\,\langle m|\,\sigma_{-\lambda}\,|-m\rangle = 4\delta_{\lambda(-m)}\delta_{m(\mp1)} = 4\delta_{\lambda(\pm1)}\delta_{m(\mp1)} \tag{D.45}$$

$$\langle m|\,\sigma_\pm\sigma_\lambda\,|m\rangle = 2\delta_{\lambda(-m)}\,\langle m|\,\sigma_\pm\,|-m\rangle = 4\delta_{\lambda(-m)}\delta_{m(\pm1)} = 4\delta_{\lambda(\mp1)}\delta_{m(\pm1)} \tag{D.46}$$

from which we see that only a few terms will stay when we consider $\sum_{m_i,\lambda}\langle\xi_i|\,\mathcal{F}^{(\lambda)\dagger}\mathcal{F}^{(\lambda)}\,|\xi_i\rangle$, namely

$$\frac{d\sigma_{\gamma\to\pi}}{d\Omega} = \frac{q}{4k}\Big[4|\mathcal{F}_1|^2 + 4|\mathcal{F}_2|^2 + 2\sin^2\theta|\mathcal{F}_3|^2 + 2\sin^2\theta|\mathcal{F}_4|^2 \tag{D.47}$$

$$- 4\cos\theta(\mathcal{F}_1^*\mathcal{F}_2 + \mathcal{F}_1\mathcal{F}_2^*) + 2\sin^2\theta(\mathcal{F}_1^*\mathcal{F}_4 + \mathcal{F}_4^*\mathcal{F}_1) \tag{D.48}$$

$$+2\sin^2\theta(\mathcal{F}_2^*\mathcal{F}_3 + \mathcal{F}_3^*\mathcal{F}_2) + 2\sin^2\theta\cos\theta(\mathcal{F}_3^*\mathcal{F}_4 + \mathcal{F}_4^*\mathcal{F}_3)\Big] \tag{D.49}$$

E Kinematics and change of frame

In this section, I will derive the Lorentz transforms to change the coordinates from the emitted pion frame to the laboratory frame.

Let me take P_γ^{lab} as the quadri-vector for the incident photon in the laboratory frame, of kinetic energy T_γ and momentum $\vec{p}_\gamma^{\,\text{lab}}$, also in the lab frame. It impinges on a target nucleus at rest which has A nucleons and a mass m_A and which is at the origin of the lab frame axes $\{\hat{\mathbf{x}}, \hat{\mathbf{y}}, \hat{\mathbf{z}}\}$, where $\hat{\mathbf{z}}$ is the beam axis. The invariant energy of the reaction s is given by

$$s^2 = (T_\gamma + m_A)^2 - T_\gamma^2 = 2m_A T_\gamma + m_A^2 \tag{E.1}$$

where I made the choice of units $\hbar = c = 1$. I need to go to the centre-of-mass reference frame (coordinates in $\{\hat{\mathbf{X}}, \hat{\mathbf{Y}}, \hat{\mathbf{Z}}\}$ axes for which the origin is considered as the interaction vertex) in which we know the cross section for the photo-production process. In this frame, the photon and target quadri-vectors are defined as P_γ and P_A (see Fig. E.1). After the reaction, a pion with quadri-vector P_π^{lab} is created and the target is deflected to $P_A'^{\text{lab}}$ (or in the COM frame, P_π and P'_A, respectively).

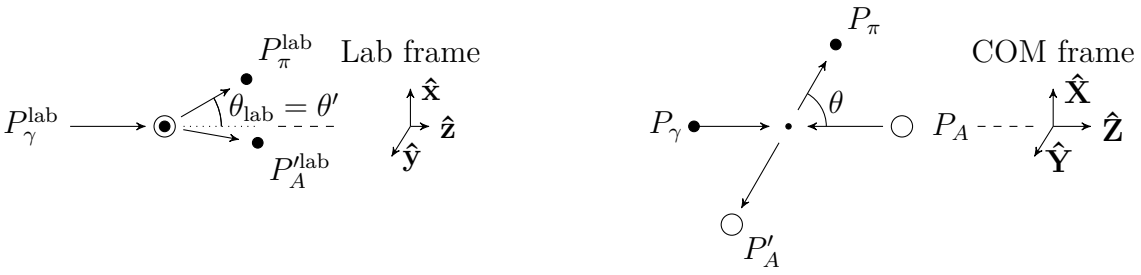

Figure E.1

In the COM frame, P_γ can be obtained by boosting the corresponding quadri-vector in the lab frame P_γ^{lab}

$$P_\gamma = \Lambda_\gamma P_\gamma^{\text{lab}} \tag{E.2}$$

where the Lorentz transform in the $\hat{\mathbf{z}}$ direction is given by [201]

$$\Lambda_\gamma = \begin{pmatrix} \gamma_\gamma & 0 & 0 & -\beta_\gamma\gamma_\gamma \\ 0 & 1 & 0 & 0 \\ 0 & 0 & 1 & 0 \\ -\beta_\gamma\gamma_\gamma & 0 & 0 & \gamma_\gamma \end{pmatrix} \quad \text{where} \quad \begin{cases} \gamma_\gamma = \dfrac{T_\gamma + m_A}{s} \\ \beta_\gamma = \dfrac{T_\gamma}{T_\gamma + m_A} \end{cases} \tag{E.3}$$

In the COM frame, I can define the pion and target energies as ω_π and ω_A, respectively, such that $\omega_\pi + \omega_A = s$ and $P_\pi = (\omega_\pi, \vec{p}_\pi)$ and $P'_A = (\omega_A, -\vec{p}_\pi)$. Since I work on-the-mass shell, we have

$$\omega_\pi^2 = m_\pi^2 + \vec{p}_\pi^{\,2} \tag{E.4}$$

$$\omega_A^2 = m_A^2 + \vec{p}_\pi^{\,2} \tag{E.5}$$

and hence

$$p_\pi = \frac{\sqrt{\left[s^2 - (m_\pi^2 + m_A^2)\right]^2 - 4m_A^2 m_\pi^2}}{2s} \tag{E.6}$$

$$\omega_\pi = \frac{s^2 + m_\pi^2 - m_A^2}{2s} \tag{E.7}$$

The quadri-vector of a pion emitted in the solid angle $\{\theta, \phi\}$ in the COM frame reads explicitly $(\omega_\pi, p_\pi \cos\phi \sin\theta, p_\pi \sin\phi \sin\theta, p_\pi \cos\theta)$. Its quadri-vector P_π^{lab} in the lab frame then reads

$$P_\pi^{\text{lab}} = \Lambda_\gamma^{-1} P_\pi \tag{E.8}$$

$$= \begin{pmatrix} \gamma_\gamma & 0 & 0 & \beta_\gamma\gamma_\gamma \\ 0 & 1 & 0 & 0 \\ 0 & 0 & 1 & 0 \\ \beta_\gamma\gamma_\gamma & 0 & 0 & \gamma_\gamma \end{pmatrix} \begin{pmatrix} \omega_\pi \\ p_\pi \cos\phi \sin\theta \\ p_\pi \sin\phi \sin\theta \\ p_\pi \cos\theta \end{pmatrix} = \begin{pmatrix} \gamma_\gamma\omega_\pi + \beta_\gamma\gamma_\gamma p_\pi \cos\theta \\ p_\pi \cos\phi \sin\theta \\ p_\pi \sin\phi \sin\theta \\ \beta_\gamma\gamma_\gamma\omega_\pi + \gamma_\gamma p_\pi \cos\theta \end{pmatrix} \tag{E.9}$$

Note how the inverse transform Λ_γ^{-1} is simply given by changing $\beta_\gamma \to -\beta_\gamma$ since I boost in the other direction. Let me define the laboratory pion energy E_π and the laboratory pion momentum $\vec{\pi}$ such that $P_\pi^{\text{lab}} = (E_\pi, \vec{\pi})$ and the angles $\{\theta', \phi'\}$ such that the unit vector $\hat{\vec{\pi}} = (\cos\phi' \sin\theta', \sin\phi' \sin\theta', \cos\theta')$. Note that this vector is the direction of the emitted pion in the lab frame and that $\phi' = \phi$.

Let me now define the boost from the lab frame $\{\hat{\mathbf{x}}, \hat{\mathbf{y}}, \hat{\mathbf{z}}\}$ to the reference frame of the emitted pion $\{\hat{\mathbf{x}}'', \hat{\mathbf{y}}'', \hat{\mathbf{z}}''\}$. To do so, let me first rotate the lab frame to an intermediate frame $\{\hat{\mathbf{x}}', \hat{\mathbf{y}}', \hat{\mathbf{z}}'\}$ such that the axis $\hat{\mathbf{z}}'$ and the direction $\hat{\vec{\pi}}$ are aligned. I will then boost this intermediate frame into the pion frame. A summary of these transformations is shown on Fig. E.2.

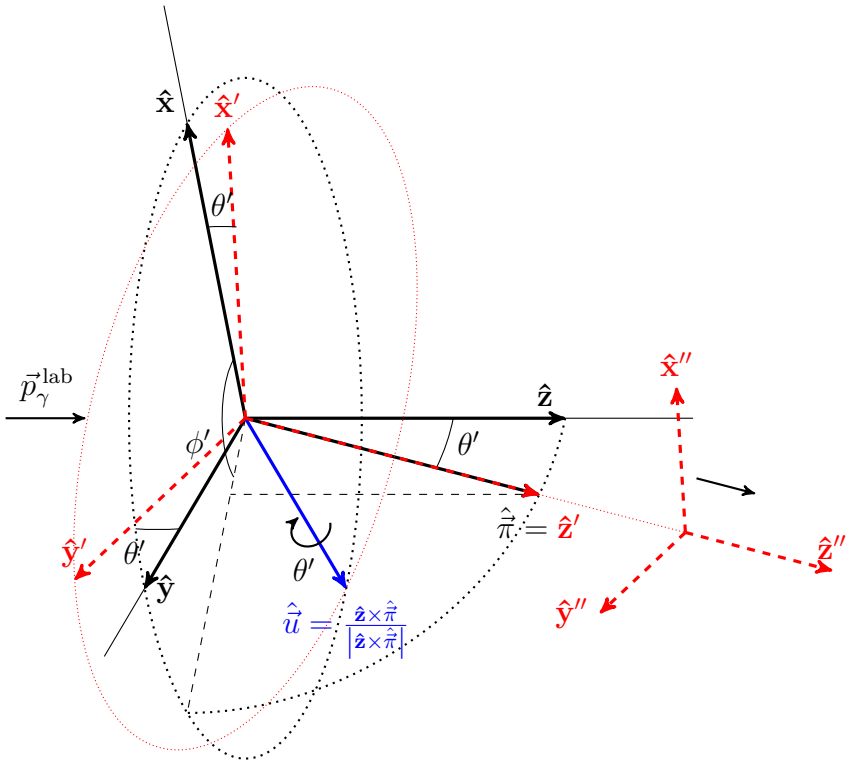

Figure E.2

Let me begin with the rotated frame $\{\hat{\mathbf{x}}', \hat{\mathbf{y}}', \hat{\mathbf{z}}'\}$. In order for $\hat{\mathbf{z}}'$ and $\hat{\vec{\pi}}$ to be aligned, I need to define the vector $\vec{u} = \hat{\mathbf{z}} \times \hat{\vec{\pi}}$ around which I will rotate by an angle θ'. This vector has components only in the $\hat{\mathbf{x}}$ and $\hat{\mathbf{y}}$ directions. The rotation of a vector around

this direction $\hat{\vec{u}} = (-\sin\phi', \cos\phi', 0) = (\hat{u}_x, \hat{u}_y, 0)$ by an angle θ' is given by the rotation matrix

$$\mathcal{R}^u_\theta = \begin{pmatrix} 1 & 0 & 0 & 0 \\ 0 & \cos\theta' + \hat{u}_x^2(1-\cos\theta') & \hat{u}_x\hat{u}_y(1-\cos\theta') & \hat{u}_y\sin\theta' \\ 0 & \hat{u}_x\hat{u}_y(1-\cos\theta') & \cos\theta' + \hat{u}_y^2(1-\cos\theta') & -\hat{u}_x\sin\theta' \\ 0 & -\hat{u}_y\sin\theta' & \hat{u}_x\sin\theta' & \cos\theta' \end{pmatrix} \tag{E.10}$$

Note that for a change of coordinates, we rather need the inverse matrix ${\mathcal{R}^u_{\theta'}}^{-1}$ either by replacing $\theta' \leftrightarrow -\theta'$ or by simply taking its transpose: ${\mathcal{R}^u_{\theta'}}^{-1} = {\mathcal{R}^u_{\theta'}}^\intercal = \mathcal{R}^u_{-\theta'}$.

The quadri-vector of the pion in the rotated lab frame $P_\pi^{\text{lab}'}$ reads

$$P_\pi^{\text{lab}'} = {\mathcal{R}^v_{\theta'}}^{-1} P_\pi^{\text{lab}} \tag{E.11}$$

In order to place ourselves in the COM frame of the pion, we need to boost in the $\hat{\mathbf{z}}'$ direction. The parameters of this boost are given by

$$\gamma_\pi = \frac{E_\pi}{m_\pi} = \frac{\gamma_\gamma\omega_\pi + \beta_\gamma\gamma_\gamma p_\pi\cos\theta}{m_\pi} \tag{E.12}$$

$$\beta_\pi = \frac{|\vec{\pi}|}{E_\pi} = \frac{\sqrt{E_\pi^2 - m_\pi^2}}{E_\pi} \tag{E.13}$$

and we then have

$$P''_\pi = \Lambda_\pi P_\pi^{\text{lab}'} \tag{E.14}$$

$$= \Lambda_\pi {\mathcal{R}^u_{\theta'}}^{-1} P_\pi^{\text{lab}} \tag{E.15}$$

where Λ_π has the same expression as Λ_γ in Eq. (E.3) with γ_π and β_π instead. The conversion from this emitted pion reference frame to the laboratory frame is hence simply the reversal of the operations of Eq. (E.15). As an example, the quadri-vectors of the two photons in the laboratory frame read

$$P_{\gamma i}^{\text{lab}} = R^u_{\theta'}\Lambda_\pi^{-1} P''_{\gamma i} \tag{E.16}$$

F Random number generation

In this section, I will detail how we can pick a random number that follows a given distribution. As we will see, in our case, this can be done from choosing one or two random numbers distributed uniformly. Only a summary of the methods that I will use are shown here. The interested reader looking for more details or different methods is referred to Ref. [202], from which most of this section is taken. Here, I will only detail the *inversion method* and the Box-Muller transforms [145].

Note that in the following, u and v are defined as random numbers distributed uniformly on $[0, 1]$.

F.1 The inversion method

In order to generate a random number θ within a domain $[\theta_i, \theta_f]$ that follows a given distribution F, let me define the normalised cumulative distribution function f, such that

$$f(y) = \frac{\int_{\theta_i}^{y} F(x)dx}{\int_{\theta_i}^{\theta_f} F(x)dx} \tag{F.1}$$

This function is normalised such that $f(y) \in [0, 1]$. It can be shown that the number

$$\theta = f^{-1}(u) \tag{F.2}$$

obtained from inverting the function f then follows the right distribution F.

A schematic example of the inversion method is shown on Fig. F.1 where we pick a random angle θ which follows the distribution $F(\theta) = \sin\theta \; d\sigma/d\Omega$, i.e. some differential cross section. On the left, the differential cross section. From this distribution, we can build the cumulative distribution function $f(\theta)$, on the right. Each random number u hence corresponds to a given angle θ.

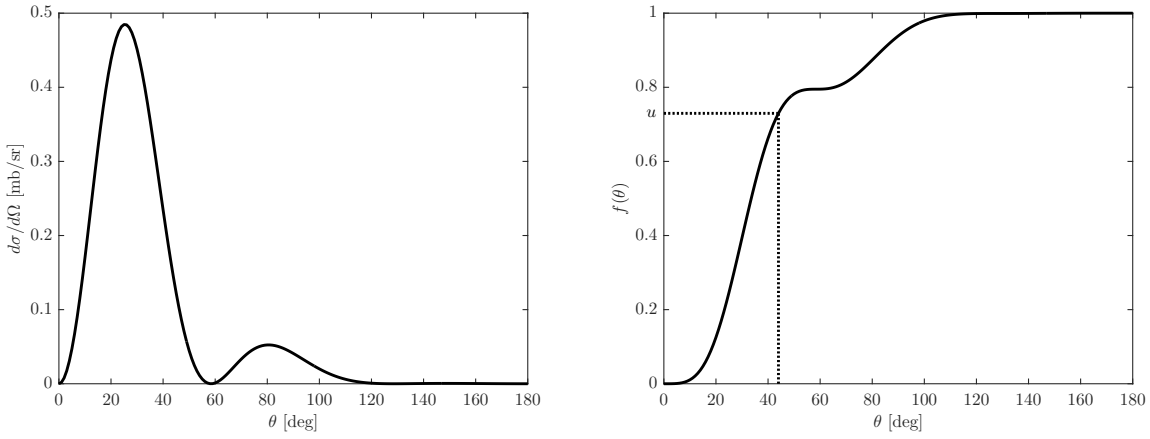

Figure F.1: Photo-production cross-section (left) and normalized cumulative distribution cross-section (right).

For some functions, this method is very effective. It is particularly the case for cumulative functions that can be inverted analytically. A good example is $F(E) = 1/E$,

which is roughly how the energy of brehmsstrahlung photons is distributed [144]. If we are interested in photons of energies $E \in [E_i, E_f]$, we have

$$f(E) = \frac{\int_{E_i}^{E} dE'/E'}{\int_{E_i}^{E_f} dE'/E'} = \frac{\ln E/E_i}{\ln E_f/E_i} \tag{F.3}$$

and the inverse function is then given by

$$f^{-1}(u) = E_i \exp\left(u \ln \frac{E_f}{E_i}\right) \tag{F.4}$$

For distributions that do not have an analytical inverse (such as the differential cross section above), numerical methods are needed to find the inverse f^{-1}.

F.2 Box-Muller transforms for normal distributions

A normal distribution of mean μ and standard deviation σ is given by the expression

$$\mathcal{N}(x; \mu, \sigma) = \frac{1}{\sqrt{2\pi\sigma^2}} e^{-\frac{(x-\mu)^2}{2\sigma^2}} \tag{F.5}$$

To draw a number x that follows this distribution, we could use the inversion method described above. However, no analytical expression exists for the inverse of its cumulative distribution function and we must rely on numerical methods to invert it. A much faster way and less computationally expensive way to draw x is through the use of Box-Muller transforms [145]. These transforms read

$$\begin{cases} x = \sqrt{-2 \ln u} \cos 2\pi v \\ y = \sqrt{-2 \ln u} \sin 2\pi v \end{cases} \tag{F.6}$$

and generate two independent normally distributed numbers x and y of mean $\mu = 0$ and standard deviation $\sigma = 1$. If we only need one, we just choose one of them and discard the other.

Note that if we want to modify the mean and standard deviation, we can then apply the linear transform

$$x' = \sigma x + \mu \tag{F.7}$$

The number x' is then distributed following a normal distribution of mean μ and standard deviation σ.

G The treatment of the Coulomb interaction in momentum space

In order to test the MSU potential of Stricker-Bauer (see Sec. 8.2.3) on charged-pion nucleus elastic scattering data, one needs a way to include the Coulomb interaction. While this Coulomb potential will not be used elsewhere in this work, it could be valuable in later works, e.g. if one desires to readjust the parameters of the potential at a different energy or for other densities, or if one wants to include charge exchange processes in the photoproduction cross sections, etc.

In this appendix, the Coulomb interaction is treated following the approximation of Deltuva *et al.* [194], where a screening of the type

$$V_C^{(n)}(r) = \pi_C Z\alpha \frac{e^{-\left(\frac{r}{R_C}\right)^n}}{r} \tag{G.1}$$

is considered. This method is analysed in details.

For $n = 1$, the potential is a Yukawa potential for which the Fourier transform is analytical and reads

$$V_C^{(1)}(q) = \pi_C Z\alpha \frac{4\pi}{q^2 + \frac{1}{Rc^2}} \tag{G.2}$$

For $n = 2$, the Fourier transform of this potential also has an analytical form which reads

$$V_C^{(2)}(q) = \pi_C Z\alpha \frac{4\pi R_C}{q} F\left(\frac{qR_C}{2}\right) \tag{G.3}$$

where $F(x)$ is the Dawson integral function [203]

$$F(x) \equiv e^{-x^2} \int_0^x e^{t^2}\, dt \tag{G.4}$$

In the limit of $n \to \infty$, we are just left with a hard cut-off at a radius R_C. The Fourier transform then simply reads

$$V_C^{(\infty)}(q) = \pi_C Z\alpha \frac{4\pi R_C}{q^2} \left(1 - \cos(qR_C)\right) \tag{G.5}$$

Other values of n (including non-integer ones) are also possible. However, the Fourier transform of the potential then has to be calculated numerically.

An illustration of these different screenings is shown in position space on left panel of Fig. G.1. The impact of n on the pure pointlike Coulomb cross sections is analysed on the right panel of the figure. Note that these are scaled to Rutherford's cross section, for which the scattering amplitude (relativistically corrected) reads [204]

$$f_C(\theta) = -\frac{\eta_\pi}{2k_0 \sin^2(\theta/2)} \frac{\mathcal{M}(k_0)}{m_\pi} \exp\left[-i\eta_\pi \ln(\sin^2(\theta/2)) + 2i\sigma_0(\eta_\pi)\right] \tag{G.6}$$

where η_π is the Sommerfeld parameter of the collision

$$\eta_\pi = \pi_C Z\alpha \frac{m_\pi}{k_0} \tag{G.7}$$

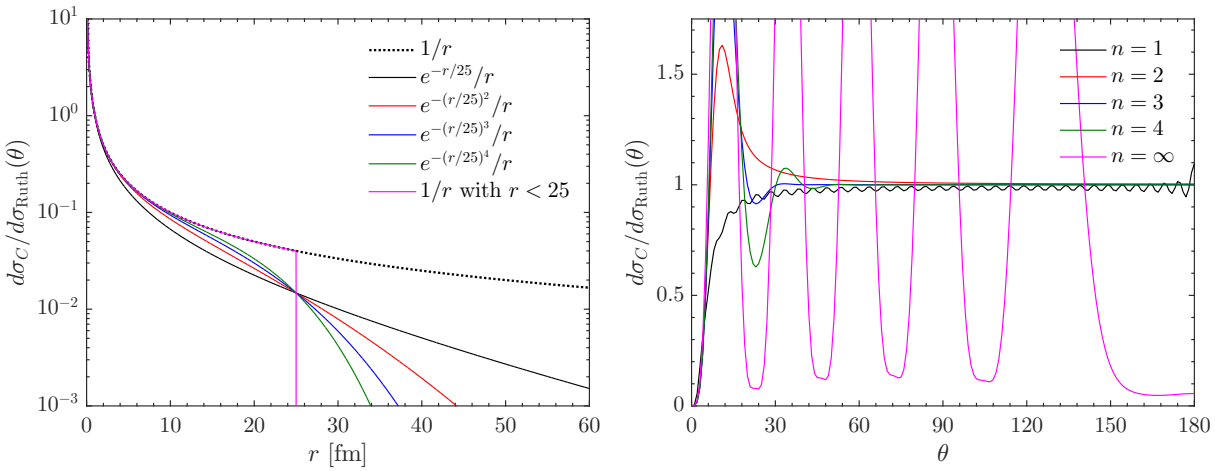

Figure G.1: Left: radial dependence of the Coulomb potential and different screenings as defined in Eq. (G.1). The screening radius is chosen as $R_C = 25$ fm. Right: result of the calculation for the pure Coulomb elastic scattering of a π^+ on ^{12}C at 50 MeV lab energy for different screenings.

and $\sigma_0(\eta_\pi) = \arg\Gamma(1 + i\eta_\pi)$ is the Coulomb phaseshift and $\mathcal{M}$ is the reduced mass defined in Eq. (7.45) and is evaluated at $k_{\pi,0}$, the on-shell momentum of the pion.

As should be first observed from left panel of Fig. G.1, the screening causes the Coulomb cross section to poorly describe the scattering at very forward angles. This is to be expected: nearly all the contribution to these angles comes from the scattering at large impact parameters, hence large radii. These are precisely the radii that have to be screened to avoid a $q = 0$ divergence. At large angles however, which correspond to small impact parameters and hence small radii which have not been cut off, the cross section converges in most of the cases to 1. Second, we already observe that for a radius of $R_C = 25$ fm, not all screenings converge. This is specially the case for the hard cut Coulomb potential (magenta) and for the Yukawa potential (black). These two screenings are the most difficult to make converge and will not be considered in the following. For the other screenings on the other hand, no numerical instabilities are found.

On Figure G.2, I analyse the influence of the screening radius on the particular case $n = 2$. The behaviour displayed in these figures is representative of what happens for all screenings. As the cut-off radius increases, the Coulomb potential at small radii is less and less touched and the cross section approaches the Rutherford cross section. However, if R_C grows too large, numerical instabilities appear. Note that these instabilities can be reduced by increasing the number of points of the grid used to calculate the integral (8.97). However, the number of points needed is large. This can cause some issues if for example one wants to fit the parameters of a potential for charged pion elastic scattering. By including Coulomb, calculations would indeed take long, which is not desirable for fitting procedures.

The data are usually situated between 30 and 160 degrees. For this reason, I would like the Coulomb interaction to be well reproduced at least in this range. The screening that satisfies these conditions the best (at least for the pure Coulomb cross section) is $n = 3$ and $R_C = 30$ fm. The cross section calculated for these values of the screening is shown on Fig. G.3 in addition to the ones for $n = 2$ and $n = 4$ (also for this value of the screening radius). As it should be noted, $n = 3$ ensures the pure Coulomb cross section

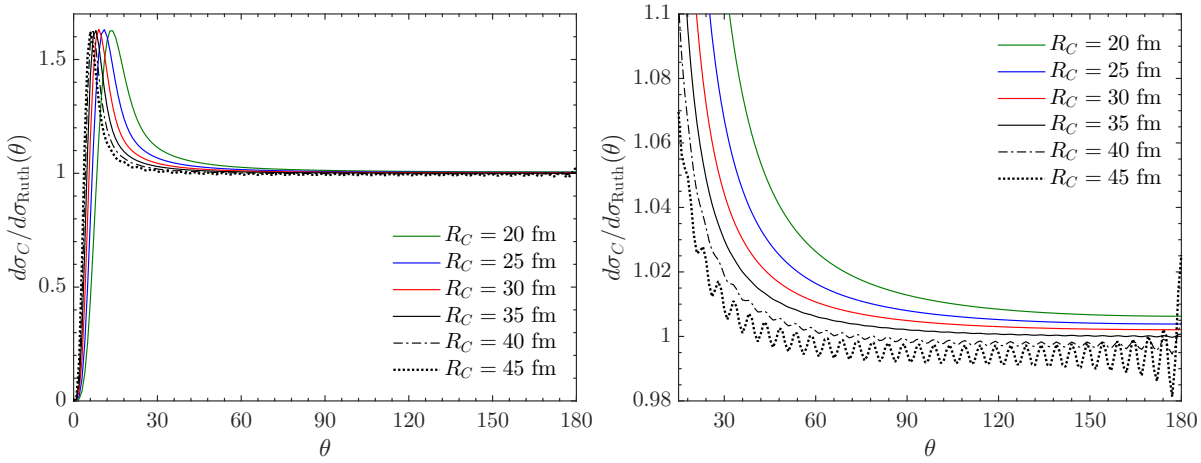

Figure G.2: Left: dependence of the pure Coulomb cross section (divided by Rutherford's) of a π^+ on ^{12}C at 50 MeV lab energy on the screening radius R_C for $n = 2$. Right: zoom around 1.

to be well within 1% of the Rutherford's cross section in the angular range of interest. It is also stable on nearly the whole range. Some instabilities are visible at these scales. However, their magnitude is at the 0.01% level. The $n = 2$ and $n = 3$ screenings achieve this precision beyond 60 and 45 degrees respectively.

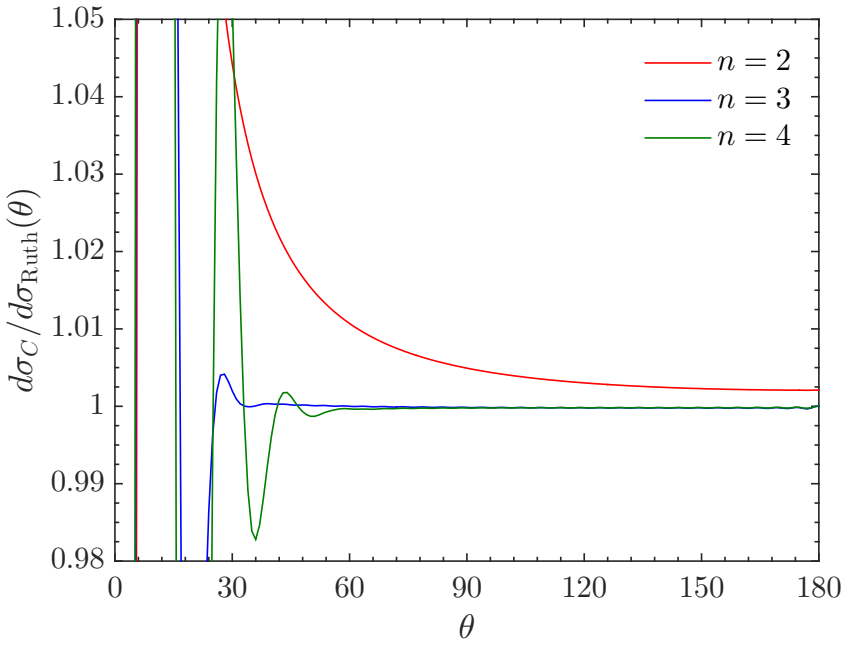

Figure G.3: Pure Coulomb cross section (divided by Rutherford's) of a π^+ on ^{12}C at 50 MeV lab energy for the $n = 2$, 3 and 4. $R_C = 30$ fm.

It is also interesting to see how this screening affects the cross sections when the target is no longer considered as pointlike. In order to account for this effect, I will simply multiply the matrix elements (8.96) by the charge density of the target $\rho_1^Z(q)$. This corresponds to a convolution of the pointlike interaction over the charge density of the nucleus in position space. Here, I will choose a simple Fermi-Dirac density (see Sec. 6.3.1). It is also interesting to see how the different screenings affect the interferences between the Coulomb and the nuclear interaction. On Fig. G.4, I have calculated the cross section of a $\pi^\pm$ on a ^{12}C target at 50 MeV lab energy. The solid red, blue and green curves correspond to the cross section calculated when considering both nuclear and Coulomb screened interactions. The dashed line corresponds to pure nuclear interaction. The solid black line corresponds to the cross section obtained when we consider that the scattering amplitude is simply the coherent sum of the nuclear and pure Coulomb scattering amplitudes, i.e. when neglecting interference between nuclear and Coulomb interactions.

As we can see, the different screenings, although having quite distinct behaviours when considering pure pointlike Coulomb scattering (see Fig. G.3) produce very similar results. In the case of the π^+ scattering, most of the visible differences are found below 30 degrees, where no data exists and where as we have seen, the screening removes most of the contribution of the Coulomb interaction. It should be noted how the interferences between the nuclear and Coulomb interactions are clearly visible between 50 and 150 degrees. At these angles, the sum of the scattering amplitudes is not significantly different. But this is mainly due to the fact that we are working on a light target and the Coulomb interaction is hence small. Similar comments can be made for the π^- scattering, for which the interferences are bigger at larger angles.

We can compare the results of this method to a resolution in position space, where the Coulomb interaction does not pose any problem. This is done for example by calculating

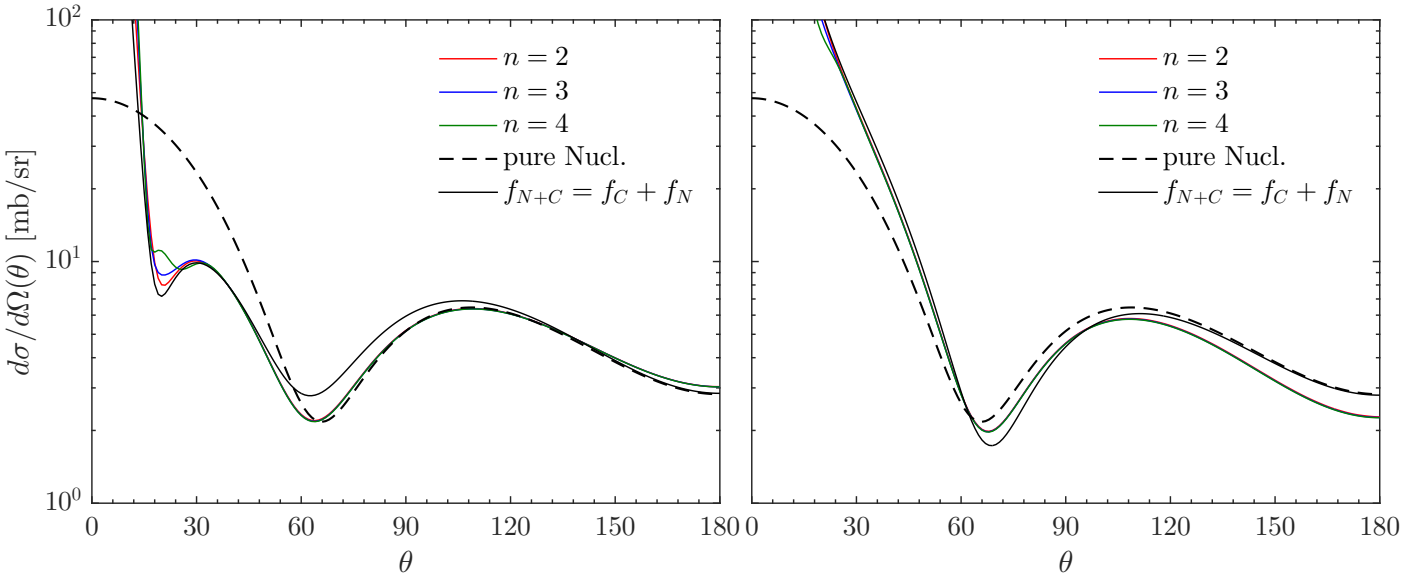

Figure G.4: Cross section of a π^+ (π^- on the right) on a ^{12}C target at 50 MeV lab energy. Solid red, blue and green curves correspond to the cross section calculated when considering both nuclear and Coulomb screened interactions. Dashed line is pure nuclear interaction. The solid black line is the coherent sum of the nuclear and pure Coulomb scattering amplitudes.

the phase shifts. However, the potential that we have used previously is non local (see also Sec. 8). In position space, non-localities are more difficult to handle (this was one of the reasons for the use of a momentum space resolution in the first place). For this reason, we will use a simpler version of the potential that has the shape of a Woods-Saxon well. Its radius is chosen equal to the radius of the Fermi-Dirac shape used to model the density. As we can see from Eq. (8.26), this would correspond to a π-A potential constructed as a purely s-wave π-N interaction folded on the nucleus density. Note finally that the Coulomb potential that I use in the position space resolution is a point-sphere Coulomb potential of the form Eq. (2.63). I will set the radius of this potential as identical to the Woods-Saxon well radius. Note however that in the case of light targets, the choice of radius has a very small impact on the elastic cross section.

The results are shown on Fig. G.5, where I compare the resolution above (black) to the coherent sum of the nuclear and pure Coulomb scattering amplitudes (blue) and to the position space resolution (red). The dashed line corresponds to the resolution for a purely nuclear potential. For a positively charged pion (left) none of the momentum space resolutions reproduce well the position space cross section. It should however be noted how the shape of the coherent sum is not the same as the one from the momentum and position space resolutions. A transition seems to occur around 90 degrees for this curve. It actually corresponds to the angle at which f_C and f_N are comparable in magnitude. After this angle, the reaction is completely dominated by the nuclear interaction while at smaller angles it is by Coulomb. This approximation is thus rather crude.

In the case of a negatively charged pion (right), note how the resolution in momentum space (black) matches much better the one in position space (red) at forward angles. Note also how again, the shape of the coherent sum (blue) is not the same as the one from

the momentum and position space resolutions. But while we could have expected the coherent sum and the momentum space resolution to have a similar behaviour at large angles, it is not the case here. Indeed, while the former tends to the pure nuclear cross section, the momentum space resolution seems to much better capture the interference between the nuclear and Coulomb potential and as such to much better reproduce the cross section at larger angles.

It should be noted that in both cases, we do not reproduce correctly the largest angles. This is unexpected if we think back at how the screening is done. Indeed, we screen only large distances, which should only contribute to small angles in the scattering cross section. We also saw on Fig. G.3 how the screening worked properly for large angles and reproduced the pure pointlike Coulomb cross section at the percent (if not permil) level. This is hence a rather unexpected result.

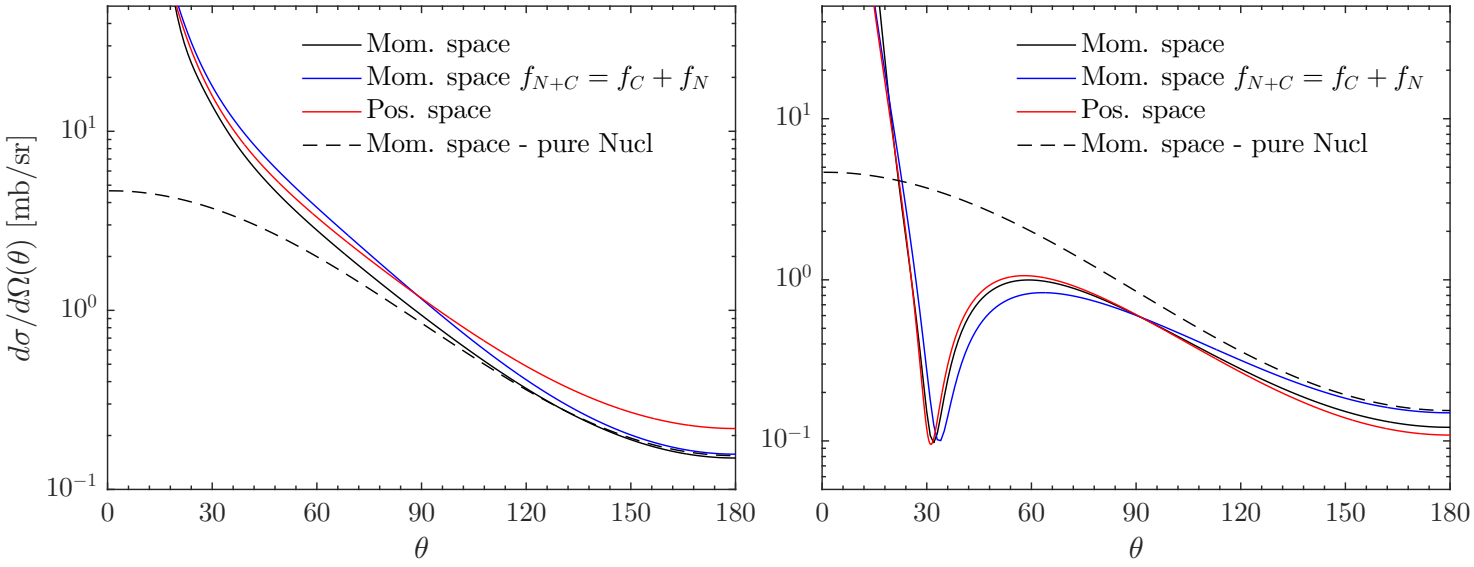

Figure G.5: The cross section calculated in momentum space by considering both nuclear and Coulomb screened interaction (black) or by considering the coherent sum of the nuclear and pure Coulomb scattering amplitudes (blue) are displayed. The solution in position space is in red and the dashed line corresponds to a pure nuclear potential. These cross sections are calculated for a π^+ (left) and π^- (right) on a ^{12}C target at 50 MeV lab energy for a Woods-Saxon well potential.

Note however that if this method gives satisfactory results for light and very light targets it does not for heavier ones. Indeed, the procedure of Deltuva *et al.* [194] becomes unstable when charges reach values of about Z = 20 and should not be applied to heavy targets such as lead. This is clearly seen on Fig. G.6, similar to Fig. G.5 but for a ^{208}Pb target, and where we have used the same simple model as for ^{12}C (i.e. a Fermi-Dirac density for the density, a Woods-Saxon well for the nuclear π-A potential and a point-sphere Coulomb potential, all with the same radii adjusted to lead).

To solve this problem, some alternatives might be explored in the future. On the one hand, there is the matching method of Vincent and Phatak [205]. In this method, the potential is separated into two zones above and below some sharp cut-off radius.

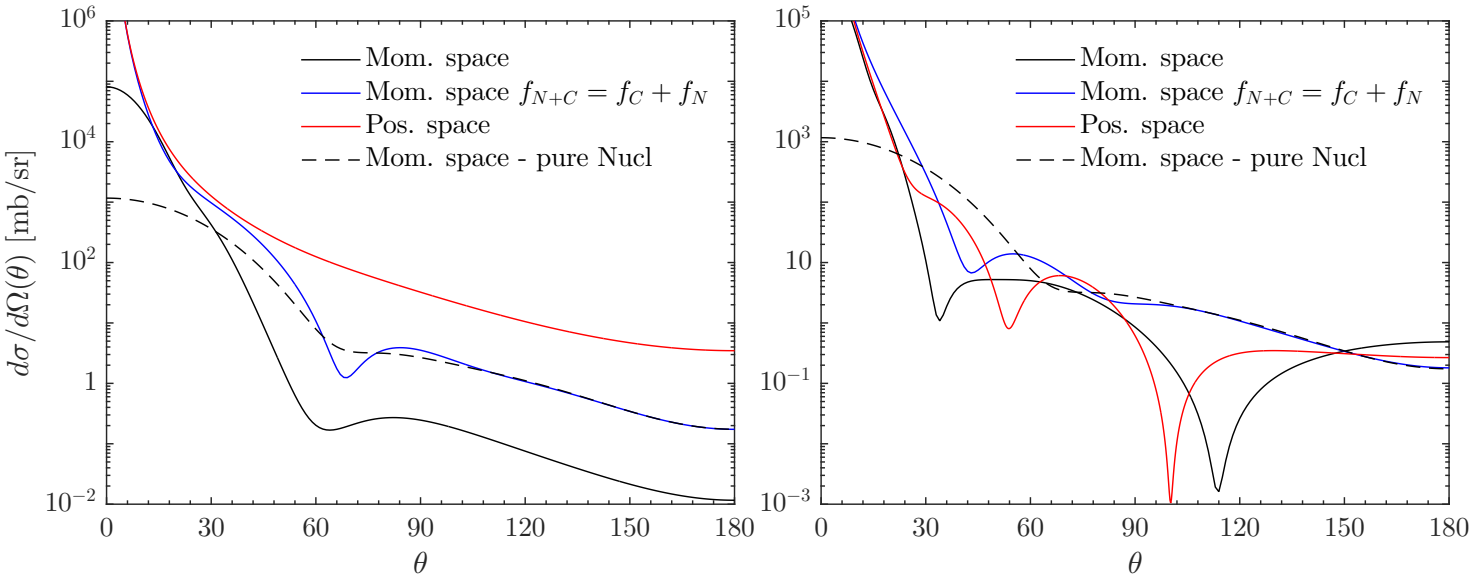

Figure G.6: Same as Fig. G.5 on a ^{208}Pb target.

This cut-off is chosen such that in the external zone, the potential is a pure Coulomb potential. For small cut-offs, we can calculate the nuclear phaseshifts, in the internal zone in momentum space without numerical instabilities. By matching these phaseshifts to those of the second zone, which can be calculated analytically, we can then have access to the phaseshifts of the whole potential. This method has been recently extended in Ref. [206] to avoid taking a sharp cut-off and hence reducing the numerical instabilities that can arise in the internal zone. On the other hand, there is the possibility to choose the momentum-space Coulomb functions as a basis in the Lippmann-Schwinger equation. Indeed, in the presence of a Coulomb interaction, this base is more suited than the plane-wave one and the divergence of Eq. (8.97) is avoided. Moreover, the Green operators have the same form as the free Green operators in the plane-wave basis Eq. (7.39). However, the calculation of the Coulomb functions is non-trivial. Eremenko *et al.* have recently regularized them in Refs. [207, 208]. Note however that this regularization has been achieved only for positive projectiles.

The solution presented here with the screening Eq. (G.1) is considered satisfactory in the case of a carbon target. This is especially true since in this work, I consider a neutral pion. The Coulomb interaction is considered only once to test the MSU potential on π-A elastic scattering data (see Fig. 8.10). I thus let these alternatives as a perspective of this work. They might be needed in future works if one wants to refit the potential on charged-pion elastic scattering data. But I also leave this as a perspective.

H Development of the second order potential in the $t\rho$ approximation

H.1 General form of the second-order potential

The first term of the second order potential in Eq. (8.27) can be re-written as

$$V^{\text{2nd},1}_{\pi A,\text{opt}}(\vec{k}'_\pi,\vec{k}_\pi) = A(A-1)\int\left(\prod_{i=1}^{A}dx_i\right)dx'_1dx'_2\frac{d\vec{p}'_1}{(2\pi)^3}\frac{d\vec{p}_1}{(2\pi)^3}\frac{d\vec{p}'_2}{(2\pi)^3}\frac{d\vec{p}_2}{(2\pi)^3}e^{i(\vec{p}'_1\vec{r}'_1+\vec{p}'_2\vec{r}'_2-\vec{p}_1\vec{r}_1-\vec{p}_2\vec{r}_2)}$$
$$\Phi^\dagger_0(x'_1,x'_2,x_3,\dots,x_A)\left\langle\vec{k}'_\pi,\vec{p}'_1,\vec{p}'_2\right|t_{\pi N,2}\frac{1}{\alpha_0}t_{\pi N,1}\left|\vec{k}_\pi,\vec{p}_1,\vec{p}_2\right\rangle\Phi_0(x_1,x_2,x_3,\dots,x_A) \tag{H.1}$$

We can introduce a closure relation on the intermediate momentum $\vec{k}''_\pi$ between the transition operators such that we have

$$V^{\text{2nd},1}_{\pi A,\text{opt}}(\vec{k}'_\pi,\vec{k}_\pi) = A(A-1)\int\left(\prod_{i=1}^{A}dx_i\right)dx'_1dx'_2\frac{d\vec{p}'_1}{(2\pi)^3}\frac{d\vec{p}_1}{(2\pi)^3}\frac{d\vec{p}'_2}{(2\pi)^3}\frac{d\vec{p}_2}{(2\pi)^3}\frac{d\vec{k}''}{(2\pi)^3}e^{i(\vec{p}'_1\vec{r}'_1+\vec{p}'_2\vec{r}'_2-\vec{p}_1\vec{r}_1-\vec{p}_2\vec{r}_2)}$$
$$\Phi^\dagger_0(x'_1,x'_2,x_3,\dots,x_A)\left\langle\vec{k}'_\pi,\vec{p}'_2\right|t_{\pi N}\left|\vec{k}''_\pi,\vec{p}_2\right\rangle\frac{1}{\alpha_0(k''_\pi)}\left\langle\vec{k}''_\pi,\vec{p}'_1\right|t_{\pi N}\left|\vec{k}_\pi,\vec{p}_1\right\rangle\Phi_0(x_1,x_2,x_3,\dots,x_A) \tag{H.2}$$

where the dependence of α_0 on k''_π has been made explicit. Note that the conservation of momentum at each step of the reaction requires

$$\begin{cases}\vec{k}''_\pi+\vec{p}'_1=\vec{k}_\pi+\vec{p}_1\\ \vec{k}'_\pi+\vec{p}'_2=\vec{k}''_\pi+\vec{p}_2\end{cases} \tag{H.3}$$

which, combined, imply the conservation of momentum $\vec{k}'_\pi+\vec{p}'_1+\vec{p}'_2=\vec{k}_\pi+\vec{p}_1+\vec{p}_2$. As in Eq. (7.73), the bra-ket is short for

$$\left\langle\vec{k}'_\pi,\vec{p}'_2\right|t_{\pi N,2}\left|\vec{k}''_\pi,\vec{p}_2\right\rangle=(2\pi)^3\delta(\vec{k}''_\pi+\vec{p}'_1-\vec{k}_\pi-\vec{p}_1)t_{\pi N}(\vec{k}'_\pi,\vec{p}'_2;\vec{k}''_\pi,\vec{p}_2) \tag{H.4}$$
$$\left\langle\vec{k}''_\pi,\vec{p}_1\right|t_{\pi N,1}\left|\vec{k}_\pi,\vec{p}_1\right\rangle=(2\pi)^3\delta(\vec{k}'_\pi+\vec{p}'_2-\vec{k}''_\pi-\vec{p}_2)t_{\pi N}(\vec{k}''_\pi,\vec{p}'_1;\vec{k}_\pi,\vec{p}_1) \tag{H.5}$$

Let me define the transfer momenta $\vec{q}_1$ and $\vec{q}_2$ at each step as

$$\begin{cases}\vec{q}_1=\vec{k}''_\pi-\vec{k}_\pi\\ \vec{q}_2=\vec{k}'_\pi-\vec{k}''_\pi\end{cases} \tag{H.6}$$

In a similar fashion as what had been done for the first order, we can shift the integration variables $\vec{p}_1=\vec{p}+\vec{q}_1/2$ and $\vec{p}'_1=\vec{p}'-\vec{q}_1/2$ as well as $\vec{p}_2=\vec{\bar{p}}+\vec{q}_2/2$ and $\vec{p}'_2=\vec{\bar{p}}'-\vec{q}_2/2$. Note also that the momentum conservation deltas then cancel the integrals on $\vec{p}'$ and $\vec{\bar{p}}'$

$$V^{\text{2nd},1}_{\pi A,\text{opt}}(\vec{k}'_\pi,\vec{k}_\pi) = A(A-1)\int\left(\prod_{i=1}^{A}dx_i\right)dx'_1dx'_2\frac{d\vec{p}}{(2\pi)^3}\frac{d\vec{\bar{p}}}{(2\pi)^3}\frac{d\vec{k}''_\pi}{(2\pi)^3}e^{i\left[\left(\vec{\bar{p}}-\frac{\vec{q}_2}{2}\right)\vec{r}'_2-\left(\vec{\bar{p}}+\frac{\vec{q}_2}{2}\right)\vec{r}_2\right]}$$
$$\Phi^\dagger_0(x'_1,x'_2,x_3,\dots,x_A)\Phi_0(x_1,x_2,x_3,\dots,x_A)e^{i\left[\left(\vec{p}-\frac{\vec{q}_1}{2}\right)\vec{r}'_1-\left(\vec{p}+\frac{\vec{q}_1}{2}\right)\vec{r}_1\right]}$$
$$t_{\pi N}(\vec{k}'_\pi,\vec{\bar{p}}-\vec{q}_2/2;\vec{k}''_\pi,\vec{\bar{p}}+\vec{q}_2/2)\frac{1}{\alpha_0(k'')}t_{\pi N}(\vec{k}''_\pi,\vec{p}-\vec{q}_1/2;\vec{k}_\pi,\vec{p}+\vec{q}_1/2) \tag{H.7}$$

If we factorize the nuclear recoil [see Eqs. (6.39)—(6.41)], we are left with

$$V^{\rm 2nd,1}_{\pi A,\rm opt}(\vec{k}'_\pi,\vec{k}_\pi) = A(A-1)\sum_{\sigma_{1,2},\sigma'_{1,2}}\sum_{\tau_{1,2},\tau'_{1,2}}\int\left(\prod_{i=1}^{A-1}d\vec{\xi}_i\right)d\vec{\xi}'_1 d\vec{\xi}'_2 d\vec{\zeta}\frac{d\vec{p}}{(2\pi)^3}\frac{d\vec{p}'}{(2\pi)^3}\frac{d\vec{k}''}{(2\pi)^3}$$
$$e^{i\left[\left(\vec{p}-\frac{\vec{q}_1}{2}\right)\left(\vec{\zeta}-\vec{\xi}'_1-\frac{\vec{\xi}'_2}{A-1}\right)-\left(\vec{p}+\frac{\vec{q}_1}{2}\right)\left(\vec{\zeta}-\vec{\xi}_1-\frac{\vec{\xi}_2}{A-1}\right)\right]}e^{i\left[\left(\vec{p}'-\frac{\vec{q}_2}{2}\right)(\vec{\zeta}-\vec{\xi}'_2)-\left(\vec{p}'+\frac{\vec{q}_2}{2}\right)(\vec{\zeta}-\vec{\xi}_2)\right]}$$
$$t_{\pi N}(\vec{k}'_\pi,\vec{p}-\vec{q}_2/2;\vec{k}''_\pi,\vec{p}+\vec{q}_2/2)\frac{1}{\alpha_0(k'')}t_{\pi N}(\vec{k}''_\pi,\vec{p}-\vec{q}_1/2;\vec{k}_\pi,\vec{p}+\vec{q}_1/2)$$
$$e^{i\vec{k}'\left(\vec{\zeta}-\frac{\vec{\xi}'_1}{A}-\frac{\vec{\xi}'_2}{A-1}\right)}\phi^\dagger_{0;\sigma'_1\sigma'_2\sigma_{3\ldots A};\tau'_1\tau'_2\tau_{3\ldots A}}(\vec{\xi}'_1,\vec{\xi}'_2,\vec{\xi}_3,\ldots,\vec{\xi}_{A-1})$$
$$\phi_{0;\sigma_1\sigma_2\sigma_{3\ldots A};\tau_1\tau_2\tau_{3\ldots A}}(\vec{\xi}_1,\vec{\xi}_2,\vec{\xi}_3,\ldots,\vec{\xi}_{A-1})e^{-i\vec{k}\left(\vec{\zeta}-\frac{\vec{\xi}_1}{A}-\frac{\vec{\xi}_2}{A-1}\right)} \tag{H.8}$$

As before for the first order, the integral on the first term of the exponential term in $\vec{\zeta}$ is simply the momentum conservation between the initial and final momenta. If we group all the remaining exponentials, we are left with an exponential of argument

$$\frac{\vec{k}_\pi\cdot\vec{\xi}_2}{A-1}-\frac{\vec{k}'_\pi\cdot\vec{\xi}'_2}{A-1}+\vec{p}\left(\vec{\xi}_2-\vec{\xi}'_2\right)+\frac{\vec{q}_2}{2}\left(\vec{\xi}_2+\vec{\xi}'_2\right)$$
$$+\frac{\vec{k}_\pi\cdot\vec{\xi}_1}{A}-\frac{\vec{k}'_\pi\cdot\vec{\xi}'_1}{A}+\vec{p}'\left[\left(\vec{\xi}_1-\vec{\xi}'_1\right)+\frac{1}{A-1}\left(\vec{\xi}_2-\vec{\xi}'_2\right)\right]+\frac{\vec{q}_1}{2}\left[\left(\vec{\xi}_1+\vec{\xi}'_1\right)+\frac{1}{A-1}\left(\vec{\xi}_2+\vec{\xi}'_2\right)\right] \tag{H.9}$$

By writing $\vec{k}_\pi$ into the trivial sum of two terms $\vec{k}_\pi/2+\vec{k}_\pi/2$ and injecting the definition of $\vec{q}_1$ Eqs. (H.6) in the second one, the alternative definition of $\vec{k}_\pi$ is $\vec{k}_\pi/2+(\vec{k}''_\pi-\vec{q}_1)/2$. Similarly, we have $\vec{k}'_\pi=\vec{k}'_\pi/2+(\vec{k}''_\pi+\vec{q}_2)/2$. Let me inject these definitions into the first line of the argument of the exponential such that we have

$$\left(\vec{p}+\frac{\vec{k}'_\pi+\vec{k}_\pi}{2(A-1)}\right)\left(\vec{\xi}_2-\vec{\xi}'_2\right)+\frac{\vec{k}_\pi\cdot\vec{\xi}'_2-\vec{k}'_\pi\vec{\xi}_2+\vec{k}''_\pi(\vec{\xi}_2-\vec{\xi}'_2)-\vec{q}_1\cdot\vec{\xi}_2-\vec{q}_2\cdot\vec{\xi}'_2}{2(A-1)}+\frac{\vec{q}_2}{2}\left(\vec{\xi}_2+\vec{\xi}'_2\right) \tag{H.10}$$

$$=\left(\vec{p}+\frac{\vec{k}'_\pi+\vec{k}_\pi}{2(A-1)}\right)\left(\vec{\xi}_2-\vec{\xi}'_2\right)+\frac{-\vec{q}_1\cdot\vec{\xi}'_2-\vec{q}_2\cdot\vec{\xi}_2-\vec{q}_1\cdot\vec{\xi}_2-\vec{q}_2\cdot\vec{\xi}'_2}{2(A-1)}+\frac{\vec{q}_2}{2}\left(\vec{\xi}_2+\vec{\xi}'_2\right) \tag{H.11}$$

$$=\left(\vec{p}+\frac{\vec{k}'_\pi+\vec{k}_\pi}{2(A-1)}\right)\left(\vec{\xi}_2-\vec{\xi}'_2\right)+\frac{1}{2}\left(\frac{A-2}{A-1}\vec{q}_2-\frac{\vec{q}_1}{A-1}\right)\left(\vec{\xi}_2+\vec{\xi}'_2\right) \tag{H.12}$$

Similarly for the term of the second line, we have

$$\left(\vec{p}+\frac{\vec{k}'_\pi+\vec{k}_\pi}{2A}\right)\left(\vec{\xi}_1-\vec{\xi}'_1\right)+\frac{\vec{p}'}{A-1}\left(\vec{\xi}_2-\vec{\xi}'_2\right)-\frac{1}{2}\left(\frac{A-1}{A}\vec{q}_1+\frac{\vec{q}_2}{A}\right)\left(\vec{\xi}_1+\vec{\xi}'_1\right)+\frac{\vec{q}_1}{2(A-1)}\left(\vec{\xi}_2+\vec{\xi}'_2\right) \tag{H.13}$$

If we sum both lines, we have

$$\left(\vec{p}+\frac{\vec{p}'}{A-1}+\frac{\vec{k}'_\pi+\vec{k}_\pi}{2(A-1)}\right)\left(\vec{\xi}_2-\vec{\xi}'_2\right)+\frac{1}{2}\frac{A-2}{A-1}\vec{q}_2\left(\vec{\xi}_2+\vec{\xi}'_2\right)$$
$$+\left(\vec{p}+\frac{\vec{k}'_\pi+\vec{k}_\pi}{2A}\right)\left(\vec{\xi}_1-\vec{\xi}'_1\right)+\frac{1}{2}\left(\frac{A-1}{A}\vec{q}_1+\frac{\vec{q}_2}{A}\right)\left(\vec{\xi}_1+\vec{\xi}'_1\right) \tag{H.14}$$

Similarly to what we had done in first order, we can shift the variables $\vec{p} \to \vec{p} - \vec{p}/(A-1) - (\vec{k}_\pi + \vec{k}'_\pi)/2(A-1)$ and then similarly $\vec{p} \to \vec{p} - (\vec{k}_\pi + \vec{k}'_\pi)/2A$. If we also plug in the definition for the the 2-body density matrix Eq. (6.45) into Eq. (H.8), we have

$$
\begin{aligned}
V^{\text{2nd,1}}_{\pi A,\text{opt}}(\vec{k}'_\pi, \vec{k}_\pi) = & \sum_{\sigma_{1,2},\sigma'_{1,2}} \sum_{\tau_{1,2},\tau'_{1,2}} \int d\vec{\xi}_1 d\vec{\xi}_2 d\vec{\xi}'_1 d\vec{\xi}'_2 \frac{d\vec{p}_1}{(2\pi)^3} \frac{d\vec{p}_2}{(2\pi)^3} \frac{d\vec{k}''_\pi}{(2\pi)^3} e^{i\vec{p}_2(\vec{\xi}_2 - \vec{\xi}'_2)} e^{i\vec{p}_1(\vec{\xi}_1 - \vec{\xi}'_1)} \\
& \rho_2(\vec{\xi}_1, \vec{\xi}_2 | \vec{\xi}'_1, \vec{\xi}'_2) e^{i\frac{1}{2}\frac{A-2}{A-1}\vec{q}_2(\vec{\xi}_2 + \vec{\xi}'_2)} e^{i\frac{1}{2}\left(\frac{A-1}{A}\vec{q}_1 + \frac{\vec{q}_2}{A}\right)(\vec{\xi}_1 + \vec{\xi}'_1)} \\
& t_{\pi N}\left(\vec{k}'_\pi, \vec{p} - \frac{\vec{p}}{A-1} - \frac{\vec{k}_\pi + \vec{k}'_\pi}{2(A-1)} - \frac{\vec{q}_2}{2}; \vec{k}''_\pi, \vec{p} - \frac{\vec{p}}{A-1} - \frac{\vec{k}_\pi + \vec{k}'_\pi}{2(A-1)} + \frac{\vec{q}_2}{2}\right) \\
& \frac{1}{\alpha_0(k''_\pi)} t_{\pi N}\left(\vec{k}''_\pi, \vec{p} - \frac{\vec{k}'_\pi + \vec{k}_\pi}{2A} - \frac{\vec{q}_1}{2}; \vec{k}_\pi, \vec{p} - \frac{\vec{k}'_\pi + \vec{k}_\pi}{2A} + \frac{\vec{q}_1}{2}\right)
\end{aligned}
\tag{H.15}
$$

Similarly to what has been done at the first order [see Eq. (7.81)], I will further simplify this integral by making the factorization approximation [169, 170]. This assumes that the $t_{\pi N}$ matrix is a slowly varying function of $\vec{p}$ and $\vec{\mathcal{p}}$ compared to the nucleus two-nucleon density. The former is then evaluated at $p = 0$ and $\mathcal{p} = 0$. After integration on $\vec{p}$ and $\vec{\mathcal{p}}$, we then have

$$
\begin{aligned}
V^{\text{2nd,1}}_{\pi A,\text{opt}}(\vec{k}'_\pi, \vec{k}_\pi) = & \sum_{\sigma_{1,2},\sigma'_{1,2}} \sum_{\tau_{1,2},\tau'_{1,2}} \int d\vec{\xi}_1 d\vec{\xi}_2 \frac{d\vec{k}''_\pi}{(2\pi)^3} \rho_2(\vec{\xi}_1, \vec{\xi}_2 | \vec{\xi}_1, \vec{\xi}_2) e^{i\frac{A-2}{A-1}\vec{q}_2\vec{\xi}_2} e^{i\left(\frac{A-1}{A}\vec{q}_1 + \frac{\vec{q}_2}{A}\right)\vec{\xi}_1} \frac{1}{\alpha_0(k''_\pi)} \\
& t_{\pi N}\left(\vec{k}'_\pi, -\frac{\vec{k}_\pi + \vec{k}'_\pi}{2(A-1)} - \frac{\vec{q}_2}{2}; \vec{k}''_\pi, -\frac{\vec{k}_\pi + \vec{k}'_\pi}{2(A-1)} + \frac{\vec{q}_2}{2}\right) t_{\pi N}\left(\vec{k}''_\pi, -\frac{\vec{k}'_\pi + \vec{k}_\pi}{2A} - \frac{\vec{q}_1}{2}; \vec{k}_\pi, -\frac{\vec{k}'_\pi + \vec{k}_\pi}{2A} + \frac{\vec{q}_1}{2}\right)
\end{aligned}
\tag{H.16}
$$

When writing explicitly the Fourier transform of the 2-body density matrix (6.47), this finally gives

$$
\begin{aligned}
V^{\text{2nd,1}}_{\pi A,\text{opt}}(\vec{k}'_\pi, \vec{k}_\pi) = & \int \frac{d\vec{k}''_\pi}{(2\pi)^3} \hat{\rho}_2\left(\left(\frac{A-1}{A}\vec{q}_1 + \frac{\vec{q}_2}{A}\right), \frac{A-2}{A-1}\vec{q}_2\right) \frac{1}{\alpha_0(k''_\pi)} \\
& t_{\pi N}\left(\vec{k}'_\pi, -\frac{\vec{k}_\pi + \vec{k}'_\pi}{2(A-1)} - \frac{\vec{q}_2}{2}; \vec{k}''_\pi, -\frac{\vec{k}_\pi + \vec{k}'_\pi}{2(A-1)} + \frac{\vec{q}_2}{2}\right) t_{\pi N}\left(\vec{k}''_\pi, -\frac{\vec{k}'_\pi + \vec{k}_\pi}{2A} - \frac{\vec{q}_1}{2}; \vec{k}_\pi, -\frac{\vec{k}'_\pi + \vec{k}_\pi}{2A} + \frac{\vec{q}_1}{2}\right)
\end{aligned}
\tag{H.17}
$$

It should be noted that for heavy nuclei, $(A-1)/A \simeq 1$, $1/A \simeq 0$ and $(A-2)/(A-1) \simeq 1$ so that we can replace the arguments of the Fourier transform of the two-nucleon density by q_1 and q_2. Since this is the second-order potential, it should not have that much of an impact. I will thus make this approximation in order to have easier expressions in the following. The final expression is thus

$$
V^{\text{2nd,1}}_{\pi A,\text{opt}}(\vec{k}'_\pi, \vec{k}_\pi) = \int \frac{d\vec{k}''_\pi}{(2\pi)^3} \frac{\hat{\rho}_2(\vec{q}_1, \vec{q}_2)}{\alpha_0(k''_\pi)} t_{\pi N}\left(\vec{k}'_\pi, \vec{p}'_{2,\text{eff}}; \vec{k}''_\pi, \vec{p}_{2,\text{eff}}\right) t_{\pi N}\left(\vec{k}''_\pi, \vec{p}'_{1,\text{eff}}; \vec{k}_\pi, \vec{p}_{1,\text{eff}}\right)
\tag{H.18}
$$

where the effective nucleon momenta read

$$\vec{p}_{1,\text{eff}} = -\frac{\vec{k}'_\pi + \vec{k}_\pi}{2A} + \frac{\vec{q}_1}{2} \qquad \vec{p}_{2,\text{eff}} = -\frac{\vec{k}_\pi + \vec{k}'_\pi}{2(A-1)} + \frac{\vec{q}_2}{2} \tag{H.19}$$

$$\vec{p}'_{1,\text{eff}} = -\frac{\vec{k}'_\pi + \vec{k}_\pi}{2A} - \frac{\vec{q}_1}{2} \qquad \vec{p}'_{2,\text{eff}} = -\frac{\vec{k}_\pi + \vec{k}'_\pi}{2(A-1)} - \frac{\vec{q}_2}{2} \tag{H.20}$$

The second term of the second order potential in Eq. (8.27) is simpler to handle and is really similar to what has been done for the first order

$$V^{\text{2nd,2}}_{\pi A,\text{opt}}(\vec{k}'_\pi, \vec{k}_\pi) = -\frac{A-1}{A} \int \frac{d\vec{k}''_\pi}{(2\pi)^3} \frac{1}{\alpha_0(k''_\pi)} t_{\pi N}\left(\vec{k}'_\pi, \vec{p}'_{2,\text{eff}}; \vec{k}''_\pi, \vec{p}_{2,\text{eff}}\right) t_{\pi N}\left(\vec{k}''_\pi, \vec{p}'_{1,\text{eff}}; \vec{k}_\pi, \vec{p}_{1,\text{eff}}\right) \hat{\rho}_1(q_2)\, \hat{\rho}_1(q_1) \tag{H.21}$$

Since this is second order, we will also consider $\tilde{q}_i \simeq q_i$, which is nonetheless a good approximation in the case of heavy nuclei. When recollecting both terms, the second-order of the potential reads

$$\begin{aligned} V^{\text{2nd}}_{\pi A,\text{opt}}(\vec{k}'_\pi, \vec{k}_\pi) = & \int \frac{d\vec{k}''_\pi}{(2\pi)^3} \frac{\hat{\rho}_2(\vec{q}_1, \vec{q}_2)}{\alpha_0(k''_\pi)} t_{\pi N}\left(\vec{k}'_\pi, \vec{p}'_{2,\text{eff}}; \vec{k}''_\pi, \vec{p}_{2,\text{eff}}\right) t_{\pi N}\left(\vec{k}''_\pi, \vec{p}'_{1,\text{eff}}; \vec{k}_\pi, \vec{p}_{1,\text{eff}}\right) \\ & - \frac{A-1}{A} \int \frac{d\vec{k}''_\pi}{(2\pi)^3} \frac{1}{\alpha_0(k''_\pi)} t_{\pi N}\left(\vec{k}'_\pi, \vec{p}'_{2,\text{eff}}; \vec{k}''_\pi, \vec{p}_{2,\text{eff}}\right) t_{\pi N}\left(\vec{k}''_\pi, \vec{p}'_{1,\text{eff}}; \vec{k}_\pi, \vec{p}_{1,\text{eff}}\right) \hat{\rho}_1(q_2)\, \hat{\rho}_1(q_1) \end{aligned} \tag{H.22}$$

In this work, I consider coherent processes only, where the nucleus remains in its ground state. The summation on spins $\sigma_1, \sigma'_1, \sigma_2, \sigma'_2$ and iso-spins $\tau_1, \tau'_1, \tau_2, \tau'_2$ that is contained in $\hat{\rho}_2$ should only contain terms where $\{\sigma_1, \sigma_2; \tau_1, \tau_2\}$ is either equal to $\{\sigma'_1, \sigma'_2; \tau'_1, \tau'_2\}$ or $\{\sigma'_2, \sigma'_1; \tau'_2, \tau'_1\}$. Let me note that there are then three different combinations for the scattering of the pion. The pion can scatter twice in an s-wave, or twice in a p-wave but it also can scatter in a p-wave and then in an s-wave (and conversely). Contrary to the results at first order [see Eq. (8.26)], the spin- and isospin-flip parts of the potential (coefficients b_1 and c_1 of the π-N scattering amplitude in Eq. (8.12)) can hence contribute at the second order. Note however that because we are left with a nucleus in its ground state, only products of the type $b_i b_i$, $b_i c_i$ or $c_i c_i$ remain.

We can split the second order further into

$$V^{\text{2nd}}_{\pi A,\text{opt}} = V^{\text{2nd,1}}_{\pi A,\text{opt}} + V^{\text{2nd,2}}_{\pi A,\text{opt}} \tag{H.23}$$

$$= V^{\text{2nd,1}}_{\pi A,\text{opt},ss} + V^{\text{2nd,1}}_{\pi A,\text{opt},sp} + V^{\text{2nd,1}}_{\pi A,\text{opt},pp} + V^{\text{2nd,2}}_{\pi A,\text{opt},ss} + V^{\text{2nd,2}}_{\pi A,\text{opt},sp} + V^{\text{2nd,2}}_{\pi A,\text{opt},pp} \tag{H.24}$$

Let me start with the first ss term $V^{\text{2nd,1}}_{\pi A,\text{opt},ss}$. On the one hand, for the isospin-flip part of the potential (b_1), only the exchange term of the two-nucleon density (see Eq. (6.14)) contributes. Moreover, a factor two appears after the summation. On the other hand, for the spin-isospin independent part (b_0), the whole two-nucleon density contributes. The first ss term of the second order potential will hence obey

$$V^{\text{2nd,1}}_{\text{opt},ss}(\vec{k}'_\pi, \vec{k}_\pi) \propto \int \frac{d\vec{k}''_\pi}{(2\pi)^3} \frac{1}{\alpha_0(k''_\pi)} \left[b_0^2 \hat{\rho}_2(\vec{q}_1, \vec{q}_2) + 2b_1^2 \hat{\rho}_{\text{ex}}(\vec{q}_1, \vec{q}_2)\right] \tag{H.25}$$

where I have used

$$\hat{\rho}_{\text{ex}}(\vec{q}_1, \vec{q}_2) = \hat{\rho}_2(\vec{q}_1, \vec{q}_2) - \hat{\rho}_1(q_2)\, \hat{\rho}_1(q_1) \tag{H.26}$$

It should be noted that according to Eq. (8.25), the $t_{\pi N}$ scattering amplitudes should be considered in the π-A centre-of-mass frame. As we have seen for photoproduction [see Eq. (7.92)] and for first-order π-A scattering [see Eq. (8.25)], the kinematical factor is dependent on the momenta of the initial and final systems. In the second-order of the potential, these kinematical factors will also depend on the intermediate momentum of the pion. This complicates expressions as the t-matrices are found inside of the integral. In order to simplify expressions, I will consider that this dependence can be taken out of the intergal. This is depicted by the use of the proportionality sign, which reminds concisely that kinematical factors should be considered.

The reasoning for sp and pp terms is the same except that we also need take the scalar products into account

$$V_{\text{opt},sp}^{\text{2nd},1}(\vec{k}'_\pi,\vec{k}_\pi) \propto \int \frac{d\vec{k}''_\pi}{(2\pi)^3} \frac{\tilde{\vec{k}}'_\pi\cdot\tilde{\vec{k}}''_\pi+\tilde{\vec{k}}''_\pi\cdot\tilde{\vec{k}}_\pi}{\alpha_0(k''_\pi)} \left[b_0c_0\hat{\rho}_2\left(\vec{q}_1,\vec{q}_2\right)+2b_1c_1\hat{\rho}_{\text{ex}}(\vec{q}_1,\vec{q}_2)\right] \tag{H.27}$$

$$V_{\text{opt},pp}^{\text{2nd},1}(\vec{k}'_\pi,\vec{k}_\pi) \propto \int \frac{d\vec{k}''_\pi}{(2\pi)^3} \frac{(\tilde{\vec{k}}'_\pi\cdot\tilde{\vec{k}}''_\pi)(\tilde{\vec{k}}''_\pi\cdot\tilde{\vec{k}}_\pi)}{\alpha_0(k''_\pi)} \left[c_0^2\hat{\rho}_2\left(\vec{q}_1,\vec{q}_2\right)+2c_1^2\hat{\rho}_{\text{ex}}(\vec{q}_1,\vec{q}_2)\right] \tag{H.28}$$

where I remind the reader that the tilde denotes momenta evaluated in the π-N centre-of-mass frame.

The second term of the second order [see eq. (H.22)] is easier to handle. For this term, only the isospin-independent part contributes after the summation has been performed. We hence have

$$V_{\text{opt},ss}^{\text{2nd},2}(\vec{k}'_\pi,\vec{k}_\pi) \propto \int \frac{d\vec{k}''_\pi}{(2\pi)^3} \frac{1}{\alpha_0(k''_\pi)} \left(-b_0^2\frac{A-1}{A}\hat{\rho}_1\left(q_2\right)\hat{\rho}_1\left(q_1\right)\right) \tag{H.29}$$

$$V_{\text{opt},sp}^{\text{2nd},2}(\vec{k}'_\pi,\vec{k}_\pi) \propto \int \frac{d\vec{k}''_\pi}{(2\pi)^3} \frac{\tilde{\vec{k}}'_\pi\cdot\tilde{\vec{k}}''_\pi+\tilde{\vec{k}}''_\pi\cdot\tilde{\vec{k}}_\pi}{\alpha_0(k''_\pi)} \left(-b_0c_0\frac{A-1}{A}\hat{\rho}_1\left(q_2\right)\hat{\rho}_1\left(q_1\right)\right) \tag{H.30}$$

$$V_{\text{opt},pp}^{\text{2nd},2}(\vec{k}'_\pi,\vec{k}_\pi) \propto \int \frac{d\vec{k}''_\pi}{(2\pi)^3} \frac{(\tilde{\vec{k}}'_\pi\cdot\tilde{\vec{k}}''_\pi)(\tilde{\vec{k}}''_\pi\cdot\tilde{\vec{k}}_\pi)}{\alpha_0(k''_\pi)} \left(-c_0^2\frac{A-1}{A}\hat{\rho}_1\left(q_2\right)\hat{\rho}_1\left(q_1\right)\right) \tag{H.31}$$

We can combine these results by separating $(A-1)/A = 1-1/A$ such that we finally have

$$V_{\text{opt},ss}^{\text{2nd}}(\vec{k}'_\pi,\vec{k}_\pi) \propto \int \frac{d\vec{k}''_\pi}{(2\pi)^3} \frac{1}{\alpha_0(k''_\pi)} \left[(b_0^2+2b_1^2)\hat{\rho}_{\text{ex}}(\vec{q}_1,\vec{q}_2)+\frac{b_0^2}{A}\hat{\rho}_1\left(q_2\right)\hat{\rho}_1\left(q_1\right)\right] \tag{H.32}$$

$$V_{\text{opt},sp}^{\text{2nd}}(\vec{k}'_\pi,\vec{k}_\pi) \propto \int \frac{d\vec{k}''_\pi}{(2\pi)^3} \frac{\tilde{\vec{k}}'_\pi\cdot\tilde{\vec{k}}''_\pi+\tilde{\vec{k}}''_\pi\cdot\tilde{\vec{k}}_\pi}{\alpha_0(k''_\pi)} \left[(b_0c_0+2b_1c_1)\hat{\rho}_{\text{ex}}(\vec{q}_1,\vec{q}_2)+\frac{b_0c_0}{A}\hat{\rho}_1\left(q_2\right)\hat{\rho}_1\left(q_1\right)\right] \tag{H.33}$$

$$V_{\text{opt},pp}^{\text{2nd}}(\vec{k}'_\pi,\vec{k}_\pi) \propto \int \frac{d\vec{k}''_\pi}{(2\pi)^3} \frac{(\tilde{\vec{k}}'_\pi\cdot\tilde{\vec{k}}''_\pi)(\tilde{\vec{k}}''_\pi\cdot\tilde{\vec{k}}_\pi)}{\alpha_0(k''_\pi)} \left[(c_0^2+2c_1^2)\hat{\rho}_{\text{ex}}(\vec{q}_1,\vec{q}_2)+\frac{c_0^2}{A}\hat{\rho}_1\left(q_2\right)\hat{\rho}_1\left(q_1\right)\right] \tag{H.34}$$

As we can see from these expressions, the two-nucleon density is needed to calculate the second order of the potential. As discussed in Sec. 6, in this work, I will apply my model to several nuclei described by different densities, for which two-nucleon densities are not always known. In order to palliate this issue, I will have to use another form of the π-A potential. This choice will be discussed in Ref. [**?**].

In future works, the influence of the uncertainty on the parameters of this potential ($b_{0,1}$ and $c_{0,1}$ [see Eq. (8.12)]) and the influence of the second order could be of interest. In the idea of laying a path for this study, I will try and particularise the expressions Eqs. (H.32)—(H.34) to the simple case of ^{12}C in the HO model. This is the subject of next section. The reader that would not be interested in this derivation, can skip this section and go back to Eq. (8.28), from which this appendix originates.

H.2 Particularisation to ^{12}C in the HO model

In this section, le me apply the HO model of Sec. 6.2.2 to calculate an analytical form of the second order of the π-A potential. While for the first order, this task is simple and only requires to insert expression (6.24) in Eq. (8.26), the evaluation of second-order terms requires a bit more work because of the integral on intermediate pion momenta.

First, let me note that the two-nucleon density distribution in the case of a closed-shell $N = Z$ nucleus reads

$$\rho_2(\vec{r}_1, \vec{r}_2) = \rho_1(\vec{r}_1)\rho_1(\vec{r}_2) - \frac{1}{4}|\rho_1(\vec{r}_1|\vec{r}_2)|^2 \tag{H.35}$$

The ^{12}C nucleus does not fall into this category as in an extreme shell-model, its $0s_{1/2}$ shell and $0p_{3/2}$ sub-shell are closed but its $0p_{1/2}$ sub-shell remains open. Because the two-nucleon density distribution is used only for the second order of the potential, I will assume the expression (H.35) to hold even for ^{12}C. From Eq. (6.23), the two-nucleon density distribution can be calculated and reads

$$\rho_2(\vec{r}_1, \vec{r}_2) = \frac{4}{\pi^3 a^6}\left[4\left(1+\frac{4}{3}\frac{r_1^2}{a^2}\right)\left(1+\frac{4}{3}\frac{r_2^2}{a^2}\right) - \left(1+\frac{4}{3}\frac{\vec{r}_1\cdot\vec{r}_2}{a^2}\right)^2\right] e^{-\frac{r_1^2+r_2^2}{a^2}} \tag{H.36}$$

Its momentum space counterpart reads

$$\hat{\rho}_2(\vec{q}_1, \vec{q}_2) = \frac{4}{3}\left[101 - \frac{34}{3}a^2(q_1^2+q_2^2) + 2a^2(\vec{q}_1\cdot\vec{q}_2) - \frac{1}{3}a^4(\vec{q}_1\cdot\vec{q}_2)^2 + \frac{4}{3}a^4 q_1^2 q_2^2\right] e^{-\frac{a^2}{4}(q_1^2+q_2^2)} \tag{H.37}$$

It should be noted how because of my assumption (H.35), the normalisation $\hat{\rho}_2(0,0) = 12\times 11 + 8/3$ is slightly different from $A(A-1)$ [see Eq. (6.11)]. However, since this term only exists in second order and the difference is of a mere percent, I will keep this form.

The exchange part of the ss term (H.32) can be rewritten as

$$V^{\text{2nd}}_{\text{opt},ss,\text{ex}}(\vec{k}'_\pi, \vec{k}_\pi) \propto (b_0^2 + 2b_1^2) \times \int \frac{d\vec{k}''_\pi}{(2\pi)^3} \frac{\frac{4}{3}\left[-7 + 2a^2(\vec{q}_1\cdot\vec{q}_2) + \frac{2}{3}a^2(q_1^2+q_2^2) - \frac{1}{3}a^4(\vec{q}_1\cdot\vec{q}_2)^2\right] e^{-\frac{a^2}{4}(q_1^2+q_2^2)}}{\alpha_0(k''_\pi)} \tag{H.38}$$

where $\hat{\rho}_{\text{ex}}$ has been replaced by its explicit expression in the HO model. Note that by taking b_0 and b_1 out of the integral, I assume that they are constant for any intermediate momentum k''_π.

The propagator α_0^{-1} can be replaced by its non relativistic [see Eq. (7.39)] or relativistic form [see Eq. (7.47)]. Because the non-relativistic one is easier and analytically tractable,

I will consider this one only. We then have

$$V^{\text{2nd}}_{\text{opt},ss,\text{ex}}(\vec{k}'_\pi,\vec{k}_\pi) \propto (b_0^2+2b_1^2) \times \int \frac{d\vec{k}''_\pi}{(2\pi)^3} \frac{\frac{4}{3}\left[-7+2a^2(\vec{q}_1\cdot\vec{q}_2)+\frac{2}{3}a^2(q_1^2+q_2^2)-\frac{1}{3}a^4(\vec{q}_1\cdot\vec{q}_2)^2\right] e^{-\frac{a^2}{4}(q_1^2+q_2^2)}}{k_{\pi,0}^2-k''^2_\pi+i\varepsilon} \tag{H.39}$$

It is useful to rewrite $\hat{\rho}_{\text{ex}}$ in a more convenient form inside this integral. To do so, note that the scalar product $\vec{q}_1\cdot\vec{q}_2$ can be rewritten in the form

$$\vec{q}_1\cdot\vec{q}_2 = \frac{(\vec{q}_1+\vec{q}_2)-(q_1^2+q_2^2)}{2} \tag{H.40}$$

$$= \frac{q^2-(q_1^2+q_2^2)}{2} \tag{H.41}$$

by using the definitions Eqs. (8.17) and (H.6). Using this expression we can simply rewrite $\hat{\rho}_{\text{ex}}$ into the form

$$\hat{\rho}_{\text{ex}}(\vec{q}_1,\vec{q}_2) = \frac{4}{3}\left[-7+2a^2(\vec{q}_1\cdot\vec{q}_2)+\frac{2}{3}a^2(q_1^2+q_2^2)-\frac{1}{3}a^4(\vec{q}_1\cdot\vec{q}_2)^2\right] e^{-\frac{a^2}{4}(q_1^2+q_2^2)} \tag{H.42}$$

$$= \frac{4}{3}\left[\left(-7+a^2q^2-\frac{a^4q^4}{12}\right)+\frac{a^2}{3}\left(-1+\frac{a^2q^2}{2}\right)(q_1^2+q_2^2)-\frac{a^4}{12}(q_1^2+q_2^2)^2\right] e^{-\frac{a^2}{4}(q_1^2+q_2^2)} \tag{H.43}$$

$$= \left[A+B(q_1^2+q_2^2)+C(q_1^2+q_2^2)^2\right] e^{-\frac{a^2}{4}(q_1^2+q_2^2)} \tag{H.44}$$

where A, B and C are only dependent on $\vec{k}_\pi$ and $\vec{k}'_\pi$ but not on $\vec{k}''_\pi$, such that they can be considered constant inside of the integral. The integral can then be written as

$$V^{\text{2nd}}_{\text{opt},ss,\text{ex}}(\vec{k}'_\pi,\vec{k}_\pi) \propto (b_0^2+2b_1^2)\int \frac{d\vec{k}''_\pi}{(2\pi)^3} \frac{\left[A+B(q_1^2+q_2^2)+C(q_1^2+q_2^2)^2\right] e^{-\frac{a^2}{4}(q_1^2+q_2^2)}}{k_{\pi,0}^2-k''^2_\pi+i\varepsilon} \tag{H.45}$$

Let me define the integral

$$I_0 = \int \frac{d\vec{k}''}{(2\pi)^3} \frac{e^{-\frac{a^2}{4}(q_1^2+q_2^2)}}{k_0^2-k''^2+i\varepsilon} \tag{H.46}$$

such that I can rewrite $V^{\text{2nd}}_{\text{opt},ss,\text{ex}}$ by simply deriving with respect to a^2 and we have

$$V^{\text{2nd}}_{\text{opt},ss,\text{ex}}(\vec{k}'_\pi,\vec{k}_\pi) \propto (b_0^2+2b_1^2)\left[AI_0-4B\frac{dI_0}{d(a^2)}+16C\frac{d^2I_0}{d(a^2)^2}\right] \tag{H.47}$$

The analytical expressions of I_0 and its derivatives are given in App. I.1.

For the *sp* and *pp* terms, the two scalar products $\tilde{\vec{k}}'\cdot\tilde{\vec{k}}''$ and $\tilde{\vec{k}}''\cdot\tilde{\vec{k}}$ in Eqs. (H.33) and (H.34) need to be converted to the πA frame. This can be done according to Eq. (7.87). In order to simplify the problem, I will consider only the dominant term and simply drop the tilde.

Similarly to the *ss* term, the exchange part of the *sp* term can then simply be rewritten as

$$V^{\text{2nd}}_{\text{opt},sp,\text{ex}}(\vec{k}'_\pi,\vec{k}_\pi) \propto (b_0c_0+2b_1c_1) \times \int \frac{d\vec{k}''_\pi}{(2\pi)^3} (\vec{k}'_\pi\cdot\vec{k}''_\pi+\vec{k}''_\pi\cdot\vec{k}_\pi) \frac{\left[A+B(q_1^2+q_2^2)+C(q_1^2+q_2^2)^2\right] e^{-\frac{a^2}{4}(q_1^2+q_2^2)}}{k_{\pi,0}^2-k''^2_\pi+i\varepsilon} \tag{H.48}$$

where I have used the same constants A, B and C as in Eq. (H.44). Similarly to $V^{\text{2nd}}_{\text{opt},ss,\text{ex}}$, this integral can be written as the sum of terms

$$V^{\text{2nd}}_{\text{opt},sp,\text{ex}}(\vec{k}'_\pi,\vec{k}_\pi) \propto (b_0c_0+2b_1c_1)\left[AI_1 - 4B\frac{dI_1}{d(a^2)} + 16C\frac{d^2I_1}{d(a^2)^2}\right] \tag{H.49}$$

where I_1 is defined as the integral

$$I_1 = \int \frac{d\vec{k}''}{(2\pi)^3}\,(\vec{k}'\cdot\vec{k}''+\vec{k}''\cdot\vec{k})\frac{e^{-\frac{a^2}{4}(q_1^2+q_2^2)}}{k_0^2-k''^2+i\varepsilon} \tag{H.50}$$

The analytical expressions of I_1 and its derivatives are given in App. I.2.

Finally, the exchange part of the pp term can be rewritten as

$$\begin{aligned} V^{\text{2nd}}_{\text{opt},pp,\text{ex}}(\vec{k}'_\pi,\vec{k}_\pi) \propto& (c_0^2+2c_1^2) \\ &\times\int \frac{d\vec{k}''_\pi}{(2\pi)^3}\,(\vec{k}'_\pi\cdot\vec{k}''_\pi)(\vec{k}''_\pi\cdot\vec{k}_\pi)\frac{[A+B(q_1^2+q_2^2)+C(q_1^2+q_2^2)^2]\,e^{-\frac{a^2}{4}(q_1^2+q_2^2)}}{k_{\pi,0}^2-k''^2_\pi+i\varepsilon} \end{aligned} \tag{H.51}$$

using the same constants A, B and C again. Similarly to the two previous terms, this integral can be written as the sum of terms

$$V^{\text{2nd}}_{\text{opt},pp,\text{ex}}(\vec{k}',\vec{k}) \propto (c_0^2+2c_1^2)\left[AI_2 - 4B\frac{dI_2}{d(a^2)} + 16C\frac{d^2I_2}{d(a^2)^2}\right] \tag{H.52}$$

where I_2 is defined as the integral

$$I_2 = \int \frac{d\vec{k}''}{(2\pi)^3}\,(\vec{k}'\cdot\vec{k}'')(\vec{k}''\cdot\vec{k})\frac{e^{-\frac{a^2}{4}(q_1^2+q_2^2)}}{k_0^2-k''^2+i\varepsilon} \tag{H.53}$$

The analytical expressions of I_2 and its derivatives are given in App. I.3.

The second term in Eqs. (H.32)—(H.34) is even more cumbersome. First, from Eq. (6.24), we can rewrite the product of the Fourier transforms of the densities inside the integral as

$$\hat{\rho}_1(\vec{q}_1)\hat{\rho}_1(\vec{q}_2) = \left(144 - 16a^2(q_1^2+q_2^2) + \frac{16}{9}a^4q_1^2q_2^2\right)e^{-\frac{1}{4}a^2(q_1^2+q_2^2)} \tag{H.54}$$

$$= \left(D + E(q_1^2+q_2^2) + Fq_1^2q_2^2\right)e^{-\frac{1}{4}a^2(q_1^2+q_2^2)} \tag{H.55}$$

The first two terms are similar to the first two terms of the exchange part of the two-body density Eq. (H.44). As such, their treatment is identical. For the last term however, a different approach is needed.

First, let me rewrite this last term as

$$Fq_1^2q_2^2e^{-\frac{1}{4}(a_1^2q_1^2+a_2^2q_2^2)} \tag{H.56}$$

where I have added artificially an index 1 and 2 to the harmonic oscillator parameter a. It should be noted that this can be cast into the form

$$Fq_1^2q_2^2e^{-\frac{1}{4}(a_1^2q_1^2+a_2^2q_2^2)} = 16F\frac{d^2}{d(a_1^2)d(a_2^2)}\left(e^{-\frac{1}{4}(a_1^2q_1^2+a_2^2q_2^2)}\right) \tag{H.57}$$

such that the last term of Eq. (H.55) is

$$Fq_1^2q_2^2e^{-\frac{1}{4}(a^2(q_1^2+q_2^2)} = 16F \lim_{\substack{a_1\to a\\ a_2\to a}} \frac{d^2}{d(a_1^2)d(a_2^2)} \left(e^{-\frac{1}{4}(a_1^2q_1^2+a_2^2q_2^2)}\right) \tag{H.58}$$

This form can be injected in the integrals Eqs. (H.32)—(H.34) and is tractable but will lead to mathematical expressions that are very cumbersome. These are left to future works (see also the thesis of V. Tsaran, in which similar developments have been performed).

I Some mathematical developments for the second order of the interaction

I.1 The integral I_0

In this appendix I will solve the integral Eq. (H.46)

$$I_0 = \int \frac{d\vec{k}''}{(2\pi)^3} \frac{e^{-\frac{a^2}{4}(q_1^2+q_2^2)}}{k_0^2 - k''^2 + i\varepsilon} \tag{I.1}$$

By recalling Eqs. (H.6), let me first rewrite $q_1^2 + q_2^2$ in the exponent in the form

$$\begin{aligned}
q_1^2 + q_2^2 &= (\vec{k}' - \vec{k}'')^2 + (\vec{k}'' - \vec{k})^2 && \text{(I.2)}\\
&= 2k''^2 - 2(\vec{k}' + \vec{k}) \cdot \vec{k}'' + k'^2 + k^2 && \text{(I.3)}\\
&= 2\left[k''^2 - 2\vec{P} \cdot \vec{k}'' + \frac{k'^2 + k^2}{2}\right] && \text{(I.4)}\\
&= 2\left[(\vec{k}'' - \vec{P})^2 - P^2 + \frac{k'^2 + k^2}{2}\right] && \text{(I.5)}\\
&= 2\left[(\vec{k}'' - \vec{P})^2 + \frac{(\vec{k}' - \vec{k})^2}{4}\right] && \text{(I.6)}\\
&= 2\left[(\vec{k}'' - \vec{P})^2 + \frac{q^2}{4}\right] && \text{(I.7)}
\end{aligned}$$

where in third line I have defined

$$\vec{P} = \frac{\vec{k}' + \vec{k}}{2} \tag{I.8}$$

The integral then reads

$$I_0 = \frac{e^{-\frac{a^2}{8}q^2}}{(2\pi)^3} \int d\vec{k}'' \frac{e^{-\frac{a^2}{2}(\vec{k}'' - \vec{P})^2}}{k_0^2 - k''^2 + i\varepsilon} \tag{I.9}$$

Note that for conciseness, I will rename $k'' \to k$ and define $\tilde{I}_0 = (2\pi)^3 e^{a^2q^2/8} I_0$. I then have

$$\begin{aligned}
\tilde{I}_0 &= \int d\vec{k} \frac{e^{-\frac{a^2}{2}(\vec{k} - \vec{P})^2}}{k_0^2 - k^2 + i\varepsilon} && \text{(I.10)}\\
&= \int_0^{2\pi} d\phi \int_{-1}^{1} d\cos\theta \int_0^{\infty} \frac{k^2 dk}{k_0^2 - k^2 + i\varepsilon} e^{-\frac{a^2}{2}k^2} e^{-\frac{a^2}{2}P^2} e^{a^2 kP\cos\theta} && \text{(I.11)}\\
&= \frac{1}{a^2 P} 2\pi \int_0^{\infty} \frac{kdk}{k_0^2 - k^2 + i\varepsilon} e^{-\frac{a^2}{2}k^2} e^{-\frac{a^2}{2}P^2} \left(e^{a^2kP} - e^{-a^2kP}\right) && \text{(I.12)}\\
&= \frac{1}{a^2 P} \hat{I}_0 && \text{(I.13)}
\end{aligned}$$

Let me pose $x = k_0^2 - k^2$ such that $-dx/2 = kdk$. We then have

$$\hat{I}_0 = \pi \int_{-\infty}^{k_0^2} \frac{dx}{x + i\varepsilon} \underbrace{e^{-\frac{a^2}{2}(k_0^2 - x)} e^{-\frac{a^2}{2}P^2} \left(e^{a^2\sqrt{k_0^2 - x}P} - e^{-a^2\sqrt{k_0^2 - x}P}\right)}_{f(x)} \tag{I.14}$$

We can use the Sokhotski–Plemelj theorem on the real line

$$\lim_{\varepsilon\to 0^+}\int_{a<0}^{b>0}\frac{f(x)\,dx}{x+i\varepsilon}=-i\pi f(x=0)+\mathcal{P}\left(\int_{a<0}^{b>0}\frac{f(x)\,dx}{x}\right) \tag{I.15}$$

where $\mathcal{P}$ denotes the principal value integral, to rewrite $\tilde{I}_0$ in the form

$$\hat{I}_0=-i\pi^2 e^{-\frac{a^2}{2}k_0^2}e^{-\frac{a^2}{2}P^2}\left(e^{a^2k_0P}-e^{-a^2k_0P}\right)+2\pi\mathcal{P}\left(\int_0^\infty\frac{kdk}{k_0^2-k^2}e^{-\frac{a^2}{2}k^2}e^{-\frac{a^2}{2}P^2}\left(e^{a^2kP}-e^{-a^2kP}\right)\right) \tag{I.16}$$

$$=-i\pi^2\left(e^{-\frac{a^2}{2}(k_0-P)^2}-e^{-\frac{a^2}{2}(k_0+P)^2}\right)+2\pi\mathcal{P}\left(\int_0^\infty\frac{kdk}{k_0^2-k^2}\left(e^{-\frac{a^2}{2}(k-P)^2}-e^{-\frac{a^2}{2}(k+P)^2}\right)\right) \tag{I.17}$$

The principal value term can be separated into two terms, such that there are two principal value integrals $\hat{I}_{0-}$ and $\hat{I}_{0+}$ such that

$$\hat{I}_0=-i\pi^2\left(e^{-\frac{a^2}{2}(k_0-P)^2}-e^{-\frac{a^2}{2}(k_0+P)^2}\right)+2\pi(\hat{I}_{0-}+\hat{I}_{0+}) \tag{I.18}$$

where

$$\hat{I}_{0\pm}=\mp\mathcal{P}\left(\int_0^\infty\frac{kdk}{k_0^2-k^2}e^{-\frac{a^2}{2}(k\pm P)^2}\right) \tag{I.19}$$

Note that by taking $k\to -k$ in $\hat{I}_{0+}$, we have

$$\hat{I}_{0+}=\mathcal{P}\left(\int_{-\infty}^0\frac{kdk}{k_0^2-k^2}e^{-\frac{a^2}{2}(k-P)^2}\right) \tag{I.20}$$

and we have

$$\hat{I}_{0-}+\hat{I}_{0+}=\mathcal{P}\left(\int_{-\infty}^\infty\frac{kdk}{k_0^2-k^2}e^{-\frac{a^2}{2}(k-P)^2}\right) \tag{I.21}$$

By using

$$\frac{k}{k_0^2-k^2}=\frac{1}{2}\left(\frac{1}{k_0-k}-\frac{1}{k_0+k}\right) \tag{I.22}$$

we can separate the principal value into

$$\hat{I}_{0-}+\hat{I}_{0+}=\frac{1}{2}\mathcal{P}\left(\int_{-\infty}^\infty\frac{dk}{k_0-k}e^{-\frac{a^2}{2}(k-P)^2}\right)-\frac{1}{2}\mathcal{P}\left(\int_{-\infty}^\infty\frac{dk}{k_0+k}e^{-\frac{a^2}{2}(k-P)^2}\right) \tag{I.23}$$

If we pose $k'=a(k-P)/\sqrt{2}$, we have

$$\hat{I}_{0-}+\hat{I}_{0+}=\frac{1}{2}\mathcal{P}\left(\int_{-\infty}^\infty\frac{dk'}{\frac{a}{\sqrt{2}}(k_0-P)-k'}e^{-k'^2}\right)-\frac{1}{2}\mathcal{P}\left(\int_{-\infty}^\infty\frac{dk}{\frac{a}{\sqrt{2}}(k_0+P)+k'}e^{-k'^2}\right) \tag{I.24}$$

$$=\frac{1}{2}\mathcal{P}\left(\int_{-\infty}^\infty dk'\frac{e^{-k'^2}}{z_1-k'}\right)+\frac{1}{2}\mathcal{P}\left(\int_{-\infty}^\infty dk'\frac{e^{-k'^2}}{z_2-k'}\right) \tag{I.25}$$

where I have defined

$$\begin{cases}z_1=\dfrac{a}{\sqrt{2}}(k_0-P)\\ z_2=-\dfrac{a}{\sqrt{2}}(k_0+P)\end{cases} \tag{I.26}$$

Note that from App. J, we have that

$$\hat{I}_{0-} + \hat{I}_{0+} = \sqrt{\pi}(F(z_1) + F(z_2)) \tag{I.27}$$

such that

$$\hat{I}_0 = (2\pi)^{3/2}\left[-i\frac{1}{2}\sqrt{\frac{\pi}{2}}\left(e^{-z_1^2} - e^{-z_2^2}\right) + \frac{\sqrt{2}}{2}(F(z_1) + F(z_2))\right] \tag{I.28}$$

If we put all these results together, we finally have for I_0

$$I_0 = \frac{e^{-\frac{a^2}{8}q^2}}{(2\pi)^{3/2}}\frac{1}{a^2 P}\left[-i\frac{1}{2}\sqrt{\frac{\pi}{2}}\left(e^{-z_1^2} - e^{-z_2^2}\right) + \frac{\sqrt{2}}{2}F\left(z_1\right) + \frac{\sqrt{2}}{2}F\left(z_2\right)\right] \tag{I.29}$$

Let me define $I_{0,0}$ such that

$$I_0 = \underbrace{\frac{e^{-\frac{a^2}{8}q^2}}{(2\pi)^{3/2}}\frac{1}{a^2 P}}_{I_{0,0}}\underbrace{\left[-i\frac{1}{2}\sqrt{\frac{\pi}{2}}\left(e^{-z_1^2} - e^{-z_2^2}\right) + \frac{\sqrt{2}}{2}F\left(z_1\right) + \frac{\sqrt{2}}{2}F\left(z_2\right)\right]}_{I_{0,1}} \tag{I.30}$$

The first order derivative of I_0 reads

$$\frac{dI_0}{d(a^2)} = -\frac{8 + a^2q^2}{8a^2}I_0 + I_{0,0}\underbrace{\left(-\frac{P}{2a} + \frac{z_1^2}{a^2}\left[i\frac{1}{2}\sqrt{\frac{\pi}{2}}e^{-z_1^2} - \frac{\sqrt{2}}{2}F(z_1)\right] - \frac{z_2^2}{a^2}\left[i\frac{1}{2}\sqrt{\frac{\pi}{2}}e^{-z_2^2} + \frac{\sqrt{2}}{2}F(z_2)\right]\right)}_{I'_{0,1}} \tag{I.31}$$

and the second order derivative reads

$$\frac{d^2I_0}{d(a^2)^2} = \frac{I_0}{a^4} - \frac{8 + a^2q^2}{8a^2}\frac{dI_0}{d(a^2)} - \frac{8 + a^2q^2}{8a^2}I_{0,0}I'_{0,1} + I_{0,0}I''_{0,1} \tag{I.32}$$

where

$$I''_{0,1} = \frac{P}{2a^3} + \frac{z_1^4}{a^4}\left[i\frac{1}{2}\sqrt{\frac{\pi}{2}}e^{-z_1^2} + \frac{\sqrt{2}}{2}F(z_1)\right] + \frac{z_2^4}{a^4}\left[i\frac{1}{2}\sqrt{\frac{\pi}{2}}e^{-z_2^2} + \frac{\sqrt{2}}{2}F(z_2)\right] - \frac{\sqrt{2}}{4a}\left[\frac{z_1^3}{a^3} + \frac{z_2^3}{a^3}\right] \tag{I.33}$$

I.2 The integral I_1

In this appendix I will solve the integral Eq. (H.50)

$$I_1 = \int \frac{d\vec{k}''}{(2\pi)^3}\,(\vec{k}' \cdot \vec{k}'' + \vec{k}'' \cdot \vec{k})\frac{e^{-\frac{a^2}{4}(q_1^2+q_2^2)}}{k_0^2 - k''^2 + i\varepsilon} \tag{I.34}$$

As I have done in Sec. I.1, I can use the definition Eq. (I.8) to write

$$I_1 = \frac{e^{-\frac{a^2}{8}q^2}}{(2\pi)^3}\int d\vec{k}''\,(2\vec{k}'' \cdot \vec{P})\frac{e^{-\frac{a^2}{2}(\vec{k}''-\vec{P})^2}}{k_0^2 - k''^2 + i\varepsilon} \tag{I.35}$$

If I rename $k'' \to k$ and define $\tilde{I}_1 = (2\pi)^3 e^{a^2q^2/8} I_1$ we have

$$\tilde{I}_1 = \int d\vec{k}\ (2\vec{k}\cdot\vec{P}) \frac{e^{-\frac{a^2}{2}(\vec{k}-\vec{P})^2}}{k_0^2 - k^2 + i\varepsilon} \tag{I.36}$$

$$= \int_0^{2\pi} d\phi \int_{-1}^{1} d\cos\theta \int_0^\infty \frac{k^2 dk}{k_0^2 - k^2 + i\varepsilon}\ 2kP\cos\theta\, e^{-\frac{a^2}{2}k^2} e^{-\frac{a^2}{2}P^2} e^{a^2 kP\cos\theta} \tag{I.37}$$

$$= 2\pi \int_0^\infty \frac{k^2 dk}{k_0^2 - k^2 + i\varepsilon}\ 2kP\, e^{-\frac{a^2}{2}k^2} e^{-\frac{a^2}{2}P^2} \frac{1}{a^4 k^2 P^2} \left[a^2 kP\left(e^{a^2kP} + e^{-a^2kP}\right) - \left(e^{a^2kP} - e^{-a^2kP}\right)\right] \tag{I.38}$$

which I will separate in two integrals

$$\tilde{I}_1 = 2\pi \frac{2}{a^2} \int_0^\infty \frac{k^2 dk}{k_0^2 - k^2 + i\varepsilon}\ e^{-\frac{a^2}{2}k^2} e^{-\frac{a^2}{2}P^2} \left(e^{a^2kP} + e^{-a^2kP}\right) \tag{I.39}$$

$$- 2\pi \frac{2}{a^4 P} \int_0^\infty \frac{k dk}{k_0^2 - k^2 + i\varepsilon}\ e^{-\frac{a^2}{2}k^2} e^{-\frac{a^2}{2}P^2} \left(e^{a^2kP} - e^{-a^2kP}\right) \tag{I.40}$$

where we recognize the second term as a multiple of $\hat{I}_0$. I can define $\hat{I}_1$ such that

$$\tilde{I}_1 = \frac{2}{a^2} 2\pi \int_0^\infty \frac{k^2 dk}{k_0^2 - k^2 + i\varepsilon}\ \left[e^{-\frac{a^2}{2}(k-P)^2} + e^{-\frac{a^2}{2}(k+P)^2}\right] - \frac{2}{a^4 P}\hat{I}_0 \tag{I.41}$$

$$= \frac{2}{a^2}\hat{I}_1 - \frac{2}{a^4 P}\hat{I}_0 \tag{I.42}$$

Let me pose again $x = k_0^2 - k^2$ such that $-k\ dx/2 = k^2 dk$

$$\hat{I}_1 = \pi \int_{-\infty}^{k_0^2} \frac{dx}{x + i\varepsilon} \underbrace{\left[\sqrt{k_0^2 - x}\left(e^{-\frac{a^2}{2}(\sqrt{k_0^2-x}-P)^2} + e^{-\frac{a^2}{2}(\sqrt{k_0^2-x}+P)^2}\right)\right]}_{g(x)} \tag{I.43}$$

use the Sokhotski–Plemelj theorem on the real line to rewrite $\hat{I}_1$ in the form

$$\hat{I}_1 = -i\pi^2 k_0 \left(e^{-\frac{a^2}{2}(k_0-P)^2} + e^{-\frac{a^2}{2}(k_0+P)^2}\right) + 2\pi\mathcal{P}\left(\int_0^\infty \frac{k^2 dk}{k_0^2 - k^2}\ \left[e^{-\frac{a^2}{2}(k-P)^2} + e^{-\frac{a^2}{2}(k+P)^2}\right]\right) \tag{I.44}$$

$$= -i\pi^2 k_0 \left(e^{-\frac{a^2}{2}(k_0-P)^2} + e^{-\frac{a^2}{2}(k_0+P)^2}\right) + 2\pi(\hat{I}_{1-} + \hat{I}_{1+}) \tag{I.45}$$

where

$$\hat{I}_{1\pm} = \mathcal{P}\left(\int_0^\infty \frac{k^2 dk}{k_0^2 - k^2}\ e^{-\frac{a^2}{2}(k\pm P)^2}\right) \tag{I.46}$$

Note again that for $k \to -k$, $\hat{I}_{1+}$ becomes

$$\hat{I}_{1+} = \mathcal{P}\left(\int_{-\infty}^0 \frac{k^2 dk}{k_0^2 - k^2}\ e^{-\frac{a^2}{2}(k-P)^2}\right) \tag{I.47}$$

so that

$$\hat{I}_{1-} + \hat{I}_{1+} = \mathcal{P}\left(\int_{-\infty}^\infty \frac{k^2 dk}{k_0^2 - k^2}\ e^{-\frac{a^2}{2}(k-P)^2}\right) \tag{I.48}$$

and that by using

$$\frac{k^2}{k_0^2-k^2}=\frac{k}{2}\left(\frac{1}{k_0-k}-\frac{1}{k_0+k}\right) \tag{I.49}$$

I can separate the principal value into

$$\hat{I}_{1-}+\hat{I}_{1+}=\frac{1}{2}\mathcal{P}\left(\int_{-\infty}^{\infty}\frac{kdk}{k_0-k}e^{-\frac{a^2}{2}(k-P)^2}\right)-\frac{1}{2}\mathcal{P}\left(\int_{-\infty}^{\infty}\frac{kdk}{k_0+k}e^{-\frac{a^2}{2}(k-P)^2}\right) \tag{I.50}$$

which from App. J, gives

$$\hat{I}_{1-}+\hat{I}_{1+}=\frac{1}{2}\mathcal{P}\left(\int_{-\infty}^{\infty}\frac{\left(\frac{\sqrt{2}}{a}k'+P\right)dk'}{z_1-k'}e^{-k'^2}\right)+\frac{1}{2}\mathcal{P}\left(\int_{-\infty}^{\infty}\frac{\left(\frac{\sqrt{2}}{a}k'+P\right)dk'}{z_2-k'}e^{-k'^2}\right) \tag{I.51}$$

$$=\sqrt{\pi}\left(k_0(F(z_1)-F(z_2))-\frac{\sqrt{2}}{a}\right) \tag{I.52}$$

where I have used the same definitions Eq. (I.26) for z_1 and z_2. We then have for $\hat{I}_1$

$$\hat{I}_1=(2\pi)^{3/2}\left[-i\frac{1}{2}\sqrt{\frac{\pi}{2}}k_0\left(e^{-z_1^2}+e^{-z_2^2}\right)+\frac{\sqrt{2}}{2}k_0(F(z_1)-F(z_2))-\frac{1}{a}\right] \tag{I.53}$$

Finally, we have for I_1

$$I_1=\underbrace{\frac{e^{-\frac{a^2}{8}q^2}}{(2\pi)^{3/2}}\frac{2}{a^2}}_{2PI_{0,0}}\left[-i\frac{1}{2}\sqrt{\frac{\pi}{2}}k_0\left(e^{-z_1^2}+e^{-z_2^2}\right)+\frac{\sqrt{2}}{2}k_0(F(z_1)-F(z_2))-\frac{1}{a}\right]-\frac{2}{a^2}I_0 \tag{I.54}$$

The first order derivative reads

$$\frac{dI_1}{d(a^2)}=-\frac{8+a^2q^2}{8a^2}I_1-\frac{2}{a^2}I_{0,0}I'_{0,1}+\frac{2}{a^4}I_0 \tag{I.55}$$

$$+2PI_{0,0}\underbrace{\left[k_0\frac{z_1^2}{a^2}\left(i\frac{1}{2}\sqrt{\frac{\pi}{2}}e^{-z_1^2}-\frac{\sqrt{2}}{2}F(z_1)\right)-k_0\frac{z_2^2}{a^2}\left(i\frac{1}{2}\sqrt{\frac{\pi}{2}}e^{-z_2^2}-\frac{\sqrt{2}}{2}F(z_2)\right)+\frac{k_0^2}{2a}+\frac{1}{2a^3}\right]}_{I_{1,1}} \tag{I.56}$$

and the second order one

$$\frac{d^2I_1}{d(a^2)^2}=\frac{I_1}{a^4}-\frac{8+a^2q^2}{8a^2}\frac{dI_1}{d(a^2)}+\frac{2}{a^4}I_{0,0}I'_{0,1}-\frac{2}{a^2}\left[\frac{d^2I_0}{d(a^2)^2}-\frac{I_0}{a^4}+\frac{8+a^2q^2}{8a^2}\frac{dI_0}{d(a^2)}\right] \tag{I.57}$$

$$-\frac{4}{a^6}I_0+\frac{2}{a^4}\frac{dI_0}{d(a^2)}-2P\frac{8+a^2q^2}{8a^2}I_{0,0}I_{1,1} \tag{I.58}$$

$$+2PI_{0,0}\left[-k_0\frac{z_1^4}{a^4}\left(i\frac{1}{2}\sqrt{\frac{\pi}{2}}e^{-z_1^2}-\frac{\sqrt{2}}{2}F(z_1)\right)+k_0\frac{z_2^4}{a^4}\left(i\frac{1}{2}\sqrt{\frac{\pi}{2}}e^{-z_2^2}-\frac{\sqrt{2}}{2}F(z_2)\right)\right. \tag{I.59}$$

$$\left.-\frac{\sqrt{2}k_0}{4a}\left(\frac{z_1^3}{a^3}-\frac{z_2^3}{a^3}\right)-\frac{k_0^2}{4a^3}-\frac{3}{4a^5}\right] \tag{I.60}$$

I.3 The integral I_2

In this appendix I will solve the integral Eq. (H.53)

$$I_2 = \int \frac{d\vec{k}''}{(2\pi)^3} (\vec{k}' \cdot \vec{k}'')(\vec{k}'' \cdot \vec{k}) \frac{e^{-\frac{a^2}{4}(q_1^2+q_2^2)}}{k_0^2 - k''^2 + i\varepsilon} \tag{I.61}$$

As I have done in Secs. I.1 and I.2, I can use the definition Eq. (I.8) to write

$$I_2 = \frac{e^{-\frac{a^2}{8}q^2}}{(2\pi)^3} \int d\vec{k}'' (\vec{k}' \cdot \vec{k}'')(\vec{k}'' \cdot \vec{k}) \frac{e^{-\frac{a^2}{2}(\vec{k}''-\vec{P})^2}}{k_0^2 - k''^2 + i\varepsilon} \tag{I.62}$$

In order to calculate this integral, let me define the different angles that characterize $\vec{k}$, $\vec{k}'$, $\vec{k}''$ and $\vec{P}$. These angles and vectors are represented on Fig. I.1. Note that θ_P satisfies

$$\begin{cases} \cos\theta_P = \dfrac{k + \cos\theta' k'}{\sqrt{k'^2 + k^2 + 2kk'\cos\theta'}} \\ \sin\theta_P = \dfrac{\sin\theta' k'}{\sqrt{k'^2 + k^2 + 2kk'\cos\theta'}} \end{cases} \tag{I.63}$$

and that $\theta_v = \pi/2 - \theta_P$.

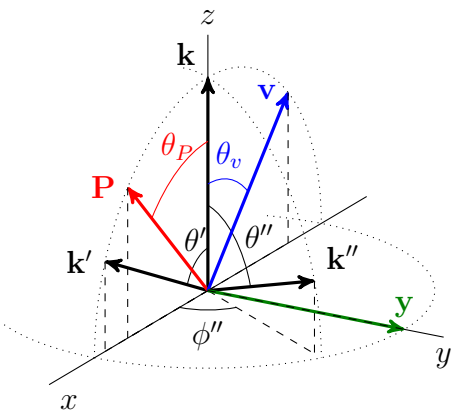

Figure I.1: Definition of angles characterising the vectors $\vec{k}$, $\vec{k}'$, $\vec{k}''$ and $\vec{P}$, $\vec{v}$ and $\vec{y}$. The vectors in bold are unit vectors.

Let me define the new system of axes $\{\mathbf{y}, \mathbf{v}, \mathbf{P}\}$. In this new system of axes, we have

$$\begin{cases} \vec{k} = k(0, \sin\theta_P, \cos\theta_P) \\ \vec{k}'' = k''(\sin\theta\cos\phi, \sin\theta\sin\phi, \cos\theta) \\ \vec{k}' = 2\vec{P} - \vec{k} = (0, -k\sin\theta_P, 2P - k\cos\theta_P) \end{cases} \tag{I.64}$$

The double product of scalar products hence reads

$$(\vec{k}' \cdot \vec{k}'')(\vec{k}'' \cdot \vec{k}) = k''^2 \Big[\quad 2(kP - k^2\sin\theta_P\cos\theta_P) \quad \sin\theta\cos\theta\sin\phi \tag{I.65}$$

$$+(2kP - k^2\cos\theta_P)\cos\theta_P \quad \cos^2\theta \tag{I.66}$$

$$-k^2\sin^2\theta_P \quad \sin^2\phi\sin^2\theta\Big] \tag{I.67}$$

The integral $\tilde{I}_2 = (2\pi)^3 e^{\frac{a^2}{8}q^2} I_2$ then reads

$$\tilde{I}_2 = \underbrace{2(kP - k^2 \sin\theta_P \cos\theta_P)}_{f} \int_0^{2\pi} d\phi \sin\phi \int_{-1}^{1} \sin\theta\cos\theta \; d\cos\theta \int_0^{\infty} \frac{k''^4 dk''}{k_0^2 - k''^2 + i\varepsilon} \; e^{-\frac{a^2}{2}(\vec{k}''-\vec{P})^2} \tag{I.68}$$

$$+ \underbrace{(2kP - k^2\cos\theta_P)\cos\theta_P}_{g} \int_0^{2\pi} d\phi \int_{-1}^{1} \cos^2\theta \; d\cos\theta \int_0^{\infty} \frac{k''^4 dk''}{k_0^2 - k''^2 + i\varepsilon} \; e^{-\frac{a^2}{2}(\vec{k}''-\vec{P})^2} \tag{I.69}$$

$$\underbrace{-k^2 \sin^2\theta_P}_{h} \int_0^{2\pi} d\phi \sin^2\phi \int_{-1}^{1} \sin^2\theta \; d\cos\theta \int_0^{\infty} \frac{k''^4 dk''}{k_0^2 - k''^2 + i\varepsilon} e^{-\frac{a^2}{2}(\vec{k}''-\vec{P})^2} \tag{I.70}$$

Note that the integral on ϕ gives zero on the first line. For the other lines, we have, by renaming $k'' \to k$,

$$\tilde{I}_2 = 2\pi g \int_{-1}^{1} \cos^2\theta d\cos\theta \int_0^{\infty} \frac{k^4 dk}{k_0^2 - k^2 + i\varepsilon} \; e^{-\frac{a^2}{2}(\vec{k}''-\vec{P})^2} \tag{I.71}$$

$$+ \pi h \int_{-1}^{1} \sin^2\theta d\cos\theta \int_0^{\infty} \frac{k^4 dk}{k_0^2 - k^2 + i\varepsilon} e^{-\frac{a^2}{2}(\vec{k}''-\vec{P})^2} \tag{I.72}$$

which, if we replace $\sin^2\theta = 1 - \cos^2\theta$, can be rewritten as

$$\tilde{I}_2 = (2\pi g - \pi h) \int_{-1}^{1} \cos^2\theta d\cos\theta \int_0^{\infty} \frac{k^4 dk}{k_0^2 - k^2 + i\varepsilon} \; e^{-\frac{a^2k^2}{2}} e^{-\frac{a^2P^2}{2}} e^{a^2kP\cos\theta} \tag{I.73}$$

$$+ \pi h \int_{-1}^{1} d\cos\theta \int_0^{\infty} \frac{k^4 dk}{k_0^2 - k^2 + i\varepsilon} \; e^{-\frac{a^2k^2}{2}} e^{-\frac{a^2P^2}{2}} e^{a^2kP\cos\theta} \tag{I.74}$$

which after integration on θ gives

$$\tilde{I}_2 = (2\pi g - \pi h) \int_0^{\infty} \frac{k^4 dk}{k_0^2 - k^2 + i\varepsilon} \; e^{-\frac{a^2k^2}{2}} e^{-\frac{a^2P^2}{2}} \left[\frac{e^{a^2kP} - e^{-a^2kP}}{a^2kP} + 2\frac{e^{a^2kP} - e^{-a^2kP}}{a^6k^3P^3} - 2\frac{e^{a^2kP} + e^{-a^2kP}}{a^4k^2P^2} \right] \tag{I.75}$$

$$+ \pi h \int_0^{\infty} \frac{k^4 dk}{k_0^2 - k^2 + i\varepsilon} \; e^{-\frac{a^2k^2}{2}} e^{-\frac{a^2P^2}{2}} \left[\frac{e^{a^2kP} - e^{-a^2kP}}{a^2kP} \right] \tag{I.76}$$

In this expression we recognize $\hat{I}_0$ and $\hat{I}_1$ such that I can write

$$\tilde{I}_2 = \frac{2g - h}{a^4P^2} \left(\frac{1}{a^2P} \hat{I}_0 - \hat{I}_1 \right) + \frac{g}{a^2P} \hat{I}_2 \tag{I.77}$$

$$= -\frac{2g - h}{a^4P^2} \frac{a^2}{2} \tilde{I}_1 + \frac{g}{a^2P} \hat{I}_2 \tag{I.78}$$

where I have defined

$$\hat{I}_2 = 2\pi \int_0^{\infty} \frac{k^3 dk}{k_0^2 - k^2 + i\varepsilon} \; e^{-\frac{a^2k^2}{2}} e^{-\frac{a^2P^2}{2}} \left[e^{a^2kP} - e^{-a^2kP} \right] \tag{I.79}$$

which reads

$$\hat{I}_2 = -i\pi^2 k_0^2 \left[e^{-\frac{a^2}{2}(k_0-P)^2} - e^{-\frac{a^2}{2}(k_0+P)^2} \right] + 2\pi \mathcal{P} \left(\int_0^{\infty} \frac{k^3 dk}{k_0^2 - k^2} \; \left[e^{-\frac{a^2}{2}(k-P)^2} - e^{-\frac{a^2}{2}(k+P)^2} \right] \right) \tag{I.80}$$

$$= -i\pi^2 k_0^2 \left[e^{-\frac{a^2}{2}(k_0-P)^2} - e^{-\frac{a^2}{2}(k_0+P)^2} \right] + 2\pi(\hat{I}_{2-} + \hat{I}_{2+}) \tag{I.81}$$

where again

$$\hat{I}_{2\pm} = \mp\mathcal{P}\left(\int_0^\infty \frac{k^3 dk}{k_0^2 - k^2}\, e^{-\frac{a^2}{2}(k\pm P)^2}\right) \tag{I.82}$$

For $k \to -k$, $\hat{I}_{2+}$ becomes

$$\hat{I}_{2+} = \mathcal{P}\left(\int_{-\infty}^0 \frac{k^3 dk}{k_0^2 - k^2}\, e^{-\frac{a^2}{2}(k-P)^2}\right) \tag{I.83}$$

so that

$$\hat{I}_{2-} + \hat{I}_{2+} = \mathcal{P}\left(\int_{-\infty}^\infty \frac{k^3 dk}{k_0^2 - k^2}\, e^{-\frac{a^2}{2}(k-P)^2}\right) \tag{I.84}$$

and that by using

$$\frac{k^3}{k_0^2 - k^2} = \frac{k^2}{2}\left(\frac{1}{k_0 - k} - \frac{1}{k_0 + k}\right) \tag{I.85}$$

I can separate the principal value into

$$\hat{I}_{2-} + \hat{I}_{2+} = \frac{1}{2}\mathcal{P}\left(\int_{-\infty}^\infty \frac{k^2 dk}{k_0 - k} e^{-\frac{a^2}{2}(k-P)^2}\right) - \frac{1}{2}\mathcal{P}\left(\int_{-\infty}^\infty \frac{k^2 dk}{k_0 + k} e^{-\frac{a^2}{2}(k-P)^2}\right) \tag{I.86}$$

which from App. J, gives

$$\hat{I}_{2-} + \hat{I}_{2+} = \frac{1}{2}\mathcal{P}\left(\int_{-\infty}^\infty \frac{\left(\frac{2}{a^2}k'^2 + \frac{2\sqrt{2}}{a}Pk' + P^2\right)dk'}{z_1 - k'} e^{-k'^2}\right) + \frac{1}{2}\mathcal{P}\left(\int_{-\infty}^\infty \frac{\left(\frac{2}{a^2}k'^2 + \frac{2\sqrt{2}}{a}Pk' + P^2\right)dk'}{z_2 - k'} e^{-k'^2}\right) \tag{I.87}$$

$$= \sqrt{\pi}\left[k_0^2(F(z_1) + F(z_2)) - \frac{\sqrt{2}P}{a}\right] \tag{I.88}$$

where I have used the same definitions Eq. (I.26) for z_1 and z_2. We then have for $\hat{I}_2$

$$\hat{I}_2 = (2\pi)^{3/2}\left[-i\frac{1}{2}\sqrt{\frac{\pi}{2}}k_0^2\left(e^{-z_1^2} - e^{-z_2^2}\right) + \frac{\sqrt{2}}{2}k_0^2(F(z_1) + F(z_2)) - \frac{P}{a}\right] \tag{I.89}$$

Finally, we have for I_2

$$I_2 = \frac{e^{-\frac{a^2}{8}q^2}}{(2\pi)^{3/2}}\frac{g}{a^2 P}\left[k_0^2\left(-i\frac{1}{2}\sqrt{\frac{\pi}{2}}\left(e^{-z_1^2} - e^{-z_2^2}\right) + \frac{\sqrt{2}}{2}(F(z_1) + F(z_2))\right) - \frac{P}{a}\right] - \frac{2g-h}{2a^2P^2}I_1 \tag{I.90}$$

$$= gk_0^2 I_0 - \frac{gP}{a}I_{0,0} - \frac{2g-h}{2a^2P^2}I_1 \tag{I.91}$$

where g and h are defined in Eqs. (I.69) and (I.70). The first order derivative

$$\frac{dI_2}{d(a^2)} = gk_0^2\frac{dI_0}{d(a^2)} + \frac{gP}{2a^3}I_{0,0} + \frac{8 + a^2q^2}{8a^2}\frac{gP}{a}I_{0,0} + \frac{2g-h}{2a^2P^2}\left[\frac{1}{a^2}I_1 - \frac{dI_1}{d(a^2)}\right] \tag{I.92}$$

and second order reads

$$\frac{d^2I_2}{d(a^2)^2} = gk_0^2\frac{d^2I_0}{d(a^2)^2} - \frac{gP}{a}I_{0,0}\left[\frac{7}{4a^4} + \frac{8 + a^2q^2}{8a^2} + \left(\frac{8 + a^2q^2}{8a^2}\right)^2\right] - \frac{2g-h}{2a^2P^2}\left[\frac{2}{a^4}I_1 - \frac{2}{a^2}\frac{dI_1}{d(a^2)} + \frac{d^2I_1}{d(a^2)^2}\right] \tag{I.93}$$

J The Hilbert Transform and the Dawson integral

The Hilbert transform of a function $f(x)$ is defined as [209]

$$H(f(x))(t) = \frac{1}{\pi}\mathcal{P}\left(\int_{-\infty}^{\infty}\frac{f(x)}{t-x}dx\right) \tag{J.1}$$

In the particular case where $f(x) = \exp(-x^2)$, we have

$$H(e^{-x^2})(t) = \frac{1}{\pi}\mathcal{P}\left(\int_{-\infty}^{\infty}\frac{e^{-x^2}}{t-x}dx\right) \tag{J.2}$$

$$= \frac{2}{\sqrt{\pi}}F(t) \tag{J.3}$$

where $F(t)$ is the Dawson integral [203, 209], defined as

$$F(t) = e^{-t^2}\int_0^t e^{y^2}dy \tag{J.4}$$

and which has the properties

$$F(-t) = -F(t) \tag{J.5}$$

$$\frac{dF(t)}{dt} = 1 - 2tF(t) \tag{J.6}$$

Note that the Hilbert transform of $xf(x)$ is then

$$H(xf(x))(t) = \frac{1}{\pi}\mathcal{P}\left(\int_{-\infty}^{\infty}\frac{xf(x)}{t-x}dx\right) \tag{J.7}$$

$$= \frac{1}{\pi}\mathcal{P}\left(\int_{-\infty}^{\infty}\frac{(t-s)f(t-s)}{s}ds\right) \tag{J.8}$$

$$= \frac{1}{\pi}\mathcal{P}\left(\int_{-\infty}^{\infty}\frac{tf(t-s)}{s}ds\right) - \frac{1}{\pi}\int_{-\infty}^{\infty}f(t-s)ds \tag{J.9}$$

$$= tH(f(x))(t) - \frac{1}{\pi}\int_{-\infty}^{\infty}f(x)dx \tag{J.10}$$

We can generalise these results for the Hilbert transform of any function $x^n f(x)$

$$H(x^n f(x))(t) = t^n H(f(x))(t) - \frac{1}{\pi}\sum_{i=1}^{n}t^{n-i}\int_{-\infty}^{\infty}x^{i-1}f(x)dx \tag{J.11}$$

In the case of $f(x) = \exp(-x^2)$, we thus have

$$H(xe^{-x^2})(t) = \frac{1}{\sqrt{\pi}}\left[2tF(t) - 1\right] \tag{J.12}$$

$$H(x^2e^{-x^2})(t) = \frac{t}{\sqrt{\pi}}\left[2tF(t) - 1\right] \tag{J.13}$$

Bibliography

[1] C. F. v. Weizsäcker. Zur theorie der kernmassen. *Zeitschrift für Physik*, 96:431, 1935. https://doi.org/10.1007/BF01337700.

[2] N. Bohr and J. A. Wheeler. The mechanism of nuclear fission. *Phys. Rev.*, 56:426–450, 1939. https://link.aps.org/doi/10.1103/PhysRev.56.426.

[3] I. Tanihata *et al.* Measurements of interaction cross sections and radii of He isotopes. *Physics Letters B*, 160(6):380 – 384, 1985. http://www.sciencedirect.com/science/article/pii/037026938590005X.

[4] P. G. Hansen and B. Jonson. The neutron halo of extremely neutron-rich nuclei. *Europhysics Letters (EPL)*, 4(4):409–414, 1987. https://doi.org/10.1209%2F0295-5075%2F4%2F4%2F005.

[5] W. Nörtershäuser *et al.* Nuclear charge radii of ^{7,9,10}Be and the one-neutron halo nucleus ^{11}Be. *Phys. Rev. Lett.*, 102:062503, 2009. https://link.aps.org/doi/10.1103/PhysRevLett.102.062503.

[6] P. Cerda-Duran and N. Elias-Rosa. Neutron stars formation and core collapse supernovae. In Jones D. Rea N. Vidaña I. Rezzolla L., Pizzochero P., editor, *The Physics and Astrophysics of Neutron Stars*, Astrophysics and Space Science Library. Springer, Cham.

[7] I. Vidaña. A short walk through the physics of neutron stars. *The European Physical Journal Plus*, 133:445, 2018. https://doi.org/10.1140/epjp/i2018-12329-x.

[8] C. J. Horowitz *et al.* A way forward in the study of the symmetry energy: experiment, theory, and observation. *Journal of Physics G: Nuclear and Particle Physics*, 41(9):093001, 2014. https://doi.org/10.1088%2F0954-3899%2F41%2F9%2F093001.

[9] M. Thiel *et al.* Neutron skins of atomic nuclei: per aspera ad astra. *Journal of Physics G: Nuclear and Particle Physics*, 46(9):093003, 2019. https://doi.org/10.1088%2F1361-6471%2Fab2c6d.

[10] M. Baldo and G. F. Burgio. The nuclear symmetry energy. *Progress in Particle and Nuclear Physics*, 91:203 – 258, 2016. http://www.sciencedirect.com/science/article/pii/S0146641016300254.

[11] X. Roca-Maza *et al.* Neutron skin of ^{208}Pb, nuclear symmetry energy, and the parity radius experiment. *Phys. Rev. Lett.*, 106:252501, 2011. https://link.aps.org/doi/10.1103/PhysRevLett.106.252501.

[12] James M. Lattimer *et al.* Direct urca process in neutron stars. *Phys. Rev. Lett.*, 66:2701–2704, 1991.

[13] J. Dong, W. Zuo, and J. Gu. Constraints on neutron skin thickness in ^{208}Pb and density-dependent symmetry energy. *Phys. Rev. C*, 91:034315, 2015. https://link.aps.org/doi/10.1103/PhysRevC.91.034315.

[14] K. Riisager, D. V. Fedorov, and A. S. Jensen. Quantum halos. *Europhys. Lett.*, 49(5):547–553, 2000. https://doi.org/10.1209/epl/i2000-00180-y.

[15] K. Riisager. Nuclear halos and experiments to probe them. In Roeckl E. Al-Khalili J., editor, *The Euroschool Lectures on Physics with Exotic Beams, Vol. II*, volume 700 of *Lecture Notes in Physics*. Springer, Berlin, Heidelberg, 2006. https://doi.org/10.1007/3-540-33787-3_1.

[16] K. Riisager and A. S. Jensen. The radius of ^{8}B and solar neutrinos. *Physics Letters B*, 301(1):6 – 10, 1993.

[17] P. Descouvemont, C. Daniel, and D. Baye. Three-body systems with Lagrange-mesh techniques in hyperspherical coordinates. *Phys. Rev. C*, 67:044309, 2003. https://link.aps.org/doi/10.1103/PhysRevC.67.044309.

[18] M. V. Zhukov *et al.* Bound state properties of borromean halo nuclei: 6he and 11li. *Physics Reports*, 231(4):151 – 199, 1993. http://www.sciencedirect.com/science/article/pii/037015739390141Y.

[19] J. Al-Khalili. An introduction to halo nuclei. In Roeckl E. Al-Khalili J., editor, *The Euroschool Lectures on Physics with Exotic Beams, Vol. I*, volume 651 of *Lecture Notes in Physics*. Springer, Berlin, Heidelberg, 2004. https://doi.org/10.1007/978-3-540-44490-9_3.

[20] M. Pfützner *et al.* Radioactive decays at limits of nuclear stability. *Rev. Mod. Phys.*, 84:567–619, 2012. https://link.aps.org/doi/10.1103/RevModPhys.84.567.

[21] K. Riisager. Halos and related structures. *Physica Scripta*, T152:014001, 2013. https://doi.org/10.1088%2F0031-8949%2F2013%2Ft152%2F014001.

[22] H. R. Ravn and B. W. Allardyce. On-line mass separators. In D.A. Bromley, editor, *Treatise on Heavy-Ion Science*, volume 8. Springer US, 1989. https://doi.org/10.1007/978-1-4613-0713-6.

[23] M. Huyse. The why and howof radioactive-beam research. In Al-Khalili J. and Roeckl E., editors, *The Euroschool Lectures on Physics with Exotic Beams, Vol. I*, volume 651 of *Lecture Notes in Physics*. Springer, Berlin, Heidelberg, 2004. https://doi.org/10.1007/978-3-540-44490-9_1.

[24] D. J. Morrissey and B. M. Sherrill. In-flight separation of projectile fragments. In Roeckl E. Al-Khalili J., editor, *The Euroschool Lectures on Physics with Exotic Beams, Vol. I*, volume 651 of *Lecture Notes in Physics*. Springer, Berlin, Heidelberg, 2004. https://doi.org/10.1007/978-3-540-44490-9_4.

[25] P. Van Duppen. Isotope separation on line and post acceleration. In Roeckl E. Al-Khalili J., editor, *The Euroschool Lectures on Physics with Exotic Beams, Vol. II*, volume 700 of *Lecture Notes in Physics*. Springer, Berlin, Heidelberg, 2006. https://doi.org/10.1007/3-540-33787-3_2.

[26] R. J. Glauber. Lectures on theoretical physics. In W. E. Brittin and L. C. Dunham, editors, *Lectures in Theoretical Physics*, volume 1. Interscience, New York, NY, USA, 1959.

[27] I. Tanihata *et al.* Measurement of interaction cross sections using isotope beams of Be and B and isospin dependence of the nuclear radii. *Physics Letters B*, 206(4):592 – 596, 1988. https://doi.org/10.1016/0370-2693(88)90702-2.

[28] I. Tanihata *et al.* Measurements of interaction cross sections and nuclear radii in the light *p*-shell region. *Phys. Rev. Lett.*, 55:2676–2679, 1985.

[29] T. Kobayashi *et al.* Projectile fragmentation of the extremely neutron-rich nucleus ^{11}Li at 0.79 GeV/nucleon. *Phys. Rev. Lett.*, 60:2599–2602, 1988. https://link.aps.org/doi/10.1103/PhysRevLett.60.2599.

[30] N. A. Orr *et al.* Momentum distributions of ^{9}Li fragments following the breakup of ^{11}Li. *Phys. Rev. Lett.*, 69:2050–2053, 1992. https://link.aps.org/doi/10.1103/PhysRevLett.69.2050.

[31] E. Sauvan *et al.* One-neutron removal reactions on neutron-rich *psd*-shell nuclei. *Physics Letters B*, 491(1):1 – 7, 2000. https://doi.org/10.1016/S0370-2693(00)01003-0.

[32] T. Aumann *et al.* One-neutron knockout from individual single-particle states of ^{11}Be. *Phys. Rev. Lett.*, 84:35–38, 2000. https://link.aps.org/doi/10.1103/PhysRevLett.84.35.

[33] T. Kobayashi *et al.* Electromagnetic dissociation and soft giant dipole resonance of the neutron-dripline nucleus ^{11}Li. *Physics Letters B*, 232(1):51 – 55, 1989. https://doi.org/10.1016/0370-2693(89)90557-1.

[34] T. Nakamura *et al.* Observation of strong low-lying E1 strength in the two-neutron halo nucleus ^{11}Li. *Phys. Rev. Lett.*, 96:252502, 2006. https://link.aps.org/doi/10.1103/PhysRevLett.96.252502.

[35] A. Di Pietro *et al.* Elastic scattering and reaction mechanisms of the halo nucleus ^{11}Be around the coulomb barrier. *Phys. Rev. Lett.*, 105:022701, 2010. https://link.aps.org/doi/10.1103/PhysRevLett.105.022701.

[36] N. Fukuda *et al.* Coulomb and nuclear breakup of a halo nucleus ^{11}Be. *Phys. Rev. C*, 70:054606, 2004. https://link.aps.org/doi/10.1103/PhysRevC.70.054606.

[37] R. C. Johnson, J. S. Al-Khalili, and J.A. Tostevin. Elastic scattering of halo nuclei. *Phys. Rev. Lett.*, 79:2771–2774, 1997. https://link.aps.org/doi/10.1103/PhysRevLett.79.2771.

[38] P. Capel, R. C. Johnson, and F. M. Nunes. One-neutron halo structure by the ratio method. *Physics Letters B*, 705(1):112 – 115, 2011. https://doi.org/10.1016/j.physletb.2011.09.105.

[39] I. Tanihata, H. Savajols, and R. Kanungo. Recent experimental progress in nuclear halo structure studies. *Progress in Particle and Nuclear Physics*, 68:215 – 313, 2013. https://doi.org/10.1016/j.ppnp.2012.07.001.

[40] R. Sánchez *et al.* Nuclear charge radii of ^{9,11}Li: The influence of halo neutrons. *Phys. Rev. Lett.*, 96:033002, 2006. https://link.aps.org/doi/10.1103/PhysRevLett.96.033002.

[41] L. B. Wang *et al.* Laser spectroscopic determination of the ^{6}He nuclear charge radius. *Phys. Rev. Lett.*, 93:142501, 2004. https://link.aps.org/doi/10.1103/PhysRevLett.93.142501.

[42] M. Smith *et al.* First penning-trap mass measurement of the exotic halo nucleus ^{11}Li. *Phys. Rev. Lett.*, 101:202501, 2008. https://link.aps.org/doi/10.1103/PhysRevLett.101.202501.

[43] T. Nilsson, G. Nyman, and K. Riisager. Halo-nuclei at isolde. *Hyperfine Interactions*, 129:67, 2000. https://doi.org/10.1023/A:1012678320350.

[44] W. Horiuchi, Y. Suzuki, P. Capel, and D. Baye. Probing the weakly-bound neutron orbit of ^{31}Ne with total reaction and one-neutron removal cross sections. *Phys. Rev. C*, 81:024606, 2010. https://link.aps.org/doi/10.1103/PhysRevC.81.024606.

[45] P. Capel, G. Goldstein, and D. Baye. Time-dependent analysis of the breakup of ^{11}Be on ^{12}C at 67 MeV/nucleon. *Phys. Rev. C*, 70:064605, 2004. https://link.aps.org/doi/10.1103/PhysRevC.70.064605.

[46] N. Austern *et al.* Continuum-discretized coupled-channels calculations for three-body models of deuteron-nucleus reactions. *Physics Reports*, 154(3):125 – 204, 1987. https://doi.org/10.1016/0370-1573(87)90094-9.

[47] D. Baye, P. Capel, and G. Goldstein. Collisions of halo nuclei within a dynamical eikonal approximation. *Phys. Rev. Lett.*, 95:082502, 2005. https://link.aps.org/doi/10.1103/PhysRevLett.95.082502.

[48] G. Goldstein, D. Baye, and P. Capel. Dynamical eikonal approximation in breakup reactions of ^{11}Be. *Phys. Rev. C*, 73:024602, 2006. https://link.aps.org/doi/10.1103/PhysRevC.73.024602.

[49] I. J. Thompson and F. M. Nunes. *Nuclear Reactions for Astrophysics: Principles, Calculation and Applications of Low-Energy Reactions*. Cambridge University Press, 2009.

[50] L. D. Faddeev. *J. Exptl. Theoret. Phys.*, 12(5):1014–1019, 1961. http://www.jetp.ac.ru/cgi-bin/dn/e_012_05_1014.pdf.

[51] M. Abramowitz and I. A. Stegun. *Handbook of Mathematical Functions*. Dover Publications, 1972.

[52] A. M. Mukhamedzhanov and F. M. Nunes. Combined method to extract spectroscopic information. *Phys. Rev. C*, 72:017602, 2005. https://link.aps.org/doi/10.1103/PhysRevC.72.017602.

[53] George H. Rawitscher. Effect of deuteron breakup on elastic deuteron - nucleus scattering. *Phys. Rev. C*, 9:2210–2229, 1974. https://link.aps.org/doi/10.1103/PhysRevC.9.2210.

[54] T. Matsumoto *et al.* New treatment of breakup continuum in the method of continuum discretized coupled channels. *Phys. Rev. C*, 68:064607, 2003. https://link.aps.org/doi/10.1103/PhysRevC.68.064607.

[55] I. J. Thompson. Coupled reaction channels calculations in nuclear physics. *Computer Physics Reports*, 7(4):167 – 212, 1988. https://doi.org/10.1016/0167-7977(88)90005-6.

[56] D. Baye and P. Capel. Breakup reaction models for two- and three-cluster projectiles. In Beck C., editor, *Clusters in Nuclei, Vol. 2*, volume 848 of *Lecture Notes in Physics*. Springer, Berlin, Heidelberg, 2012. https://doi.org/10.1007/978-3-642-24707-1_3.

[57] P. Capel, H. Esbensen, and F. M. Nunes. Comparing nonperturbative models of the breakup of neutron-halo nuclei. *Phys. Rev. C*, 85:044604, 2012. https://link.aps.org/doi/10.1103/PhysRevC.85.044604.

[58] P. Capel, D. Baye, and V. S. Melezhik. Time-dependent analysis of the breakup of halo nuclei. *Phys. Rev. C*, 68:014612, 2003. https://link.aps.org/doi/10.1103/PhysRevC.68.014612.

[59] T. Fukui, K. Ogata, and P. Capel. Analysis of a low-energy correction to the eikonal approximation. *Phys. Rev. C*, 90:034617, 2014. https://link.aps.org/doi/10.1103/PhysRevC.90.034617.

[60] R. A. Broglia and A. Winther. *Heavy Ion Reaction Lecture Notes, Volume I: Elastic and Inelastic Reactions*. Benjamin/Cummings Publishing Company, San Francisco, 1981.

[61] K. Alder and A. Winther. *Electromagnetic Excitation*. North-Holland, Amsterdam, 1975.

[62] J. Margueron, A. Bonaccorso, and D. M. Brink. A non-perturbative approach to halo breakup. *Nuclear Physics A*, 720(3):337 – 353, 2003. https://doi.org/10.1016/S0375-9474(03)01092-3.

[63] P. Capel, D. Baye, and Y. Suzuki. Coulomb-corrected eikonal description of the breakup of halo nuclei. *Phys. Rev. C*, 78:054602, 2008. https://link.aps.org/doi/10.1103/PhysRevC.78.054602.

[64] R. C. Johnson. Elastic scattering and elastic break-up of halo nuclei in a special model. In *Proceedings of European Conference on Advances in Nuclear Physics and Related Areas*, Thessaloniki, Greece, 8–12 July 1997.

[65] R. D. Woods and D. S. Saxon. Diffuse surface optical model for nucleon-nuclei scattering. *Phys. Rev.*, 95:577–578, 1954. http://dx.doi.org/10.1103/PhysRev.95.577.

[66] A. J. Koning and J. P. Delaroche. Local and global nucleon optical models from 1 keV to 200 MeV. *Nuclear Physics A*, 713:231 – 310, 2003. http://dx.doi.org/10.1016/S0375-9474(02)01321-0.

[67] L. H. Thomas. The motion of the spinning electron. *Nature*, 117:514, 1926.

[68] P. Capel, R. C. Johnson, and F. M. Nunes. The ratio method: A new tool to study one-neutron halo nuclei. *Physical Review C*, 88:044602, 2013. http://dx.doi.org/10.1103/PhysRevC.88.044602.

[69] B. Davids *et al.* Measurement of E2 transitions in the coulomb dissociation of ^{8}B. *Phys. Rev. Lett.*, 81:2209–2212, 1998. https://link.aps.org/doi/10.1103/PhysRevLett.81.2209.

[70] G. Goldstein, P. Capel, and D. Baye. Analysis of coulomb breakup experiments of ^{8}B with a dynamical eikonal approximation. *Phys. Rev. C*, 76:024608, 2007. https://link.aps.org/doi/10.1103/PhysRevC.76.024608.

[71] **F. Colomer** *et al.* Extension of the ratio method to low energy. *Phys. Rev. C*, 93:054621, 2016. https://link.aps.org/doi/10.1103/PhysRevC.93.054621.

[72] J. H. Kelley *et al.* Energy levels of light nuclei A=11. *Nuclear Physics A*, 880:88 – 195, 2012. https://doi.org/10.1016/j.nuclphysa.2012.01.010.

[73] C. C. Sahm *et al.* *Phys. Rev. C*, 34:2165–2170, 1986. http://dx.doi.org/10.1103/PhysRevC.34.2165.

[74] D. Robson. Elastic scattering and elastic break-up of halo nuclei in a special model. In *Proceedings of the Symposium on Heavy-ion Scattering*, edited by R. H. Siemmsen, G. C. Morrison, and J. P. Schiffer (Argonne National Laboratory, Argon), vol. ANL-7837, 239 1971.

[75] C. M. Perey and F. G. Perey. Compilation of phenomenological optical-model parameters 1954–1975. *Atomic Data and Nuclear Data Tables*, 17(1):1 – 101, 1976. https://doi.org/10.1016/0092-640X(76)90007-3.

[76] F. D. Becchetti and G. W. Greenlees. Nucleon-nucleus optical-model parameters, A>40, E<50 MeV. *Phys. Rev.*, 182:1190–1209, 1969. https://link.aps.org/doi/10.1103/PhysRev.182.1190.

[77] P. Capel and F. M. Nunes. Influence of the projectile description on breakup calculations. *Phys. Rev. C*, 73:014615, 2006. https://link.aps.org/doi/10.1103/PhysRevC.73.014615.

[78] P. Capel, M. Hussein, and D. Baye. Influence of the halo upon angular distributions for elastic scattering and breakup. *Phys. Lett.*, B693:448, 2010. https://doi.org/10.1016/j.physletb.2010.08.072.

[79] B. V. Carlson, M. P. Isidro Filho, and M. S. Hussein. Near/far decomposition of the proton-nucleus and antiproton-nucleus elastic angular distributions. *Physics Letters B*, 154(2):89 – 92, 1985. https://doi.org/10.1016/0370-2693(85)90563-5.

[80] J. S. Al-Khalili, J. A. Tostevin, and J. M. Brooke. Beyond the eikonal model for few-body systems. *Phys. Rev. C*, 55:R1018–R1022, 1997. https://link.aps.org/doi/10.1103/PhysRevC.55.R1018.

[81] X. Y. Yun and **F. Colomer** *et al.* Extension of the ratio method to proton-rich nuclei. *Journal of Physics G: Nuclear and Particle Physics*, 46(10):105111, 2019. https://doi.org/10.1088%2F1361-6471%2Fab355e.

[82] D. Baye, P. Descouvemont, and N. K. Timofeyuk. Matter densities of ^{8}B and ^{8}Li in a microscopic cluster model and the proton-halo problem of ^{8}B. *Nucl. Phys. A*, 577(3):624 – 640, 1994. http://dx.doi.org/10.1016/0375-9474(94)90936-9.

[83] J. Mortimer, I. J. Thompson, and J. .A. Tostevin. Higher-order and E2 effects in medium energy ^{8}B breakup. *Phys. Rev. C*, 65:064619, 2002. https://link.aps.org/doi/10.1103/PhysRevC.65.064619.

[84] H. Esbensen and G. F. Bertsch. Effects of E2 transitions in the coulomb dissociation of ^{8}B. *Nucl. Phys. A*, 600(1):37, 1996. http://www.sciencedirect.com/science/article/pii/0375947496000061.

[85] J. Cook. Global optical-model potentials for the elastic scattering of ^{6,7}Li projectiles. *Nucl. Phys. A*, 388(1):153–172, 1982. http://www.sciencedirect.com/science/article/pii/0375947482905139.

[86] A. Nadasen *et al.* Unique potentials for the elastic scattering of 350 MeV ^{7}Li from ^{12}C and ^{28}Si. *Phys. Rev. C*, 52:1894–1899, 1995. https://link.aps.org/doi/10.1103/PhysRevC.52.1894.

[87] H. L. Clark, Y. W. Lui, and D. H. Youngblood. Alpha particle optical potentials at 240 MeV. *Nucl. Phys. A*, 589(3):416, 1995. http://www.sciencedirect.com/science/article/pii/037594749500121G.

[88] V. I. Chuev *et al.* Elastic scattering of ^{6}Li ions on medium and heavy nuclei. *J. Phys. Colloques*, 32(C6):157, 1971. https://jphyscol.journaldephysique.org/articles/jphyscol/abs/1971/06/jphyscol197132C626/jphyscol197132C626.html.

[89] P. Schumacher *et al.* Lithium elastic and inelastic scattering and lithium-induced single nucleon transfer reactions. *Nucl. Phys. A*, 212(3):573, 1973. http://www.sciencedirect.com/science/article/pii/0375947473908245?via%3Dihub.

[90] F. C. Barker. The ^{7}Be$(p,\gamma)^{8}$B cross section at low energies. *Australian Journal of Physics*, 33:177–190, 1980. http://adsabs.harvard.edu/abs/1980AuJPh..33..177B.

[91] G. Hagen, T. Papenbrock, and M. Hjorth-Jensen. *Ab Initio* computation of the ^{17}F proton halo state and resonances in $A = 17$ nuclei. *Phys. Rev. Lett.*, 104:182501, 2010. http://link.aps.org/doi/10.1103/PhysRevLett.104.182501.

[92] J.-M. Sparenberg, D. Baye, and B. Imanishi. Coupled-reaction-channel calculations of the ^{16}O+^{17}O and ^{16}O+^{17}F charge-symmetric systems. *Phys. Rev. C*, 61(5):054610, 2000. 10.1103/PhysRevC.61.054610.

[93] L. J. Sun *et al.* (RIBLL Collaboration). β-decay spectroscopy of ^{27}S. *Phys. Rev. C*, 99:064312, 2019. https://link.aps.org/doi/10.1103/PhysRevC.99.064312.

[94] R. B. Firestone. Nuclear data sheets for a = 25. *Nucl. Data Sheets*, 110(8):1691 – 1744, 2009. http://www.sciencedirect.com/science/article/pii/S009037520900057X.

[95] M. Shamsuzzoha Basunia. Nuclear data sheets for A=27. *Nucl. Data Sheets*, 112(8):1875 – 1948, 2011. https://doi.org/10.1016/j.nds.2011.08.001.

[96] Y. P. Xu and D. Y. Pang. Toward a systematic nucleus-nucleus potential for peripheral collisions. *Phys. Rev. C*, 87:044605, 2013. https://link.aps.org/doi/10.1103/PhysRevC.87.044605.

[97] R. L. Varner *et al.* A global nucleon optical model potential. *Phys. Rep.*, 201(2):57 – 119, 1991. https://doi.org/10.1016/0370-1573(91)90039-O.

[98] E. Bauge, J. P. Delaroche, and M. Girod. Lane-consistent, semimicroscopic nucleon-nucleus optical model. *Phys. Rev. C*, 63:024607, 2001. https://link.aps.org/doi/10.1103/PhysRevC.63.024607.

[99] B. Alex Brown. New skyrme interaction for normal and exotic nuclei. *Phys. Rev. C*, 58:220–231, 1998. https://link.aps.org/doi/10.1103/PhysRevC.58.220.

[100] Bao-An Li *et al.* Towards understanding astrophysical effects of nuclear symmetry energy. *The European Physical Journal A*, 55:117, 2019. https://doi.org/10.1140/epja/i2019-12780-8.

[101] M. Dutra *et al.* Skyrme interaction and nuclear matter constraints. *Phys. Rev. C*, 85:035201, 2012. https://link.aps.org/doi/10.1103/PhysRevC.85.035201.

[102] P. Möller *et al.* New finite-range droplet mass model and equation-of-state parameters. *Phys. Rev. Lett.*, 108:052501, 2012. https://link.aps.org/doi/10.1103/PhysRevLett.108.052501.

[103] X. Viñas *et al.* Density dependence of the symmetry energy from neutron skin thickness in finite nuclei. *The European Physical Journal A*, 50:27, 2014. https://doi.org/10.1140/epja/i2014-14027-8.

[104] L. Ray and G. W. Hoffmann. Relativistic and nonrelativistic impulse approximation descriptions of 300–1000 MeV proton + nucleus elastic scattering. *Phys. Rev. C*, 31:538–560, 1985. https://link.aps.org/doi/10.1103/PhysRevC.31.538.

[105] L. Ray, G. W. Hoffmann, and W. R. Coker. Nonrelativistic and relativistic descriptions of proton-nucleus scattering. *Physics Reports*, 212(5):223 – 328, 1992. https://doi.org/10.1016/0370-1573(92)90156-T.

[106] V. E. Starodubsky and N. M. Hintz. Extraction of neutron densities from elastic proton scattering by ^{206,207,208}Pb at 650 MeV. *Phys. Rev. C*, 49:2118–2135, 1994. https://link.aps.org/doi/10.1103/PhysRevC.49.2118.

[107] J. Zenihiro *et al.* Neutron density distributions of ^{204,206,208}Pb deduced via proton elastic scattering at $E_p = 295$ MeV. *Phys. Rev. C*, 82:044611, 2010. https://link.aps.org/doi/10.1103/PhysRevC.82.044611.

[108] J. Piekarewicz and S. P. Weppner. Insensitivity of the elastic proton–nucleus reaction to the neutron radius of ^{208}Pb. *Nuclear Physics A*, 778(1):10 – 21, 2006. https://doi.org/10.1016/j.nuclphysa.2006.08.004.

[109] H. Laumer and G. G. Seaman. Total cross sections for the ^{19}F(^{13}C, ^{12}C)^{20}F and ^{23}Na(^{13}C, ^{12}C)^{24}Na reactions. *Phys. Rev. C*, 10:2159–2165, 1974. https://link.aps.org/doi/10.1103/PhysRevC.10.2159.

[110] E. Friedman and C. J. Batty. Neutron radii of ^{204,206,208}Pb determined from 104 MeV α particle scattering. *Phys. Rev. C*, 16:1425–1430, 1977. https://link.aps.org/doi/10.1103/PhysRevC.16.1425.

[111] G. Dugan *et al.* Elastic scattering of low-energy pions and muons from lead. *Phys. Rev. C*, 8:909–921, 1973. https://link.aps.org/doi/10.1103/PhysRevC.8.909.

[112] A. Trzcinska *et al.* Information on antiprotonic atoms and the nuclear periphery from the PS209 experiment. *Nuclear Physics A*, 692(1):176 – 181, 2001. https://doi.org/10.1016/S0375-9474(01)01176-9.

[113] J. Jastrzebski *et al.* Signature of a neutron halo in 232Th from antiproton absorption. *Nuclear Physics A*, 558:405 – 414, 1993. https://doi.org/10.1016/0375-9474(93)90409-Q.

[114] J. Jastrzebski *et al.* Neutron density distributions from antiprotonic atoms compared with hadron scattering data. *International Journal of Modern Physics E*, 13(01):343–351, 2004. https://doi.org/10.1142/S0218301304002168.

[115] T. W. Donnelly, J. Dubach, and Ingo Sick. Isospin dependences in parity-violating electron scattering. *Nuclear Physics A*, 503(3):589 – 631, 1989. https://doi.org/10.1016/0375-9474(89)90432-6.

[116] S. Abrahamyan *et al.* (PREX Collaboration). Measurement of the neutron radius of ^{208}Pb through parity violation in electron scattering. *Phys. Rev. Lett.*, 108:112502, 2012. https://link.aps.org/doi/10.1103/PhysRevLett.108.112502.

[117] C. J. Horowitz *et al.* Weak charge form factor and radius of ^{208}Pb through parity violation in electron scattering. *Phys. Rev. C*, 85:032501, 2012. https://link.aps.org/doi/10.1103/PhysRevC.85.032501.

[118] K. Paschk *et al.* (Spokespersons). Proposal to Jefferson Lab PAC 38, PREX-II: Precision parity-violating measurement of the neutron skin of lead. https://hallaweb.jlab.org/collab/PAC/PAC38/prexII.pdf.

[119] J. Mamme *et al.* (Spokespersons). Proposal to Jefferson Lab PAC 40 CREX: Parity-violating measurement of the weak charge distribution of ^{48}Ca to 0.02 fm accuracy. https://hallaweb.jlab.org/parity/prex/c-rex2013_v7.pdf.

[120] D. Becker *et al.* The P2 experiment. *The European Physical Journal A*, 54:208, 2018. https://doi.org/10.1140/epja/i2018-12611-6.

[121] M. N. Harakeh and A. van der Woude. *Giant Resonances-Fundamental High-Frequency Modes of Nuclear Excitation*. Oxford: Clarendon, 2001.

[122] A. Bracco, E. G. Lanza, and A. Tamii. Isoscalar and isovector dipole excitations: Nuclear properties from low-lying states and from the isovector giant dipole resonance. *Progress in Particle and Nuclear Physics*, 106:360 – 433, 2019. https://doi.org/10.1016/j.ppnp.2019.02.001.

[123] A. Tamii *et al.* Complete electric dipole response and the neutron skin in ^{208}Pb. *Phys. Rev. Lett.*, 107:062502, 2011. https://link.aps.org/doi/10.1103/PhysRevLett.107.062502.

[124] I. Poltoratska *et al.* Pygmy dipole resonance in ^{208}Pb. *Phys. Rev. C*, 85:041304, 2012. https://link.aps.org/doi/10.1103/PhysRevC.85.041304.

[125] P. G. Reinhard and W. Nazarewicz. Information content of a new observable: The case of the nuclear neutron skin. *Phys. Rev. C*, 81:051303, 2010. https://link.aps.org/doi/10.1103/PhysRevC.81.051303.

[126] J. Piekarewicz *et al.* Electric dipole polarizability and the neutron skin. *Phys. Rev. C*, 85:041302, 2012. https://link.aps.org/doi/10.1103/PhysRevC.85.041302.

[127] X. Roca-Maza and N. Paar. Nuclear equation of state from ground and collective excited state properties of nuclei. *Progress in Particle and Nuclear Physics*, 101:96 – 176, 2018. https://doi.org/10.1016/j.ppnp.2018.04.001.

[128] D. Drechsel *et al.* Medium effects in coherent pion photo- and electroproduction on ^{4}He and ^{12}C. *Nuclear Physics A*, 660(4):423 – 438, 1999. https://doi.org/10.1016/S0375-9474(99)00412-1.

[129] B. Krusche *et al.* Coherent π^0-photoproduction from atomic nuclei. *Physics Letters B*, 526(3):287 – 294, 2002. https://doi.org/10.1016/S0370-2693(01)01503-9.

[130] J. E. Leiss and R. A. Schrack. Nuclear matter distributions from coherent neutral pion production. *Rev. Mod. Phys.*, 30:456–461, 1958. https://link.aps.org/doi/10.1103/RevModPhys.30.456.

[131] R. A. Schrack, J. E. Leiss, and S. Penner. Neutral meson photoproduction from complex nuclei. *Phys. Rev.*, 127:1772–1783, 1962. https://link.aps.org/doi/10.1103/PhysRev.127.1772.

[132] Tarbert *et al.* (Crystal Ball at MAMI and C. M. A2 Collaboration). Neutron skin of ^{208}Pb from coherent pion photoproduction. *Phys. Rev. Lett.*, 112:242502, 2014. https://link.aps.org/doi/10.1103/PhysRevLett.112.242502.

[133] R. A. Eramzhyan *et al.* Nuclear pion photoproduction: a theory and the 16O(γ,π^+)16N (bound) example. *Journal of Physics G: Nuclear Physics*, 9(6):605–619, 1983. https://doi.org/10.1088%2F0305-4616%2F9%2F6%2F006.

[134] A. Gardestig, C. J. Horowitz, and Gerald A. Miller. Comment on "neutron skin of ^{208}Pb from coherent pion photoproduction", 2015. https://arxiv.org/abs/1504.08347.

[135] The Editors. Editorial: Uncertainty estimates. *Phys. Rev. A*, 83:040001, 2011. https://link.aps.org/doi/10.1103/PhysRevA.83.040001.

[136] Mainz institute for theoretical physics 2016 workshop: Neutron skins of nuclei. (https://indico.mitp.uni-mainz.de/event/47/timetable).

[137] M. I. Bondy Ferretti. Neutron skin studies in heavy nuclei with coherent π^0 photoproduction. *PoS, Bormio2015*, page 008, 2015. https://doi.org/10.1088%2F0305-4616%2F9%2F6%2F006.

[138] D. P. Watts, C. Sfienti, and L. Zana (Spokespersons). Proposal to Mainz Microtron MAMI: sospin asymmetry dependence of neutron skins with coherent pion-photoproduction. https://www.blogs.uni-mainz.de/fb08-mami-experiments/files/2016/09/proposal-A2-06-2016.pdf.

[139] Particle Data Group. Review of particle physics. *Phys. Rev. D*, 98:030001, 2018. https://link.aps.org/doi/10.1103/PhysRevD.98.030001.

[140] J. C. McGeorge *et al.* Upgrade of the Glasgow photon tagging spectrometer for Mainz MAMI-C. *The European Physical Journal A*, 37:129, 2008. https://doi.org/10.1140/epja/i2007-10606-0.

[141] R. Partridge *et al.* Decay $J/\psi \to 3\gamma$ and a search for the η_c. *Phys. Rev. Lett.*, 44:712–716, 1980. https://link.aps.org/doi/10.1103/PhysRevLett.44.712.

[142] R. Novotny. The BaF-2 photon spectrometer TAPS. *IEEE Trans. Nucl. Sci.*, 38:379–385, 1991. https://doi.org/10.1109/23.289329.

[143] M. Unverzagt *et al.* Determination of the Dalitz plot parameter α for the decay $\eta \to 3\pi^0$ with the Crystal Ball at MAMI-B. *Eur. Phys. J. A*, 39(2):169–177, 2009. https://doi.org/10.1140/epja/i2008-10710-7.

[144] D. J. Griffiths. *Introduction to Electrodynamics*. Cambridge University Press.

[145] G. E. P. Box and Mervin E. Muller. A note on the generation of random normal deviates. *Ann. Math. Statist.*, 29(2):610–611, 1958. https://doi.org/10.1214/aoms/1177706645.

[146] A. Antonov, P. E. Hodgson, and I. Z. Petkov. *Nucleon Correlations in Nuclei*. Springer-Verlag Berlin Heidelberg, 2001.

[147] Per-Olov Löwdin. Quantum theory of many-particle systems. I. Physical interpretations by means of density matrices, natural spin-orbitals, and convergence problems in the method of configurational interaction. *Phys. Rev.*, 97:1474–1489, 1955. https://link.aps.org/doi/10.1103/PhysRev.97.1474.

[148] M. Bender, P. H. Heenen, and P. G. Reinhard. Self-consistent mean-field models for nuclear structure. *Rev. Mod. Phys.*, 75:121–180, 2003. https://link.aps.org/doi/10.1103/RevModPhys.75.121.

[149] A. Baran. Relativistic mean field calculations of single particle potentials. *Phys. Rev. C*, 61:024316, 2000. https://link.aps.org/doi/10.1103/PhysRevC.61.024316.

[150] Brian D. Serot and John Dirk Walecka. The Relativistic Nuclear Many Body Problem. *Adv. Nucl. Phys.*, 16:1–327, 1986.

[151] B. G. Todd-Rutel and J. Piekarewicz. Neutron-rich nuclei and neutron stars: A new accurately calibrated interaction for the study of neutron-rich matter. *Phys. Rev. Lett.*, 95:122501, 2005. https://link.aps.org/doi/10.1103/PhysRevLett.95.122501.

[152] B. G. Todd and J. Piekarewicz. Relativistic mean-field study of neutron-rich nuclei. *Phys. Rev. C*, 67:044317, 2003. https://link.aps.org/doi/10.1103/PhysRevC.67.044317.

[153] L. C. Chamon *et al.* Toward a global description of the nucleus-nucleus interaction. *Phys. Rev. C*, 66:014610, 2002. https://link.aps.org/doi/10.1103/PhysRevC.66.014610.

[154] B. Dreher *et al.* The determination of the nuclear ground state and transition charge density from measured electron scattering data. *Nuclear Physics A*, 235(1):219 – 248, 1974. https://doi.org/10.1016/0375-9474(74)90189-4.

[155] J. P. Elliott, T. H. R. Skyrme, and John Douglas Cockcroft. Centre-of-mass effects in the nuclear shell-model. *Proceedings of the Royal Society of London. Series A. Mathematical and Physical Sciences*, 232(1191):561–566, 1955. https://royalsocietypublishing.org/doi/abs/10.1098/rspa.1955.0239.

[156] L. J. Tassie and F. C. Barker. Application to electron scattering of center-of-mass effects in the nuclear shell model. *Phys. Rev.*, 111:940–940, 1958. https://link.aps.org/doi/10.1103/PhysRev.111.940.

[157] J. Piekerawicz. personal communication.

[158] G. Hagen *et al.* Neutron and weak-charge distributions of the ^{48}Ca nucleus. *Nature Phys.*, 12:186–190, 2016. https://doi.org/10.1038/nphys3529.

[159] A. K. Kerman, H. McManus, and R. M. Thaler. The scattering of fast nucleons from nuclei. *Annals of Physics*, 8(4):551 – 635, 1959. https://doi.org/10.1016/0003-4916(59)90076-4.

[160] S. S. Kamalov, L. Tiator, and C. Bennhold. Coherent π^0 and η photoproduction on the deuteron. *Phys. Rev. C*, 55:98–110, 1997. https://link.aps.org/doi/10.1103/PhysRevC.55.98.

[161] Gerald A. Miller. Coherent-nuclear pion photoproduction and neutron radii. *Phys. Rev. C*, 100:044608, 2019. https://link.aps.org/doi/10.1103/PhysRevC.100.044608.

[162] G. F. Chew *et al.* Relativistic dispersion relation approach to photomeson production. *Phys. Rev.*, 106:1345–1355, 1957. https://link.aps.org/doi/10.1103/PhysRev.106.1345.

[163] F. A. Berends, A. Donnachie, and D. L. Weaver. Photoproduction and electroproduction of pions (I) dispersion relation theory. *Nuclear Physics B*, 4(1):1 – 53, 1967. https://doi.org/10.1016/0550-3213(67)90196-4.

[164] D. Drechsel *et al.* A unitary isobar model for pion photo- and electroproduction on the proton up to 1 GeV. *Nuclear Physics A*, 645(1):145 – 174, 1999. https://doi.org/10.1016/S0375-9474(98)00572-7.

[165] D. Drechsel, S. S. Kamalov, and L. Tiator. Unitary isobar model MAID2007. *The European Physical Journal A*, 34:69, 2007. https://doi.org/10.1140/epja/i2007-10490-6.

[166] T. Fujii *et al.* Photoproduction of charged π mesons from protons and neutrons in the energy range between 250 and 790 MeV. *Nuclear Physics B*, 120(3):395 – 422, 1977. https://doi.org/10.1016/0550-3213(77)90084-0.

[167] Menze *et al. Physics Data*, 7-1, Fachinformationszentrum Karlsruhe (1977).

[168] Kenneth M. Watson. Some general relations between the photoproduction and scattering of π mesons. *Phys. Rev.*, 95:228–236, 1954. https://link.aps.org/doi/10.1103/PhysRev.95.228.

[169] K. L. Kowalski and D. Feldman. Elastic nucleon-deuteron scattering. *Phys. Rev.*, 130:276–291, 1963. https://link.aps.org/doi/10.1103/PhysRev.130.276.

[170] D. J. Ernst and Gerald A. Miller. Relativistic kinematics for elastic pion-nucleus scattering. *Phys. Rev. C*, 21:1472–1479, 1980. https://link.aps.org/doi/10.1103/PhysRevC.21.1472.

[171] D. J. Ernst, Gerald A. Miller, and D. L. Weiss. Fermi integration in the pion-nucleus optical potential. *Phys. Rev. C*, 27:2733–2741, 1983. https://link.aps.org/doi/10.1103/PhysRevC.27.2733.

[172] E. Breitmoser and H. Arenhövel. Coherent eta photoproduction on the deuteron in the S11 resonance region. *Nuclear Physics A*, 612(3):321 – 345, 1997. https://doi.org/10.1016/S0375-9474(96)00403-4.

[173] E. J. Moniz *et al.* Nuclear fermi momenta from quasielastic electron scattering. *Phys. Rev. Lett.*, 26:445–448, 1971. https://link.aps.org/doi/10.1103/PhysRevLett.26.445.

[174] T. E. O. Ericson and W. Weise. *Pions and Nuclei.* Clarendon Press, Oxford, UK, 1988.

[175] R. A. Arndt *et al.* Extended partial-wave analysis of πn scattering data. *Phys. Rev. C*, 74:045205, 2006. https://link.aps.org/doi/10.1103/PhysRevC.74.045205.

[176] R. L. Workman *et al.* Parameterization dependence of t-matrix poles and eigenphases from a fit to πn elastic scattering data. *Phys. Rev. C*, 86:035202, 2012. https://link.aps.org/doi/10.1103/PhysRevC.86.035202.

[177] M. L. Goldberger and K. M. Watson. *Collision Theory.* Wiley J. and Son Inc., 1964.

[178] R. D. McKeown *et al.* Inclusive reactions of pions on nuclei. *Phys. Rev. C*, 24:211–220, 1981. https://link.aps.org/doi/10.1103/PhysRevC.24.211.

[179] M. J. Vicente Vacas and E. Oset. Pion absorption in medium and heavy nuclei. *Nuclear Physics A*, 568(4):855 – 872, 1994. https://doi.org/10.1016/0375-9474(94)90363-8.

[180] H. J. Weyer. Pion absorption in light nuclei. *Physics Reports*, 195(6):295 – 367, 1990. https://doi.org/10.1016/0370-1573(90)90076-E.

[181] D. *et al.* Rowntree. π^+ absorption on N and Ar. *Phys. Rev. C*, 60:054610, 1999. https://link.aps.org/doi/10.1103/PhysRevC.60.054610.

[182] R. H. Landau, S. C. Phatak, and F. Tabakin. Improved theoretical pion-nucleus optical potentials. *Annals of Physics*, 78(2):299 – 339, 1973. https://doi.org/10.1016/0003-4916(73)90261-3.

[183] M. Ericson and T. E. O. Ericson. Optical properties of low-energy pions in nuclei. *Annals of Physics*, 36(3):323 – 362, 1966. https://doi.org/10.1016/0003-4916(66)90302-2.

[184] J. A. Carr, H. McManus, and K. Stricker-Bauer. Nuclear absorption of low energy pions and the pion-nucleus optical potential. *Phys. Rev. C*, 25:952–961, 1982. https://link.aps.org/doi/10.1103/PhysRevC.25.952.

[185] J. Chai and D. O. Riska. The reactive two-body part of the pion-nucleus optical potential. *Nuclear Physics A*, 329(3):429 – 449, 1979. https://doi.org/10.1016/0375-9474(79)90385-3.

[186] M. Gmitro, S. S. Kamalov, and R. Mach. Momentum-space second-order optical potential for pion-nucleus elastic scattering. *Phys. Rev. C*, 36:1105–1117, 1987. https://link.aps.org/doi/10.1103/PhysRevC.36.1105.

[187] K. Stricker-Bauer. *A study of the pion-nucleus optical potential*. PhD thesis, Michigan State University, 1979. https://doi.org/10.25335/M5PC2TD7H.

[188] K. Stricker, H. McManus, and J. A. Carr. Nuclear scattering of low energy pions. *Phys. Rev. C*, 19:929–947, 1979. https://link.aps.org/doi/10.1103/PhysRevC.19.929.

[189] K. Stricker, J. A. Carr, and H. McManus. Pionic atoms and low energy elastic scattering. *Phys. Rev. C*, 22:2043–2051, 1980. https://link.aps.org/doi/10.1103/PhysRevC.22.2043.

[190] C. A. Bertulani and P. Danielewicz. *Introduction to Nuclear Reactions*. CRC Press, Boca Raton, FL, 2004.

[191] C. F. Gauss. *Comment. Soc. Reg. Scient. Gotting. Recent.*, pages 39–76, 1814.

[192] E. Waring. Problems concerning interpolations. *Philosophical Transactions of the Royal Society*, 69:59, 1779. https://doi.org/doi:10.1098/rstl.1779.0008.

[193] D. Baye. The Lagrange-mesh method. *Physics Reports*, 565:1 – 107, 2015. https://doi.org/10.1016/j.physrep.2014.11.006.

[194] A. Deltuva, A. C. Fonseca, and P. U. Sauer. Momentum-space treatment of the coulomb interaction in three-nucleon reactions with two protons. *Phys. Rev. C*, 71:054005, 2005. https://link.aps.org/doi/10.1103/PhysRevC.71.054005.

[195] B. G. Ritchie *et al.* 50 MeV π^+ and π^- scattering from ^{12}C. *Phys. Rev. C*, 41:1668–1673, 1990. https://link.aps.org/doi/10.1103/PhysRevC.41.1668.

[196] M. A. Moinester *et al.* Elastic scattering of positive pions on ^{12}C at 49.9 MeV. *Phys. Rev. C*, 18:2678–2682, 1978. https://link.aps.org/doi/10.1103/PhysRevC.18.2678.

[197] K. K. Seth *et al.* Negative pion-nucleus elastic scattering at 30 and 50 MeV. *Phys. Rev. C*, 41:2800–2808, 1990. https://link.aps.org/doi/10.1103/PhysRevC.41.2800.

[198] B. M. Preedom *et al.* Positive pion-nucleus elastic scattering at 30 and 50 MeV. *Phys. Rev. C*, 23:1134–1140, 1981. https://link.aps.org/doi/10.1103/PhysRevC.23.1134.

[199] R. J. Sobie *et al.* Elastic and inelastic scattering of 50 MeV pions from ^{12}C, ^{32}S, and ^{34}S. *Phys. Rev. C*, 30:1612–1621, 1984. https://link.aps.org/doi/10.1103/PhysRevC.30.1612.

[200] A. A. Chumbalov, R. A. Eramzhyan, and S. S. Kamalov. DWIA in the momentum space for (γ, π^0) reaction near threshold. *Zeitschrift für Physik A*, 328:195, 1987. https://link.aps.org/doi/10.1007/BF01290662.

[201] Claude Semay and Bernard Silvestre-Brac. *Relativite restreinte*. Dunod, 2016.

[202] Luc Devroye. *Non-Uniform Random Variate Generation*. Springer-Verlag New York, 1986. https://doi.org/10.1007/978-1-4613-8643-8.

[203] N. M. Temme. Error functions, Dawson's and Fresnel integrals. In Frank W. J. Oliver, Daniel M. Lozier, Ronald F. Boisvert, and Charles W. Clark, editors, *NIST Handbook of Mathematical Functions*. Cambridge University Press.

[204] Albert Messiah. *Quantum Mechanics*. Dover Publications, 1962.

[205] C. M. Vincent and S. C. Phatak. Accurate momentum-space method for scattering by nuclear and Coulomb potentials. *Phys. Rev. C*, 10:391–394, 1974. https://link.aps.org/doi/10.1103/PhysRevC.10.391.

[206] Y. Fujiwara and K. Fukukawa. A practical method of solving cutoff Coulomb problems in momentum space: Application to the Lippmann-Schwinger resonating-group method and the *pd* elastic scattering. *Progress of Theoretical Physics*, 128(2):301–347, 2012. https://doi.org/10.1143/PTP.128.301.

[207] N. J. Upadhyay *et al.* Coulomb problem in momentum space without screening. *Phys. Rev. C*, 90:014615, 2014. https://link.aps.org/doi/10.1103/PhysRevC.90.014615.

[208] V. Eremenko *et al.* Coulomb wave functions in momentum space. *Computer Physics Communications*, 187:195 – 203, 2015. https://doi.org/10.1016/j.cpc.2014.10.002.

[209] Frederick W. King. *Hilbert Transforms*. Cambridge University Press, 2009. https://doi.org/10.1017/CBO9780511735271.